INFORMATION TO USERS

This manuscript has been reproduced from the microfilm master. UMI films the text directly from the original or copy submitted. Thus, some thesis and dissertation copies are in typewriter face, while others may be from any type of computer printer.

The quality of this reproduction is dependent upon the quality of the copy submitted. Broken or indistinct print, colored or poor quality illustrations and photographs, print bleedthrough, substandard margins, and improper alignment can adversely affect reproduction.

In the unlikely event that the author did not send UMI a complete manuscript and there are missing pages, these will be noted. Also, if unauthorized copyright material had to be removed, a note will indicate the deletion.

Oversize materials (e.g., maps, drawings, charts) are reproduced by sectioning the original, beginning at the upper left-hand corner and continuing from left to right in equal sections with small overlaps. Each original is also photographed in one exposure and is included in reduced form at the back of the book.

Photographs included in the original manuscript have been reproduced xerographically in this copy. Higher quality 6" x 9" black and white photographic prints are available for any photographs or illustrations appearing in this copy for an additional charge. Contact UMI directly to order.

UMI

A Bell & Howell Information Company
300 North Zeeb Road, Ann Arbor MI 48106-1346 USA
313/761-4700 800/521-0600

Shock Wave Interactions With Turbulence and Vortices

by

Juan H. Agui

A Dissertation Submitted to the Graduate Faculty in Engineering in partial fulfillment of the requirements for the degree of Doctor of Philosophy, The City University of New York.

1998

This manuscript has been read and accepted for the Graduate Faculty in Engineering in satisfaction of the dissertation requirement for the degree of Doctor of Philosophy.

9/15/98
Date

Professor Yiannis Andreopoulos
Chair of Examining Committee

9/15/98
Date

Dean Gerald Lowen
Executive Officer

Professor Yiannis Andreopoulos
Dept. of Mech. Eng., CCNY

Professor Peter Ganatos
Dept. of Mech. Eng., CCNY

Dean Charles B. Watkins
Dept. of Mech. Eng., CCNY

Prof. Nadine Aubry
Dept. of Mech. Eng., NJIT

Prof. Iraj Kalkhoran
Dept. of Mech., Manufacturing and Aerospace Eng., Polytechnic Univ.

Supervisory Committee

THE CITY UNIVERSITY OF NEW YORK

Abstract

Shock Wave Interactions With Turbulence and Vortices

by

Juan H. Agui

Adviser: Professor Yiannis Andreopoulos

The interactions of a planar shock wave with an induced vortical, vortex dominated and turbulence dominated, flow have been investigated experimentally in the CCNY Shock Tube Research Facility (STURF). Time-dependent measurements of total pressure, total temperature, three-dimensional velocity and vorticity were undertaken. A custom made hot-wire vorticity probe for non-isothermal flows was successfully validated in a turbulent boundary layer prior to its use for measurements of the interactions.

Three types of interactions were investigated through the use of various grid and wing models to produce: (1) turbulence - shock wave, (2) streamwise vortex - shock wave, and (3) spanwise vortex - shock wave interactions. Analysis of the turbulence - shock wave interaction revealed that fluctuations in longitudinal velocity and spanwise and normal vorticity were amplified most through the interaction. Wavenumber spectral amplification showed that all velocity and vorticity fluctuations were amplified mostly in the large wavenumber range. After interaction the enstrophy spectra gave the clearest evidence that there was a shift in rotational energy to higher wavenumbers. Examination of the stretching signals demonstrated the bursting behavior of the stretching process.

Enhanced stretching fluctuations and bursting behavior was found in most cases after interaction.

The effects of the shock wave on a concentrated streamwise vortex were more dramatic producing a two fold increase in the vorticity fluctuations at the two investigated Mach numbers. Wavenumber spectra of longitudinal vorticity indicated that most of the energy resided in the small wavenumbers, with a shift to higher wavenumbers after interaction. Particle Flow Visualization images provided evidence of core growth through the interaction.

The spanwise vortex - shock wave interaction indicated that significant vortex distortion and/or tilting of the vortex axis occurred through the interaction. The signals of spanwise vorticity through the uncompressed vortex strongly indicated larger fluctuations in on leading part of the vortex as it propagated downstream which were tied to larger fluctuations in the normal velocity. The flow visualization images provided some physical insight into this turbulent structure. These images also indicated the existence of longitudinal roll structures.

Acknowledgments

I would like to thank all those who have helped me through this wonderful educational journey. First of all, I need to thank my mentor and friend Dr. Yiannis Andreopoulos for his constant guidance throughout my years as a Ph.D. student. I profited from his expansive knowledge of the field and the ambitious goals he set on my research project. I am also thankful to the Mechanical Engineering technical staff, Mr. Jin Rui Chen and Mr. Luis Hernandez, for their assistance through the years.

I would also like to express my appreciation to my colleagues. I am thankful to my good friend and Laboratory partner, Dr. George K. Briassulis, whose company and technical discussions made things go much smoother in the lab. Also, I would like to make special mention of my dear friend, the late Dr. Apostoles Kostazos, whose abrupt and untimely death brought an end to such a young and kindly spirited person.

This culmination of all my research years would not have been possible without the support of my family. I am grateful to my wife who was most supportive and understanding in dealing with all aspects of this endeavor, and for bringing two beautiful daughters into our lives. Also, the love and constant pats on the back of my father and mother were ever present. Lastly, the persistent encouragement provided by my sisters and by my extended family, aunts, uncles, and cousins, has also helped me to continue on this journey. This is why this work is wholeheartedly dedicated to them.

The financial support provided by the CASI Department at the City College and the Magnet Program of the Graduate Center was deeply appreciated.

Table of Contents

Chapter 6

Chapter 7

Chapter 8

Chapter 9

Chapter 10

Chapter 11

Chapter 12

Appendices

References

Nomenclature

C	Chord length
c_p	Specific heat
c_f	Friction coefficient
G	Amplification ratio
h	Enthalpy
i	tensor index
k_l	Longitudinal wavenumber
L	Lift
M	Mach number
m	Mesh size
p	Pressure
Re	Reynolds number
Q	Magnitude of velocity vector (used in hot-wire calibration)
T	Temperature
t	Time
u	Streamwise velocity
u'	Fluctuating velocity or rms of fluctuations

u_τ	Friction velocity
v	Normal velocity
$\bar{v}$	Three dimensional velocity vector
w	Spanwise velocity

Greek symbols

ϕ	Power Spectral Density
ϕ'	Normalized Power Spectral Density by the square of the rms
μ	Dynamic viscosity
ν	Kinematic viscosity
ρ	Density
ω	Vorticity
ω'	Vorticity fluctuations

Subscripts

∞	External free-stream flow condition.
1	Atmospheric condition in front of incident shock.
2	External free-stream flow behind the incident shock.
D	Downstream of reflected shock; or after passage of the reflected shock.
inc	Incident flow condition

m	Measured quantity
R	Porous wall reflected shock property, or relative to the reflected shock
S	Shock wave property
t	turbulent
U	Upstream of reflected shock; or before arrival of reflected shock.

Superscripts

D	Downstream of reflected shock; or after passage of the reflected shock.
U	Upstream of reflected shock; or before arrival of reflected shock.

List of Tables

List of Figures

Chapter 1

1. Introduction

In recent years, interest has resurged in studying the interaction effects of shock waves on several important class of flows. This resurgence is a result, in part, of the current national initiative to invest in high speed research, which is primarily focused towards the development of a High Speed Civil Transport Vehicle (HSCT), and of a resource of new and more sophisticated research tools. Building upon research of the past 50 years, the current research efforts aim at developing a very accurate and realistic description of the interactions by providing a more detailed analysis of the corresponding flow field and shock structure. Specifically, the emphasis is placed on shedding more light on the unstable, violent and short lived phenomenon of vortex breakdown, turbulence amplification, and aerodynamic noise which is known to feed on these interactions.

Numerous recent studies have been motivated by the following interactions: (1) Streamwise vortices which are shed off the canard of a high speed jet plane flying at high angles of attack, and high transonic speeds, can travel downstream and interact with the shock wave formed on the main wing, or alternately, be sucked into the supersonic intake of the engine and interact with the shock wave formed at the inlet. (2) The flow field in the tip region of state-of-the-art transonic compressors, which are low-aspect-ratio, high through flow, highly loaded configuration, produces tip vortex structures which can interact with the passage shock waves formed in the core region between the surfaces of consecutive blades. (3) Concentrated vortices ejected from the aircraft engine can

encounter shocks on downstream structures. (3) Turbulent boundary layers in transonic and supersonic flows can interact with the impinging shock system. These interactions also occur in other applications which have received less attention, such as in combustion processes where energetic eddies (small but concentrated vortices) interact constantly with propagating and wall reflecting shock waves. Another example of propagating shock waves are what are known as *hammer shocks* which are evolved from pressure surges along the supersonic inlet nozzle of ramjet and Scramjet engines which propagate and strengthen towards the inlet encountering incoming vortices and turbulence along the way.

From these examples it is clear to see that the effects of shock wave interactions are evident in a wide range of practical applications. Each case involves a specific type of interaction. This leads to a formal classification of three types of interactions:

1) Shock wave - streamwise vortex interaction
2) Shock wave - spanwise vortex interaction
3) Shock wave - turbulence interaction

Research on the first interaction type, shock waves with streamwise vortices, is concerned with the need to more fully describe the influential role played by vortex structures in high speed compressible flows, particularly in those flows pertaining to aircraft and aerospace vehicle design. Also, turbomachinery is particularly susceptible to this interaction occurring in the blade tip region, where this region is known to significantly contribute to the overall system losses. The second interaction is usually associated with aerodynamic noise where concentrated vortices mostly spanwise in

orientation produce an amplification of the emanating acoustic field. The research focus on the third interaction, shock wave - turbulence interaction, is aimed at determining the mechanisms responsible for the turbulence amplification with particular application to boundary layers. The range of Mach number investigated in the literature extend from the slightly compressible, M=0.3, to high supersonic, M=3. The transonic region also poses an interesting problem in which shock waves appear and disappear locally producing a very unsteady phenomenon which in turn can lead to control or performance problems.

From a physical standpoint, these interactions pose a very interesting and challenging problem stemming from the abrupt nature of the shock that tends to produce sudden changes to both the shock structure itself and the incoming flow field. For vortex dominated flows the first two interactions are important. Figure 1.1 depicts the two types of interaction just before the respective structures meet with the shock. In real applications a combination of the two types of interactions exist in which either the vortex or shock is oriented obliquely to the other. In a random turbulent field eddies of all possible orientation impinge on the shock.

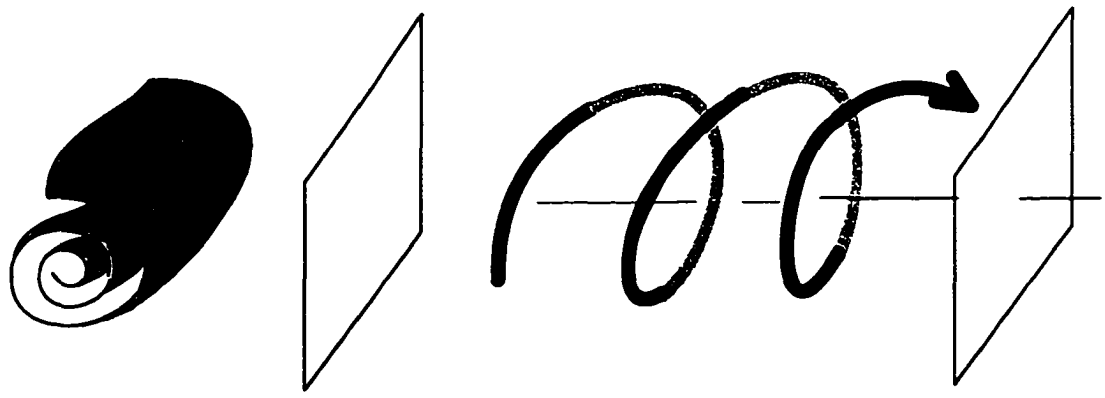

Figure 1.1: Vortex/shock wave interactions (a) spanwise vortex (b) streamwise vortex.

The presence of shock waves is known to significantly modify the flow field by producing strongly non-isentropic and compressible effects. In fact, the mean kinetic energy, translational energy mode, of the flow encountering the shock wave is lost to the rotational and vibrational energy modes, resulting in an increase in production of vorticity and entropy and significantly affecting their transport dynamics. Therefore characterizing vorticity transport, as well as entropy transport (not covered here), can provide valuable information on the interaction process.

A detailed analysis would require investigating the phenomenom at both the global and local scales as well monitoring time dependent flow properties. Quite a few studies have reported on the global aspect through Schlieren photography and have demonstrated that significant structural changes occur. Numerical studies have provided much of the detail flow analysis of the interaction. However, only a few of the experimental studies have attempted to obtain measurements through these interactions. Another aspect which has not received much attention is that of propagating shock waves which further complicate the interaction through the dynamics of the shock itself. Apparently much can be done in the way of experimental measurements and the results of which can be used as validation for the numerical results.

The present research will attempt to provide spatially and temporally well resolved measurements of the interaction. The prime focus will be to obtain vorticity measurements. Vorticity measurements, which were very scarce just a few years ago throughout the whole Fluid Dynamics and Aerospace community, have been shown to provide valuable dynamical information. This type of measurement is particularly

advantageous when studying unsteady, separated, and vortex dominated flows. The present study also makes use of other types of time-dependent measurement techniques as well as flow visualization techniques.

Chapter 2

2. Previous Work

This chapter provides an extensive look at previous work on three class of interactions: (1) shock wave - homogeneous and isotropic turbulence interaction, (2) shock wave - streamwise vortex interaction, (3) shock wave - spanwise vortex interaction,. Due to the independent interest in the physics behind each of the different interactions, past research work has treated each interaction independently.

2.1 Shock Wave - Turbulence Interaction

The interaction of shock wave with a homogeneous and isotropic turbulent field is of practical and fundamental interest. The development of modern transonic and supersonic airfoil and engine inlet design rely on designs which can manage the turbulence and shock system to produce the most favorable flow configurations. Wing structures, on the one hand, require that the effects of turbulence in the boundary layers be reduced in order to minimize of the turbulent momentum transfer and thereby the skin friction drag. The presence of a shock or shock systems amplifies the turbulence of the flow and therefore increases the drag. Shock waves, however, have very beneficial mixing properties and can be used advantageously to enhance the mixing the fuel and oxidizer. Fundamentally, study of this interaction can contribute greatly to the study of compressible turbulence.

Early investigations began with a linear analysis of the problem where the turbulence was treated as a perturbation to the velocity field. The governing equations

were linearized making possible theoretical treatment of the interaction. The disturbances were represented specifically by small vorticity, entropy and acoustic waves. Kovasznay (1953) first pointed out that these three modes were linearly independent. Lighthill (1953) investigated the energy which is scattered from the interaction of turbulence with sound and shock waves. Other researches by Ribner (1953), Moore (1953), Kerrebrock (1956), Chang (1957), and McKenzie and Westphal (1968) made use of linear theories in flows where three-dimensional disturbances interacted with shock waves. The main focus of these early researches was sound generation due to the interaction. Later Anyiwo and Bushnell (1982) began looking at turbulence enhancement (vorticity mode) from the interaction of acoustic and entropy wave modes with a shock wave. They also reported that oscillations in the shock wave structure produced a turbulence "pumping" effect. Debieve, Gouin, and Gaviglio (1982a, 1982b) used the Reynolds Stress Transport equation to track the evolution of the turbulence by using the Rapid Distortion Theory of Hunt (1973). They were able to identify the effects of convection and production as sources of turbulence which were different from those of the mean flow.

Zang, Hussainin and Bushnell (1984) numerically investigated the effects of amplification and generation of turbulence in a shock/turbulent boundary layer interaction and placed limits on the validity of the linear analysis.

Rotman (1991) used a second order Godunov's method for the time-dependent Euler's equation to solve for a passing shock over the turbulent flow. He found that the shock causes an increase in the Turbulent Kinetic Energy and that the length scale of the turbulent field behind the shock is smaller compared to that in front. He also found that an increase in initial turbulent Kinetic Energy caused an initially turbulent shock front to

become distorted. A disagreement with some experiments was brought out in terms of a comparison of length scales before and after the interaction.

Lee, Lele and Moin (1991) performed a numerical simulation of the interaction of a shock wave with turbulence using three different computational methods. The Turbulent Mach numbers investigated were large compared to experiments, of the order 0.6. They reported amplification of vorticity which compared well with the predictions of linear analysis. Correspondingly, enstrophy was amplified through the shock wave and then decayed with downstream distance. The turbulent kinetic energy evolution behind the shock showed significant non-linear effects. Their energy spectrum showed an enhancement at the smaller scales which resulted in a decrease in the overall length scale.

More recent and significant experimental investigations of this interaction have been reported for nearly the last two decades. The experiments have been carried out under three types of interactions:

(a) Shock wave - boundary layer interactions

(b) Shock wave - free shear layer interactions

(c) Traveling normal shock - compressible pipe flow interactions.

A breakdown of the significant works on each of the three interactions is provided below.

(a) Shock wave - boundary layer interactions

Ardonceau (1983) used Hot-Wire Anemometry (HWA) and Laser Doppler Anemometry (LDA) to measure turbulence quantities in a shock wave/ boundary layer interaction with an upstream M=2.25. He reported that the large eddies appearing downstream seem to encompass most of the turbulent kinetic energy. Also, the turbulent

kinetic energy and the Reynolds Stress increased rapidly during the initial phase of the interaction and then decreased further downstream. However, it was noted that this analysis does not hold for weak shock waves. Smits and Muck (1987) experimented with compression corners inclined at 8°, 16° and 20° to determine their effects on the compressible boundary layer with an upstream flow at M=2.9. They found significant increases on the turbulent stresses. The amplified stresses became greater with increasing effective normal Mach number, i.e. with increasing ramp angle. They also reported that the structure parameter $\overline{u'_1 u'_2} / \overline{u'^2_1}$ increased significantly and they attributed this mainly to the shock unsteadiness. Andreopoulos and Muck (1987) reported on the wall pressure fluctuations of a shock wave/ boundary layer interaction over a two-dimensional ramp in an upstream M=2.9 flow. Their pressure measurements confirmed the unsteadiness of the shock and they found that the frequency of the unsteadiness was of the same order as the bursting frequency of the upstream boundary layer, but independent of the downstream separated flow.

Kuntz, Amatucci, and Addy (1987) used a 2-D Laser Doppler Velocimetry (LDV) technique to study the effects of increasing shock strength and varying ramp angles on the turbulence of the shock/wave boundary layer interaction. Varying degrees of boundary layer separation were produced. They found that turbulent intensities as well as Reynolds' stresses were significantly increased and that the amount of the increase depended on shock strength.

Brown, Kussoy and Coakly (1985) pointed out that when the flow becomes separated additional effects arise which complicate the interaction, namely shock unsteadiness and large turning angles of the streamlines. They reported that with the

shock wave unsteadiness came an increase in turbulence intensities as well as a rise in the normal stresses. By performing a corresponding numerical analysis using the Navier-Stokes equation with a two eddy viscosity turbulence model they were able to predict the experimental mean flow field but not the fluctuating flow field.

Kussey, Brown, Brown, Lockman and Horstman (1987) employed an LDV technique in their analysis of the interaction at M=2.85. They also reported finding a discrepancy between the experimental and computed intensity of the turbulent kinetic energy. They concluded that the shock unsteadiness produced a "pseudo-turbulence" which a stronger effect for highly separated flow fields.

Deckker and Weeks (1976) investigated the shock wave/boundary layer interaction in a shock tube for shock strengths varying from 1.28 to 2.24. They found that stronger waves in addition to producing disturbances in the longitudinal direction also produced lateral disturbances which were significant.

(b) Shock wave - free shear layer interaction

Settles, Williams, Baca and Bogdonoff (1982) studied the interaction of a shock/free shear layer with a HWA technique and mean pressure probes. They found a small tremble of the wave system which was attributed to an unsteadiness of the flow field, and an amplification of the mean mass flux. Hayakawa, Smits and Bogdonoff (1984) used a HWA technique for the measurement of mass flow fluctuations in a shear layer/shock wave interaction. They found a substantial increase in turbulence intensity of mass flow rate and an increase in length scale through the interaction. Debieve and Lacharme (1985) experimented with compression corners to produce a shock wave/free

turbulence interaction. Their findings showed that the interaction brought about an increase in the turbulence levels by as much as 10 fold, an increase in slope of the velocity spectra and a transfer of energy to the lower frequencies

Velocity measurements using an LDV technique were performed on a shock wave/ free shear layer interaction by Samimy, Petrie and Addy (1986). Substantial increases in turbulence intensities, shear stresses and turbulent triple products were reported through the interaction .

Gutmark, Schadow, and Yu (1995) offers the most recent review of compressible turbulence in compressible shear layers.

(c) Traveling normal shock - compressible pipe flow interactions

Keller and Merzkirch (1990) looked at the interaction of grid generated turbulence with a shock wave in a shock tube. They showed that turbulence intensities were amplified and that this amplification was confined to the lower wavenumber spectrum. Troiler and Duffy (1985) used a 4 inch diameter shock tube to investigate the effects of shock wave interaction on the free stream turbulence. Despite the fact that grids were not used to introduce the turbulence, they found amplification of turbulence through the shock wave.

Honkan and Andreopoulos (1992) conducted experiments on grid generated turbulence a normal shock wave in an 1 ¾ inch diameter shock tube. They concluded that the turbulent intensities and length scales were increased after the interaction and it was argued that eddies had coalesced and amalgamated to form a larger eddy. The amplification was found to vary with wavenumber and the amplification was greater for

smaller eddies. Honkan, Watkins and Andreopoulos (1994) further investigated the shock wave interaction with grid generated turbulence, complimenting their results with total temperature measurements. Amplification of length scales, velocity and temperature fluctuations were found. Anisotropy arose after the interaction and was attributed to the increases in velocity fluctuations. They identified the ratio of the time scale of the mean strain across the shock wave to the length scale of turbulence as a new controlling parameter which can determine the time range (small values of this ratio) where Rapid Distortion Theory (Hunt, 1973) and its extension to compressible flows (Debieve et al. 1980, 1985) may be applied to describe the bulk characteristic of the interaction.

Jacquin, Blin and Geffroy (1991) looked at the interaction of a normal shock wave with grid generated turbulence and a turbulent jet and made comparison to linear analysis. They found that no considerable turbulence amplification was produced and the decay of turbulent kinetic energy increased downstream of the shock.

Briassulis (1996) performed an experimental study of a planar traveling shock wave interacting with an isotropic and homogeneous turbulent field generated some distance behind a grid. He found that turbulence amplification of pressure fluctuations through the shock waves depended on the initial turbulence level, as dictated by the grid mesh size, and the shock strength. Spectral analysis revealed that the amplification showed variation through the wavenumber spectrum. The dissipation rate of the kinetic energy was found to decrease after the interaction while the dissipative length scales analysis revealed that the turbulent eddies are always significantly compressed in the longitudinal direction. However, the length scales in the normal direction indicated a variation existed with shock strength: from no change in length scale for weak

interactions, to an increase in scales for higher shock strengths, to a decrease in scales, indicating compression for the highest shock strengths. He concluded by stating that the largest eddies with low velocity fluctuations are affected most by the interaction with the shock.

Of the three experimental interactions, the third category produces the cleanest interaction, i.e. to say interactions without added effects. In the first two cases shear flow, bounded or free, interacts with an oblique shock generated by a compression corner. In this category, large gradients in static pressure and, skin friction and mass flow rate occur and if the turning angle is large enough the flow separates and becomes unsteady due to shock oscillation. The previous works show: (1) the shock oscillation occurring downstream of the interaction causes even more unsteadiness in the flow field; (2) oscillation in the shock wave develops in the longitudinal direction with wrinkles in the spanwise direction; (3) continued compression downstream of the shock; (4) streamline curvature due to high turning angles; (5) wall proximity effects which result in high turbulence intensities and therefore, high flow anisotropy. As a consequence of all these influences, the phenomenon of turbulence amplification as a direct result of the Rankine-Hugonoit jump conditions is considerably distorted and all previous results are masked by these additional effects. The present work makes use of this third type of experimental interaction.

2.2 Shock Wave - Streamwise Vortex Interaction

The first comprehensive study on the shock wave - streamwise vortex interaction was reported in the work of Delery, Horowitz, Leuchter, and Solignac (1984). The

authors were motivated by an interest in understanding the process which leads to vortex breakdown of the streamwise vortex. Two external conditions which can significantly influence the characteristic structure of the streamwise vortex as well as the conditions which bring about vortex breakdown are strong adverse pressure gradients and interactions with shock waves.

In the first part the work of Delery et al. (1984), the destabelizing effect of an impressed adverse pressure gradient on a leeward drifting vortex was studied. Two type of vortex structures were looked at. One vortex was generated at the trailing edge of two oppositely curved blades mounted onto a small core sting. The vortex formed took on a dual-branch spiral shape. The other vortex was generated by means of a delta wing, where a pair of counter rotating streamwise vortices are generated. The objective of studying the first vortex type was to determine its effects on the turbulence, while the latter was used to determine the requirements for vortex breakdown which is relevant to the present topic. The delta wing vortex was observed to have a pronounced depression region at the center which gave an equally pronounced speed surplus at the same positions. In general, destabelization was characterized by a helical distortion of the vortex core, forming of a reverse flow bubble when breakdown occurred, a substantial dip in axial velocity at the center, and deformation of the tangential velocity profile. A criterion for vortex breakdown was established based on vortex strength and the strength of the adverse pressure gradient.

The other aspect of their study involved determining vortex breakdown due to the interaction of a streamwise vortex from a delta wing with a planar shock. The two controlling parameters in their interaction was the swirl rate, which is defined by the ratio

of maximum tangential velocity to the external axial velocity component, and the other was the shock strength defined in terms of the ratio of upstream to downstream pressure, p_2/p_1. They found that, in the absence of vortex breakdown, the general structure of vortex does not undergo any significant change through the shock. Specifically, the maximum tangential velocity remains invariant so long as the vortex does not burst. However when vortex breakdown does occur the swirling component is seen to collapse. The most significant changes were sensed in the axial velocity component. The drop of the axial velocity in the external flow seen to follow the theoretical drop predicted from the Hugoniot jump conditions, however the axial velocity at the core center which was slightly higher than the external flow before the interactions underwent an even sharper drop through the interaction. As a consequence the swirl rate increased drastically. It is rather well known that the stability of the vortex decreases when the relative intensity in swirl motion increases. They showed, in fact, that breakdown occurs when the helix angle $\gamma = \tan^{-1}(V_t/V_x)$, i.e. the angle formed from the tangential and axial velocity components, locally reaches a value of some 50°. The passage of the shock significantly increases the helix angle everywhere by reducing V_x, but more so at the core center where the largest drop in axial velocity is encountered. Therefore after the interaction the velocities in the vortex core can potentially produce helix angles which approach the critical value of 50°, locally, a state in which the vortex will burst with the slightest disturbance.

In general, it was found that the interaction with the shock wave showed an aggravated effect of destablelization. Vortex breakdown was marked by and expansion of the dissipative core of the vortex. A vortex breakdown limit was again established based on swirl rate, which is related to vortex strength, and the shock strength. The

interaction was also modeled numerically using Euler's equation which showed that viscous effects play a negligible role. In the absence of vortex breakdown, the numerical model accurately described the flow. It also predicted a vortex breakdown limit, under inviscid flow conditions, that was in good agreement with experiment.

Metwally, Settles and Hortsman (1989) and Cattafesta and Settles (1992) studied the interaction of a normal shock wave with streamwise vortices generated through swirl vanes, where the vortex strength increased with vane angle. Both researches reported that the interaction always produced an unsteady flow and a distortion of the shock front. The shock distortion was characterized by a bulged shock structure which was inclined forward (towards the incoming flow) and its size was of the order of the incoming vortex core for weak interactions. For strong interactions the distortion was marked by a larger forward bulged shock structure. Additionally, the two researches extended the vortex breakdown curve proposed by Delery et al. (1984) to include a wider range of Mach numbers.

Kandil, Kandil and Liu (1991) performed unsteady Navier-Stokes calculation of the interaction of a quasi-axisymmetric vortices with normal shocks. Several modes of vortex breakdown were presented. Kandil and Kandil (1993) performed a full Navier-Stokes calculations of the shock wave induced vortex breakdown over a 65° delta wing. Their results showed that the vortex core experiences an unsteady, supersonic breakdown upon passing through the spanwise shock formed near the trailing edge of the delta wing.

The work of Kalkhoran (1994) detailing the effects of vortex distortion of a traveling streamwise vortex through a shock wave formed in front of wedge leading edge

obstruction in a Mach 3 stream revealed through spark shadowgraph photography the nature of the altered vortex structure downstream of the shock. Although the vortex core oscillated slightly in the spanwise direction there were instances where the vortex underwent a head on collision with the leading edge of the shock front, which was also aligned with the wedge leading edge. The shock wave that formed during the head on collision was detached at the leading edge and this, the authors argued, was attributed most likely to the passage of the vortex center through this part of the shock wave where lower streamwise Mach number are encountered or where high flow deflection angles created by the vortex induced flow angularity can arise. Behind the shock, the vortex dominated flow was markedly contained within a conical region surrounded by a supersonic flow region. A slipstream delineated the two flow regimes: the vortex induced and dominated inner region and the outer supersonic region. The subsonic condition in the transmitted core region also tended to induce to the shock to propagate further upstream. When the incident vortex flow veered slightly away from the leading edge this marked the disappearance of the detached shock wave. The shock wave then becomes attached to one side of the wedge surface depending on the direction of the vortex's deviation. The vortex core distortion was manifested by a growth or expansion of the core downstream of the detached shock wave. Later Kalkhoran, Smart and Betti (1996), investigated the interaction of a supersonic wing tip vortex with a normal shock, formed by a choked inlet, in a 2.49 Mach number flow. Spark shadowgraph, laser sheet planar flow visualization and pitot type pressure measurements using high response transducers were used in the analysis. The spark shadowgraph revealed that the interaction led to a conical shape shock wave and core growth downstream of the shock wave. They also

showed that the flow downstream of the shock was highly turbulent. The laser sheet visualization showed a significantly larger core downstream of the interaction. The pressure signal indicated a higher frequency oscillation after the interaction.

From the two preceeding analysis which included the work of Delery et al. (1984) and Kalkhoran (1994) and Kalkhoran et al. (1996) helpful details were learned about the effects of the shock wave streamwise vortex interaction. The work of Delerey et al. quite fully portrayed the phenomena that leads to vortex breakdown while Kalkhoran provided a visual aid showing some indication that vortex core distortion might be enhanced by the subsonic condition downstream of the shock, while influencing the shape and position of the shock structure. Neither of these two researches accounted for any direct measurement of rotational activity of the vortex. During breakdown the vortex flow suddenly dies and leaves behind a reverse flow bubble region. It would be advantageous to make measurements of vorticity of the vortex flow through the shock to determine how and when rotationallity is suddenly halted. Also the instability of the state leading to breakdown can effectively be analyzed by the fluctuations in vorticity.

2.3 Shock Wave - Spanwise Vortex Interaction

Shock wave and spanwise vortex interactions were studied quite extensively in the 1950's and 1960's primarily by Ribner (1954), Hollingswoth and Richards (1955). Dosanjh and Weeks (1964), and Weeks and Dosanjh (1967). With a mixture of linearized wave theory and schlieren and shock tube experiments utilizing inteferometry techniques for visualization, a consistent theory of the interaction was possible. The primary interest of these researchers was the production of noise from this interaction and their results

reflect this interest, however the vortex flow field did receive some discussion. Ribner (1954) first studied the interaction of a plane shear wave with a plane shock wave and found that a sound wave is produced which is inclined at the Mach angle to the refracted shear wave. He then postulated from a fundamental consideration the concept of decomposing the spanwise vortex into shear layers inclined at different angles to the flow. The full vortex is then represented as a superposition of the effects of such shear waves and plane shock wave interactions. Later Hollingsworth and Richards (1955) applied Ribner's analysis to the vortex - shock wave interaction complimenting it with observations from a schlieren experiment performed in a shock tube facility. In their analysis they represented the vortex by a distribution of isentropic and sinusoidal shear waves. They found that the sound wave produced varied circumferentially in intensity, however this variation was not symmetric producing alternating compression and rarefaction regions and a strong compression region behind the transmitted shock.

The interaction of a traveling columnar starting vortex a planar shock wave was experimentally investigated in a shock tube facility by Dosanjh and Weeks (1964). The interaction was found, from the resulting measured pressure field, to generate a cylindrical sound wave with asymmetric varying intensity confirming Hollingswoth and Richards' (1955) finding and which they represented using monopole, dipole and quadrupole functions. This was accompanied by an abrupt distortion of both the shock front and the vortex core. The shock front is deformed by the relative velocities associated with the incoming vortex. The columnar starting vortex which rotates in a negative spanwise sense deflects the upper part of the shock front forward relative to its propagation direction while the lower part is tilted back by the opposing flow velocities.

The vortex core is suddenly compressed in the direction of shock wave propagation after the interaction while the dimension of its other axis is preserved. Further, a slight preccesing of the now elliptical vortex core in the direction of vortex rotation was also reported which was a consequence of shock front distortion. After some relaxation time of the order of 200 μs the vortex resumed its original shape after which it continued its normal rate of decay until high pressure front arrived and hasten the decay. Later Weeks and Dosanjh (1967) applied Kirchoff's theorem for the non-homogeneous wave equation using Stratton's method in two dimensions to account theoretically for the monopole. dipole, and quadrupole source terms.

Nuemann and Hermanns (1973) also showed through experiment that curved diffracted shocks were produced on either side of the vortex. The vortex's rotation influenced the development of these shock structures by accelerating one relative to the other, the two structures finally merged to form a transmitted shock which was distorted from the initial planar shape. In addition the transmitted shock also consisted of additional shock structures, which were more prominent for strong interactions where these shock structures appeared as Mach structures attached to the transmitted shock.

Numerical work has been performed very recently by Ellzey, Picone and Oran (1992). In this work the spanwise vortex flow was modeled as a composite vortex. The composite vortex is defined as a nonsingular vortex flow characterized by an inner core of uniform vorticity with circulation Γ and an outer region consisting of opposite vorticity with a total circulation $-\Gamma$. Then a counterclockwise rotating vortex in the two-dimensional polar coordinate is expressed by,

$$v_\theta = \frac{v_{max}}{r_1} \cdot r \qquad 0 < r < r_1 \qquad (1.1)$$

and

$$v_\theta = Ar + \frac{B}{r} \qquad r_1 < r < r_2 \qquad (1.2)$$

where v_{max} is the maximum velocity defined at $r = r_1$. The strength of the vortex is defined by the maximum tangential velocity while twice the radius r_1 is referred to as the core diameter. Outside of the range of r_2 the velocity is zero everywhere. In addition the pressure field is assumes the form of equation 1.2.

Ellzey et al. (1992) took a two part numerical approach to the analysis to the interaction of spanwise vortices with a plane normal shock. In the first analysis they were able to describe pictorially the evolving shape of the shock distortion due to the interaction of a counter rotating vortex pair and a plane shock. Four degrees of interactions were investigated: (1) weak vortex - weak shock, (2) weak vortex - strong shock, (3) strong vortex - weak shock, and (4) strong vortex -strong shock. It was found that only the strong vortex interaction with both the weak and strong shock resulted in a significant distortion of the shock front, the type of structure observed being classified as a regular reflection and a Mach reflection for the two interactions respectively. The transmitted shock front showed a merger of the incident shock structures and additional reflected shocks. The second part of the analysis focused on the acoustic wave structure which emanates from the interaction of a single vortex and a plane shock. The process by which the acoustic wave acquires asymmetrical intensity at the cylindrical wave front was made clearer. Unlike the linear wave theory of Ribner, the simulation showed more

similarity to the experimental results of Hollingsworth and Richards (1955) and Dosanjh and Weeks (1964) in which an intense compression region was attached to the propagating shock front. The simulation produced initially a quadrupolar acoustic wave front and additionally a reflected curved shock front. An intense compression wave attached to the shock front was most evident for the strong vortex - strong shock interaction, where the reflected shock structure propagated faster and finally merged with the quadrupole acoustic wave. Shock distortion was accompanied by a system of curved reflected shocks in its wake. The vortex core also became distorted taking on an elliptical shape. The major axis which was oriented parallel to the shock front preserved its original dimension. The vortex then after some time resumed back to now a steady-state circular shape, however this recovery to steady state was much quicker for the strong vortex interaction. It was also found that the dominant mechanism controlling vorticity was a redistribution due to compression of the vortex as oppose to the baroclinic pressure mechanism which dominates in stratified flows. Finally one of the most important results which indicates how strongly vorticity is effected by the interaction is the time evolution of the total enstrophy of the vortex flow. It was found that rapid amplification of vorticity resulted when a strong vortex interacted with a strong shock wave.

This final conclusion reached by Ellzey et al. (1992) regarding amplification of vorticity through the shock serves as the impetus for the present research . In their case they measured the total enstrophy of the flow through the shock. A more representative measure of vortical changes would require monitoring the local time resolved vorticity through the shock and its mean statistics.

Chapter 3

3.1 Research Objectives

In reviewing the existing work on the three types of interactions, it became evident that a deficiency existed in terms of time-dependent measurements of these interactions. While the existing numerical work does provide a significant amount of data on the fluctuating nature of these flows, only scarcely available, corresponding, measured data exists. Obviously, to bridge this gap more time-dependent measurements have to become available to validate the numerical results.

The objectives of the present research is two-fold. An attempt is made to improve our understanding of: (1) how different vorticity components are transferred through the shock wave; and (2) how concentrated vortices are affected by the shock wave. Closely associated with this is a study to identify the mechanisms that may be responsible for turbulence/vorticity amplification. Also, a consideration of Haye's (1957) analytical relation of vorticity jumps across a surface of discontinuity, in light of the present data, is addressed.

The approach to meet the research objectives requires the development of new experimental techniques some of them being applied the first time in such flows. Specifically, vorticity measurement techniques are particularly challenging and difficult, and the present case is no exception. Because of compressibility effects this difficulty is further compounded. Consequently, vorticity measurements are currently scarce in incompressible flows and nonexistent in high speed compressible flows. The author has been motivated and encouraged by recently published vorticity measurements (see e.g.

Honkan and Andreopoulos, 1997), and by the prospect of obtaining high quality vorticity measurements in compressible flows for the first time.

The shock tube is a suitable facility to investigate these interactions. The flows generated in this facility are very clean since it is not powered by any electromechanical machine. The CCNY facility, in particular, employed here is one of the largest diameter shock tubes in existence. Therefore the shock waves produced have a rather large planar mid-section, not affected by the boundary layers from the pipe wall, with which to interact with relatively large vortex structures. Interactions are possible by having the incident shock wave reflect off a porous end wall, which then propels it upstream to interact with the incoming flow. The porosity of the end wall, also, allows a partial mass flux escape thereby sustaining a flow behind the reflected shock. Experiments were performed independently on each type of interaction using a suitable vortex or turbulence generator. Wing models were used to generate both the streamwise and spanwise vortices, while heavy gauge wire screens were used to generate the turbulent flows all of which interacted with the reflected shock wave.

The statistics of the present data is used to characterize the flow field before and after interaction with shock wave. A length scale analysis utilizing spectral techniques is performed in order to determine of the dominant scales for both the velocity and vorticity fluctuations. A comparison of scales before and after interaction with the shock wave is used to show which scales are amplified or attenuated through the interaction.

Lastly, as it has become fashionable and revealing to supplement results with flow visualization images, the current effort also includes the results of a Particle Flow-Visualization technique applied to the vortex flows.

3.2 Thesis Organization

In addition to the experimental goals, chapter 4, offers a compilation of useful equations and their scope of application to the current flows. An analysis of the role of each individual term in the governing equations, it is believed, are always useful in providing physical interpretation to a particular flow application, and so this type of analysis is offered in chapter 4.

Chapter 5 gives an extensive description of the experimental facility, instrumentation and experimental techniques employed in the current research. Chapter 6 provides details of the data reduction techniques and experimental uncertainties.

Due to the importance of the vorticity probe to this study, chapter 7 is devoted entirely to the design and testing of this probe. Reasons for why this particular probe was selected is explained. In the last section of this chapter, the results of validating the probe are presented.

The following chapters, 8 through 10, will give individual analysis of each interaction in terms of all pertinent measurements and flow visualizations obtained from experiment. Each of these chapters will provide a table of operating conditions of the related experiments. The presentation and discussion of results are provided thereafter.

For the turbulence interactions, covered in chapter 8, extensive statistical and spectral tools are used to characterize the turbulence before and after the interaction. In chapters 9 and 10, the structure of the vortex before the interaction is given considerable attention. Its state after the interaction are either studied or inferred from the resulting data. Flow-visualization images are used to aid in the analysis.

Chapter 11 examines the distortion of the shock wave through its interaction with the tip vortex flows. A mathematical approach to determine shock distortion by using the three velocity components right before and right after the interaction with the shock wave is presented. A discussion of Haye's (1957) relation to present data is presented.

The Concluding remarks, chapter 12, will bring out the most notable results and will show the similarity and differences among the different interactions. After all, these flows are intrinsically related given the vortical nature of turbulent flows. The appendices provide supplementary topics.

Chapter 4

4.1 Governing Laws

This section will provide some theoretical background into the physics of the flows and the interactions involved. Related governing equations will be covered as well as some useful relations. The governing equations are useful because they represent conservation laws and therefore they serve as a window into the physics of the flow. The magnitude, increase or decrease, of each term in a particular equation determines how a specific variable might be affected. With this perspective, some analysis of the governing equations will be offered

A mix of tensor and vector representations will be used for the equations set forth in this chapter. Each form of notation has its advantages. For example the very important strain rate tensor which is involved in such mechanisms as the viscous processes and vortex stretching is readily recognized in tensor notation by S_{ij}. On the other hand, vector notations are useful in yielding concise representative equation of vector variables and they do away with sometimes complex tensor notation.

The mass conservation equation for compressible flows is given by

$$\frac{\partial \rho}{\partial t} = -\frac{\partial (\rho u_i)}{\partial x_i} \tag{4.1}$$

When compressibility is a factor in the flow, equation 4.1 shows that density plays a role in the velocity field, and therefore the two fields are coupled.

Fluid motion is manifested in three modes: translation, straining, and rotation.

The various forms of the momentum equation, for both incompressible and compressible flows, describes the relation between the velocity and straining fields of the flow. Rotation is best described by equations involving the vorticity vector.

The momentum equation is expressed as,

$$\frac{\partial}{\partial t}(\rho u_i) = -\frac{\partial}{\partial x_j}(\rho u_i u_j + p\delta_{ij}) + \frac{\partial \tau_{ij}}{\partial x_j} \tag{4.2a}$$

or alternately,

$$\frac{\partial u_i}{\partial t} = -\frac{\partial}{\partial x_j}(u_i u_j + p\delta_{ij}) + u_i \frac{\partial u_j}{\partial x_j} + \frac{\partial \tau_{ij}}{\partial x_j} \tag{4.2b}$$

where,

$$\tau_{ij} = \frac{\mu}{Re}\left(\frac{\partial u_i}{\partial x_j} + \frac{\partial u_j}{\partial x_i} - \frac{2}{3}\frac{\partial u_k}{\partial x_k}\delta_{ij}\right) \tag{4.2c}$$

If the curl operation, $\varepsilon_{pqi}\frac{\partial}{\partial x_q}$, is performed on equation (4.2b), an equation for vorticity is obtained,

$$\frac{\partial \omega_i}{\partial t} + u_j \frac{\partial \omega_i}{\partial x_j} = \omega_j S_{ij} - \omega_i \frac{\partial u_j}{\partial x_j} + \varepsilon_{ijm}\frac{1}{\rho^2}\frac{\partial \rho}{\partial x_q}\frac{\partial (p)}{\partial x_j} + \varepsilon_{ijm}\frac{\partial^2 \tau_{ij}}{\partial x_q \partial x_j} \tag{4.3a}$$

This can be compared to the incompressible form of the vorticity equation,

$$\frac{\partial \omega_i}{\partial t} + u_j \frac{\partial \omega_i}{\partial x_j} = \omega_j S_{ij} + \nu \frac{\partial^2 \omega}{\partial x_q \partial x_j} \tag{4.3b}$$

It is evident that equation (4.3a) contains more source terms (2 more) of vorticity than its incompressible counterpart, equation (4.3b). The first term on the right, present in both

equations, is the very important stretching term which expresses the effects of vortex line stretching or reorientation. This term can also be considered in terms of amplification and attenuation of vorticity. The term $\omega_i \frac{\partial u_i}{\partial x_i}$ can be considered to be an added stretching/tilting term due to dilitational effects. The next term shows that vorticity can be influenced by the product of gradients of density and pressure, where this term is different from zero only when the gradients of density and pressure exists in different directions. This term is zero in isothermal flows or when density is a function of pressure. The last term represents viscous effects which act to generate or destroy vorticity near boundaries.

The energy equation is given by,

$$\frac{\partial E_t}{\partial t} = -\frac{\partial}{\partial x_i}[(E_t + p)u_i] - \frac{\partial q_i}{\partial x_i} + \frac{\partial}{\partial x_j}(u_i \tau_{ij}) \qquad (4.4a)$$

where,

$$E_t = \frac{p}{(\gamma - 1)} + \tfrac{1}{2}\rho u_i u_i \qquad (4.4b)$$

Compressible flows are characterized by high energy and high thermodynamic properties. The total energy, equation 4.4b, is composed of sum of the enthalpy in terms of pressure, and the kinetic energy. Thus, the total energy can also be interpreted in terms of potential energy, the energy stored in terms of the fluid's thermodynamic properties, and of course the kinetic energy which is due to the fluid's motion.

The first term on the right hand side of the energy equation, equation (4.4a), represents the advection of total energy flux, E_t, and the work done by pressure. The

advection part represents the action energy due to fluid lumps, possessing a specific E_t, passing over some point in a fixed coordinate system and thereby changing the energy at this point. Pressure work represents the transfer of energy produced by the local pressure field deforming in the normal direction the boundaries of a fluid element. This can be thought of in terms of changes in the size of the specific volume of the fluid element and therefore the thermodynamic properties. The second term on the right hand side of equation (4.4b) represents the heat conduction in the fluid medium. This becomes important when temperature gradients become large. The last term represents the work done by viscous forces. Therefore the transport of total energy flux is governed by advection, heat conduction, pressure work, and work done by shear forces.

One great simplification that can be made to the governing equations is the assumption of inviscid flow. This assumption has been the foundation of most of the work on compressible flows particularly in the study of shock waves and the field of acoustics. Theoretical treatment of uniform flows through shock waves, which is well established, is possible because viscous effects are considered negligable. Acoustics makes the further assumption that disturbunces are small compared to their mean values. This is known as linear theory.

Invscid theory leads to much simplified equations which are more treatable. An equation which governs the vorticity field of compressible inviscid flows and relates it to thermodynamic properties is Crocco's equation,

$$\frac{\partial \bar{v}}{\partial t} - \bar{v} \times \bar{\omega} - T\nabla s = -\nabla\left(h + \frac{1}{2}\bar{v} \cdot \bar{v}\right) \tag{4.5}$$

This equation is extremely important in establishing the generation of vorticity through shocks, a flow structure which is strongly non-isentropic. The term $\nabla\left(h+\frac{1}{2}\vec{v}\cdot\vec{v}\right)$ is the total enthalpy, or total energy, of the flow which is considered to remain unchanged through the shock in the absence of heat addition. Therefore, under steady conditions new vorticity can be generated behind the shock if a variation of entropy, represented by entropy gradients, exists. Notice that any new vorticity produced through the shock, which must abide by the $\vec{v}\times\vec{\omega}$ term, must be oriented perpendicular to the local velocity vector in the absence of viscous effects.

4.2 Shock Wave Relations

Shock waves which are physically very thin layers, with a thickness of the order of the mean free path of molecules, are generally not treated with the conservation laws, (presented in section 4.1) although numerical codes have with varying success been able to model the shock front. Therefore the shock wave is treated as a surface of discontinuity and the conservation laws are applied on either side of this discontinuity.

The plane shock wave relations have a strong theoretical foundation rooted in the continuity, momentum, and energy equation of inviscid fluids complimented with the Rankine-Hugoniot jump conditions. Equations for the plane shock wave relations are readily available in many textbooks (see .e.g Anderson, 1990 , Saad, 1993).

4.3 Reflection Off a Porous Wall.

When the incident shock reflects off the end wall of the shock tube, depending on the porosity of the wall, it will be returned with diminished strength. Even in the case of a solid wall viscous losses occur due the reversed and stagnant flow behind the reflected shock, which takes energy away from the shock. The viscous and momentum losses associated with the flow escaping through the porous wall can be modeled. The governing equations at the porous wall are given by,

$$\rho_2(W_r + U_p) = \rho_5(W + U_5) \tag{4.6}$$

$$p_2 + \rho_2(W_r + U_p)^2 = p_5 + \rho_5(W_r + U_5)^2 \tag{4.7}$$

$$c_p T_2 + \frac{(W_r + U_p)^2}{2} = c_p T_5 + \frac{(W_r + U_5)^2}{2} \tag{4.8}$$

Here the subscripts p and 5 correspond to piston velocity, or flow velocity behind the incident shock, and the velocity behind the reflected shock which is non-zero. W_r is the reflected shock speed.

If the resistance to flow imposed by the porous wall is modeled as a pressure loss with an associated loss factor, K, the exiting velocity is then given by,

$$U_5 = U_{\text{porous wall}} = \sqrt{\frac{2\Delta p}{\rho_5 K}} \tag{4.9}$$

This porous wall modeling is used for the numerical simulation presented in section 5.1.2.

4.4 Vortex Flows

Free vortex flows refer to those flows where the large scale fluid motion, separated from bounding surfaces, displays coherent rotational behavior. Vortex flows originate from viscous forces felt near solid boundaries. At some distance along an aerodynamic structure a local negative pressure gradient may develop which in turn induces boundary layer separation. This process is marked by a lifting of the turbulent part of the boundary layer, an increase in boundary layer thickness, and reverse flow regions associated with vortical structures at the edge of the boundary layer. Further along, separation creates a viscous vortex sheet which can subsequently become detached from bounding surfaces and then incorporates itself into the free stream flow. Secondly, vortex flows can also originate from separation of the shear layer in the leading edge region of a bluff body, such as circular cylinder. This is the well known mechanism of vortex shedding which occurs in the wake flows of bluff bodies with bluff leading and trailing edges. A third method of vortex generation is derived from lift theory, where the lift on the wing is produced as a result of the circulation that develops around the wing. A starting vortex is generated downstream of the wing at the instant a sudden change in flow properties is experienced, which counteracts the circulation formed around the wing due to a reaction moment to counteract the torque imposed by the flow. The origin of all these vortical flows is consequently derived from viscous stresses at the walls, constituting then a viscous and dissipative flow in vortex core region.

Vortices produced by airfoil structures pertain to the last method of vortex generation. In this case the initial circulation of the detached vortex core is given by the circulation formed over the wing, which is related to the lift produced by the wing.

$$L = \Gamma \rho U_{\infty} \tag{4.10}$$

The circulation decays with time and downstream distance from the wing due it its viscous nature.

Saffman (1992) identifies specific layers in the viscous vortex which characterize different rotational behavior. Also, Bershader (1994) gives an account of layered structures as shown in figure 4.1: (1) Region I is analogous to the viscous sublayer in the turbulent boundary layer and is virtually in solid body rotation. ($\Gamma \sim r^2$, $v_\theta \sim r$, where Γ, v_θ, and r are the circulation, tangential velocity and radius from center of vortex respectively). (2) Region II is analogous to the law of the wall in the turbulent boundary layer. v_θ reaches its maximum value here ($\Gamma \sim \ln r$). (3) Region III is a transition region to the outer inviscid region analogous to the Defect Law in boundary layers). (4) Region IV. this is the irrotational region where circulation becomes constant.

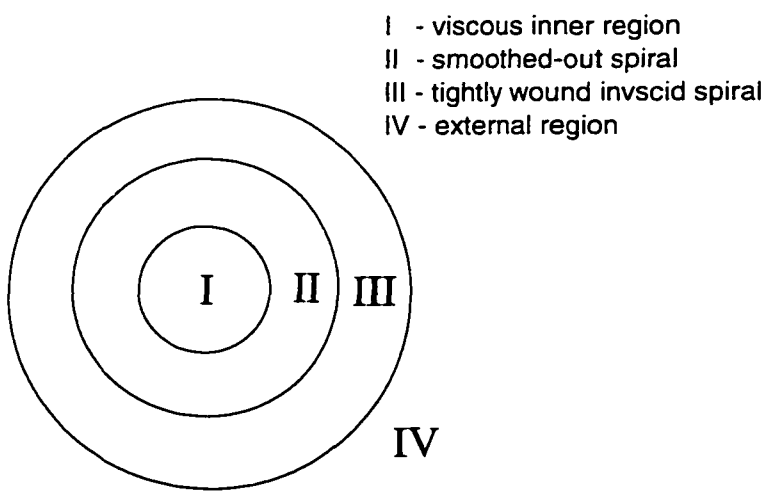

Figure 4.1: Sketch of viscous vortex structure

Colonius, Lele and Moin (1991) argued that the free compressible vortex flow can evolve on two time scales, the fast acoustic time scale and the slow viscous time scale. In the present work the faster acoustic time scale dominates first during the vortex's interaction with the shock wave simply because the shock phenomenon occurs on this and even faster time scales. On this time scale viscous effects are negligible and if the radial velocity is also assumed negligible or nonexistent then the momentum equation gives a balance between the pressure gradient and the centripetal force,

$$v_\theta^2 = \frac{1}{\rho}\frac{\partial p}{\partial r} \tag{4.11}$$

The slow viscous time scale dominates after the initial acoustic wave has emerged and it accounts for the decay of the vortex. At this time scale viscosity diffuses vorticity outward from the vortex core and thereby gradually weakens the vortex until it becomes virtually unnoticeable.

A condition that sometimes affects longitudinal vortices is the vortex breakdown phenomenon. This condition is characterized by an initially slender vortex tube which exhibits a rapid change. There are two general modes to the breakdown phenomenon. The breakdown assumes the form of a symmetrical bubble in appearance with reverse flow known as 'bubble mode', or secondly, in the form of non-symmetrical spiraling or helical shape known as the 'helical mode'.

4.5 Vorticity Through Shock Waves

By a similar process a velocity shear wave can also create new vorticity by creating an entropy gradient behind the shock, reflecting the variable velocity front in

front of the shock. This is depicted in figure 4.2 Ribner (1954) proposed that a spanwise vortex can be decomposed into shear waves at symmetric angles to the shock wave front. Figure 4.3 represents this decomposition

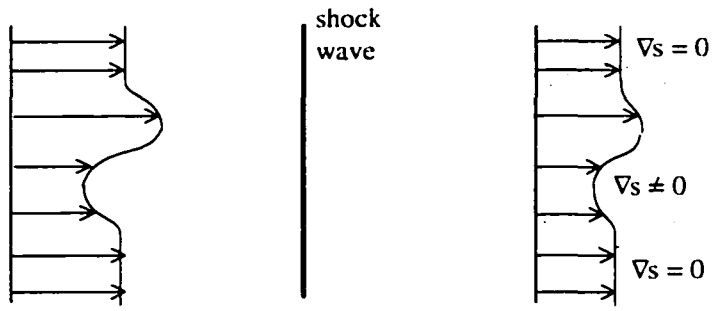

Figure 4.2: Shear wave through a shock wave

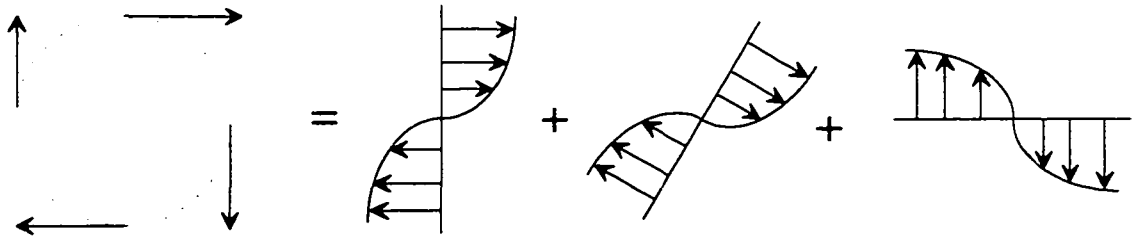

Figure 4.3: Decomposition of vortex into shear waves.

Given that this is a correct representation of the vortex flow we can then expect from the previous analysis of the shear layer - shock wave interaction that the vorticity will also be considerably changed through the shock for the vortex - shock wave interaction. Here the entropy change will be the additive effect of many shear waves interacting with the shock wave.

Experimental evidence suggests that the shock front undergoes considerable distortion when it interacts with the spanwise vortex. Experimental visual techniques have revealed that the shock front gets diffracted around the top and bottom portions of the vortex core perimeter and, as well, the vortex core becomes elliptical with the major axis parallel to the shock. An explanation for this transformed shape was implied by Ribner (1985) in which he showed how a shear wave after getting refracted upon crossing the shock wave produced a squeezing effect of the profile. A representation of this effect is shown in figure 4.6 in which refraction consists of the shear wave being angularly deflected a through the shock and at same time since the passage of the shock wave distorted the shock front, caused the width of the profile to shrink. Since, as Ribner discussed, a vortex can be decomposed into shear waves at varying angles to the flow, or shock front, then the vortex will undergo a squeezing in the longitudinal direction due to the principle just discussed for the shear wave. Figure 4.4b shows how one of the shear waves making up the vortex flow exhibits the same refraction and shock front distortion related effect as the case in figure 4.4a. Thus the vortex shape is most dramatically changed at the upper and lower parts and less changed near the center producing the elliptical shape.

Hayes (1957) derived an equation for the vorticity jump across a surface of discontinuity in unsteady flows, given as follows

$$\delta\vec{\omega}_t = \vec{n}\times\left[\nabla_t(\rho\vec{v}_r)\delta\left(\frac{1}{\rho}\right)-\frac{(D_t\vec{v}_t+\vec{v}_s D_t\vec{n})\delta(\rho)}{(\rho v_n)}\right] \tag{4.12}$$

$$\delta\vec{\omega}_n = 0 \tag{4.13}$$

Here the subscript n and t represent components in the directions normal and tangential to the surface of discontinuity respectively, the vector $\vec{n}$ being the unit normal vector to the surface of discontinuity. The δ represents the change in the variable across the shock and $\vec{\omega}$ and $\vec{v}$ represent the vorticity and velocity vectors respectively. Subscript r represents the relative velocity of the normal component from that of the surface velocity, i.e. $\vec{v}_r = \vec{v}_a - \vec{v}_s$. The D_t operator is the tangential part of the total derivative operator (or the material derivative for an observer moving with and along the shock surface with velocity $\vec{n}v_s + \vec{v}_t$), where

$$D_t = \left(\frac{d\vec{v}_t}{dt}\right)_t + \vec{v}_t \nabla_t \vec{v}_t \tag{4.14}$$

and where

$$\frac{d\vec{v}_t}{dt} = \frac{\partial \vec{v}_t}{\partial t} + v_s \frac{\partial \vec{v}_t}{\partial n} \tag{4.15}$$

$D_t \vec{n}$ is obtained by

$$D_t \vec{n} = -\nabla_t v_s - \vec{v}_t \cdot K \tag{4.16}$$

K is the curvature tensor, $K = -\nabla \vec{n}$. Equation 4.12 shows that vorticity change across the shock is determined from the density jump across the shock and by the gradients, tangential to the surface of discontinuity, of the incoming flow velocity profile. Equation 4.13 indicates that the surface normal component of vorticity survives unaffected through the shock.

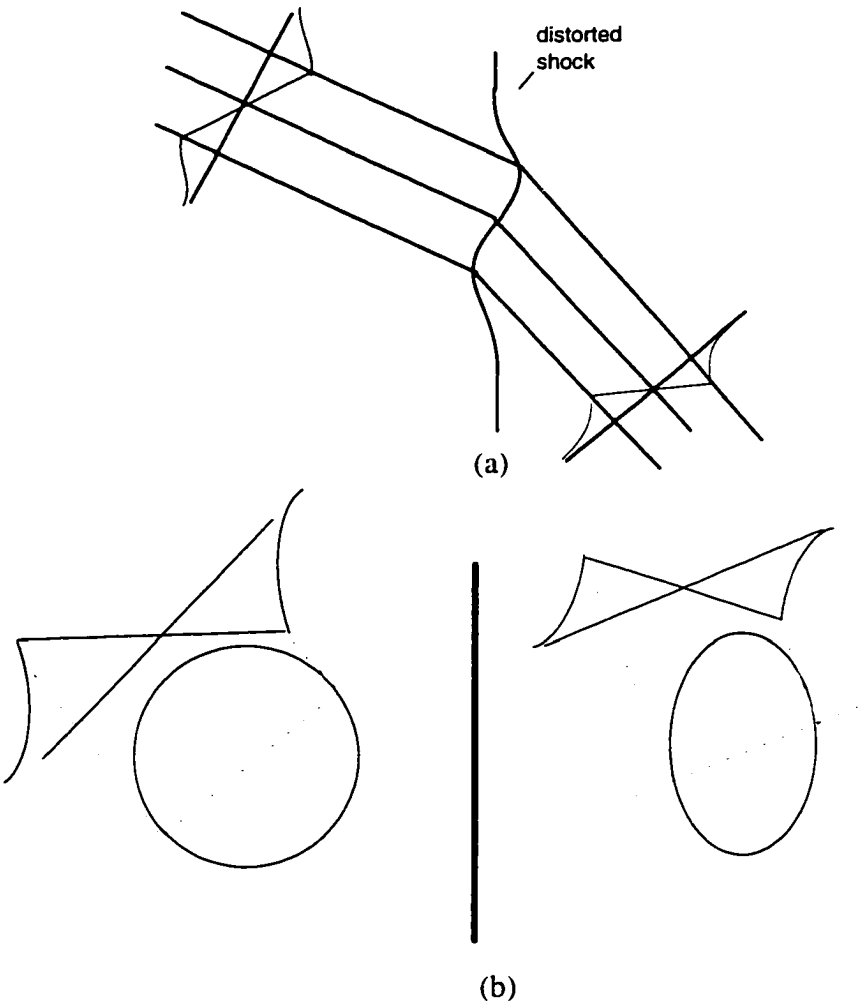

Figure 4.4: (a) shear wave through distorted shock.

4.6 Compressible Turbulence

The fluctuating nature of a fluid lump or compressible body can be described by three fluctuating fields.

1. acoustic - fluctuating pressure (irrotational velocity)
2. turbulence -fluctuating vorticity
3. entropy - fluctuating temperature

The third fluctuating field can also be used to represent the fluctuating density mode under constant pressure. In general these three modes are non-linearly coupled, although Kovasznay (1953) pointed out that these modes may be considered linearly independent in weak turbulence. When these fields encounter a shock wave each mode not only generates the other two complimentary modes but may itself be amplified after passage through the shock.

If the fluctuating intensities can be considered weak compared to the relative mean flow field distortion intensity, then the fluctuating modes can be linearly decomposed into a spectrum of linear wave disturbances and in which each component interacts independently of each other. Therefore a single component can be represented by a harmonic wave of the form $A'e^{i(\vec{k}\,\vec{r}-\omega t)}$. This single component is transferred, in general, at an oblique angle to the shock front through the shock. The integration over all the frequencies and all incident angles (or wavenumbers) yields the first order transfer and/or generation functions used in the analysis of shock wave/turbulence interaction.

The acoustic mode is propagated at the speed of sound relative to the medium while the entropy and turbulence modes propagate with the medium. A perturbation analysis applied to the inviscid governing equations of the flow provides a set of property and flow relations for each of the modes, while a wave equation consideration provides the dispersion relations. Therefore the three modes are described by,

Acoustic waves

$$p' \neq 0 \qquad s' = 0 \tag{4.14}$$

$$U' = \frac{p'}{\bar{\rho}c}\{\alpha, \beta\} \tag{4.15}$$

$$\rho' = \frac{p'}{c^2} \tag{4.16}$$

$$\omega - \vec{u} \cdot \vec{k} = \pm ck \tag{4.17}$$

Entropy mode

$$s' \neq 0 \qquad U' = p' = 0 \tag{4.18}$$

$$\rho' = \left(\frac{\partial \bar{\rho}}{\partial \bar{s}}\right)_{\bar{p}} s' \tag{4.19}$$

$$\omega - \vec{u} \cdot \vec{k} = 0 \tag{4.20}$$

Turbulence (vorticity) mode

$$U' = U'\{-\beta, \alpha\} \neq 0 \tag{4.21}$$

$$p' = s' = \rho' = 0 \tag{4.22}$$

$$\omega - \vec{u} \cdot \vec{k} = 0 \tag{4.23}$$

As the disturbance or perturbation crosses the shock boundary the wavenumber vector is refracted across the shock due to the change in thermodynamic property and therefore diverges at a different angle from the incident. The condition that the phases should remain unchanged yields,

$$\omega(\text{incident wave}) = \omega(\text{diverging wave}) \tag{4.24}$$

$$k_y(\text{incident wave}) = k_y(\text{diverging wave}) \tag{4.25}$$

The longitudinal component of the wavenumber, however, is changed by the local velocity vector. On the downstream side of the shock the velocity is substantially lower and therefore the normal wavenumber becomes larger.

Turning now to the governing equations, Lee et al. (1993) offer an expression for the transport of vorticity variance, $\overline{\omega'^2_\alpha}$,

$$\bar{u}_i \frac{\partial \overline{\omega'^2_\alpha}}{\partial x_i} = 2\overline{\omega'_\alpha \omega'_i \bar{s}_{\alpha i}} + 2\overline{\omega'_\alpha \omega'_i s'_{\alpha i}} - 2\overline{\omega'^2_\alpha \bar{s}_{ii}} - \overline{\omega'^2_\alpha s'_{ii}} + 2\varepsilon_{\alpha ik}\overline{\omega'_\alpha \rho_{,i} p_{,k}/\rho^2} - \overline{(\omega'^2_\alpha u'_k)_{,k}} + \Phi_\alpha \tag{4.26}$$

where $s_{ij}=\frac{1}{2}(u_{i,j}+u_{j,i})$ is the strain rate. The last term is the viscous dissipation transport. What is relevant here is the first four terms on the right hand side which represent vorticity stretching and compression terms. The first two terms represent vortex stretching by the mean and turbulent fields, respectively. The next two terms represent vorticity compression due the dilatation s_{ij}. Lee et al. (1993) have identified the vorticity compression terms as the leading terms in transverse vorticity amplification vorticity through a shock wave.

Chapter 5

5.1 Shock Tube Facility

The interactions will be simulated experimentally in the CCNY Shock tube Facility (STURF). The shock tube is a powerful flow generating tool providing controllable high speed flows and shock waves. The capabilities of this facility have been extensively documented in Briassulis, Agui, Watkins and Andreopoulos (1996). These authors, additionally, present the results of quality tests and a supplementary numerical simulation of the one-dimensional shock tube flow, also presented in this chapter.

The shock tube facility is of large scale dimension with an inside diameter of 12 inches and total length of 90 feet including all components. The facility consists of the following: (1) the driver section; (2) the conical reducer; (3) two driven sections; (4) the working section; (5) the viewport section; (6) the Dump Tank & Vacuum System.

Photographs of the facility are shown in figures 5.1 and 5.2.

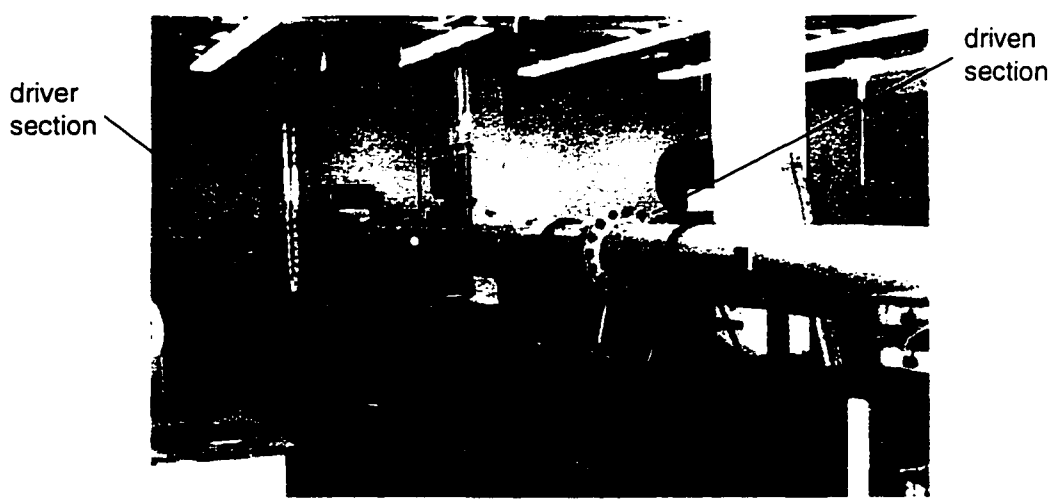

Figure 5.1: Photograph - perspective view of the shock from driven side.

Figure 5.2: Photograph - perspective view from driver side of shock tube.

5.1.1 Operation of Shock Tube

Initially, a circular aluminum diaphragm is inserted in between connecting flanges which separate the driver (dark section seen in figure 5.2, red in true color) from the rest of the facility, thus creating a partition. The 18 ½ inch diameter diaphragms have been machined with an inscribed score mark to create a stress concentration which will aid in rupturing the diaphragm and in controlling the bursting pressure. The basic operation consists of pressurizing the driver section until the dividing diaphragm ruptures. Immediately after the diaphragm ruptures there is a simultaneous generation of a shock wave which travels downstream (into the driven section) at supersonic speed and expansion waves which travels at the local sonic speed in the opposite direction, upstream. The interface which separates the gas initially in the driver section from the gas in the driven section is known as the contact surface. This interface is associated with

sharp changes in density and temperature between the two gases. The shock which is marked by a sharp jump in pressure induces uniform flow behind it while the expansion fan produces a gradual drop in pressure. These events are also present in figure 10a a short time after the rupture of the diaphragm. A change of events takes place when the two wave structures reflect off the end walls. This scenario is presented in figure 10b. In the working and viewport section it is possible to study the interaction of the reflected shock wave with the induced flow which was initially behind it. The flow that interacts with the reflected shock wave may contain induced turbulence or vortex structures produced by subjecting the flow at a suitable upstream location to a turbulence or vortex generator. The end wall of the shock tube can be solid producing a reflected shock with zero flow behind it or it can be porous which damps the strength of the reflected shock and induces a non zero flow behind the reflected shock. Structurally the facility can withstand a maximum pressure differential between driver and drives sections of roughly 1000 to 1 which has the potential of producing shock Mach numbers of 3.2 and an induced flow which reaches an asymptotic value of 1.89.

5.1.2 Numerical Simulation of 1-D Flow

A FORTRAN program originally developed in by Saad (1993) was modified to simulate the flow in the current shock tube and to account for the reflecting boundary condition at the end plates. The program is based on the unsteady equations of continuity, momentum and energy of inviscid non-conducting flows, and is solved numerically using the MacCormack scheme which is used widely for the solution of partial differential equations. This scheme is of second order accuracy, and it's numerical instability is

controlled through the proper choice of a Courant-Friedrich-Lewy Stability number. A convergence test was performed to assess the effects of decreasing the spatial step size, which is done by increasing the total number of points used to discretize the length of the shock tube. The only benefit obtained by increasing the total number of nodal points was a slight reduction in numerical observations after a jump in value, while arrival times and mean values of the incident and reflected shock, contact surface, and expansion fan remained the same. It was found that two hundred nodal points was adequate for resolving the length of the shock tube which corresponded to a $\Delta x/L = 0.005$. A Courant-Friedrich-Lewy stability number, $\Delta t/\Delta x$, of 0.02 was used , which was substantially lower than the stability criterion limit. Numerical oscillations were further reduced by incorporating a second-order artificial viscosity term.

The mass and energy equations include a variable area turn that accounts for the reduction in cross -sectional area at conical nozzle of the STURF. Wall-friction effects of the pipe where compensated by the friction term in the momentum equation, which used friction coefficient values obtain from experiments.

An x-t contour map can be developed from calculated time histories of one specific flow variable (the contour variable) at multiple x/L locations. Figure 5.3 offers three distinct contour plot for pressure, density and temperature slides (b), (c), and (d) respectively. Slide (a) shows a contour obtained from experimental pressure values. As can be seen there is very good agreement with experimental and numerically pressure data.

This program has the potential to produce the time history of pressure, temperature, density, and velocity within all flow regions and at a wide range of driver to driven pressures.

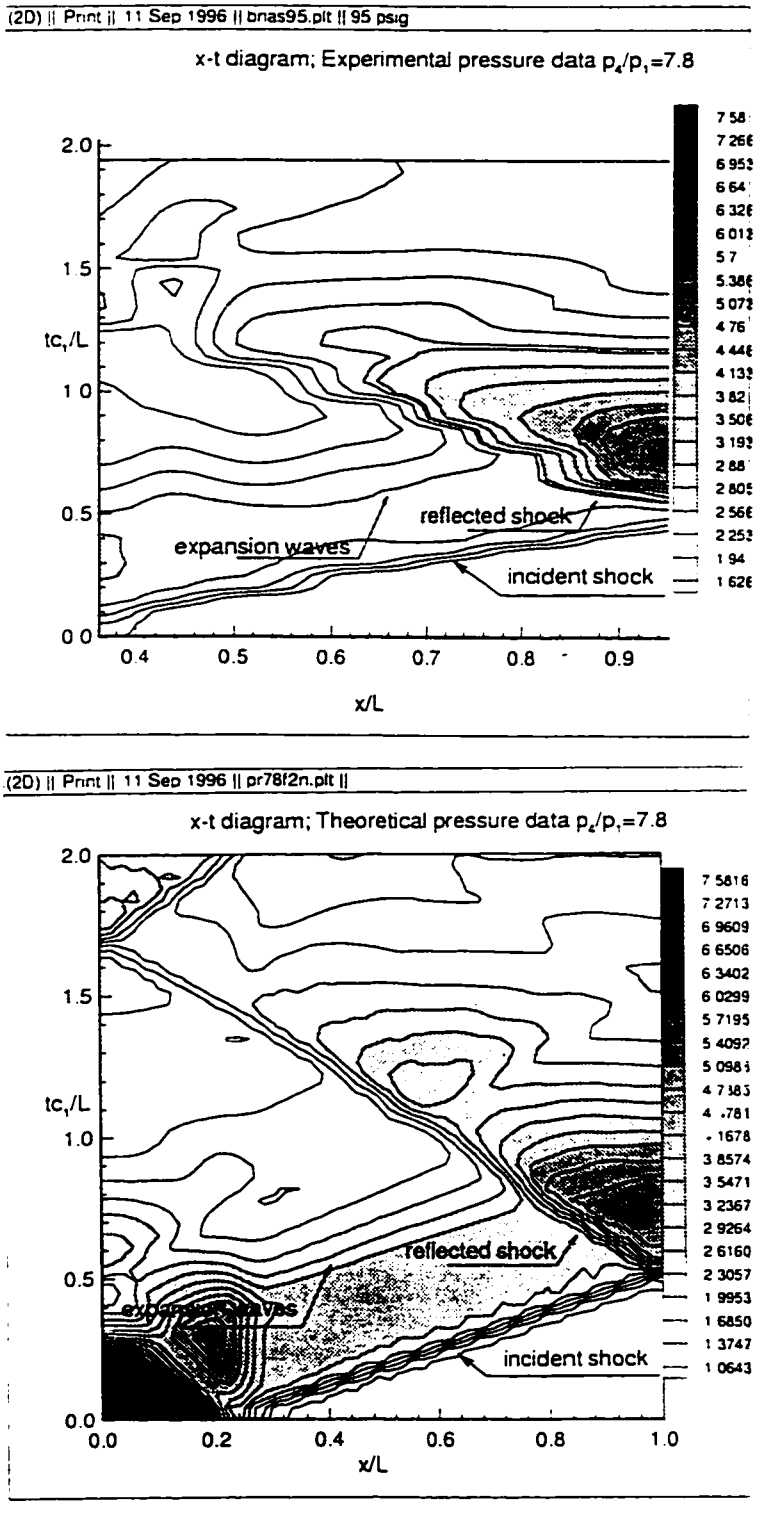

Figure 5.3: x-t contour maps of (a) experimental pressure, (b) theoretical pressure, (c) theoretical density, and (d) theoretical temperature

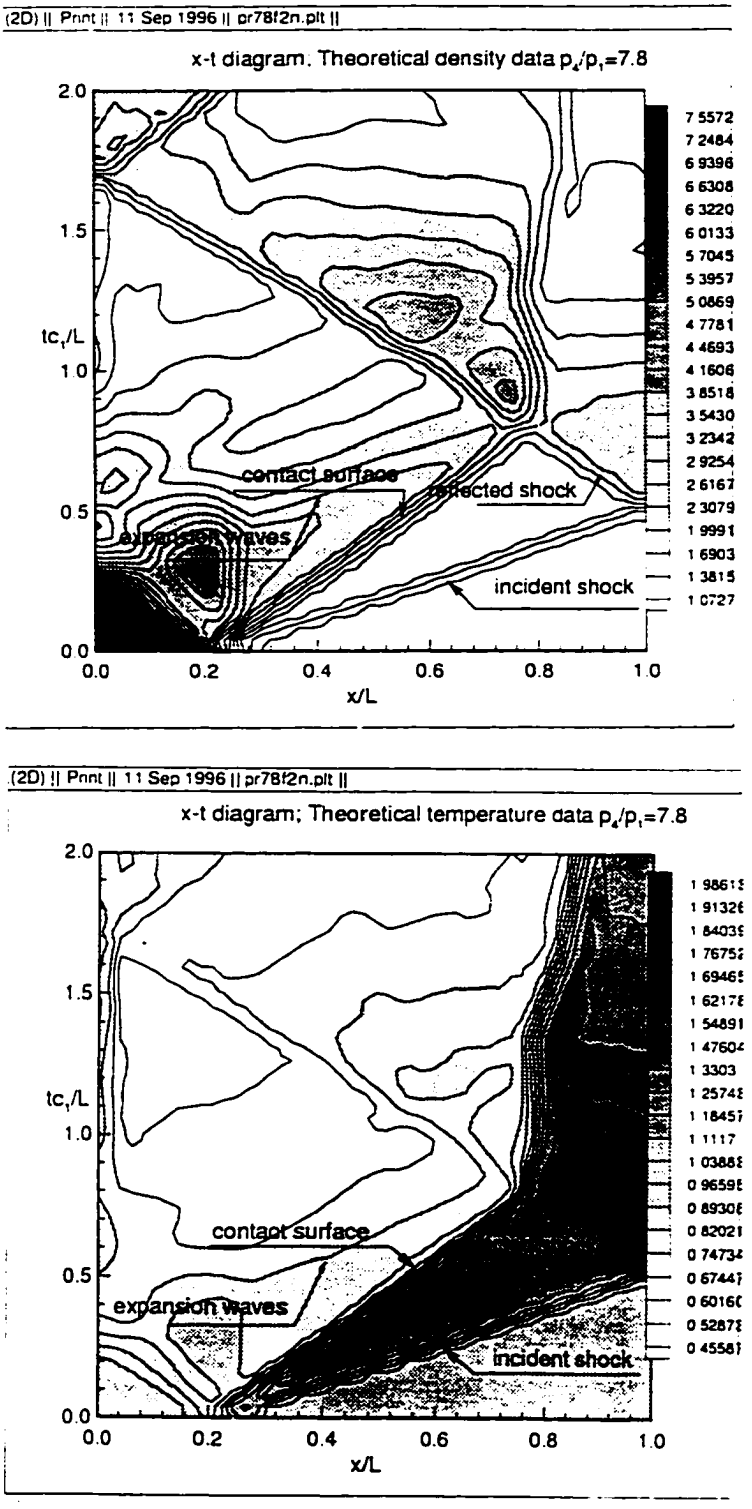

Figure 5.3 cont'd.

5.2 Vortical Flow Generators

Wing models were used to generate the particular type of vortex to be studied. After the incident shock passes over the wing model the induced flow behind it also passes over the model and produces the vortex structure.

Starting vortex generator:

The spanwise vortex flow can be generated as a starting vortex from a slender airfoil section. In this case a nearly full-span wing with a NACA-0012 profile, 178 mm chord and 203.2 mm span, with end-plates was used. A schematic of the flow model is shown in figure 5.4a. The initial flow which is produced from the passage of the incident shock generates a starting vortex after it passes over the airfoil section. The incident shock then gets reflected by the end wall and returns to interact with the induced vortex flow. The interaction occurs somewhere downstream of the wing model.

Tip vortex generator:

For the generation of the streamwise vortex flow two model types were initially proposed. One of these was a 60^0 swept back delta 86 mm chord wing model which would be mounted at a pitched position to the oncoming flow. The other model was a half span, 152 mm, NACA-0012 wing model used to produce a trailing tip vortex. As will be explained later the delta wing model was not used due to undesirable vortex characteristics. The schematic of this flow is shown in figure 5.4b. The interaction again occurs somewhere downstream of the model.

The generated tip vortex is continuously generated by the wing until a sudden change in flow conditions is experienced. This can be marked by the passage of the reflected shock wave over the wing, first to occur, or the arrival of the contact surface. Consequently there should be ample time to obtain measurements the first tip vortex structure which has been affected by the reflected shock wave before the arrival of the second tip vortex structure is sensed by the probe.

Grid turbulence generator:

Two stainless steel screens of square pattern formed by circular rods sintered between stainless steel or aluminum rings were flange mounted in front of the working section in order to introduce the turbulence. The level of turbulence and length scales introduced depended on the porosity (or open area ratio) of the screen chosen. The two grid sizes used in the present investigation were identified by nominal densities of 2 x 2 and 3 x 3 corresponding to mesh sizes (dimension of square opening in screen) of 12.7 and 7.62 mm respectively.

When the incident shock wave is transmitted through the grid, the turbulence of the incident flow behind it is suddenly increased. The turbulence produced right after the grid is characterized by a system of wakes shed off the screen wires which take an initial distance to merge. The position where this mergence takes place relative to the grid is what is known as the virtual origin. The virtual origin has been found to be of the order of 5 to 35 mesh sizes in the present facility (see Briassulis, 1996) and it depends on Reynolds and Mach numbers. Experimental measurements take place amply downstream of the virtual origin.

Porous end wall:

The porous end wall is used to partially reflect the incident shock wave at the driven section end of the shock tube. A series of screens similar to those used for the turbulence generators are stacked together to produce a densely packed porous medium. The medium is inserted in between the last flanges of the shock tube, one being an open-area detached flange mated to the pipe flange. The porosity of the screens also allows part of the convecting mass behind the incident shock wave to escape through it. This in turn sustains a continuous flow in the region behind the upstream propagating reflected shock wave and prevents stagnating flow conditions there. The strength of the reflected shock wave depended on the incident shock strength and the porosity of the end wall.

The numerical simulation of section 5.1.2 also mathematically modeled the flow and shock wave strength produced by the porous end wall.

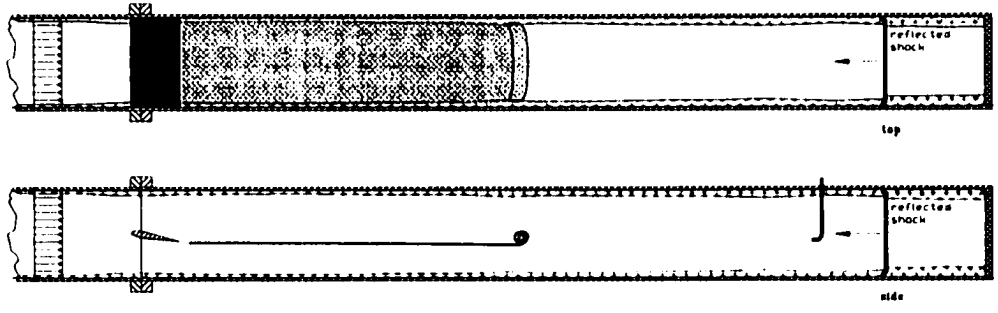

(a) Starting Vortex Model

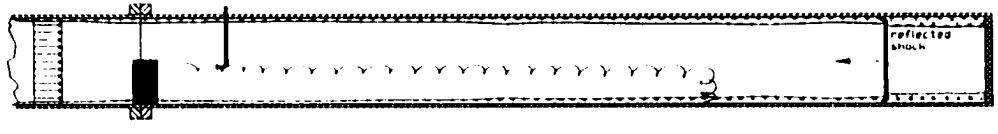

(b) Semi-Span Wing Model (tip vortex generator)

Figure 5.4: Sketch of the two evolving flows in the shock tube. The reflected shock wave is about to interact with the vortex.

5.3 Measurement Techniques

5.3.1 Data Acquisition System

All data was digitized through multiple 12 bit data acquisition boards supplied by ADTEC Corporation, model AD830. Each channel is operated on independent Analog to Digital Converters. These boards require an EISA interface to take advantage of the DMA Burst mode. When acquiring, the data is channeled through the DMA transfer directly onto RAM memory for maximum sampling rate of 333 kHz and 13.5 MB of data storage, and subsequently stored onto disk. This mode of transfer is necessary in order to attain very high sampling rates. Each board accepts eight differential input channels.

The highest sampling rate was used for all experimental cases. It was possible to link multiple cards in master-slave mode. At most, three of these cards were used for a total of 24 simultaneously sampled channels.

5.3.2 Amplifier and Filter

Conditioning of the signal prior to digitizing was achieved through EG&G PARC Pre-amplifier/filters, model 5113. The units provide multiple filter and amplifier settings. The units allow for single ended and differential inputs modes. Also AC and DC coupling modes are available. Maximum input voltage depends on coupling mode. There are two rolloff filter settings 6 dB/octave and 12 dB/octave and the rolloff is centered about the chosen cut-off frequency.

All signals were low-passed filtered at 100 kHz with a response of 12 dB/octave during the linear segment of the rolloff. Input signal amplitude gain settings varied depending on type of input signal:

probe/transducer	gain
Kulite pressure transducer	50 - 500
hot-wire/constant temperature anemometer	16
hot-wire/ constant current anemometer (temp. wires)	1000-2000

Different settings in each category of probe/transducer reflected the variation in individual probe design. Amplitude variation among the Kulite transducers depended on whether a 0 - 100 psia range or a 0-250 psia range pressure transducer was used. Variation among temperature-wire/constant current anemometers depended on individual wire resistance which could be as 1.1 Ω in variation. The hot-wire/constant temperature anemometers despite minor drifts in offset voltages in the anemometers showed little variation in output voltage and therefore their gains were set equally in this category. By comparison the variation in resistance of these wires was .4 Ω

It was found that the voltage given by the hot-wire anemometer were in excess of the voltage input limit of the pre-amp filter (i.e. 1 volt), thereby saturating the filters. Therefore attenuators were constructed for this purpose and were interfaced between the hot-wire anemometers and the pre-amp filters..

Figure 5.5 shows the arrangement of pre-amp filters (white electronic units) during a typical experiment.

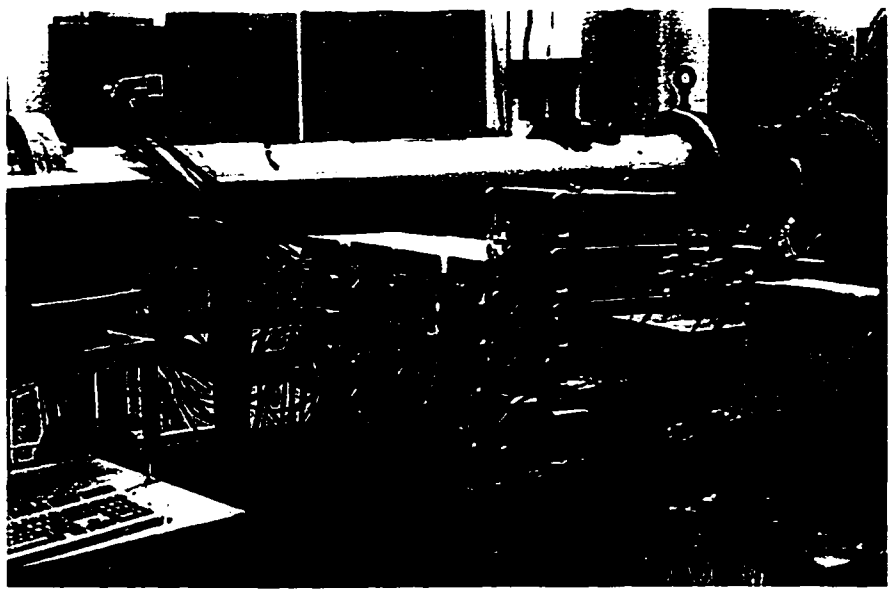

Figure 5.5: Arrangement of Pre-amp filter units during a typical experimental setup.

5.3.3 Constant Temperature Anemometers

The probe was run in constant temperature mode through a Dantec 56C01CTA/56C17 Bridge combination. The frequency response of the bridge found from a square wave test was in the range of 25 Khz. The frequency response improves under flow conditions.

Attenuators:

Signal attenuators became necessary when using the hot-wire signals. The Dantec anemometers produced signals higher in value than the allowable input voltage of the EG&G Parc 5113 Pre-amp filters. The design is quite simple and is shown if figure 5.6.

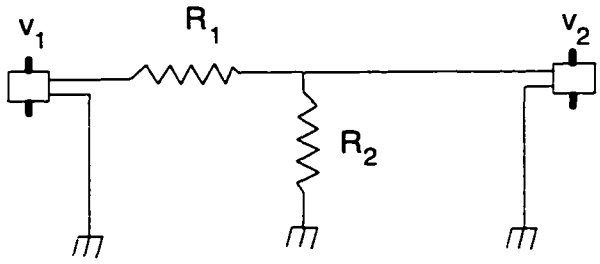

Figure 5.6 Electronic schematic of signal attenuator.

The principle of the attenuator is based on Kirchhoff's second rule which states that *the sum of changes in potential encountered in making a complete loop is zero.* Therefore if this principle is applied to the two loops above separated by resistor R_2, the following two equations are obtained:

$$V_1 - iR_1 - iR_2 = 0 \qquad (5.1)$$

$$V_2 - iR_2 = 0 \qquad (5.2)$$

The two equations combined give the attenuation factor.

$$\frac{V_2}{V_1} = \frac{R_2}{R_1 + R_2} \qquad (5.3)$$

5.4 Probes and Techniques

5.4.1 3-Kulite Total Pressure Probe

Measurements of total pressure were achieved through the use piezoresistive pressure transducers model XCQ-062-100, manufactured by Kulite® Semiconductors Incorporated. A module consisting of 3 such piezoresistive transducers, and herein referred to as the 3-K probe, shown in rendered format in figure 5.7, was used to obtain a local profile of total pressure. The distance on centers of individual probes was 5.08 mm. The probe was case tested in a uniform flow field in the shock tube (in the absence of any vortex structure). These tests showed that the probe produced a small pressure drop on the two side transducers of the order of 0.5%. Possibly, this is a result of a more direct stagnation point on the center transducer while having slight flow effects on the side transducers. As will be shown later in the results the pressure deficit encountered in the vortex core is substantially greater than this pressure drop produced by the shape of the probe. Overall, the three transducers seem to produce uniform pressure profiles in test case.

5.4.2 Hot-Wire Rake

The hot-wire rake probe is presented in rendered format in figure 5.8. This probe was used to obtained profiles of the vortex in order to determine the relative location and influence of the vortex core. The probe incorporates 16 tungsten wire sensors: 8 for velocity measurement in constant-temperature and 8 for temperature measurement in constant current mode. The sensors are paired into one velocity and one temperature, constituting eight modules separated by a distance of .25 inch or 6.4 mm. The supporting body directly holding the wires is 5 mm thick and 2 inches or 50 mm long. The supporting stem holder is made from SS 316 stainless steel with an outside diameter of

.375 inch and .040 inch wall thickness. All wires are oriented normal to the flow optimized to respond to the normal velocity components. Calibration of this probe was performed in the shock tube facility at varying shock strengths with uniform flows.

5.4.3 Vorticity Probe

The vorticity probe was used for single point vorticity measurements and multi-point velocity/mass flux measurements inside the vortex core region and in the grid generated turbulent field. The reader is referred to chapter 7 where this probe is discussed at length.

5.4.4 Particle Flow-Visualization

A method of flow visualization was adapted which involved the use of solid particles sprinkled onto the vortex generator thereby entraining the particles within the vortex core path. A schematic of the technique is shown in figure 5.9. It was found that corn starch used in baby powder produce excellent image quality. These particles are very fine of sub-micron size. Judging from the timing in which the pictures were taken, it seems that the particles convected properly with flow velocities, based on the time of flight of the particles, comparable to the free-stream velocities.

A Spectraphysics Nd:Yag laser, model GCR-14s, was used as the light source. The laser emits in the 1064 nm, infra-red, wavelength and uses KD*P crystals, in-line through its HG-2 Harmonic Generator, to produce higher harmonics in addition to the 1064 beam. In the present case an additional 532 wavelength (green) component is produced. The laser produces a pulse width of 6 - 7 ns and uses a Q-switch to pump to

higher energies. A dichroid beam splitter attachment is also used which directs the 1064 wavelength beam into a beam dump and redirects the higher harmonics to separate independent output windows. The beam size is approximately 6 mm in diameter in nearly Tem_{00} (Guassian) mode. Through a combination of lenses the beam size and therefore the width of the laser sheet thickness was reduced to less than 2 mm.

The triggering sequence is covered in figure 5.10. In order to fire the laser in external trigger mode it required first triggering the flash lamps followed by a trigger with a 150 μs delay to the Q-switch. The beam is released with the second trigger. For this purpose an EG&G delay generator, model 9650, was used which has mult-channel multi-setting outputs. The input trigger to the delay generator came from the Kulite pressure sensor placed on the wall of the shock tube. When the delay generator sensed the signal from the pressure transducer it, in turn, sent out the two required TTL pulse, after a specified delay, to fire the laser. The cumulative delay of the TTL pulses corresponded to the time estimate of the shock in going from the trigger transducer, to getting reflected off the end wall and then arrive at the image area. All three pressure signals were collected on computer through an A/D board. The signals during a typical experiment are shown in figure 5.11. The location of each Kulite pressure transducer is shown in figure 5.9.

An Astromed 3200 Series TR3 water-cooled CCD camera was employed to capture the image whose shutter was left open during the experiment. This is a very high sensitivity camera, up to 1 grayscale/photon, with a high spatial pixel resolution of 578 x 385. Each pixel on the CCD chip is resolved with 16 bits of accuracy. This camera is software controlled allowing the user to store the images directly to disk. The software allowed for setting the capturing parameters: sensitivity, exposure times from 1ms to 1

hour, and readout rate. A Nikon lens was 105 mm used together with a 532 optimized interference line. All laboratory lighting was shut off, this together with the interference line filter eliminated virtually all background light.

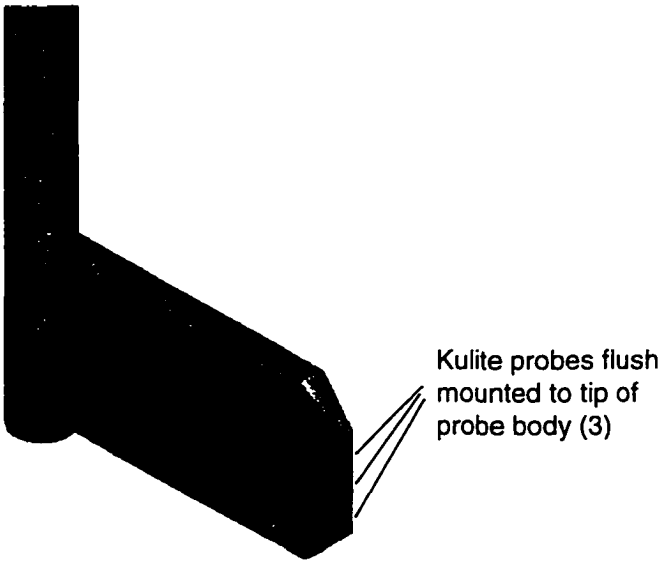

Figure 5.7: Rendering of 3-Kulite probe.

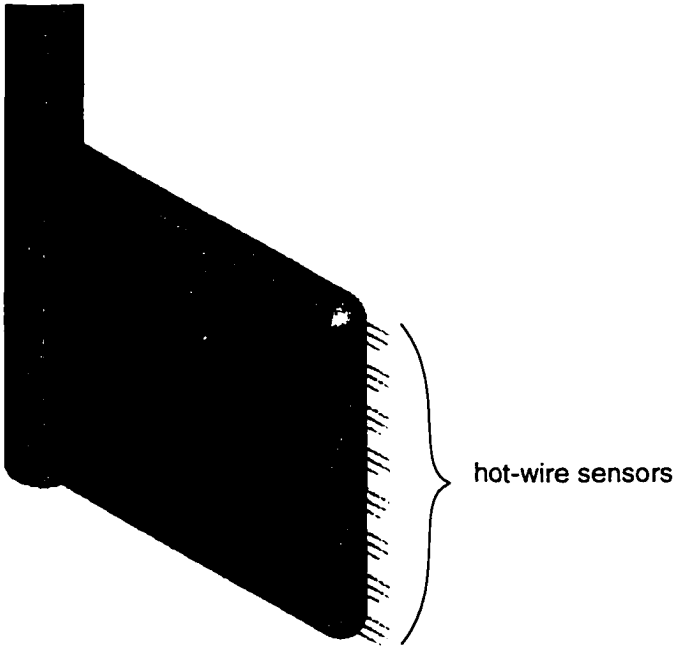

Figure 5.8: Rendering of hot-wire rake probe.

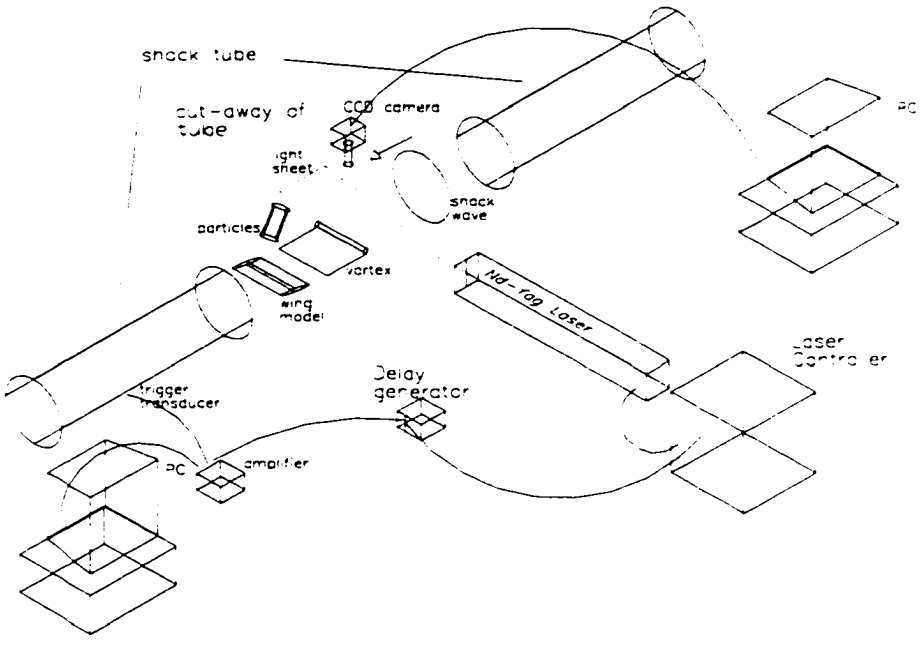

Figure 5.9: Setup for particle flow-visualization.

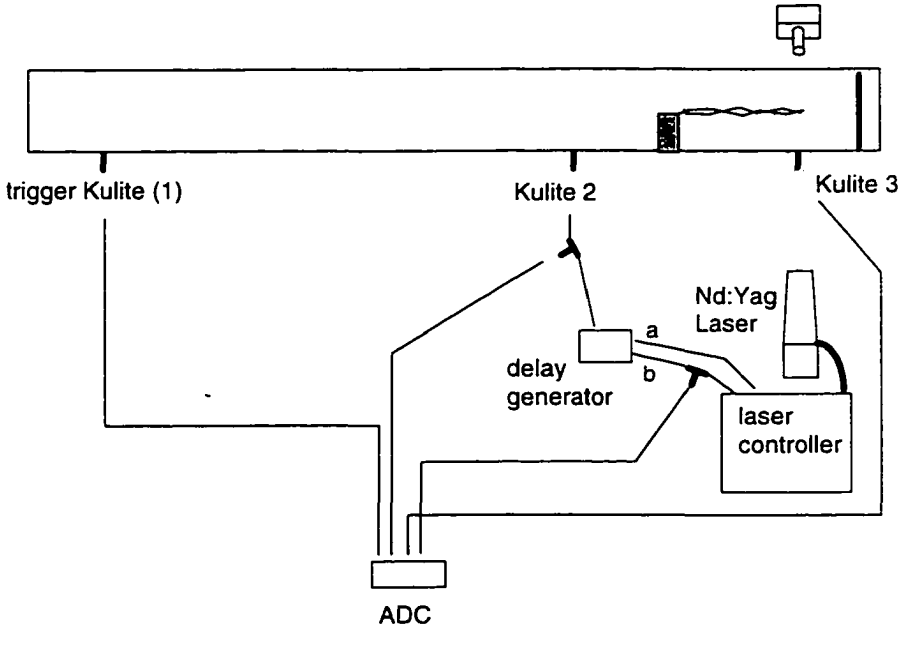

Figure 5.10: Triggering sequence for Particle Flow Visualization Experiment.

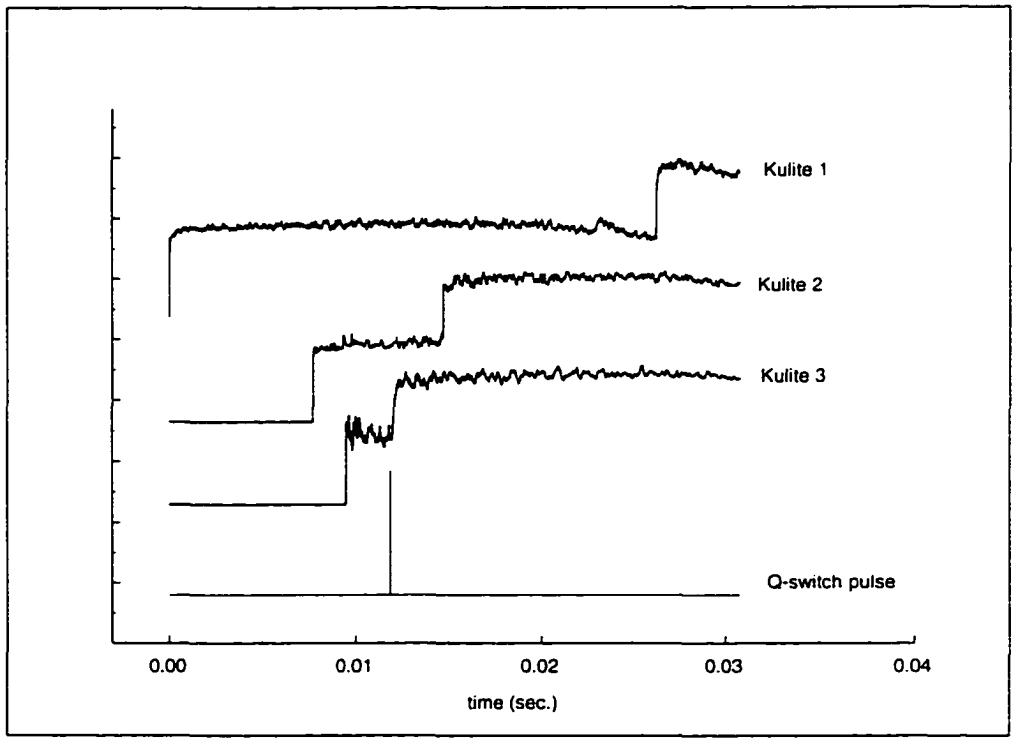

Figure 5.11: Wall pressure signals and Q-switch pulse obtained from a particle flow-visualization experiment.

Chapter 6

6.1 Conversion of Raw Data

Experimental data was acquired through Analog to Digital Conversion (ADC) in binary hexidecimal format. These data were unpacked into ASCII format through a Micorsoft® Quick Basic program for subsequent analysis. The data acquisition software provided by ADTEK corporation when used in multi-board mode saves the data in alternating blocks of 8 Kbytes. The conversion program read the hexadeximal numbers in the alternating blocks of 8 Kb and then stored them in ASCII decimal in single column per channel format onto a file.

6.2 Data Analysis

Calibration constants for static pressure, total pressure, and total temperature which are characterized by a linear response, were obtained by linear curve fitting using available spreadsheet/graphical software, including Microsoft® Excel and Mathsoft Axum. Axum was also used extensively to produce the plots presented in this work. The contours of total pressure presented in chapter 8 were created with using a UNIX based plotting package.

The majority of data analysis of was performed by using Mathcad professional 7.0, a Windows 95 based mathematical package. This mathematical package allows the user to very quickly develop program and graphics. The biggest advantage is that graphical checks can be performed during program writing. Calibration constants for the hot-wire data were obtained through Mathcad because of the non-linear relation between

raw voltage and mass flux. Because of the involved spectral analysis applied on the grid turbulence data, a test was performed on Mathcad's Fast Fourier Transform (FFT) functions by processing a sine wave of known frequency and amplitude. Although the calculated amplitude is dependent on frequency content and block size of the input data, it was found that the amplitude value converge to the correct one for moderate sample block size. Therefore the spectral results in chapter 10 seem to be satisfactory. These spectral data was also checked by comparing the spectral energy with rms levels for each particular processed file. A final note on another of Mathcad's function, is the convenience of the complex FFT function which is an alternative FFT function which accepts any size block of data as oppose to the conventional FFT routine which only accepts data block sizes containing 2^N elements (where N is any integral number).

6.3 Numerical Filtering

Occasionally signals that contained an excess of electronic noise were digitally filtered. Although electronic filtering was used through pre-amp filter units, high frequency noise of large amplitude could still be present due to the rather large bandwidth of the useful signal. Electronic low-pass filtering was in a range from 0 - 100 kHz in order to obtain the maximum useful bandwidth of the signal and to account for the Nyquist Sampling criterion. Two methods of numerical filtering were used depending on the level of noise in the signal.

The first filtering method involves time-domain filtering by using a Guassian kernel, K(t), given by:

$$K(t) = \frac{1}{\sqrt{2\pi}\sigma} e^{-\frac{t^2}{2\sigma^2}} \tag{6.1}$$

where σ is the standard deviation of a Gaussian distribution, its value being 0.37. The data was numerically convolved with this Guassian kernel to obtain a new data set for the signal. If *y* and *t* represents the original data and time arrays, and y' the new data array, then the numerical scheme for obtaining y' is given by,

$$y'_i = \frac{\sum_j K\left(\frac{t_i - t_j}{b}\right) \cdot y_j}{\sum_j K\left(\frac{t_i - t_j}{b}\right)} \tag{6.2}$$

The parameter *b* is used to control the spread or influence of the Guassian kernel over time at a specified time, t_i, on the original data y_i. The term in the denominator normalizes the output value of y'. This type of filtering produces signals with a smooth appearance. This filtering was used for noisier signals, and also when it was desired to match a noisy signal with that of the adjacent cleaner signals from same type probes. The amount of filtering was determined so that it was not allowed to suppress any useful frequency content. An analysis of the frequency response of this kernel (presented in appendix B) shows that if the value of b was kept below .3 ms, significant rolloff filtering occurs after 10 kHz and 3 dB attenuation occurs at 25 kHz. Thus, useful frequency content of the signal was not compromised.

The second method was less intrusive. A manual notch filter was used to suppress isolated peaks in the spectra of a signal. The peak value was replaced by an averaged value over adjacent amplitude values including the peak amplitude. Averages ranged

from 3 points (i.e. the peak point and the adjacent values) to 6 points. Average over more than 3 points involved using the peak frequency point as a median over which the total number of points were averaged.

6.4 Experimental Uncertainty.

Any measurement depends on a chain of components, from the probe to the A/D converter, or digitizer, and on the response characteristics of the sensor. The total measurement uncertainty then depends on the propagation of individual inaccuracies of each of these factors. Therefore if Q represents a measured quantity which depends on a set of independent variables, i.e.

$$Q = Q(x_1, x_2, x_3, ...) \tag{6.3}$$

then an estimate of the uncertainty can be obtained by applying the general form of the uncertainty equation,

$$U_Q = \left[\left(\frac{\partial Q}{\partial x_1} U_{x_1} \right)^2 + \left(\frac{\partial Q}{\partial x_2} U_{x_2} \right)^2 + \left(\frac{\partial Q}{\partial x_3} U_{x_3} \right)^2 + ... \right]^{\frac{1}{2}} \tag{6.4}$$

The pressure and total temperature measurements depended directly, through obtained calibration constants, on the raw voltage data from individual sensors. These probes because of their linear response produced two calibration constants: d.c. offset,a, and sensitivity, b. Therefore $p = p(E, a, b)$ and $T_0 = T_0(E, a, b)$ where E is the captured voltage. Therefore, estimates of the uncertainty of pressure and total temperature acquired through a 12 bit A/D converter depended mostly on the bit resolution and the residual

errors from the calibration constants. Uncertainties in the range of less than .5% in pressure and around 2% for total temperature were found for typical measurements of these two quantities.

The mass flux measurements were tied to a significantly more complex relation which depended on data from multiple sensors and the non-linear response of these sensors. The measurement also depended on the individual and relational geometry of different sensors. Sections 7.3.1 and Appendix A offer an analysis of the triple-wire sensor used to obtain mass flux measurements. Mass flux was found to depend on the following variables:

- Captured raw voltage data, E
- Reference temperature, T_r (usually chosen as the ambient temperature)
- Total temperature measurement, T_0 (obtained from independent sensor)
- Wire temperature, T_w
- A and B' (individual calibration constants, see Appendix A)
- Yaw coefficient,

Estimates of the uncertainty of mass flux considering all the above factors was found to be of the order of 1 - 2 %. No uncertainty was assumed for the reference temperature and average uncertainty values were used for A , B' and h. Final velocity depended on the type of flow measured, but intrinsically relied on the static pressure measurement (either directly or indirectly through the total pressure measurement). Little change was found in the uncertainty of velocity from that of the uncertainty range found for mass flux. Uncertainties in the velocity gradients or vorticity which involve calculations of second order spatial gradients were not attempted.

Chapter 7

7.1 Vorticity Probes and Requirements

Vorticity is defined in Cartesian coordinates by its three components,

$$\omega_x = \frac{\partial w}{\partial y} - \frac{\partial v}{\partial z} \qquad \omega_y = \frac{\partial u}{\partial z} - \frac{\partial w}{\partial x} \qquad \omega_z = \frac{\partial v}{\partial x} - \frac{\partial u}{\partial y} \tag{7.1}$$

Measurements of vorticity, therefore, can be performed by directly measuring velocity gradients or alternately by applying the principle of circulation around a closed loop. The validity of approximating velocity gradients by utilizing velocity measured at two distinct, but nearby, points depends on neglecting second order and higher terms from a Taylor expansion of the velocity. For instance a gradient of velocity in the y direction is obtained by the following Taylor's expansion:

$$u(x_0, y_0 + h) = u(x_0, y_0) + h \cdot \frac{\partial u}{\partial y}(x_0, y_0) + h^2 \cdot \frac{\partial^2 u}{\partial y^2}(x_0, y_0) + h^3 \cdot \frac{\partial^3 u}{\partial y^3}(x_0, y_0) + \ldots\ldots \tag{7.2}$$

If second order and higher terms are neglected then the velocity gradient is approximated by

$$\frac{\partial u}{\partial y}(x_0, y_0) = \frac{u(x_0, y_0 + h) - u(x_0, y_0)}{h} \tag{7.3}$$

Due to spatial resolution the accuracy of the technique increases with decreasing separation distance, h.

The circulation method requires the size of the area enclosed within a closed loop. referred to in equation 7.4, to be chosen small enough so that the vorticity contained within can be considered constant.

In this case,

$$\Gamma = \oint \vec{u} \cdot d\vec{\ell} = \int_A \vec{\omega} \cdot d\vec{A} \tag{7.4}$$

$$\omega_n \vec{n} = \frac{\int_C \vec{u} \cdot d\vec{\ell}}{\delta A} \tag{7.5}$$

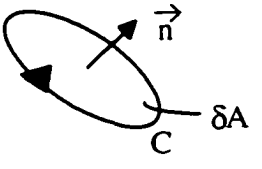

Figure 7.1 Elemental area with contour C.

If the closed loop is chosen such that it forms a square shape then this virtually results in an equivalence of the two techniques, velocity gradient and circulation, provided that the above two respective criteria are met.

An extension of this analysis can be applied in three dimensions to obtain the three components of vorticity. For the present vorticity probe which is presented in the next section an extensive three-dimensional analysis is presented.

Several other items are worth mentioning as they relate to the accuracy of the measurement. The first is the absolute accuracy of a single point velocity measurements which is limited by hardware and design uncertainties as well as uncertainty in the

calibration curve. Taking the difference of two velocities which are very close in value can possibly compound the error involved from that of a single realization by bringing into play the sampling resolution. If care has been taken to maintain a high signal-to-noise ratio and high resolution A/D conversion is used this error can be minimized. By the same token better accuracy can be attained if the separation distance, h, is accurately estimated. The most serious problems concerning closely spaced intrusive probes are the aerodynamic and thermal interference these probes produce on one another and their spatial resolution. This is typical of hot-wire probes in which up to twelve individual hot-wire probes have been recently implemented for three-dimensional vorticity measurements (see e.g. Tsinober, Kit, and Dracos, 1992).

Two alternate techniques for the measurement of one component of vorticity have been tried. Laser Speckle Velocimetry or more familiarly known as Particle Image Velocimetry which was used by Lourenco and Krothapalli (1987) . This technique relies critically on tracing distinct particles within specific small planar regions of the flow and determining the particles' velocities from before and after positions taken from images at specified time intervals. If traced particles go in and out the image plane then the tracing of individual particles is disrupted, causing ambiguity. Another source of ambiguity is the possibility of particles crossing paths. Given the sensitivities of the technique is viability lies only in low speed flows. A more exotic method was used by Frisch and Webb (1981) in which specially designed tiny transparent spherical particles containing embedded planar crystal mirrors were suspended in a refractive index-matched liquid and their rotations measured. This technique is overly complex and because of its dependence on index-matched medium it precludes its use in air.

The only reported vorticity measurement using Laser Doppler Anemometry are those of Lang (1985) and Lang and Dimotakis (1984). They measured the spanwise vorticity in a shear layer generated in Caltech's Free Surface Water Tunnel. Their transmitting and receiving optics were developed in house because of the lack of commercially available LDA system providing measurements at closely spaced positions. By running the laser beam from an argon Lexel laser model 85 through two cube beam splitters and then a diffraction grating, four pairs of beams were separated resulting in four probe volumes in the flow. The probe volumes for detecting the 'v' velocity component were frequency shifted using a Bragg cell also developed by them. A quadrant detector situated at the back of the receiving optics was used to separate the signal coming from the four different probe volumes. Their method although far less complicated then setting up four independent LDA one component systems is still rather complicated. The accuracy of laser Doppler measurements depends greatly on the optics used to generate the probe volumes in the flow. Also, typical receiving optics bring in particle velocity information from within virtually all of the probe volume, thus velocities detected could reflect those from extreme ends of the probe volume. It seems that the optics developed by the above authors could possibly bring about errors due to the length the beams have to travel in between optical components, the dependence on splitting and reflecting the beams at critical angles, and finally the actual size of the probe volume, although not stated, might not be advantageously small to provide sufficiently improved probe spatial resolution. The separation distance used was 1.9 mm although it was claimed that the separation distance can range from 1 mm to 4 mm.

Lately, Particle Image Velocimetry (PIV) has been given a boost by integrating it with new technologies. The more modern version of PIV uses a double pulsed Nd:Yag laser, faster camera, and more intelligent software. The double pulsed laser is actually two lasers in one unit which transmits the two beams through the same front end optics. The delay between the two pulses, which is variable, can achieve delays of the order of microseconds providing a platform for high speed measurement. The camera incorporates fast frame capturing providing two independent images from the two quick laser pulses. The software provides the triggers, communication to the camera, and more efficient spectral interrogation of the particle images to extract the velocities. There are still, however, some drawbacks to this technique. The time gap between velocity maps is limited to the repetition rate of the individual laser which is of the order of 15 Hz. Also, continuos and homogenous seeding are still serious issues for proper operation.

7.2 Choice of Vorticity Probe

A vorticity probe based on Laser Doppler type measurements was initially developed. The system makes use of state-of-the art LDA components and a custom made fiber optical receiving system which is able to extract two distinct velocity measurements of the same component from a single elongated probe volume. This technique has already been used by Fraser, Felton, Bracco and Santavica (1986) and Johns, Pitcher, and Winkelhofer (1986) for cross correlation measurements. By orienting two elongated probe at 90° to each other, the two velocity gradients necessary for one component of vorticity can be obtained.

This laser probe was tested in a large scale wind tunnel housed in the same laboratory where measurements of a thick two-dimensional subsonic turbulent boundary layer were taken for validation purposes. The results from the validation were encouraging and were presented at the 1994 ASME Symposium on Laser Anemometry: Advances and Applications, Lake Tahoe, Nevada (see Agui, 1994). The probe was dubbed the Laser Doppler Vorticity probe (LAVOR).

This probe which incorporated extensive optics, testing and code modification to capture data, despite its success in the turbulent boundary layer, was ultimately not used for the shock tube. The decision not to use this probe was based partly on the literature which discouraged the use of LDA methods in a shock tube primarily due to contamination and continuous seeding problems, and from a trial using a high speed jet supplied by a high pressure liquid nitrogen tank and using conventional 1-D LDA measurement to simulate high speed seeding. The latter did not provide favorable results as the processor, a Burst Spectrum Analyzer developed by Dantec Corp., had to be readjusted intermittently. This intermittent jet behavior might have been due to a less than perfect regulator on the tank, which however, also provided a test for intermittent seeding. In addition, the reflected shock wave which interacts with the flow brings about a sudden change in velocity. The LDA processor could not be optimally set to measure the flow before as well as after the reflected shock on the same run.

Ultimately, following a more conventional and tried technique a hot wire probe was chosen for vorticity measurements. The hot wire probe has the significant advantage of being able to measure all components of vorticity and velocity. One the other hand, the LAVOR was designed and restricted to one component vorticity measurement due to

beam accessibility and price constraints. Other advantages include a continuous signal and high sampling rates as dictated by the Analog to Digital Converter used.

Very recently an attempt was made to use a Particle Image Velocimetry system developed by Dantec Corporation in the shock tube. Although, the system has potential no proper images were obtained. The primary reason for this was the shock tube flow (with or without the vortex flow) is non-stationary occurring over a time scale of 40 ms. Although, both software or external triggering of the laser and camera were attempted, the internal delay before the beams are released was locked into the 15 Hz cycle of the laser. Therefore given the 40 ms duration of the flow it would be highly coincidental for the laser to provide the double pulse at desired time in the flow. There were also seeding problems associated with the shock tube facility.

7.3 The Vorticity Probe

A new vorticity probe was designed, fabricated and tested which was capable of measuring three-dimensional time-dependent vorticity in non-isothermal flows. The vorticity probe consists of twelve wires: nine hot-wire velocity sensors, or three sets of triple wires, and three temperature wire sensors. The design of the probe is adapted from Honkan and Andreopoulos (1997). The design was given to Auspex Corporation for fabrication. The prime design consideration was that the velocity wires should be mutually orthogonal to the axial flow direction.

The probe is shown in figure 7.1 in rendered format and a close-up view in figure 7.2 showing the orientation of the wires. The laboratory coordinate system is given in figure 7.1 where the supporting structure of the probe is shown. The overall size of the

probe determined by the centriod to centroid distance between triple wire sets is 1.73 mm (center to center of extreme wire position is 2.6 mm and extreme prong distances is 3.5 mm). Each triple wire set is labeled in figure 7.2 by letter designation. The supporting stem holder is made from a rugged 316 SS stainless steel tubing with an outside diameter of .375 inch and .040 inch wall thickness machined bent at 90^0. This stem construction showed no sign of deformation after many experimental runs. The prongs are made from fine stainless steel rods which have been tapered towards the hot-wire contacts. 30 gauge lead wiring was soldered to the other end of the prongs. The complete set of prongs are electrically isolated from each other through several ceramic holders and the whole assembly is epoxied onto the aluminum tubing. Figure 7.3 shows actual photograph using a digital CCD camera and a .42X AF macrolense.

Calibration of the probe required first a study of the yaw and pitch response. This was performed in the wind tunnel housed in the same laboratory. The probe demonstrated that it had a smooth and distinct response to both yaw and pitch angle. The probe was also validated by testing it in a two-dimensional incompressible turbulent boundary layer. Final calibration occurred in the shock tube. Calibrations were performed for every day of experimentation.

7.3.1 The Triple Wire Probe

The vorticity probe consists of three sets of triple wires. Each triple wire is designed to measure the three local velocity components which are referenced with respect to centroid of the triple wire set. Figure 7.3 shows the layout of the centroids of each triple wire set (1,2, and 3) in relation to the probe centroid (0). The probes conforms

to longitudinal axis-symmetry in that each wire oriented at a common angle of 54.7° to a longitudinal axis going through the centroid. No common prongs are used in the present configuration allowing each wire to be operated independently.

King's law governs to the voltage output of the wire,

$$E^2 = A + B(\rho U_{eff})^n \tag{7.6}$$

Here the effective mass flux (ρU_{eff}) is the independent calibration variable which in this form account for compressibility. The most general form of U_{eff} is given by,

$$U^2_{eff} = U^2_N + k^2 U^2_T + h^2 U^2_B \tag{7.7}$$

where U_N, U_T, and U_b are the normal, tangential, and binormal components of the velocity vector with respect to the local individual wire coordinate system. The weighting variables k and h are the yaw and pitch coefficients. Because of the non-linear relation between the raw voltage and the three wire coordinate velocity components through equation 7.7, multiple solutions can arise. Andreopoulos (1997) describes how the acceptance cone for this probe type is found by applying a 'realizability' condition which is dictated by evaluating the sign of the Jacobian of the raw voltage as a function of the velocity magnitude, and yaw and pitch angles, formed between the probe coordinate system and the lab coordinates system, over a range of these angles. The validity domain or acceptance cone is determined by the range over which the Jacobian does not change sign. They found that the Jacobian criteria held for virtually the entire range investigated.

The calibration of the wires involved both a velocity/mass flux and yaw and pitch response calibrations to determine the yaw and pitch coefficient. The reader is referred to Appendix A for details of this calibration.

7.4 Computation of Velocity Gradients

In high speed flows where compressibility becomes a factor, the simpler relation between raw voltage and the velocity vector in subsonic flows, in which density is considered constant, does not hold. The present probe output obtained by applying the calibration procedure of Appendix A.1, yields the three components of mass flux and the total temperature at each of the triple wires. Still, these two flow variables are not sufficient to uniquely determine the velocity vector. Additional data or assumptions need to be made concerning one of the static variables, i.e. density, pressure or temperature. This is discussed in sections 8.1 and 9.5.1 for homogeneous turbulent flows and vortex flows respectively. After properly extracting three velocity components from the data of each of the three sets of triple wires, the velocity data can be used to compute all three vorticity components and the six distinct rate of strain terms.

By following the one component gradient analysis initiated in section 7.1 and applying a probe coordinate system shown in figure 7.3, a Taylor's expansion for each velocity component is obtained. Namely,

$$u_{1_1} = u_{1_0} + \left(\frac{\partial u_{1_0}}{\partial x_2}\right)_{x_{1_0}, x_{2_0}, x_{3_0}} \Delta x_{2_1} + \left(\frac{\partial u_{1_0}}{\partial x_3}\right)_{x_{1_0}, x_{2_0}, x_{3_0}} \Delta x_{3_1} \tag{7.8}$$

$$u_{1_2} = u_{1_0} + \left(\frac{\partial u_{1_0}}{\partial x_2}\right)_{x_{1_0}, x_{2_0}, x_{3_0}} \Delta x_{2_2} + \left(\frac{\partial u_{1_0}}{\partial x_3}\right)_{x_{1_0}, x_{2_0}, x_{3_0}} \Delta x_{3_2} \tag{7.9}$$

$$u_{1_3} = u_{1_0} + \left(\frac{\partial u_{1_0}}{\partial x_2}\right)_{x_{1_0}, x_{2_0}, x_{3_0}} \Delta x_{2_3} + \left(\frac{\partial u_{1_0}}{\partial x_3}\right)_{x_{1_0}, x_{2_0}, x_{3_0}} \Delta x_{3_3} \tag{7.10}$$

This forms a system of linear equations,

$$\begin{bmatrix} u_{1_1} \\ u_{1_2} \\ u_{1_3} \end{bmatrix} = \begin{bmatrix} 1 & \Delta x_{2_1} & \Delta x_{3_1} \\ 1 & \Delta x_{2_2} & \Delta x_{3_2} \\ 1 & \Delta x_{2_3} & \Delta x_{3_3} \end{bmatrix} \begin{bmatrix} u_{1_0} \\ \dfrac{\partial u_{1_0}}{\partial x_2} \\ \dfrac{\partial u_{1_0}}{\partial x_3} \end{bmatrix} \tag{7.11}$$

The streamwise derivatives are obtained by applying the momentum equation in each component and neglecting pressure and viscous forces. The final expressions yield,

$$\frac{\partial u_{1_0}}{\partial t} + u_{1_0} \frac{\partial u_{1_0}}{\partial x_1} + u_{2_0} \frac{\partial u_{1_0}}{\partial x_2} + u_{3_0} \frac{\partial u_{1_0}}{\partial x_3} = 0 \tag{7.12}$$

and thus,

$$\frac{\partial u_{1_0}}{\partial x_1} = -\frac{1}{u_{1_0}} \left[\frac{\partial u_{1_0}}{\partial t} + u_{2_0} \frac{\partial u_{1_0}}{\partial x_2} + u_{3_0} \frac{\partial u_{1_0}}{\partial x_3} \right] \tag{7.13}$$

The other two streamwise derivatives are obtained similarly as,

$$\frac{\partial u_{1_0}}{\partial x_1} = -\frac{1}{u_{1_0}} \left[\frac{\partial u_{1_0}}{\partial t} + u_{2_0} \frac{\partial u_{1_0}}{\partial x_2} + u_{3_0} \frac{\partial u_{1_0}}{\partial x_3} \right] \tag{7.14}$$

$$\frac{\partial u_{1_0}}{\partial x_1} = -\frac{1}{u_{1_0}} \left[\frac{\partial u_{1_0}}{\partial t} + u_{2_0} \frac{\partial u_{1_0}}{\partial x_2} + u_{3_0} \frac{\partial u_{1_0}}{\partial x_3} \right] \tag{7.15}$$

The temporal derivatives contained in equations 7.13 - 7.15 can be easily computed from differencing two successive velocity values and dividing by the sampling interval, Δt.

7.5 The Two-Dimensional Incompressible Boundary Layer Experiment

In order to asses the performance of the vorticity probe, measurements using this probe were obtain in a two-dimensional, incompressible, turbulent boundary layer. The reasons for this test were, first of all, convenience since a 4 ft. by 4 ft. cross sectional wind tunnel resided in the same laboratory and was accessible. Adapting the wind tunnel for traversed measurements using the current probe was relatively easy and quick. The other reason is that the turbulent boundary layer has been extensively studied and therefore adequate data is available for comparison, including vorticity measurements taken in the same wind tunnel facility using a different probe (Honkan and Andreopoulos, 1997).

The CCNY Wind Tunnel

The Measurements were taken in the CCNY wind tunnel housed in the Experimental Fluid Mechanics and Aerodynamics Laboratory of The Department of Mechanical Engineering. This an open-ended suction type wind tunnel with a 4 ft. x 4 ft. cross section and 28 ft. long working section. The velocity can be varied through a frequency varying controller to a maximum free-stream velocity of 11.5 m/s. Low noise levels are maintained by housing the motor and fan assembly in a sound absorbing diffuser. The fan assembly structural support is also mounted on spring mounts to minimize vibration and to isolate it from the working section. The inlet flow is conditioned through a set of screens and a honeycomb in proper order to damp the inlet turbulence levels to less than 0.1% of the maximum speed in the working section. The flow velocity is increases through 9:1 area contraction.

The probe was run in constant temperature mode though Dantec 56C01CTA/56C17Bridge combinations as discussed in Appendix A. Since the flow is incompressible a calibration curve in terms of raw voltages and velocities directly is obtained. Appendix A also covers extensively the calibration of the probe. Traversing was performed manually through a custom made traversing mechanism. Yaw and pitch free rotations used for calibration were also incorporated into the mechanism. An overheat ratio of 0.8 was used (as defined by $R=\alpha(T_w-T_0)$, where R is the overheat ratio, 'w' is for wire, and '0' is for total quantity).

The flow parameters are given in Table 7.1 below:

U_∞ (m/s)	δ (mm)	θ (mm)	c_f	u_τ (m/s)	Re_θ
8.91	97	9.21	0.00295	0.34	5,254

Table 7.1: Boundary layer experiment flow parameters

Results:

Figure 7.5 shows the measured velocity points superimposed on the classical logarithmic layer given by Coles (1962),

$$U^+ = 2.44 \ell n y^+ + 4.9 \qquad (7.16)$$

The figure shows the measured data initially to align with the logarithmic profile and then diverge according to the Defect Law. The three symbols correspond to the measurements taken by the individual triple wire probes. The symbols are slightly displaced vertically

because of the relative vertical distances between triple wire sets. An indication of how well vertical mean gradients are measured by the probe, can be determined by comparing them to the corresponding mean gradient profile obtained by differentiation of the Log Law equation, equation 7.16, giving

$$\frac{\partial U^{+}}{\partial y^{+}} = \frac{2.44}{y^{+}} \tag{7.17}$$

This comparison is shown in figure 7.6, which also provides a fit in the buffer layer given by (Bradshaw and Huang, 1995)

$$\frac{\partial U^{+}}{\partial y^{+}} = 1 - A(y^{+})^{4} \tag{7.18}$$

The agreement of the data in figures 7.5 and 7.6 establishes first that the design of the probe yields proper local mean measurements, and second that the spacing between triple wire sets is correct.

The remaining figures report on the more important turbulence quantities. The following figure, 7.7, is of the turbulence intensity of the boundary layer. The present data is compared to the experimental data of Balint, Wallace, and Vukoslavcevic (1991) and the numerical simulation of Spalart (1988), Klebanoff (1954), and the more recent data Honkan and Andreopoulos (1997) obtained in the same facility, although at a lower Re_{θ}. The present data seems to show slightly elevated values from that of previous data.

The next figure, 7.8, presents the Reynolds stress results. The fits seems better in this case except for the initial point which lies a little low. The last three figures, 7.9 - 7.11, show the three normalized rms vorticity components plotted for comparison. The

present data is compared additionally to the experimental data of Lemonis (1995). The numerical data of Spalart (1988) are systematically lower than the experimental in the three cases. The present values of ω_x' seems to agree very well with the experimental data. The fit is closer to Balint et al. (1991) for low y/δ and subsequently follows the data of Honkan and Andreopoulos (1997). The lateral vorticity fluctuations shows that the present data starts to follow, at low y/δ, again the data of Balint et al. (1991) and both follow the numerical data of Spalart (1988), while all other experimental data lie above this initial trend. At larger y/δ the present data follows that of Honkan and Andreopoulos (1997). The plot of ω_z' shows that lower values of the present data, although closer to Balint et al. (1991), which tends to follow the data of Spalart (1988) and then for the upper range meets with the data of Honkan and Andreopoulos (1997).

Overall the comparison of the present data with other experimental data, in particular the data of Balint et al. (1991) and Honkan and Andreopoulos (1997), and the numerical data of Spalart (1988), seem to indicate that the current probe is able to produce very reasonable results.

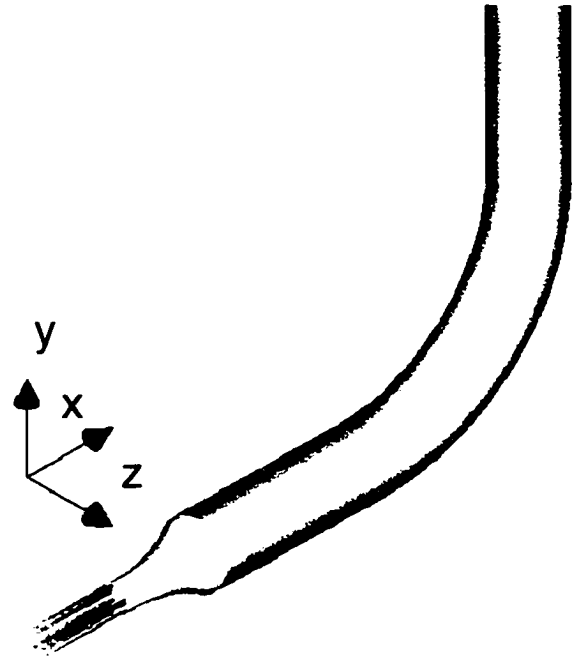

Figure 7.1 Rendered view of probe oriented in terms of the facility coordinate system. The probe points into the flow.

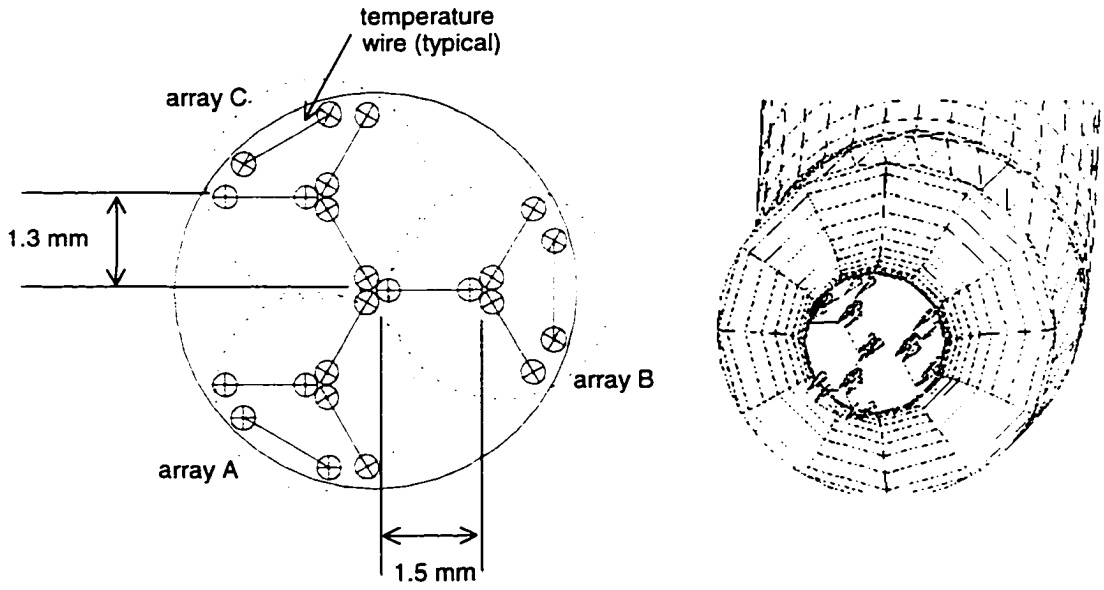

Figure 7.2: Close-up view of wire orientation & wireframe close-up.

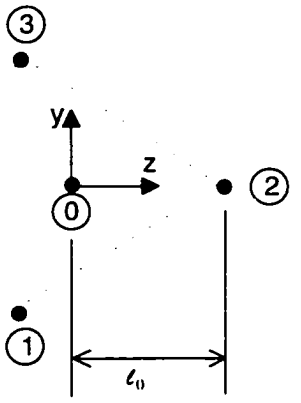

Figure 7.3: Layout of probe centroids

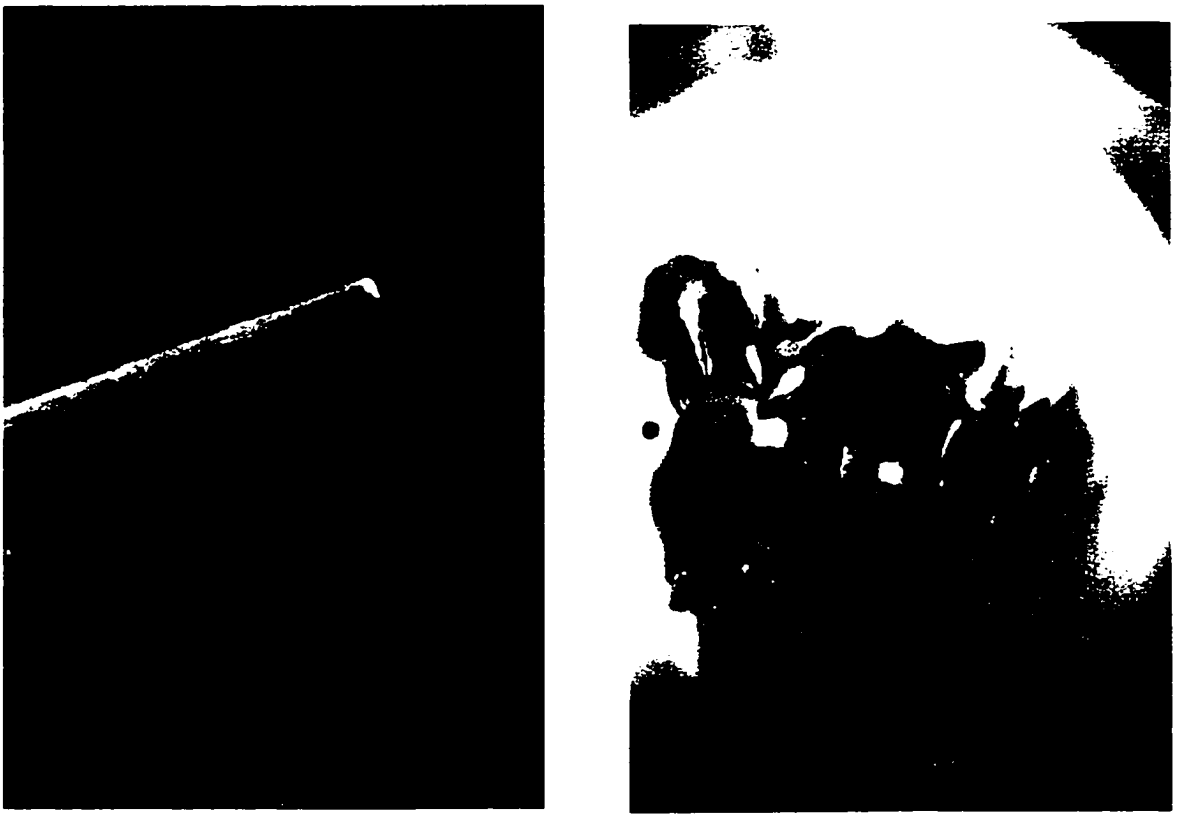

(a) (b)

Figure 7.4 Photographs of the vorticity probe: (a) size comparison with a medium tooth pick, (b) close-up view directly into the probe.

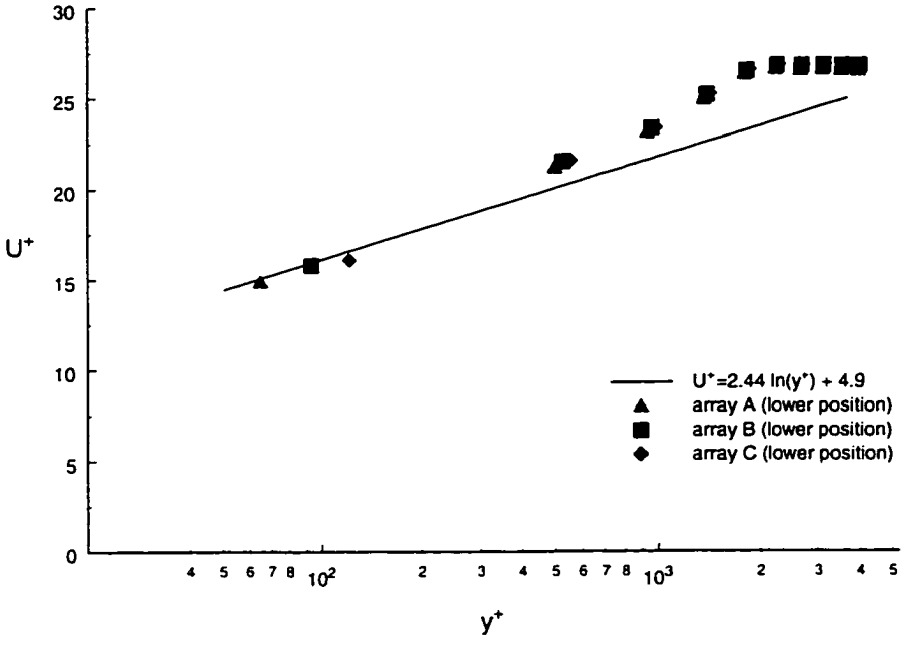

Figure 7.5: Boundary layer longitudinal velocity profile

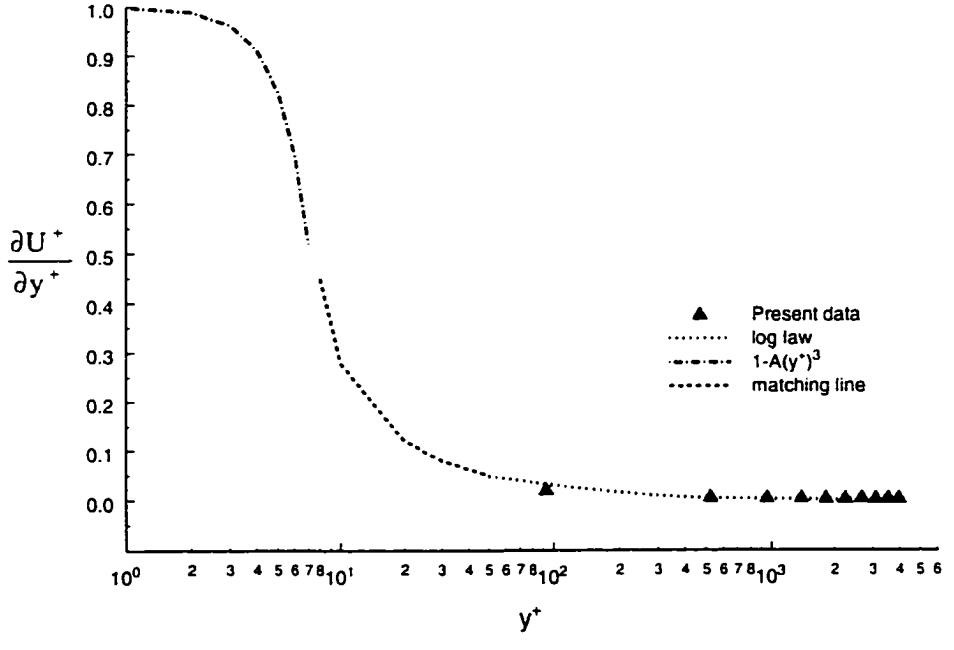

Figure 7.6: Mean velocity gradient, $\frac{\partial U^+}{\partial y^+}$, profile

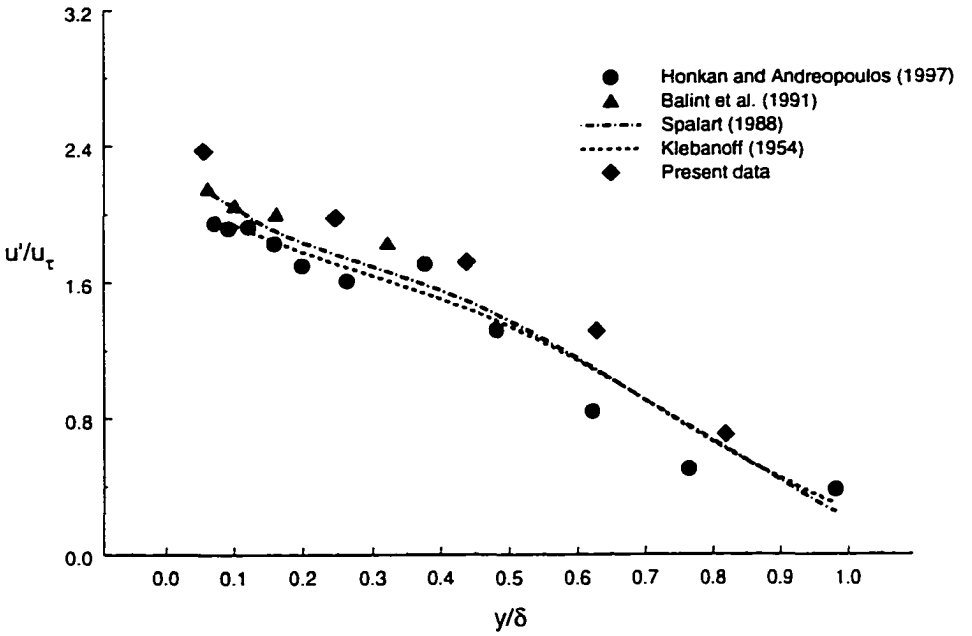

Figure 7.7: Rms of longitudinal velocity profile

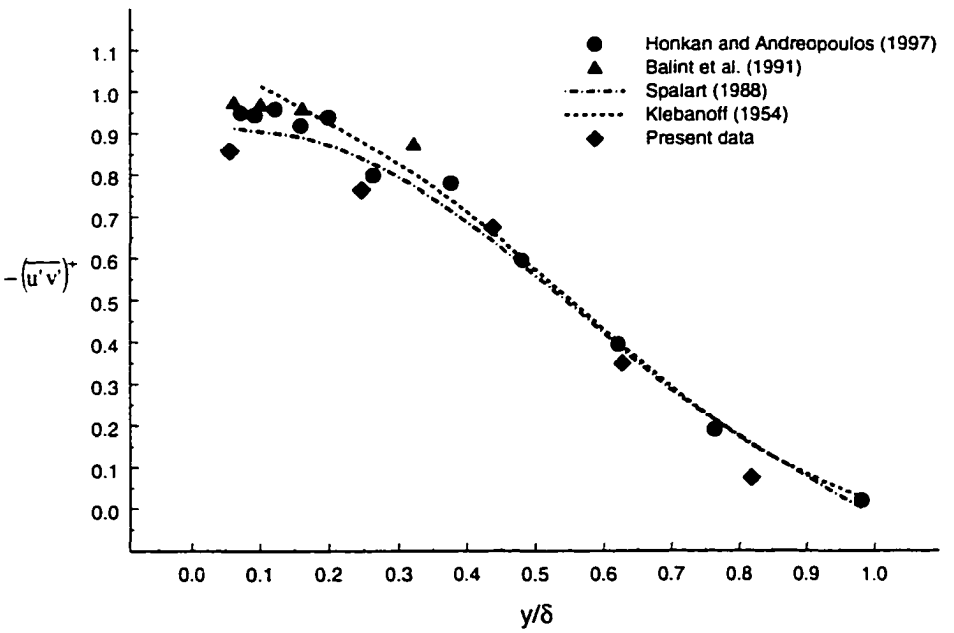

Figure 7.8: Reynolds stress profile

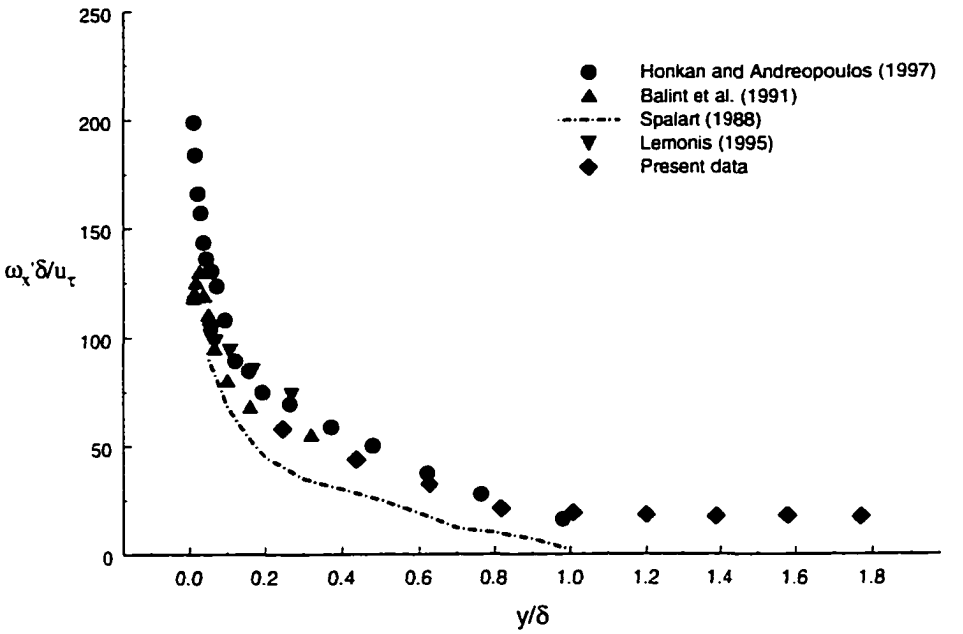

Figure 7.9 Rms of longitudinal vorticity profile.

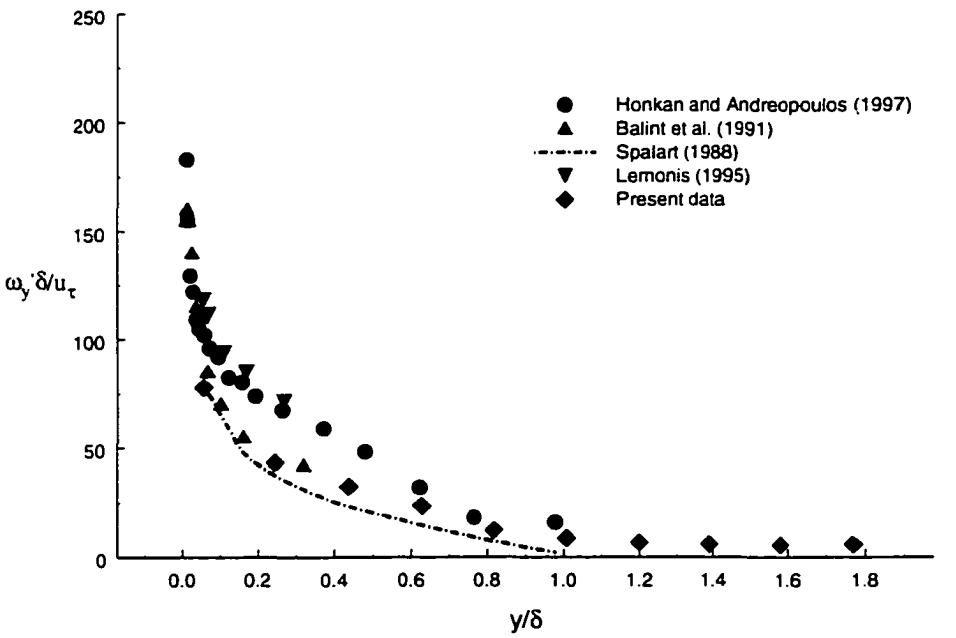

Figure 7.10: Rms of normal vorticity profile.

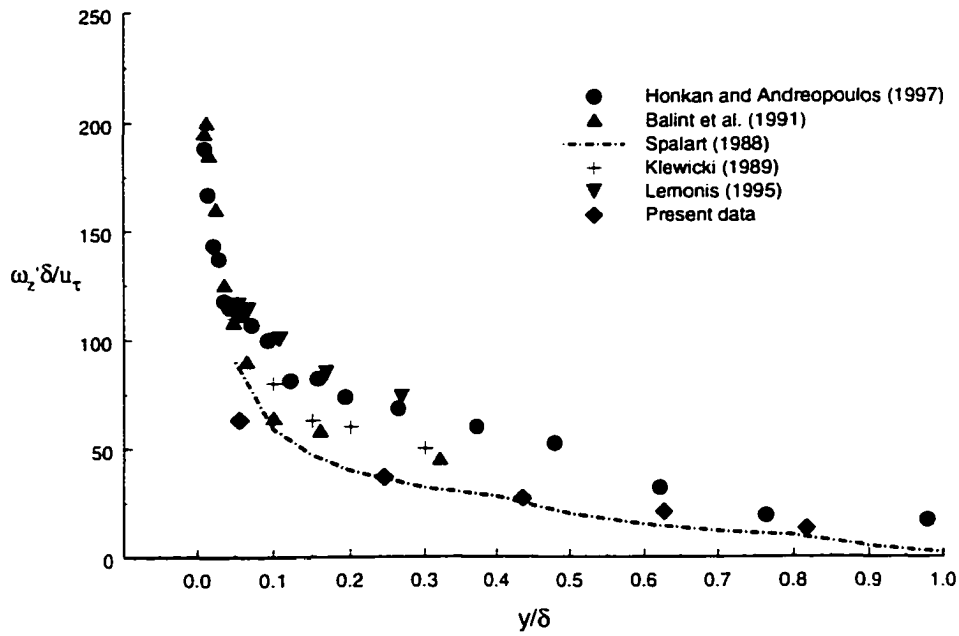

Figure 7.11: Rms of spanwise vorticity profile.

Chapter 8

8. Results & Discussion I - Shock Wave/turbulence interaction.

This chapter deals with the interaction of shock waves with grid generated turbulence. The turbulent flow is produced by a rigid wire mesh placed in front of the working section. Two different grids were used in the present experiment. The relative Mach number, $M_{s,R}$, is introduced here as a more suitable Mach number representation of the interaction. It accounts for the relative speed of the incident flow with respect to the upstream propagating reflected shock, given by,

$$M_{s,R} = \frac{U + W_R}{a} \tag{8.1}$$

A table of pertinent experiments and operating conditions are given in Table 8.1 below.

No.	Grid model	Probe(s)	x/m	p_2/p_1	M_s	$M_{s,R}$
1	2 x 2	vorticity	48	1.56	0.308	1.04
2	2 x 2	vorticity	48	1.77	0.388	1.115
3	3 x 3	vorticity	72	1.7	0.362	1.104
4	3 x 3	vorticity	72	1.87	0.425	1.191

Table 8.1: Grid turbulence experiments.

Turbulence in experiments is characterized the fluctuating behavior of measured quantities. In grid generated turbulence the fluctuating levels and scales of eddies is dictated by the porosity (open area ratio) of the grid mesh. Two different grids were used in the present work, 2 x 2 and 3 x 3 cells/per inch^2, with corresponding mesh sizes

(dimension of square cell) of 12.7 mm and 7.62 mm. The results presented in this chapter correspond to these two grid models subjected to several incident relative Mach numbers.

8.1 Decoupling of denstiy and velocity

The method of decoupling density from the mass flux signals was adapted from Briassulis et al. (1996). Basically the mean static pressure was assumed to be constant throughout a cross-sectional plane, at one x-location. Also, the static pressure fluctuation were assumed to be relatively small in comparison to the velocity fluctuations according to Markovin's hypothesis (1960) of "Strong Reynolds analogy". Although this hypothesis claims that both pressure and temperature fluctuations are very small, the present work only assumes that the former is small and makes use of the direct measurements of fluctuating total temperature to indirectly provide the fluctuating temperature. Temperature fluctuations were calculated by assuming that $(v^2+w^2)/2c_p$ where v and w are the fluctuations in the normal and spanwise directions, are is very small in comparison to $T_0-u^2/2c_p$ where u is the instantaneous velocity in the longitudinal direction.

The procedure involves deriving an expression for mass flux, m, in terms of the total temperature and pressure,

$$m = \rho u = \frac{pu}{RT} = \frac{pu}{R\left(T_0 - \frac{u^2}{2c_p}\right)} \tag{8.2}$$

This relation can be rearranged to derive a quadratic equation in U,

$$\frac{Rm}{2c_p}u^2 + pu - mRT_0 = 0 \tag{8.3}$$

For each sampled time step, the instantaneous measurements of total temperature and mass flux, m, were available at the same measuring location, while the instantaneous pressure was measured on the wall. If the thin layer approximation of the boundary layer is invoked, then the pressure appearing in equation 8.3 is substituted by the local mean wall pressure. Due to the nature of quadratic equations, equation 8.3 yields two distinct roots. One root is negative therefore unrealistic. Consequently only the positive root was used as a solution to equation 8.3. This calculation was performed at each time step.

8.2 Velocity and Vorticity Signals

This section gives an analyses of the signals option for the four experiments. Figures 8.1 to 8.4 present the signals of the three velocity components for each experiment. What should be observed here is the quality of the signal and the velocity range of each experiment which is related to the incident shock strengths.

The first jump in velocity is due to the arrival of the incident shock, while the sudden drop in longitudinal velocity is due to the arrival of the reflected shock. The signals visually seemed to be relatively clean devoid of any electronic noise characteristics such as spikes. Notice that the normal and spanwise velocity components are centered about zero before and after the arrival of the reflective shock. The flow after the interaction with the shock, although experiencing a sudden drop in longitudinal velocity, tends to show a mean value which is either constant or has a slight deceleration. Consequently, the data size for statistical analysis is limited. It was found through the reference wall pressure data taken for each grid experiment, that the arrival of a small shock wave which is reflected off the grid model, brought about a minimal velocity jump.

The arrival of this shock was taken as the upper limit of the data. The lower limit was taken from the instant right after the passage of the reflected shock.

Figures 8.5 - 8.6 provide the corresponding vorticity signals given for a smaller time window centered about the arrival of the reflected shock. The signals which in reality lie right on top of each other have been displaced for viewing purposes. It seems the arrival of the shock brings about visually subtle differences in the interacted flow (right of shock reference line). In most cases there seems to be a slight amplification of the fluctuations. Also, the nature of the frequency of the fluctuations seems to change. Further along in time, the fluctuations again change. This change seems to correspond with the arrival of the grid shock sensed on the wall pressure signal. Therefore only the initial interacted flow is taken for statistical consideration, which provided a range of 800 - 1000 useful data points, depending on the experiment.

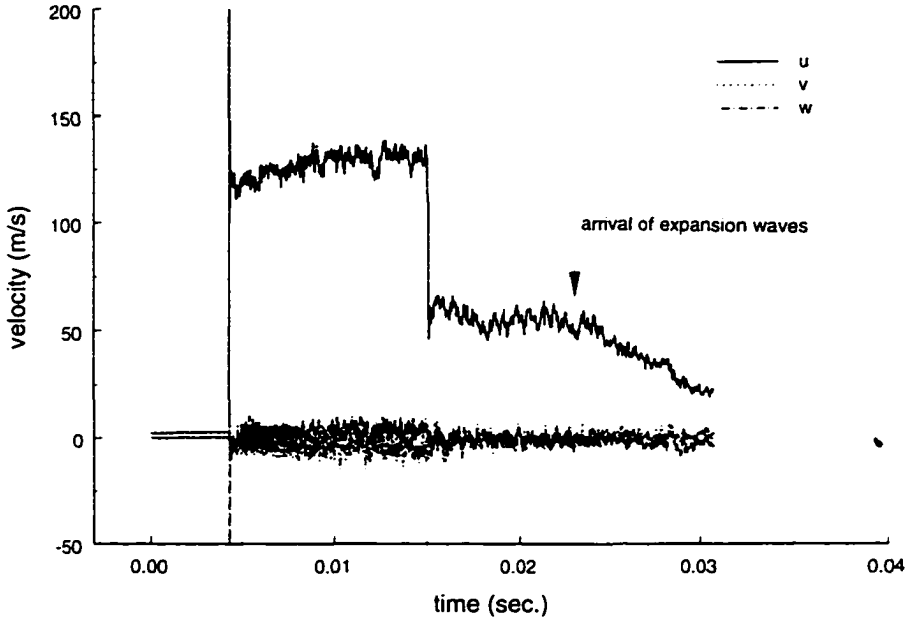

Figure 8.1: Velocity signals of 2 x 2 grid model at $M_{*,R}$ =1.04

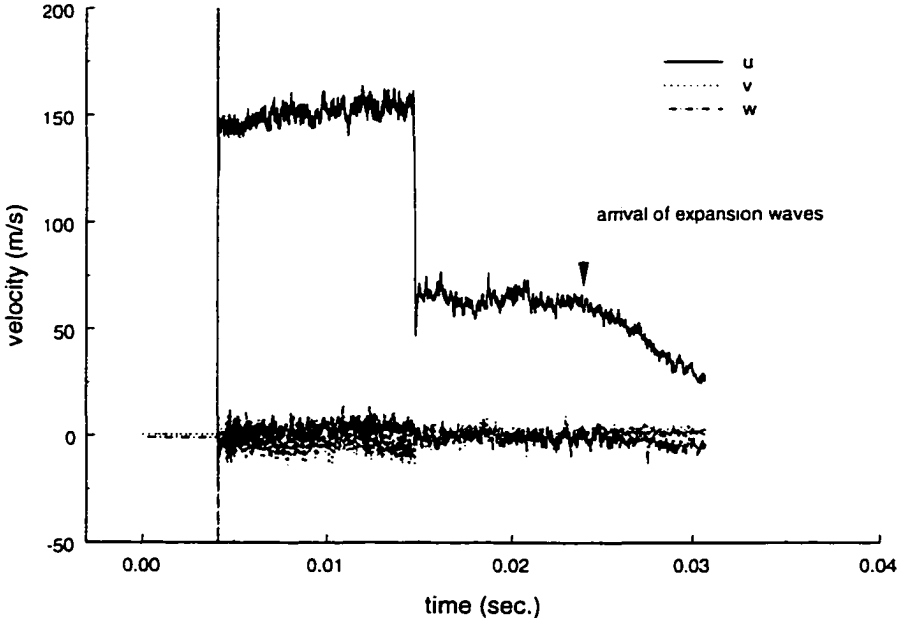

Figure 8.2: Velocity signals of 2 x 2 grid model at $M_{*,R}$ =1.115

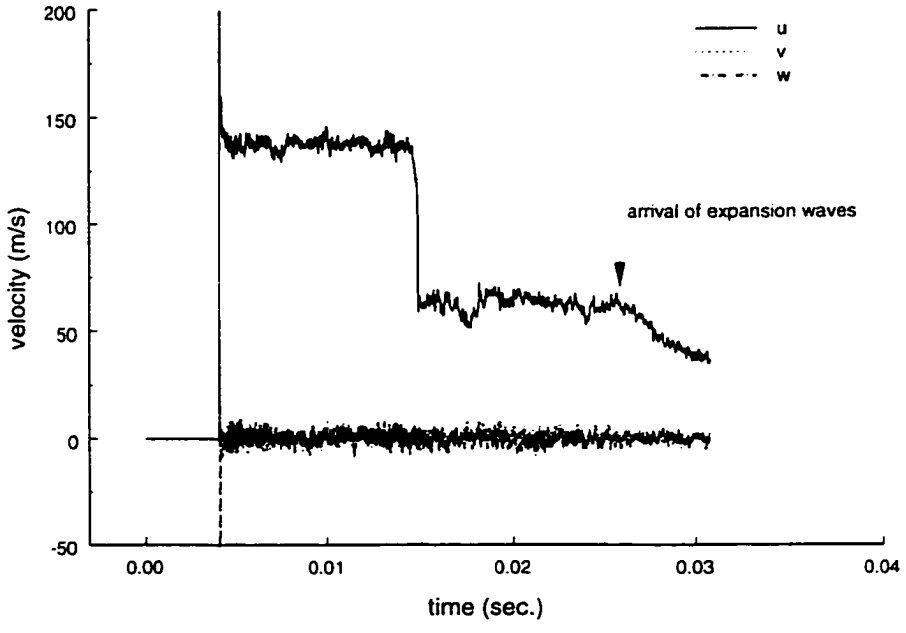

Figure 8.3: Velocity signals of 3 x 3 grid model at $M_{\infty,R}$ =1.104

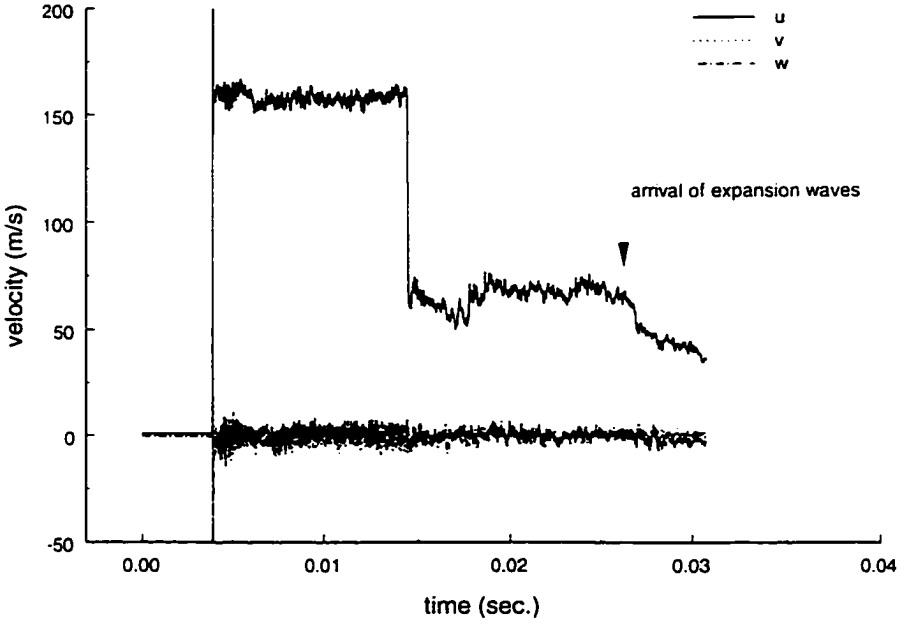

Figure 8.4: Velocity signals of 3 x 3 grid model at $M_{\infty,R}$ =1.191

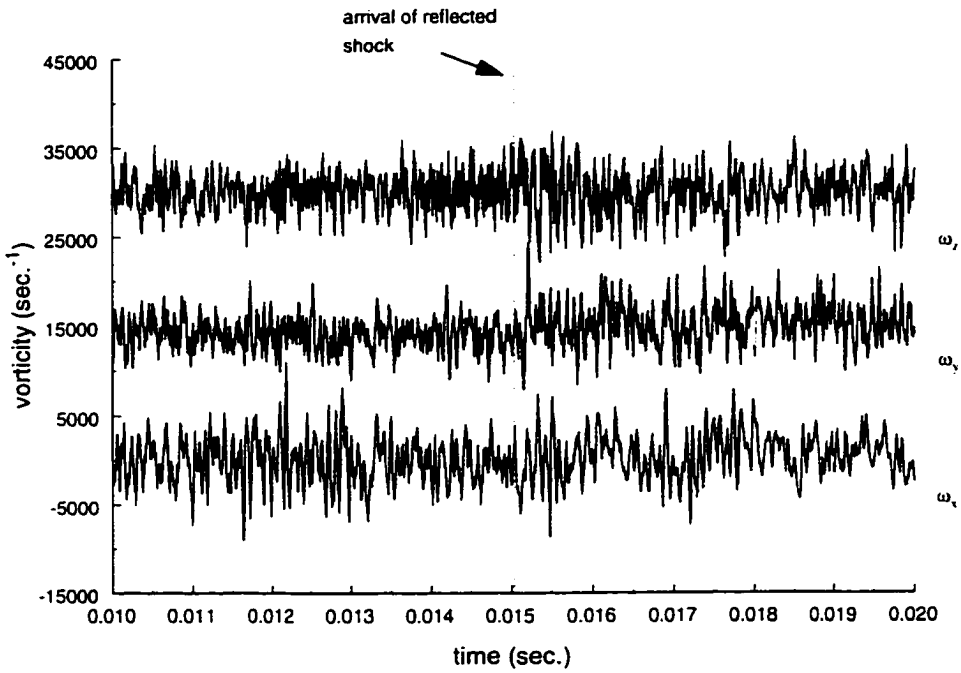

Figure 8.5: Vorticity signals of 2 x 2 grid model at $M_{\infty,R}$ =1.04 (signals are displaced)

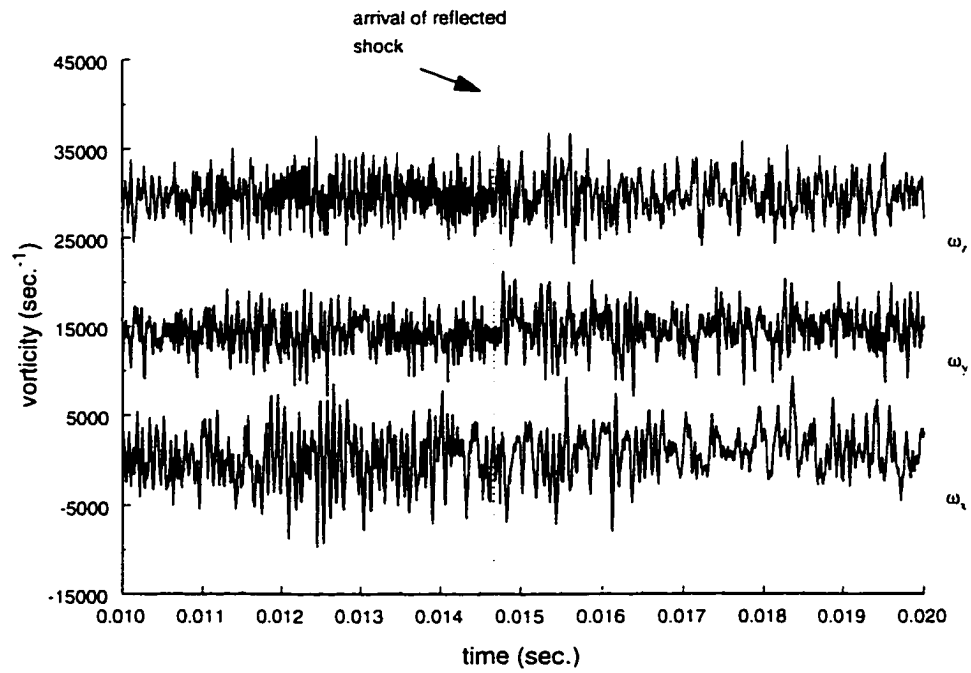

Figure 8.6: Vorticity signals of 2 x 2 grid model at $M_{\infty,R}$ =1.15 (signals are displaced)

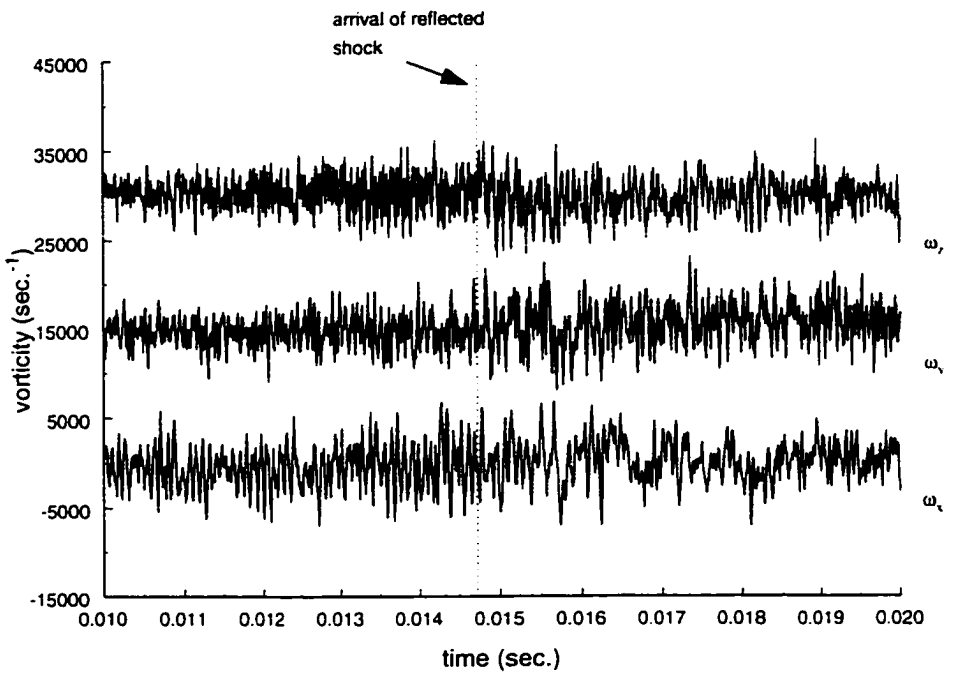

Figure 8.7: Vorticity signals of 3 x 3 grid model at $M_{\infty,R}$ =1.104 (signals are displaced)

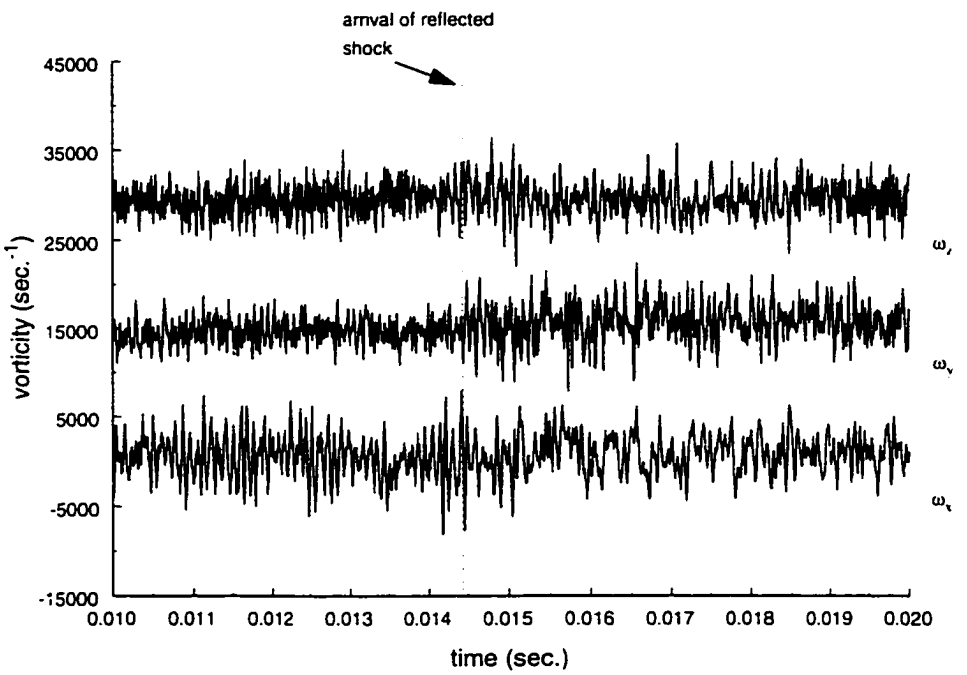

Figure 8.8: Vorticity signals of 3 x 3 grid model at $M_{\infty,R}$ =1.191 (signals are displaced)

8.3 Statistics

The present work incorporates measurements taken at two different Mach number cases for each grid model. Although the intention was not to perform a compressibility study (the Mach number change is not very large between different experiments), the two Mach numbers provided independent data on which to draw comparison or observe similar trends.

Given in figure 8.9 is a plot of the ratio of the square rms of the velocity fluctuations, $u_D'^2/u_U'^2$. It shows that the 2 x 2 grid, the coarser grid, at the lower Mach number produced amplification of all fluctuating velocity, and that at the high Mach number only the longitudinal velocity rms increased while the other two components decreased. For finer grids, longitudinal velocity rms increased significantly more while the other two components experienced slight attenuation at both Mach numbers.

The vorticity amplifications shown in figures 8.10 show a different trend. They are plotted together with the Linear Interaction Analysis (LIA) predictions and the numerical simulation of Lee, Lele and Moin (1993). It shows most importantly that in all cases the spanwise and normal vorticity rms components are amplified through the interaction while the longitudinal velocity rms are in most cases suppressed by the interaction (ω_x rms for the 3 x 3 grid at the lower Mach number is slightly increased). However, it shows that for the 2 x 2 grid the amplification decreases with Mach number, while the opposite trend is noticed for the 3 x 3 grid. Also a disparity in amplification levels between ω_y and ω_z exits for the 3 x 3 grid, with ω_y having much higher amplifications.

Linear Interaction Analysis (LIA) (see e.g. Lee, Lele and Moin, 1993) which predicts that the streamwise vorticity remains constant through the shock wave, while spanwise (or normal) vorticity amplification grows with increasing Mach number. The simulation of Lee, Lele and Moin (1993) also clearly shows amplification of spanwise (or normal) vorticity fluctuations downstream of the shock, although they investigated much higher initial turbulence levels, of the order of 10%, than the present work. They found that their data was systematically lower the LIA predictions. Although the present data shows some scatter and an incident turbulence level dependence, it was in general agreement with the results of LIA and Lee et al. (1993). The data of Lee et al. also showed an initial turbulence level dependence.

The Probability Density Functions are given in figures 8.11 - 8.14. The PDFs of all variables in one experiment are given in one figure. It seems that the PDFs show a close to symmetric distribution except for certain rare cases. The PDFs that show the most change before and after the interaction are those associated with the velocities of the flow. Usually PDFs are used to reveal the likelihood of any high amplitude rare events marked by tails of the distribution significantly greater than +/- 3. None of these distributions seem to show any indication of these high amplitude events. Not even the PDFs of vorticity, which by their nature are characterized by high amplitude intermittent events, show any strong signs of these events, although their tails extend slightly beyond those of the velocity. It is also interesting to note that the vorticity PDF's, in general, are relatively more symmetric than those of velocity.

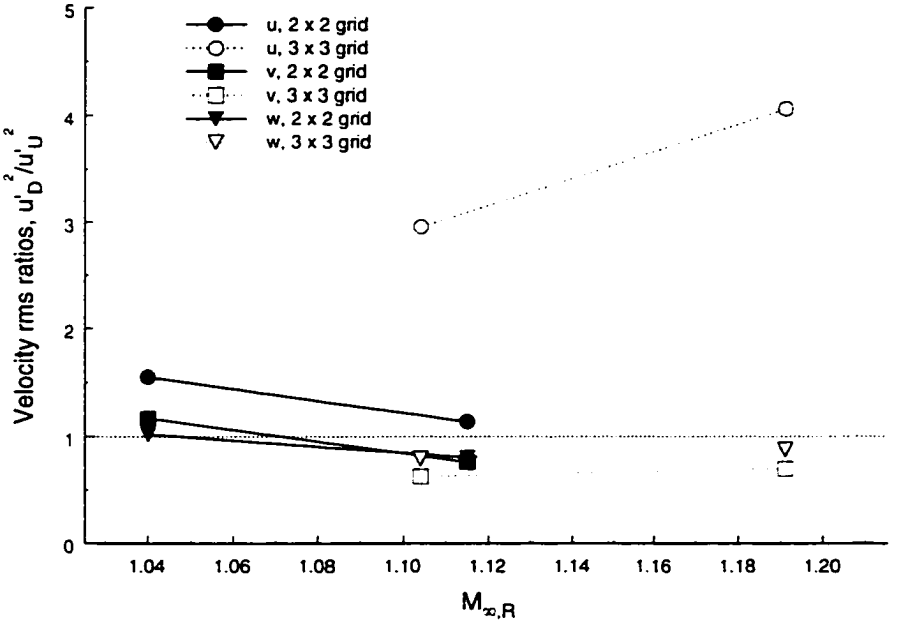

Figure 8.9: Velocity rms ratio.

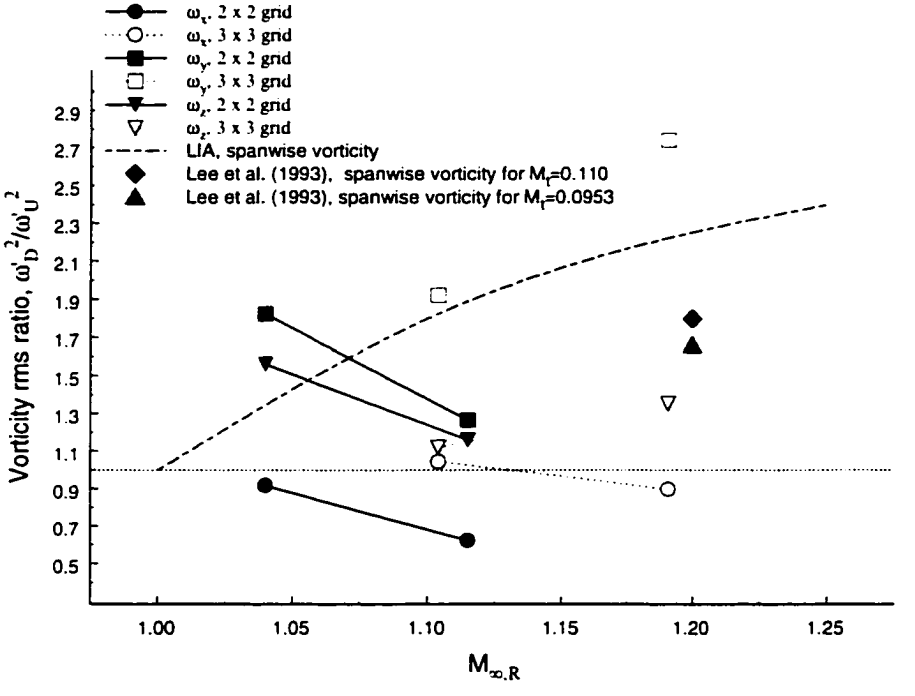

Figure 8.10: Vorticity rms ratio.

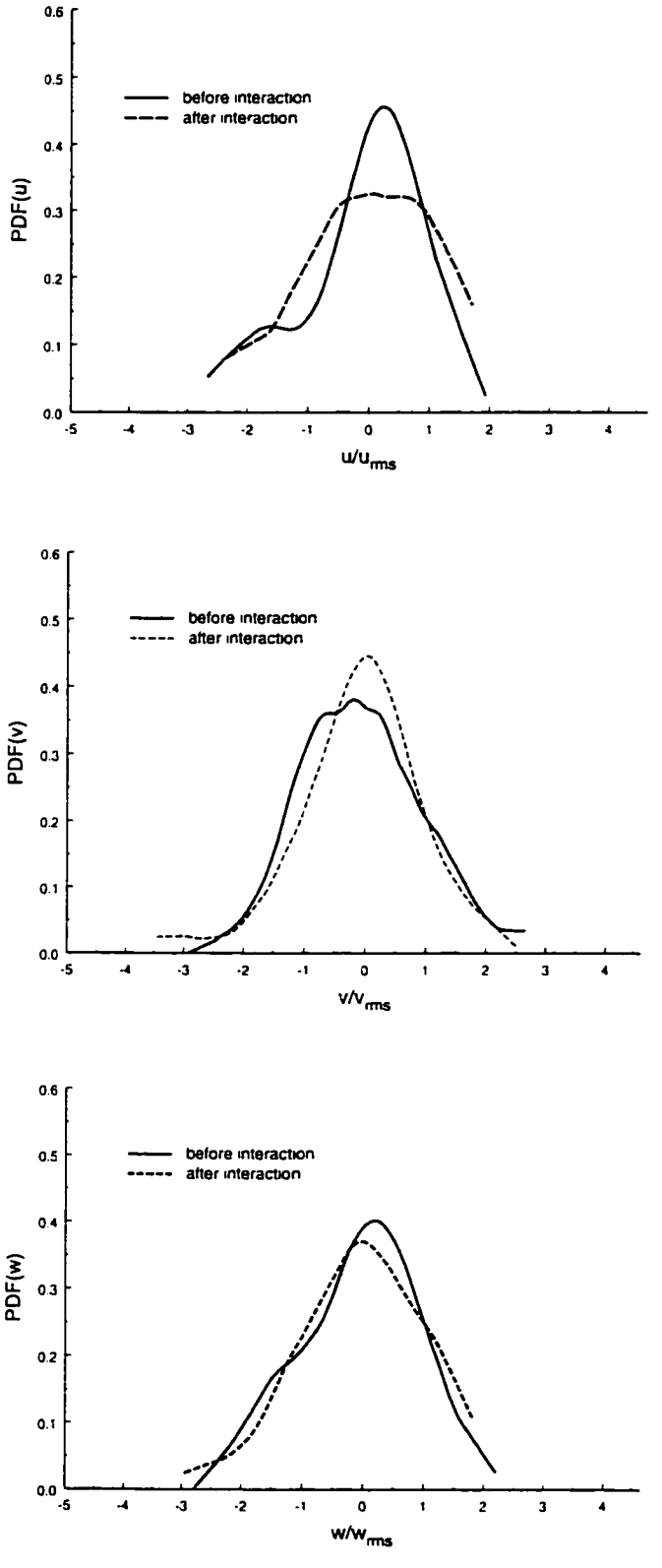

Figure 8.11: PDF's of :(a) u, (b) v, (c) w, (d) ω_x, (e)ω_y, (f) ω_z, for 2 x 2 grid. M=1.04.

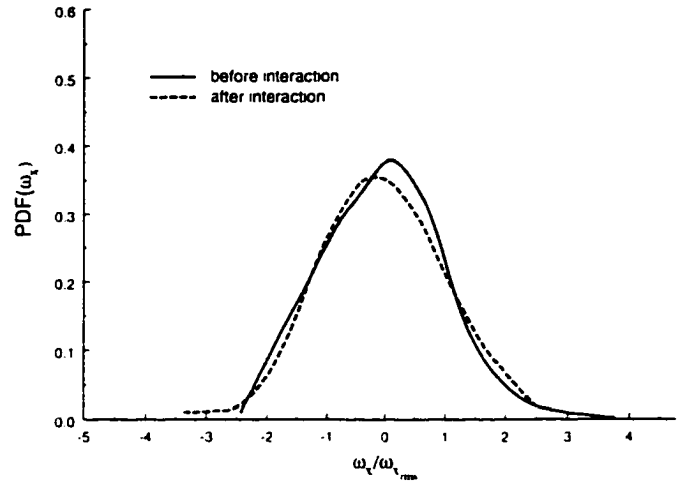

(d)

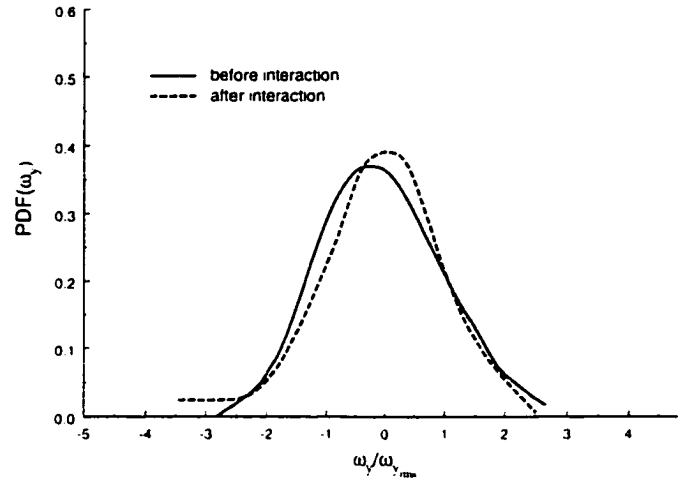

(e)

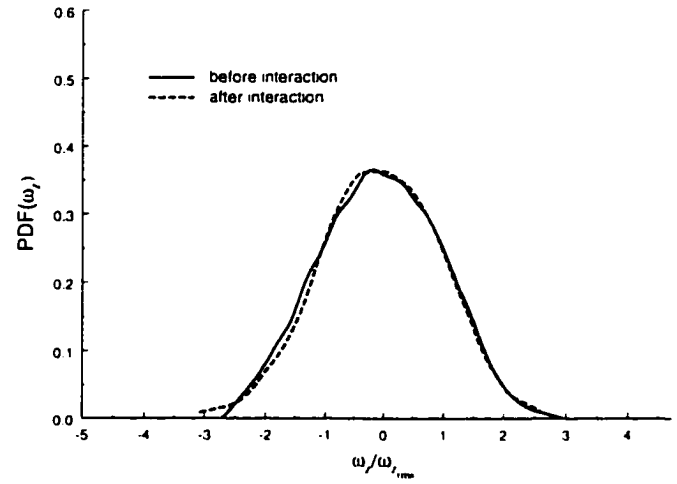

(f)

Figure 8.11 cont'd.

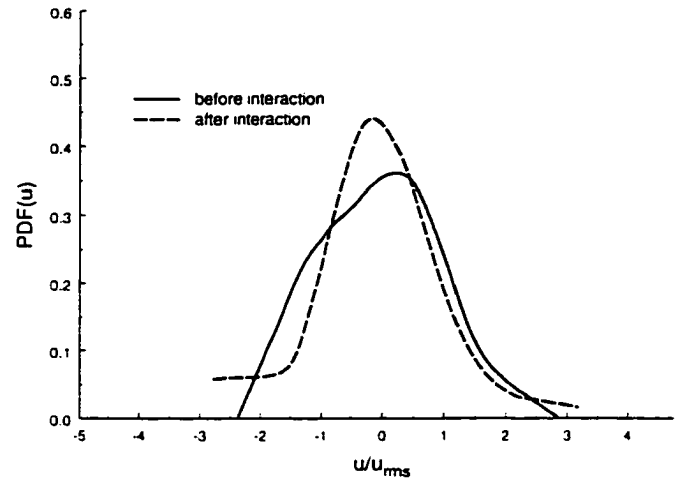

(a)

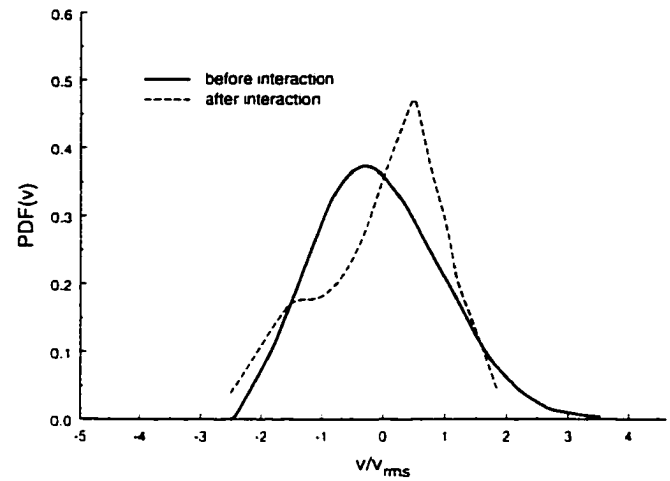

(b)

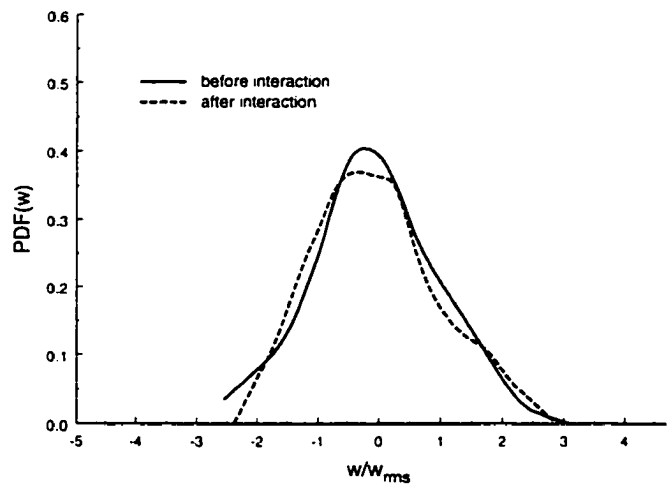

(c)

Figure 8.12: PDF's of :(a) u, (b) v, (c) w, (d) ω_x, (e)ω_y, (f) ω_z, for 2 x 2 grid. M=1.15.

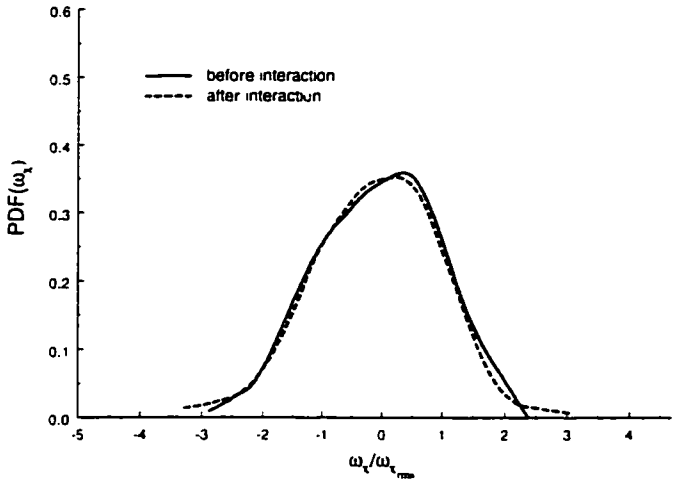

(d)

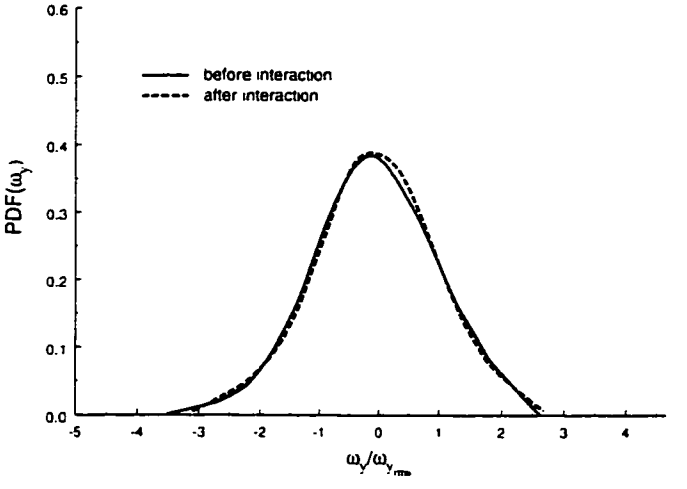

(e)

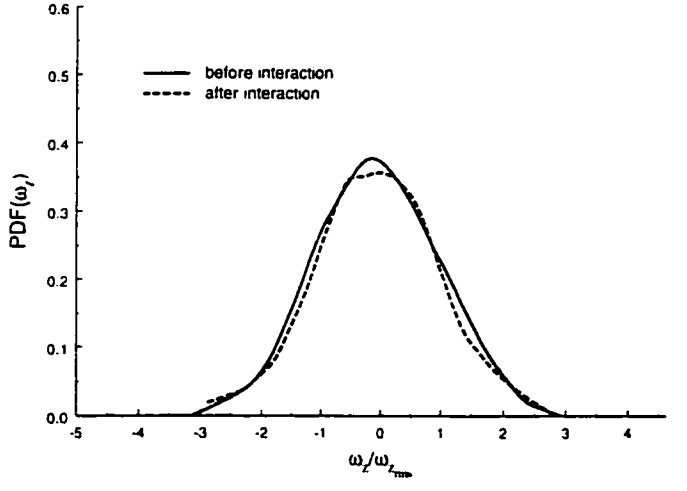

(f)

Figure 8.12 cont'd.

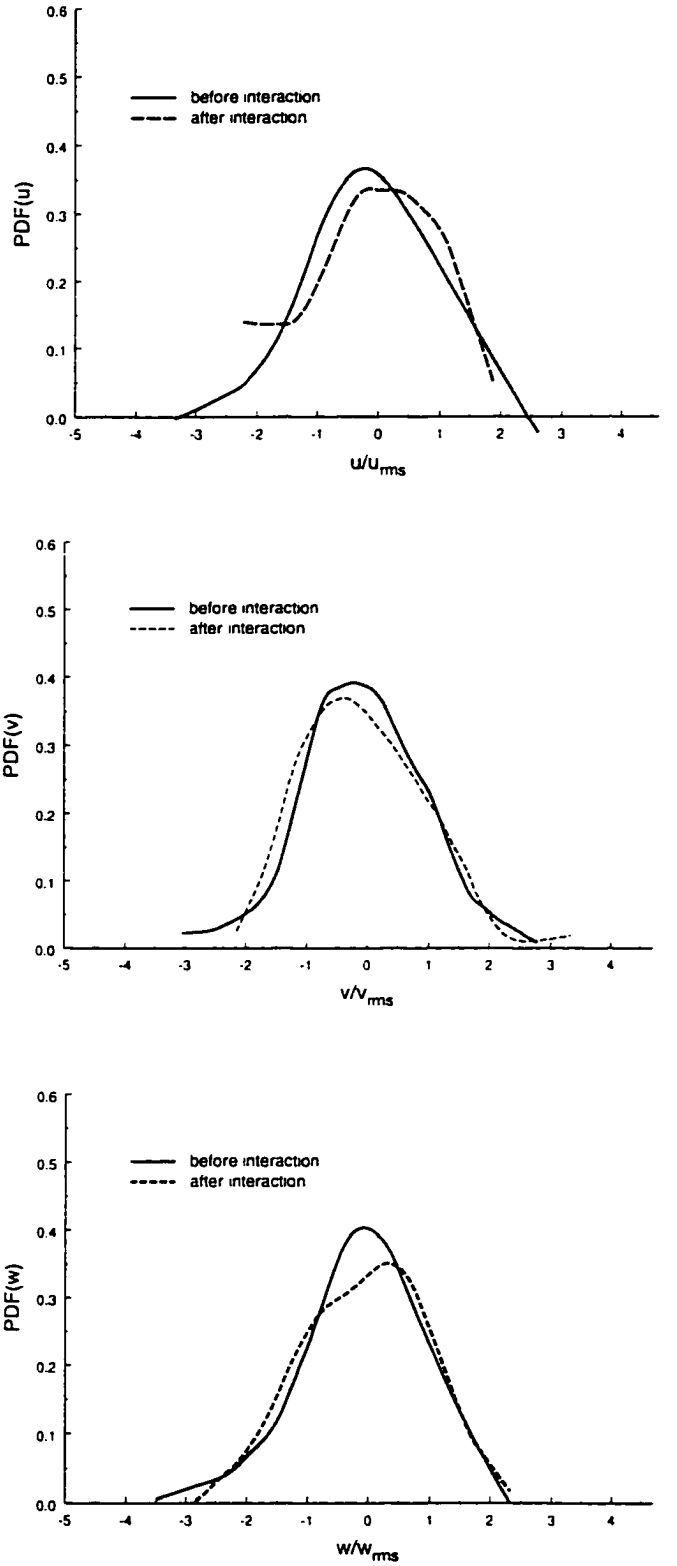

Figure 8.13: PDF's of :(a) u, (b) v, (c) w, (d) ω_x, (e)ω_y, (f) ω_z, for 3 x 3 grid. M=1.104.

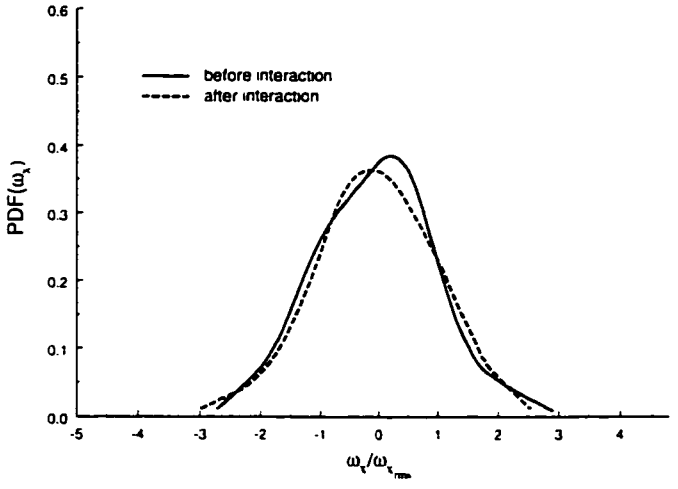

(d)

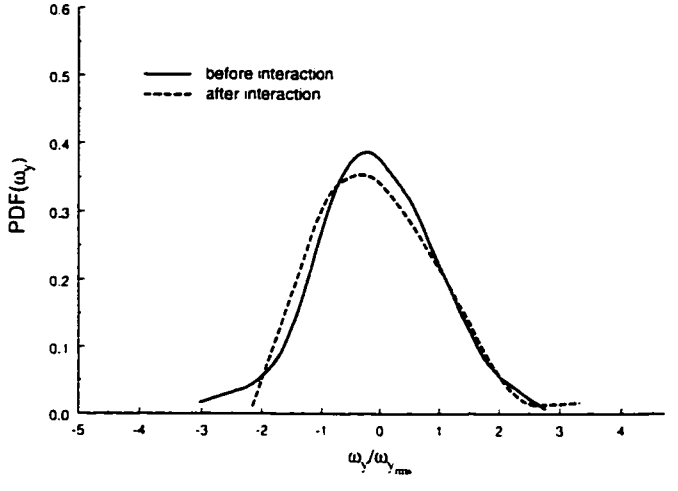

(e)

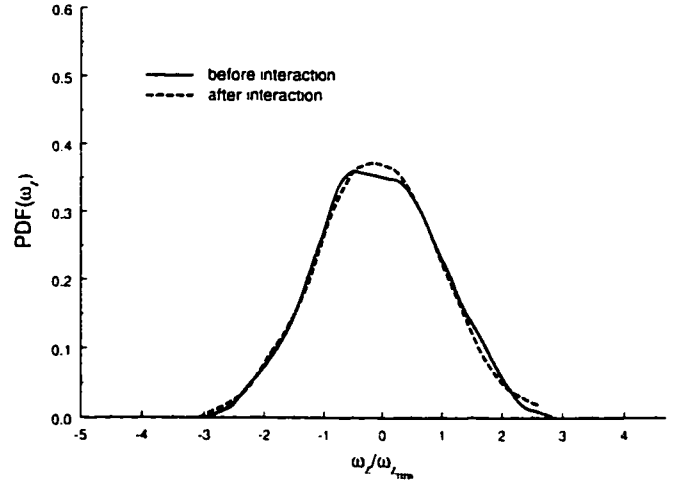

(f)

Figure 8.13 cont'd.

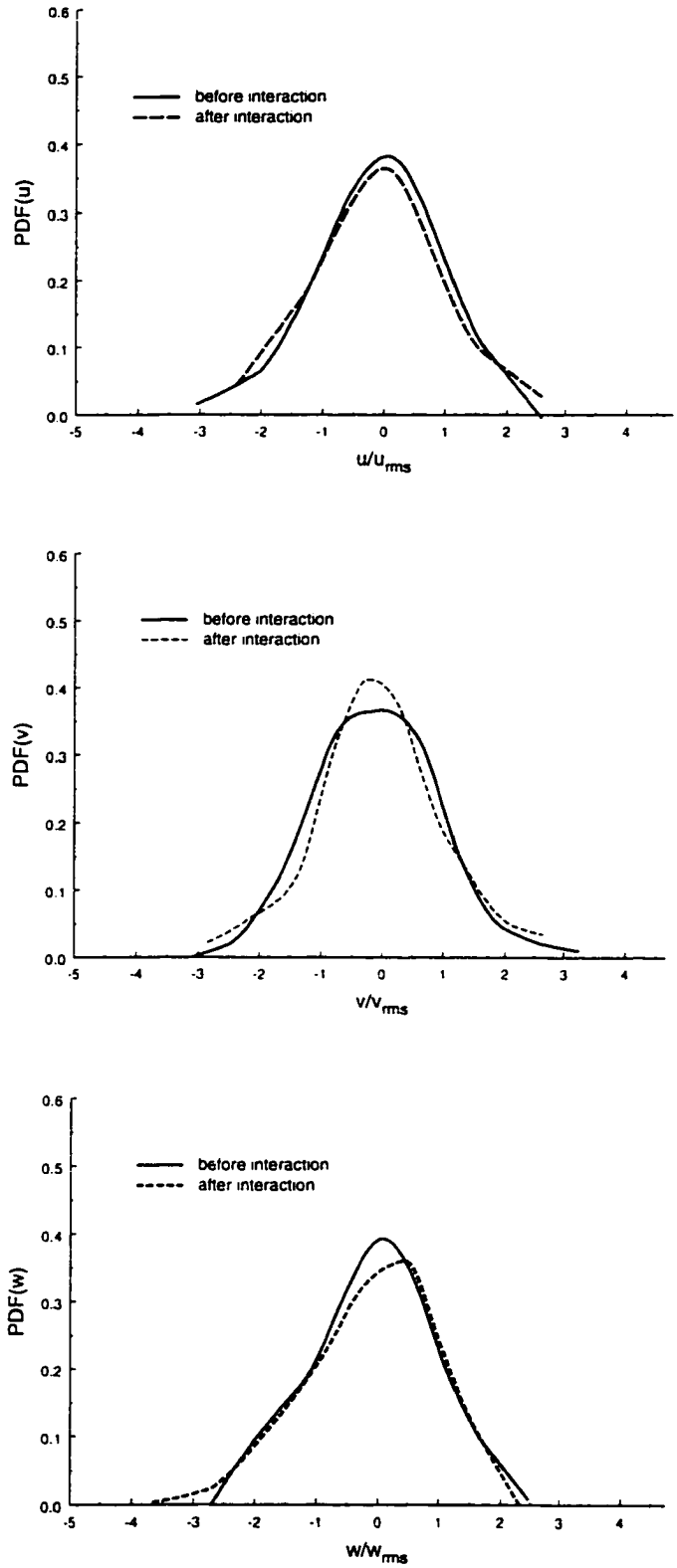

Figure 8.14: PDF's of :(a) u, (b) v, (c) w, (d) ω_x, (e)ω_y, (f) ω_z, for 3 x 3 grid. M=1.191.

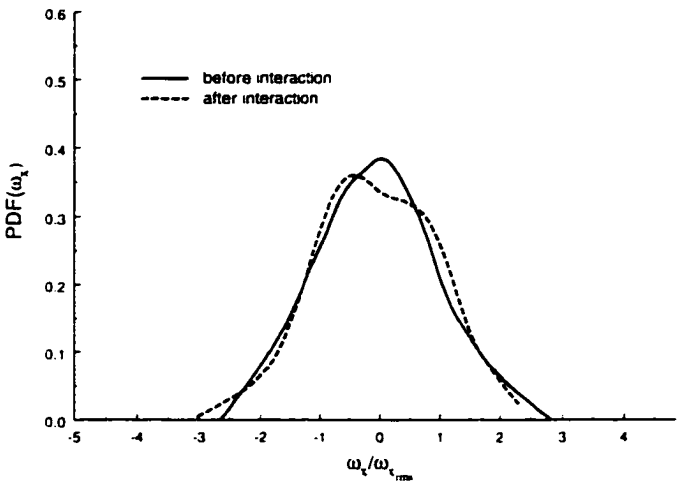

(d)

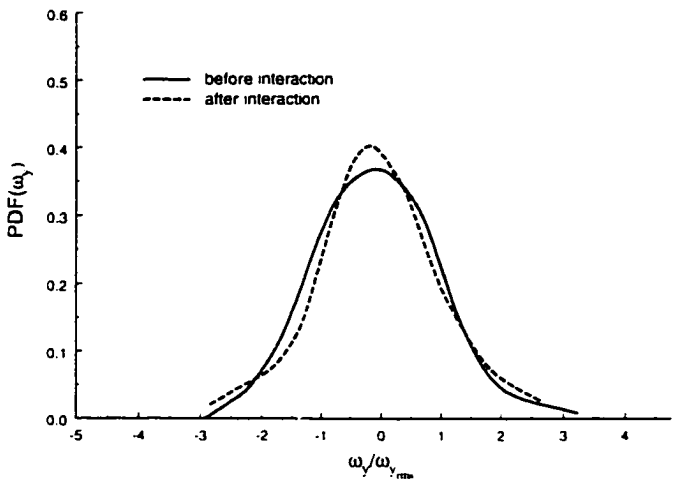

(e)

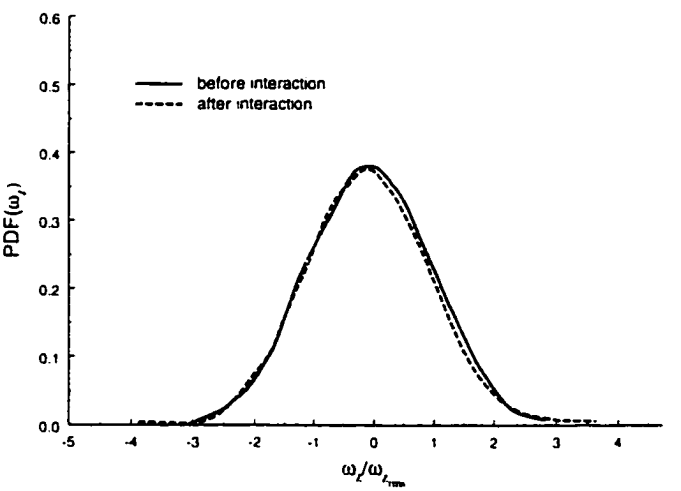

(f)

Figure 8.14 cont'd.

8.3 Spectral Analysis

Spectral analysis has been used extensively to characterize turbulent flows. Spectra can provide valuable information in terms of the frequency content of a particular flow. An important aspect of turbulent spectra is identifying the inertial subrange where viscous dissipation of the energy of turbulence proceeds at a constant rate. The amplitude level in spectral values indicates the frequency, or range of frequencies, over which the fluctuations are most energetic.

There has been some question raised as to how to properly plot pre- and post-spectra. Here, the strong suggestion expounded by Lee et al. (1993) that *the upstream wavenumber spectrum should be compared to the downstream wavenumber spectrum* has been followed. In this case, the two local mean velocities before and after the passage of the shock have been used to evaluate the upstream and downstream wavenumber spectra respectively. Notice that the pre- and post wavenumber range willl be different because of the difference in velocities.

The spectra presented here are plotted against wavenumber, which is defined as

$$k = \frac{2\pi f}{U} \tag{8.4}$$

where U is the local mean velocity in laboratory coordinates and f is the frequency.

Figures 8.15 - 8.38 present the Power Spectral Densities of velocity and vorticity for all cases. The first four figures provide the spectra of longitudinal velocity which includes the -5/3 slope for reference. By inspection, it is seen that the flow before interaction, in general, possesses a smaller inertial subrange than the corresponding flow

after the interaction. The spectra of normal and spanwise velocity show almost no sign of the existence of the -5/3 slope range.

Figure 8.28 - 8.38. present the spectra of vorticity. All spectra show two different slopes which dominate the dynamics of vorticity. The slope at the smaller wavenumbers seems to vary for different cases, while the larger wavenumber slope seems to be consistent. The longitudinal vorticity spectra was found to have a -5 slope in the wavenumber range. This slope seemed to persist as well after the interaction but is shifted to the right.

Figures 8.39 - 8.42 show the comparison of spectra of the turbulent kinetic energy to that of the rotational energy, or enstrophy $1/2\omega_i\omega_j$. It is clear to see that for all cases the enstrophy spectra possesses more energy at the larger wavenumbers than does the turbulent kinetic energy. However with larger incident Mach number the enstrophy spectra starts to shift to lower wavenumbers, approaching the spectral signature of the corresponding turbulent Kinetic energy.

Through the interaction the spectral signature of both turbulent kinetic energy and enstrophy changes significantly. Figures 8.43 - 8.46 present this spectral effect for the kinetic energy. The most revealing pattern is that after the interaction the spectra is consistently above the one before interaction. This clearly indicates an amplification of the turbulent kinetic energy. This amplification occurs over the whole range of wavenumbers presented here.

The enstrophy, in figures 8.47 - 8.50, also shows increases. However the increases depends on the grid model used. The 2 x 2 grid produces an enhancement in spectral value at the very large wavenumbers while showing suppression at the smaller

wavenumbers to mid-range scale of wavenumbers. For the 3 x 3 grid the enhancement is over the whole range of wavenumbers. Therefore the wavenumber range of the enstrophy spectral enhancement depends on the initial turbulence level. It is interesting to see that the larger turbulent intensities as well as larger turbulent scales, produced by the coarser grid are suppressed at by the interaction.

Comparisons of the turbulent kinetic energy and enstrophy after the interaction are shown in figures 8.51 - 8.54. When compared to their relative trends before the interaction, these spectra show an even bigger shift of the rotational energy to the higher wavenumbers.

In order to ascertain the amplification at each wavenumber figures 8.55 to 8.62 present the wavenumber amplification ratio defined as

$$G(k_1) = \frac{\phi^p(k_1)}{\phi^u(k_1)} \tag{8.5}$$

One aspect as it relates to the wavenumber spectra should be kept in mind. The spectral values at the low wavenumbers correspond to the largest scales of the flow, which in turn have the largest time scales. Due to this, longer sampling are required for these larger scales. Therefore the small wavenumber spectral values are not as statistically independent as the larger ones. As a consequence the reader should view the small wavenumber spectral amplitudes or amplification ratio with some caution.

Figures 8.55 - 8.62 show the spectral amplification ratios for velocity and vorticity for all experimental cases. The overriding trend in all this figures is more amplification at the higher wavenumbers. Peak amplification values of nearly 20 fold

were found for both velocity and vorticity spectra. The peak in velocity amplification seems to correspond with that of vorticity for each experimental case. However the peak value occurs at different wavenumbers for each experimental case. For the 2 x 2 grid at the lower Mach number cases, the peak occurs at k_1m of 12 corresponding to a wavelength given by $\lambda = 2\pi/k$, of 40% of the mesh size. For the higher Mach number case, the peak occurs at 8, corresponding to a wavelength of 63% of the mesh size. For the 3 x 3 grid, the peaks occur at wavenumbers of 6.6 and 5.5 corresponding to wavelength sizes of 97% and 114% of the mesh size lower and larger Mach numbers respectively.

Grid	2 x 2	2 x 2	3 x 3	3 x 3
$\mathbf{M_{\infty,R}}$	1.04	1.115	1.104	1.191
$\varepsilon^D/\varepsilon^U$	14.16	4.83	5.76	3.5
λ^D/λ^U	0.114	0.416	0.196	0.243

Table 8.2: Dissipation and Taylor microscale ratios

Table 8.2 provides a quick reference to the ratio of measured values of dissipation and Taylor microscale, upstream of the traveling shock, to the values downstream (after the shock passes by). Dissipation was found directly by

$$\varepsilon = \tau_{ij}\frac{\partial u_i}{\partial x_j} = \tau_{ij}s_{ij} = 2\mu s_{ij}s_{ij} - \tfrac{2}{3}\mu\frac{\partial u_k}{\partial x_k}\frac{\partial u_p}{\partial x_p} \qquad (8.1)$$

and the Taylor microscale was found from the *Production equals Dissipation* relation $\varepsilon=15\nu u'^2/\lambda^2$.

It is very clearly seen that dissipation increases substantially through the interaction where as the microscale is equally compressed through the interaction. The

lowest Mach number for both grid models produced the largest dissipation increase, and correspondingly the largest compression of the Taylor microscale. This fits in nicely with the argument that large wavenumbers, and therefore the smaller scales, are enhanced through the interaction. The general trend found here of large wavenumber enhancement, increase in dissipation and a decrease in Taylor microscale seems to in fairly good agreement with the numerical work of Lee et al. (1993).

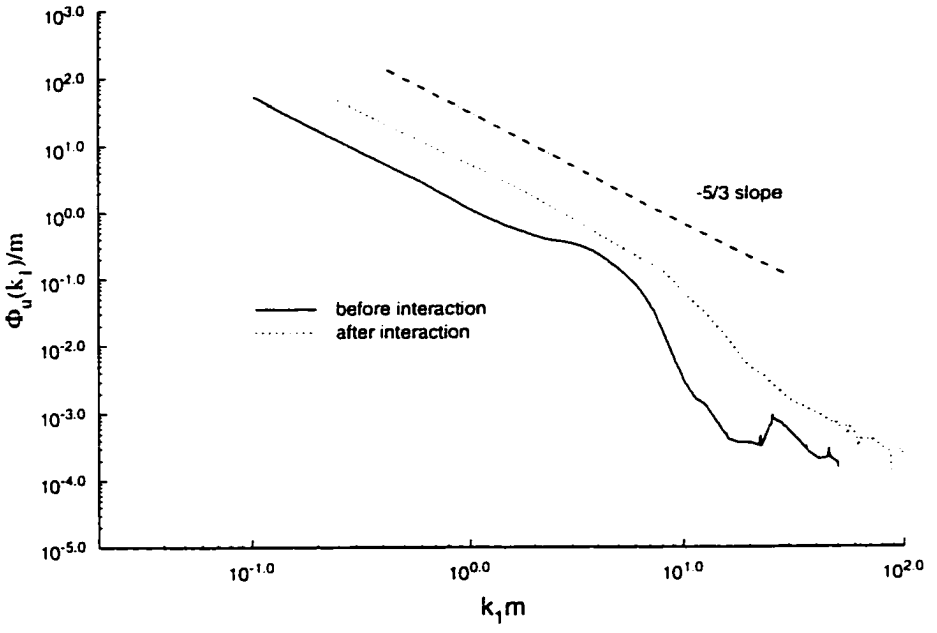

Figure 8.15: Smoothed longitudinal velocity PSD. 2 x 2 grid $M_{\infty,R}$=1.04.

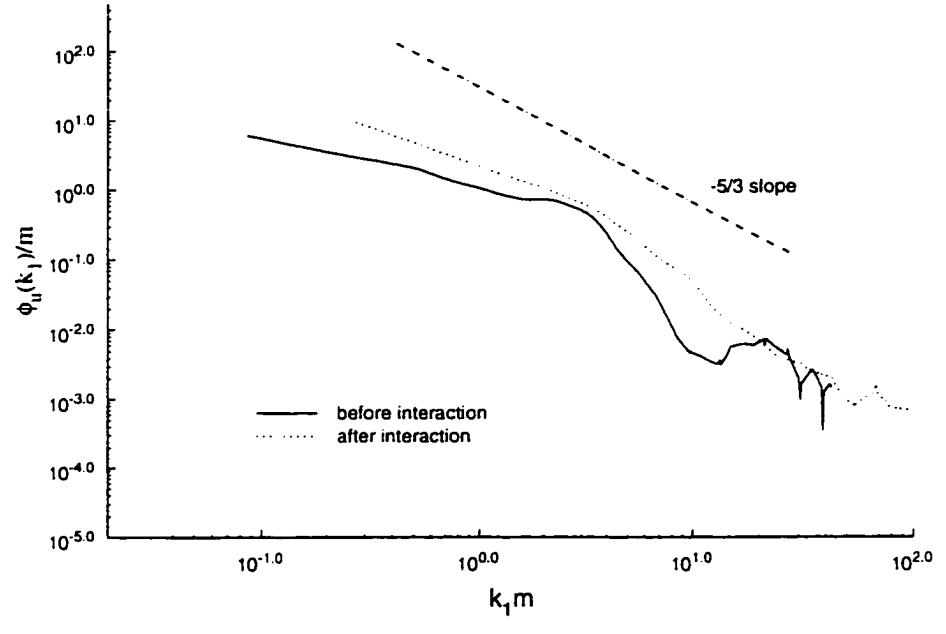

Figure 8.16: Smoothed longitudinal velocity PSD. 2 x 2 grid $M_{\infty,R}$=1.115.

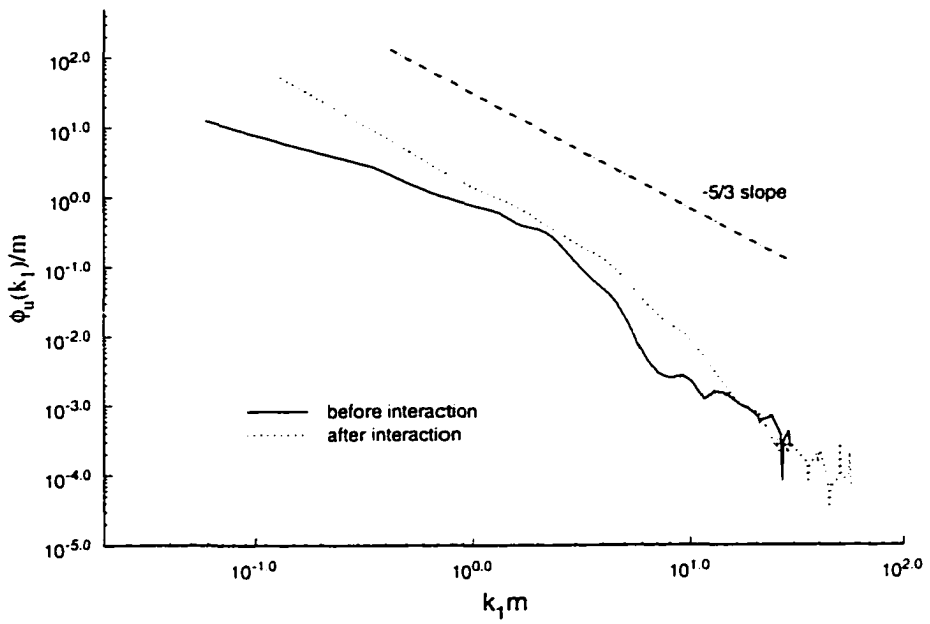

Figure 8.17: Smoothed longitudinal velocity PSD. 3 x3 grid $M_{\infty,R}$=1.104.

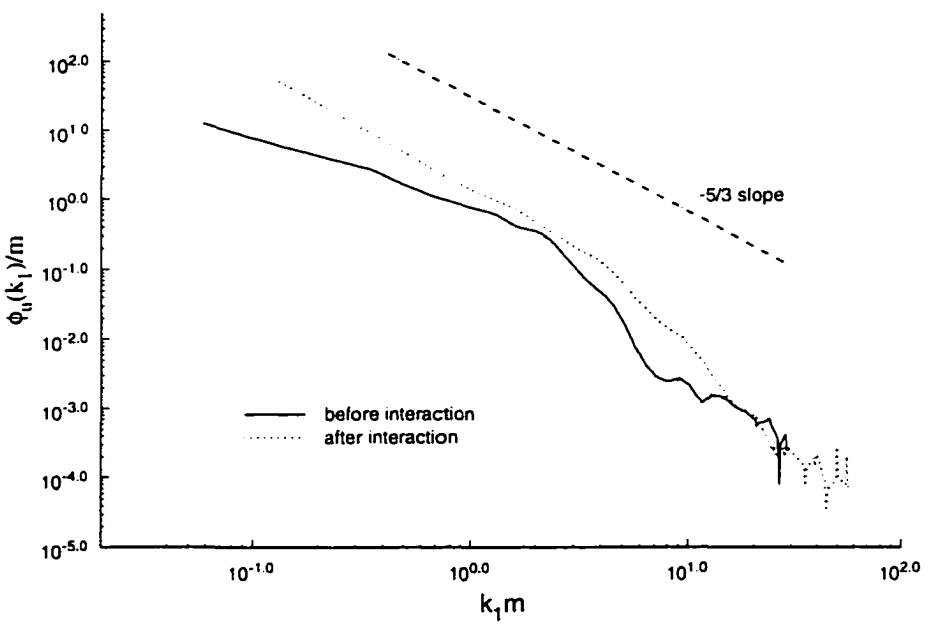

Figure 8.18: Smoothed longitudinal velocity PSD. 3 x3 grid $M_{\infty,R}$=1.191.

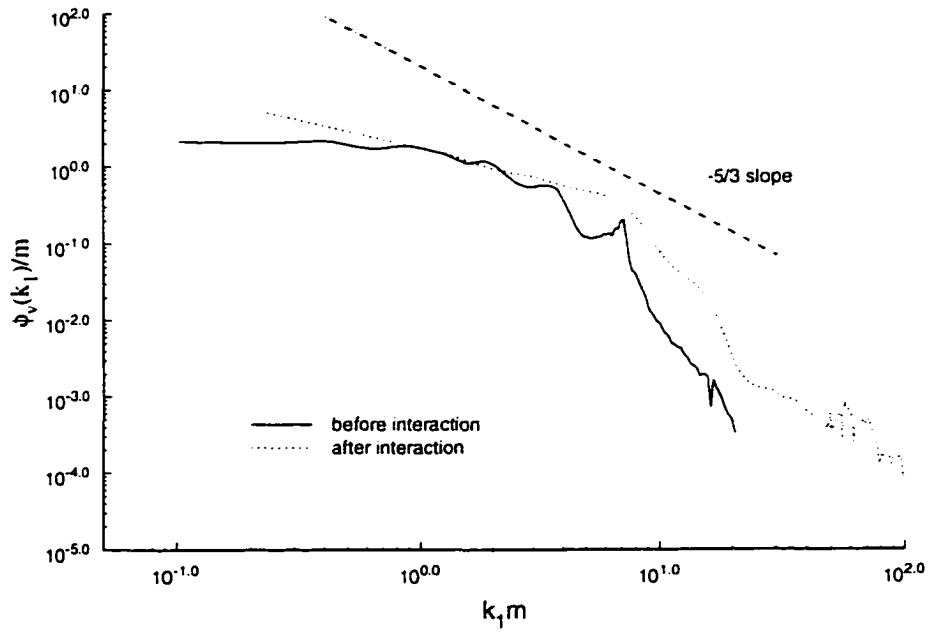

Figure 8.19: Smoothed normal velocity PSD. 2 x 2 grid $M_{\infty,R}$=1.04.

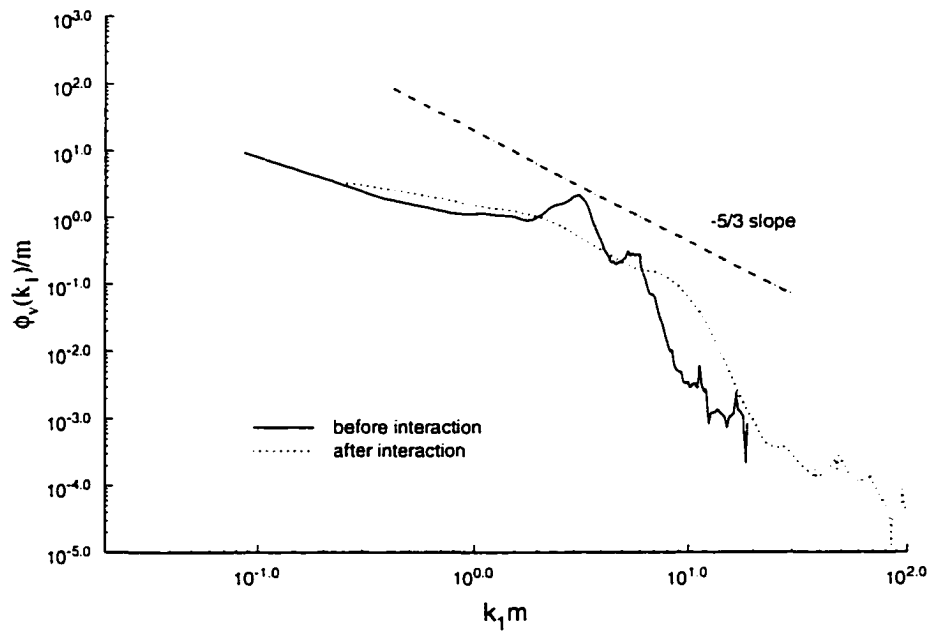

Figure 8.20: Smoothed normal velocity PSD. 2 x 2 grid $M_{\infty,R}$=1.115.

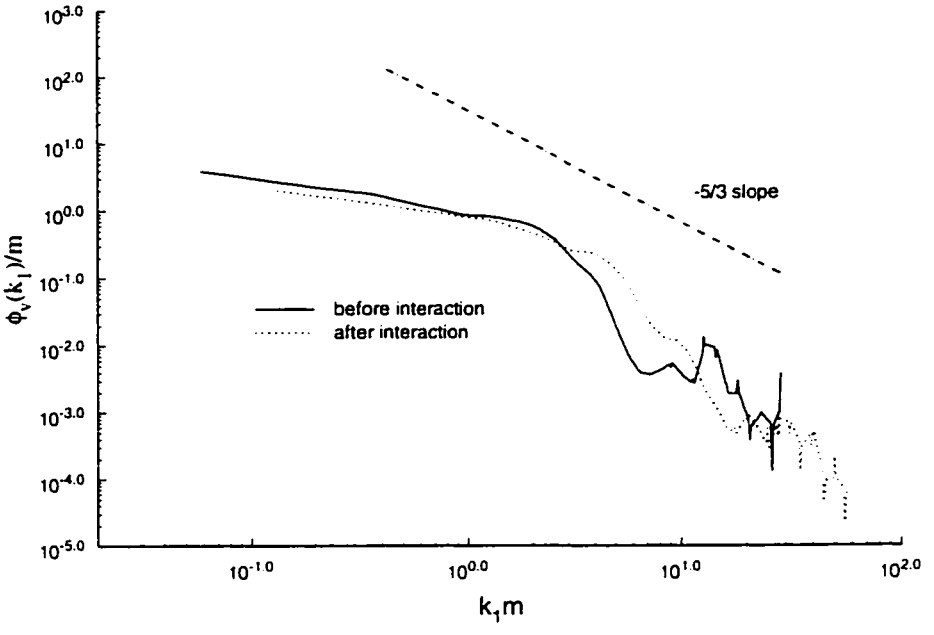

Figure 8.21: Smoothed normal velocity PSD. 3 x3 grid $M_{\infty,R}$=1.104.

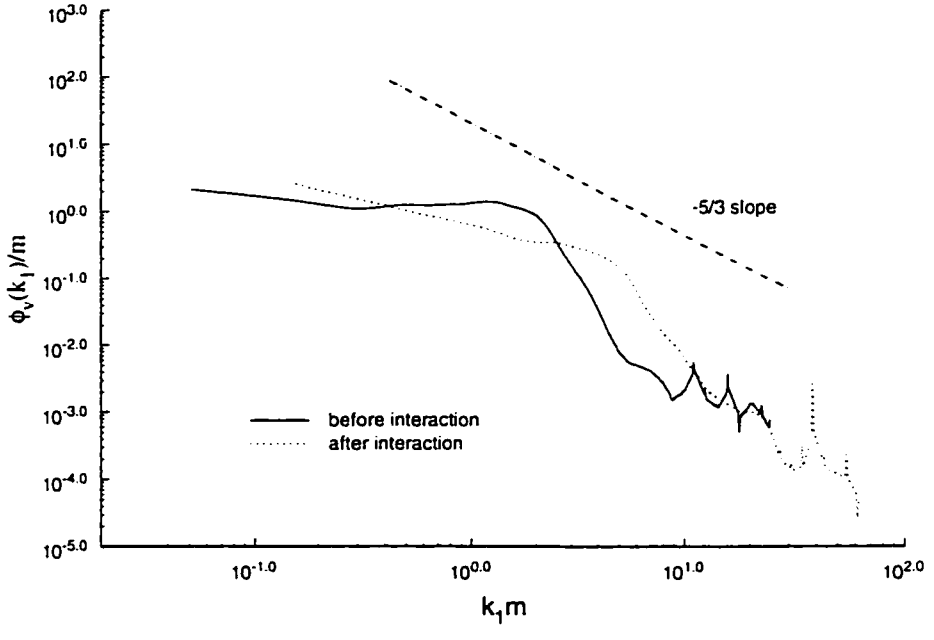

Figure 8.22: Smoothed normal velocity PSD. 3 x3 grid $M_{\infty,R}$=1.191.

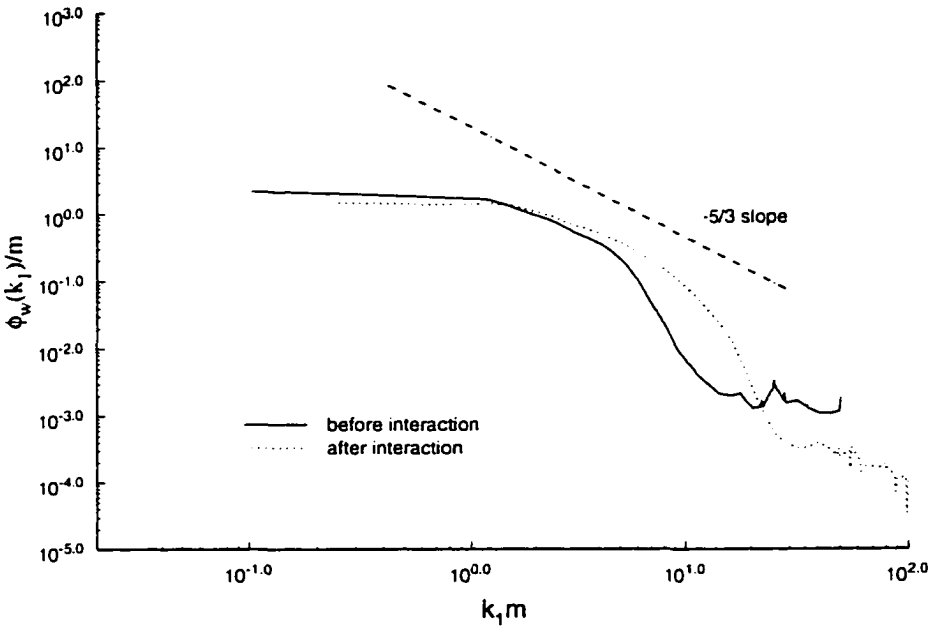

Figure 8.23: Smoothed spanwise velocity PSD. 2 x 2 grid $M_{\infty,R}$=1.04.

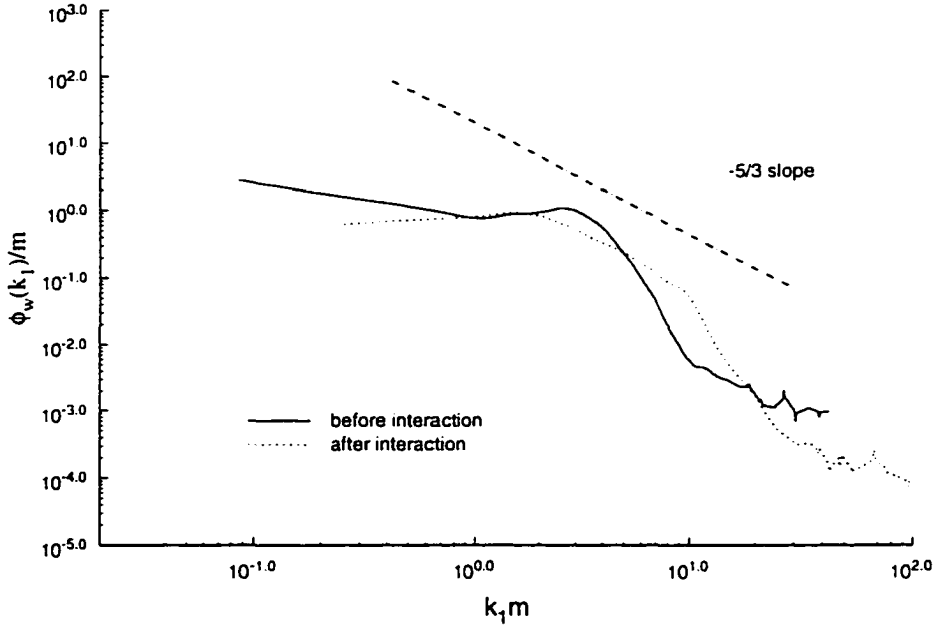

Figure 8.24: Smoothed spanwise velocity PSD. 2 x 2 grid $M_{\infty,R}$=1.115.

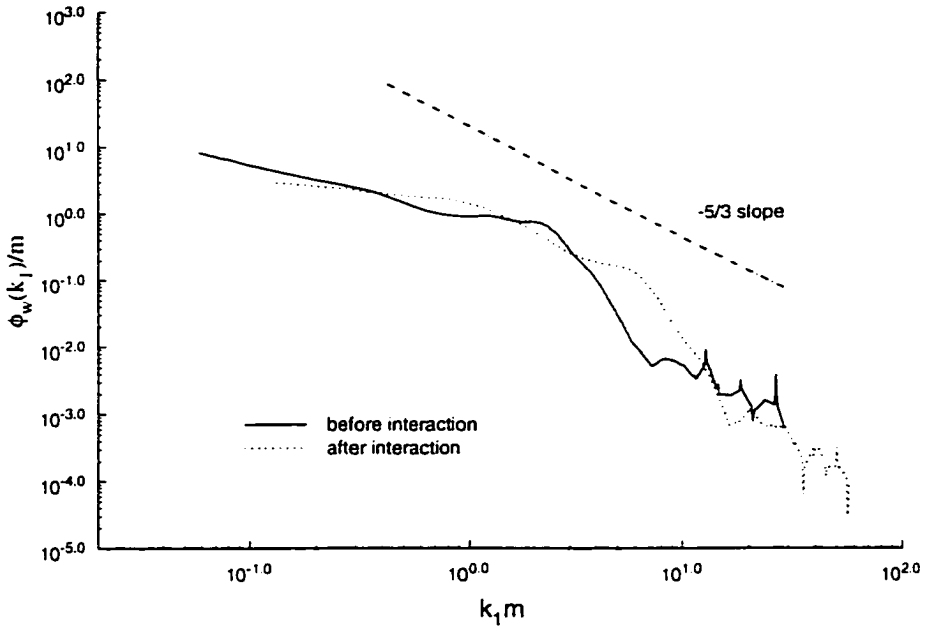

Figure 8.25: Smoothed spanwise velocity PSD. 3 x3 grid $M_{\infty,R}$=1.104.

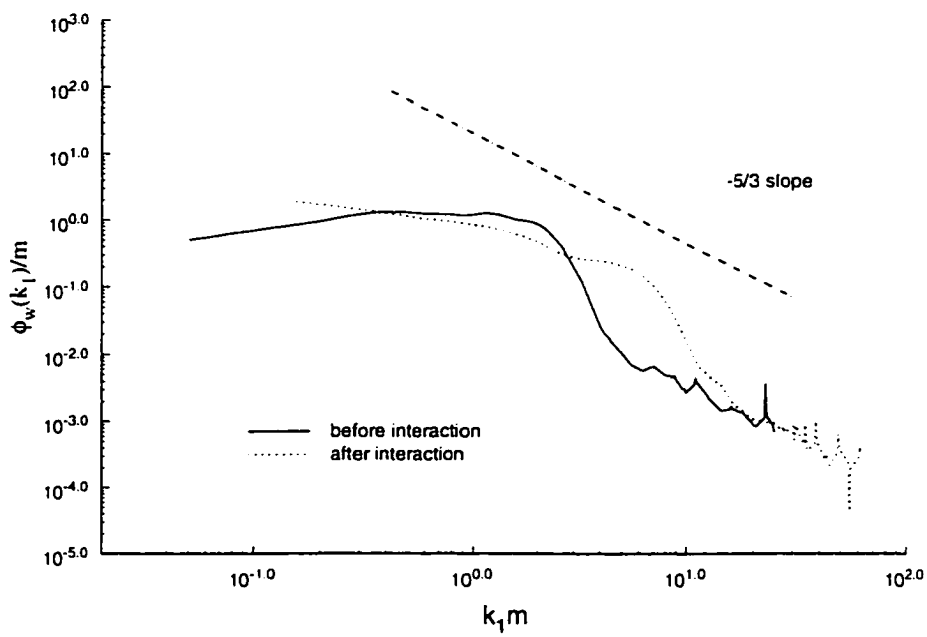

Figure 8.26: Smoothed spanwise velocity PSD. 3 x3 grid $M_{\infty,R}$=1.191.

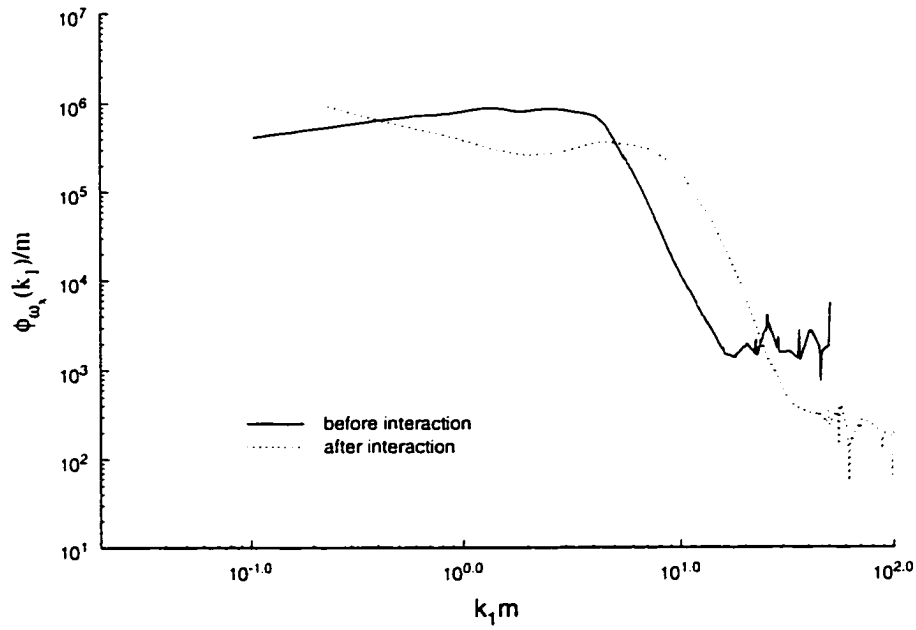

Figure 8.27: Smoothed PSD of longitudinal vorticity. 2 x 2 grid,$M_{\infty,R}$=1.04.

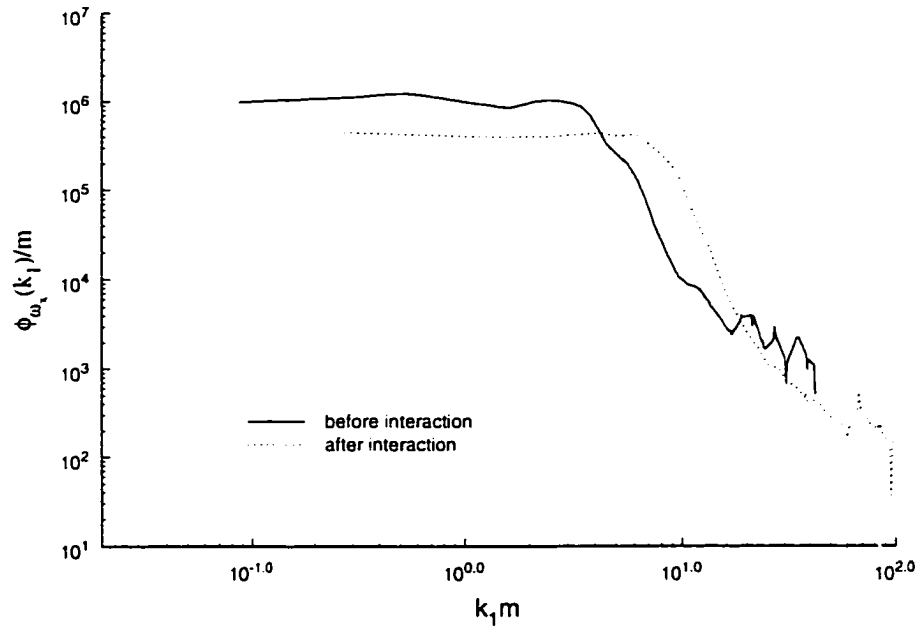

Figure 8.28: Smoothed PSD of longitudinal vorticity. 2 x 2 grid, $M_{\infty,R}$=1.115

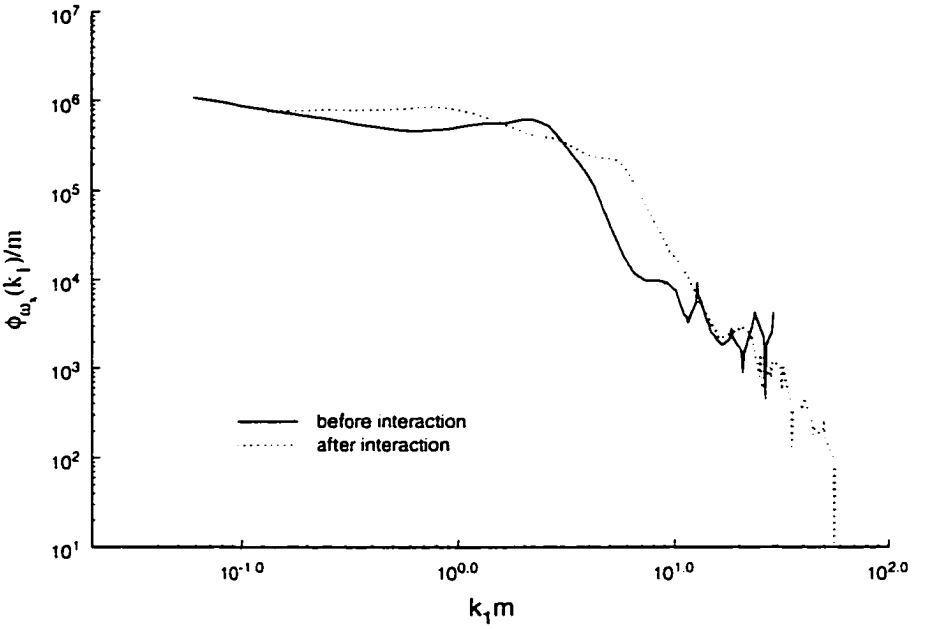

Figure 8.29: Smoothed PSD of longitudinal vorticity. 3 x 3 grid, $M_{\infty,R}$=1.04.

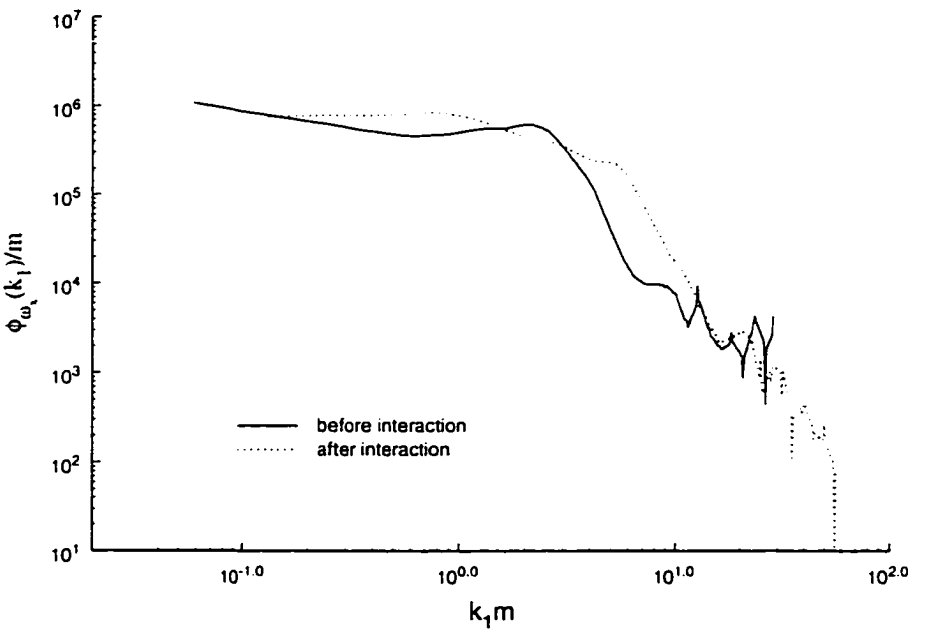

Figure 8.30: Smoothed PSD of longitudinal vorticity. 3 x 3grid $M_{\infty,R}$=1.191.

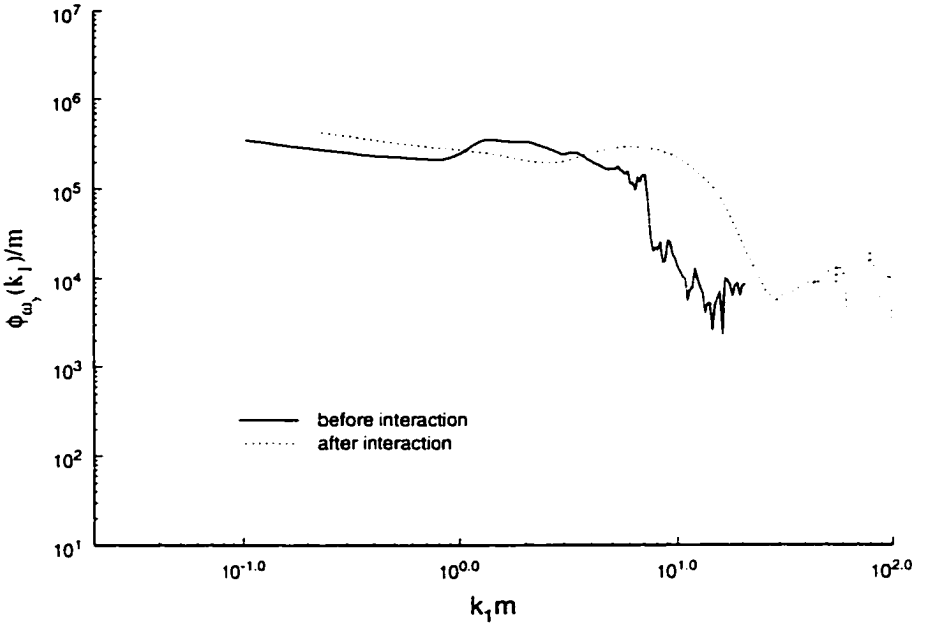

Figure 8.31: Smoothed PSD of ω_y. 2 x 2 grid,$M_{\infty,R}$=1.04.

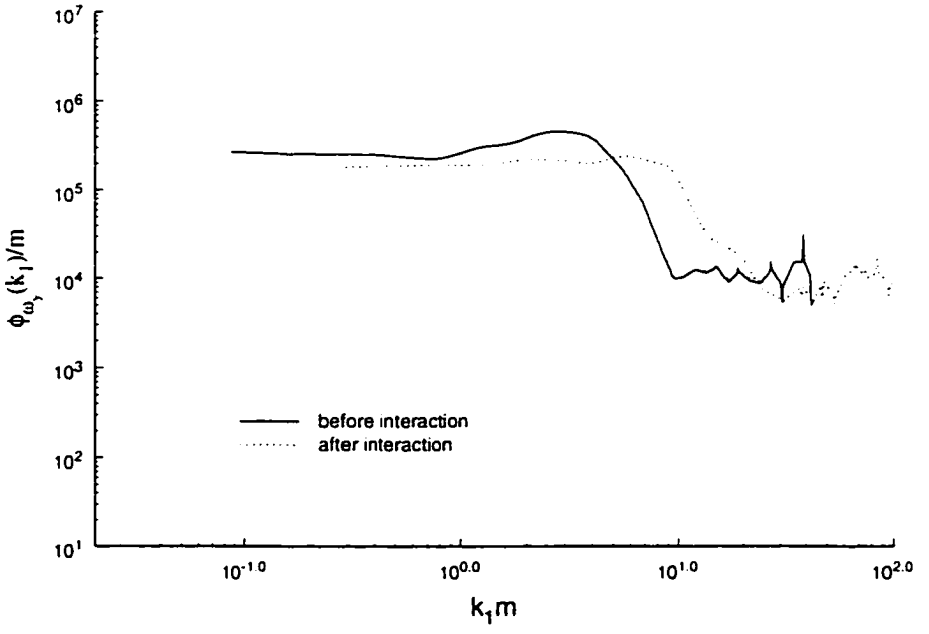

Figure 8.32: Smoothed PSD of ω_y. 2 x 2 grid, $M_{\infty,R}$=1.115

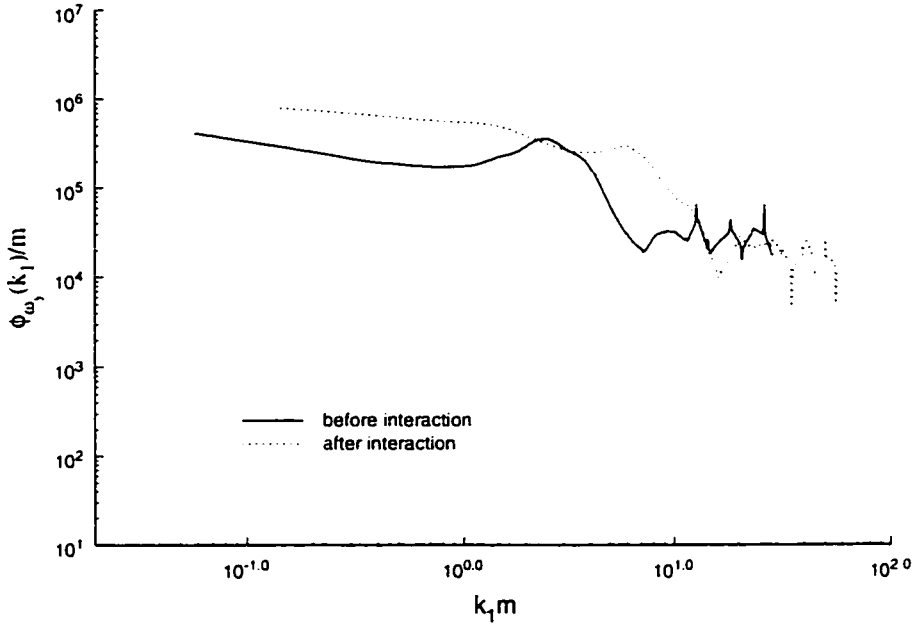

Figure 8.33: Smoothed PSD of ω_y. 3 x 3 grid, $M_{\infty,R}$=1.104.

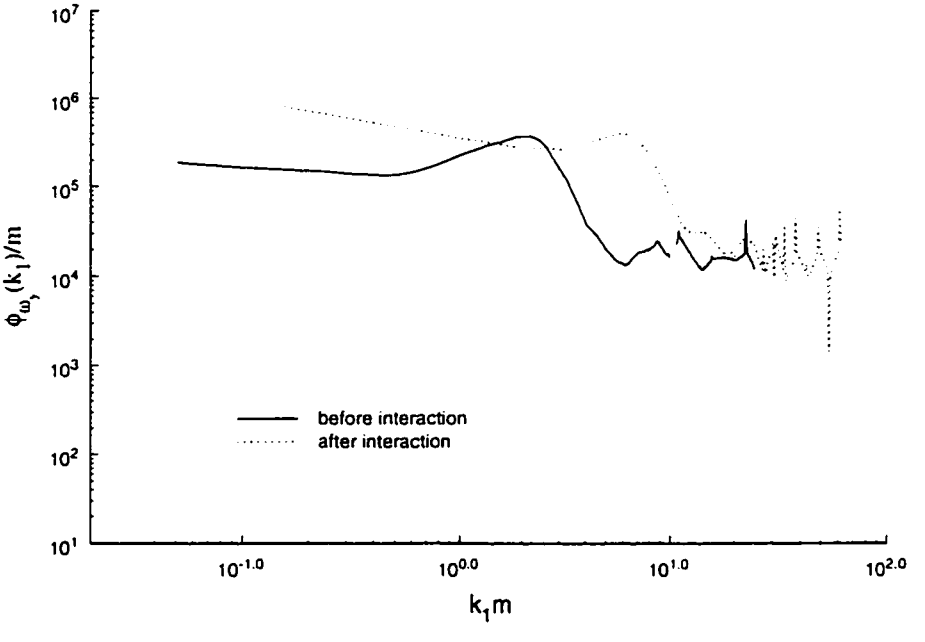

Figure 8.34: Smoothed PSD of ω_y. 3 x 3grid, $M_{\infty,R}$=1.191.

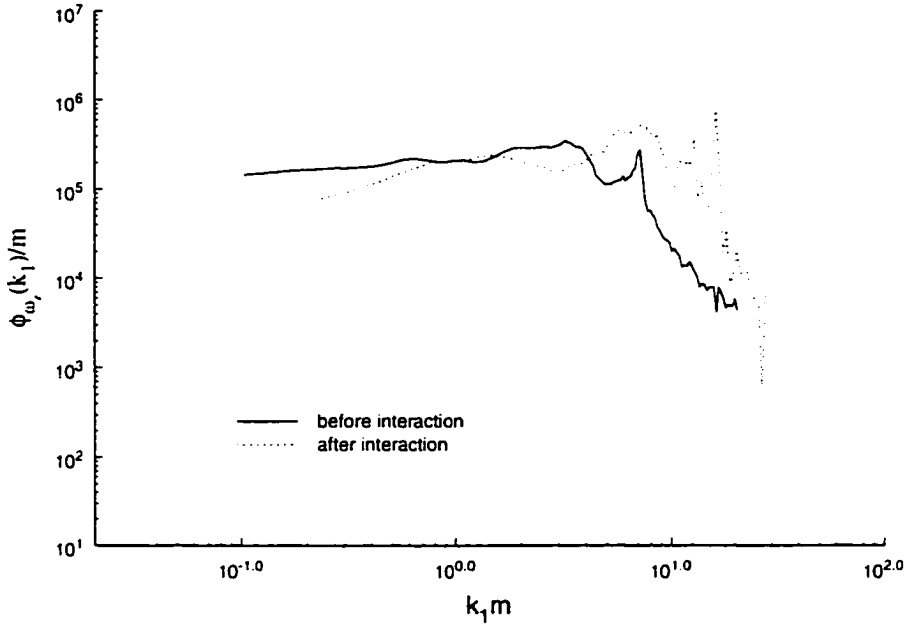

Figure 8.35: Smoothed PSD of ω_z. 2 x 2 grid,. $M_{\infty,R}$=1.04.

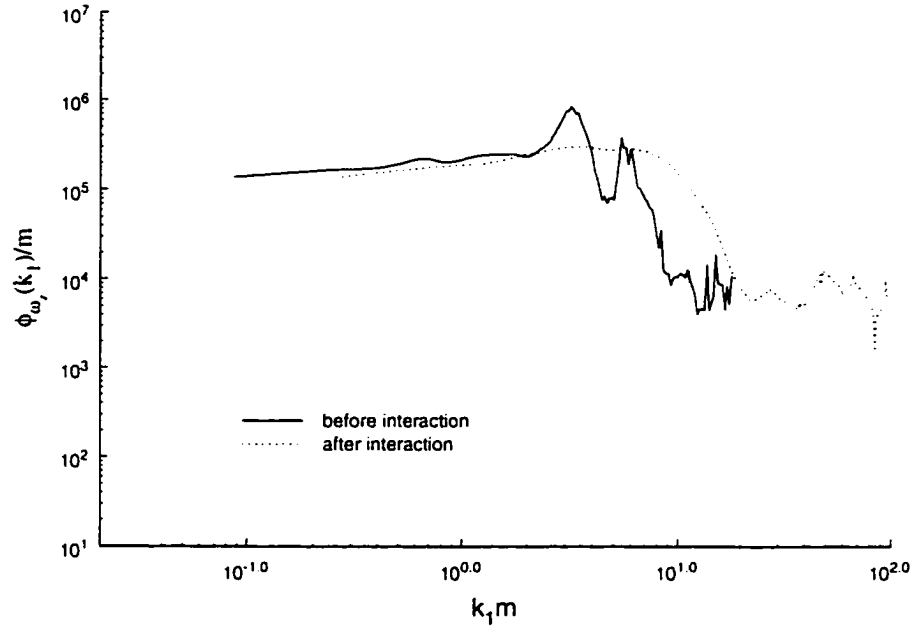

Figure 8.36: Smoothed PSD of ω_z. 2 x 2 grid, M=.115

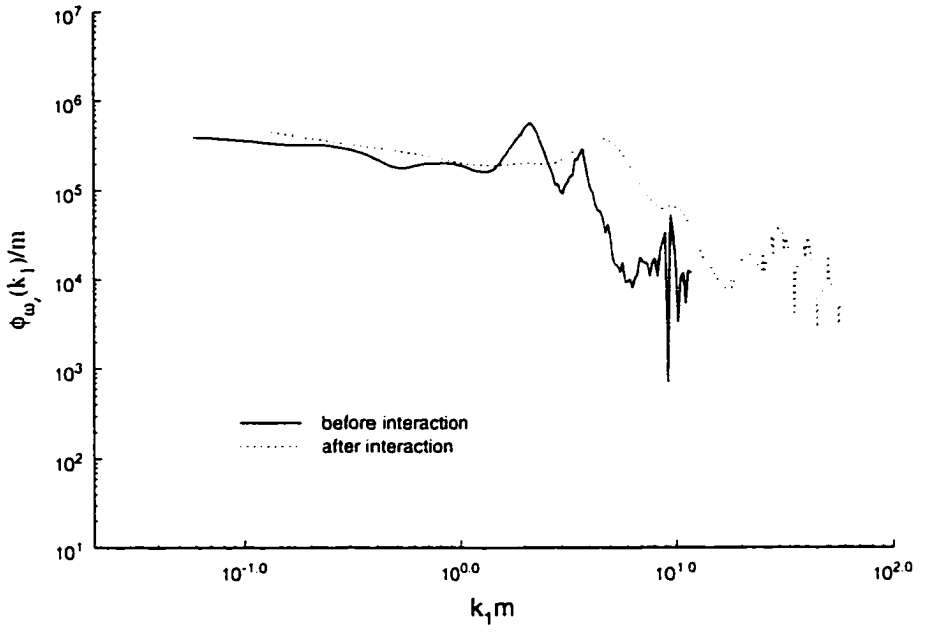

Figure 8.37: Smoothed PSD of ω_z. 3 x 3 grid,$M_{\infty,R}$=1.104

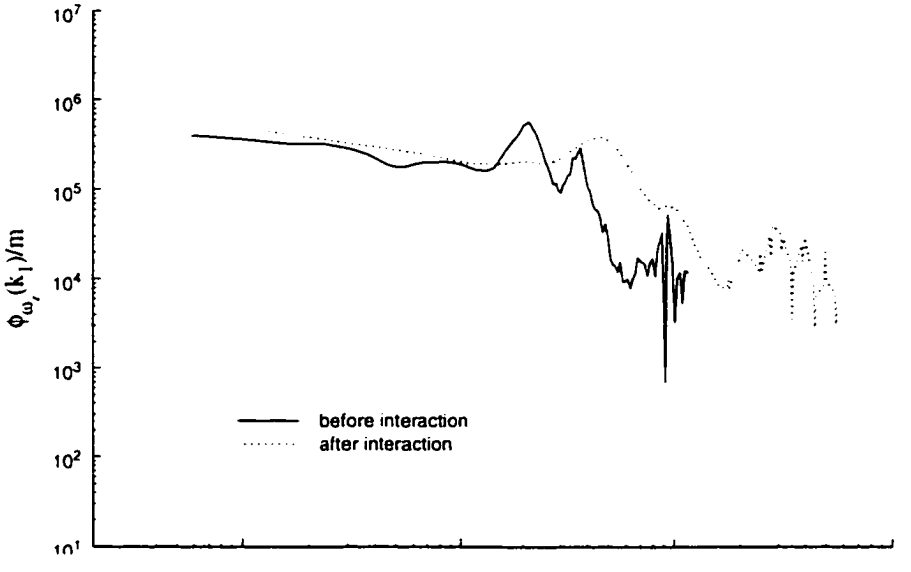

Figure 8.38: Smoothed PSD of ω_z. 3 x 3grid, $M_{\infty,R}$=1.191.

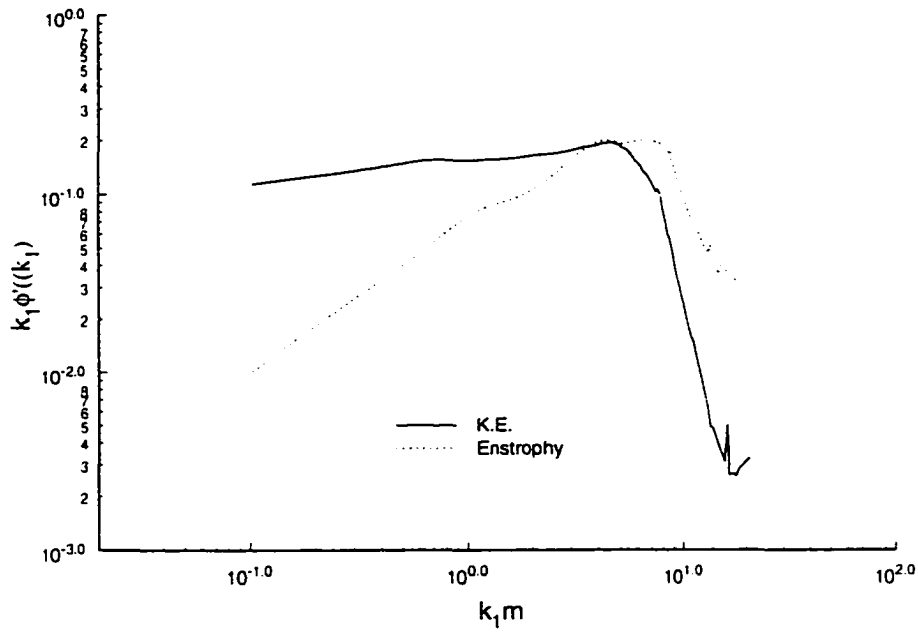

Figure 8.39: Smoothed noramlized wavenumber weighted PSD of kinetic energy and enstrophy before interaction. 2 x 2 grid M_2=1.04.

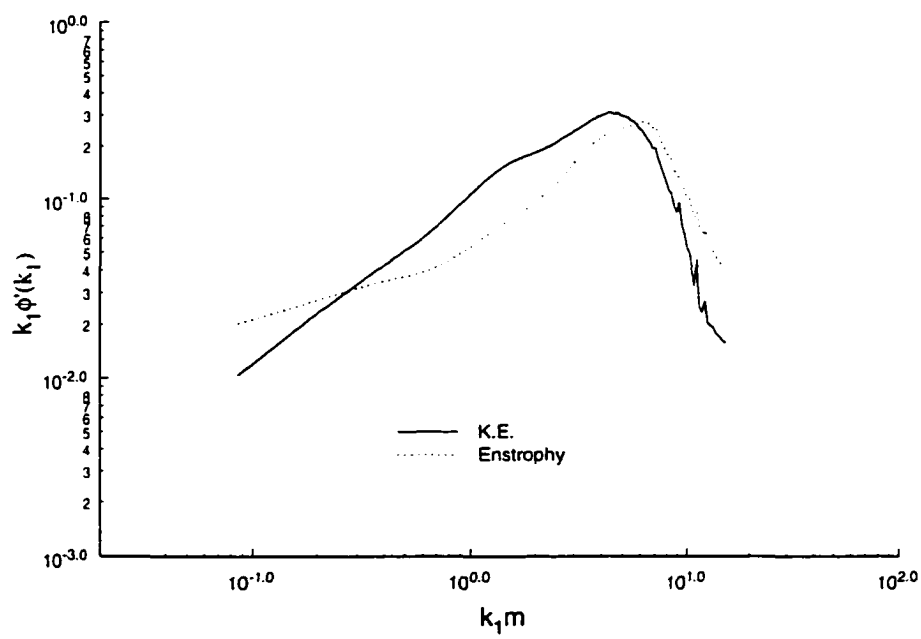

Figure 8.40: Smoothed normalized wavenumber weighted PSD of kinetic energy and enstrophy before interaction. 2 x 2 grid $M_{\infty,R}$=1.115.

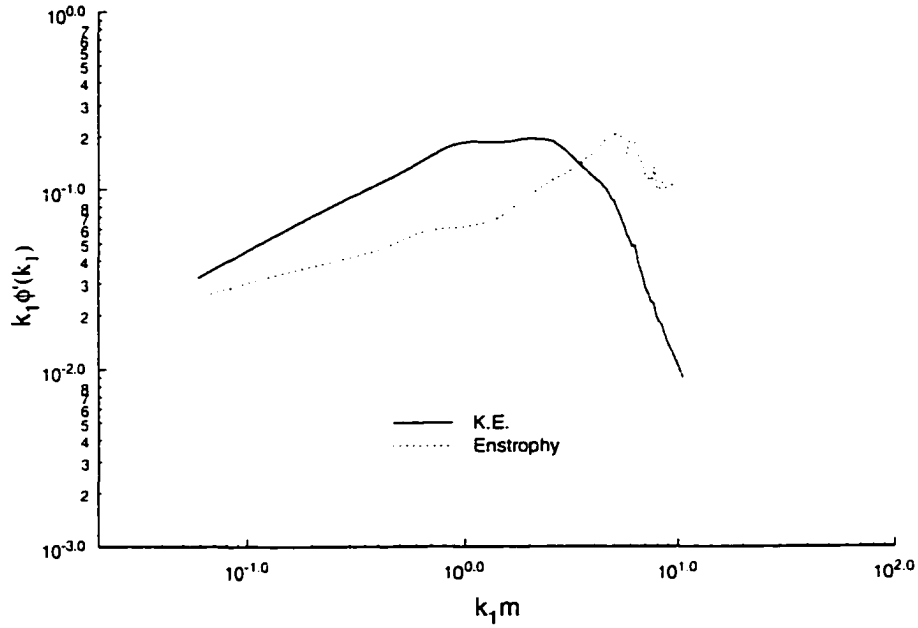

Figure 8.41: Smoothed normalized wavenumber weighted PSD of kinetic energy and enstrophy before interaction. 3 x 3 grid M_2=1.115.

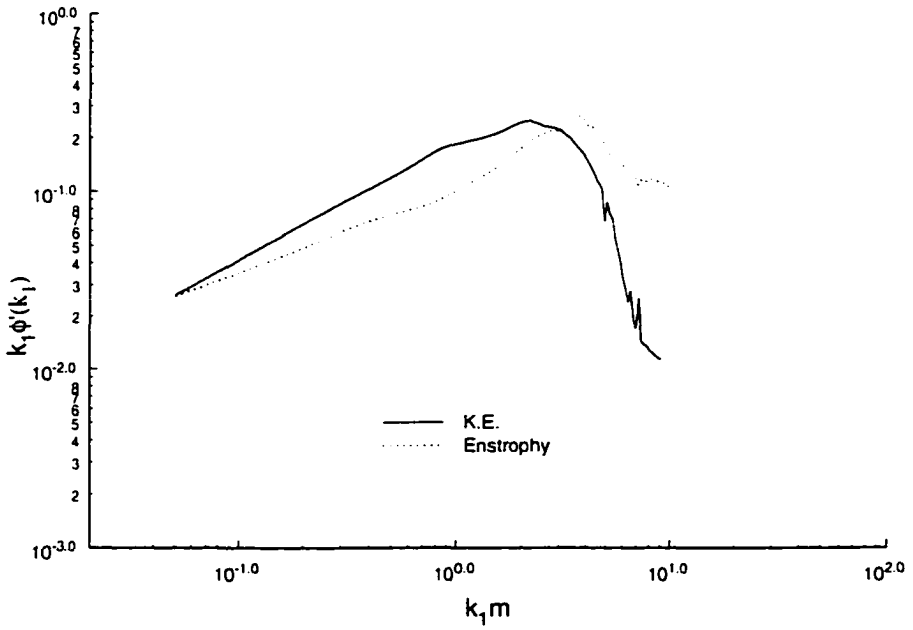

Figure 8.42: Smoothed normalized wavenumber weighted PSD of kinetic energy and enstrophy before interaction. 3 x 3 grid $M_{\infty,R}$=1.191.

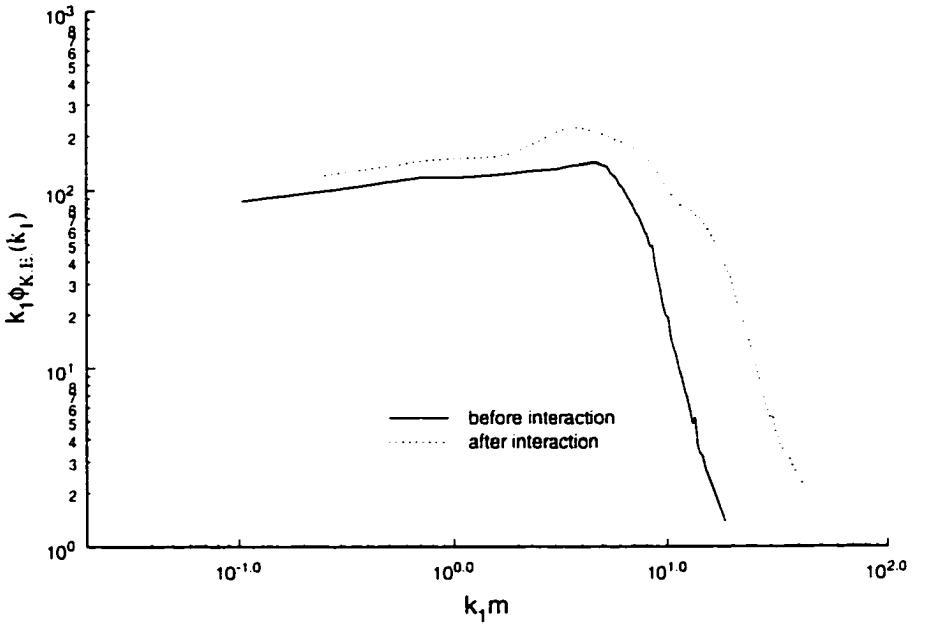

Figure 8.43: Smoothed wavenumber weighted PSD of kinetic energy before and after interaction. 2 x 2 grid $M_{\infty,R}$=1.04.

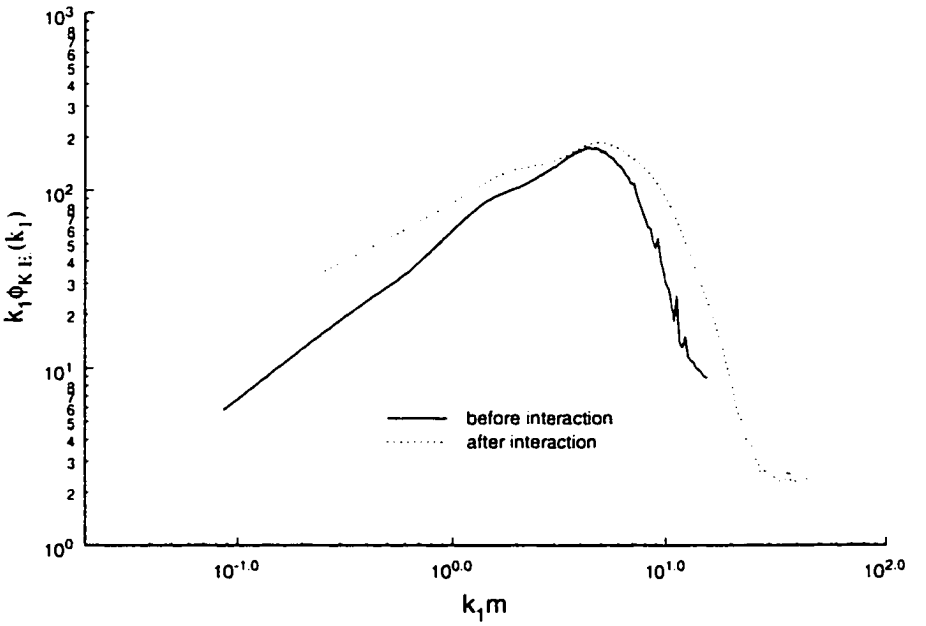

Figure 8.44: Smoothed wavenumber weighted PSD of kinetic energy before and after interaction. 2 x 2 grid $M_{\infty,R}$=1.115.

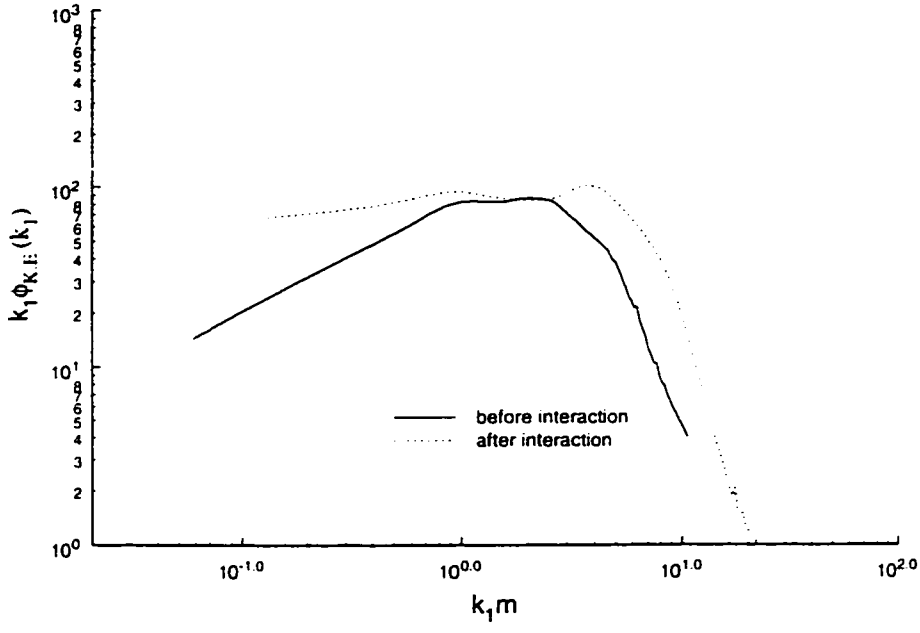

Figure 8.45: Smoothed wavenumber weighted PSD of kinetic energy before and after interaction. 3 x 3, grid $M_{\infty,R}$=1.115.

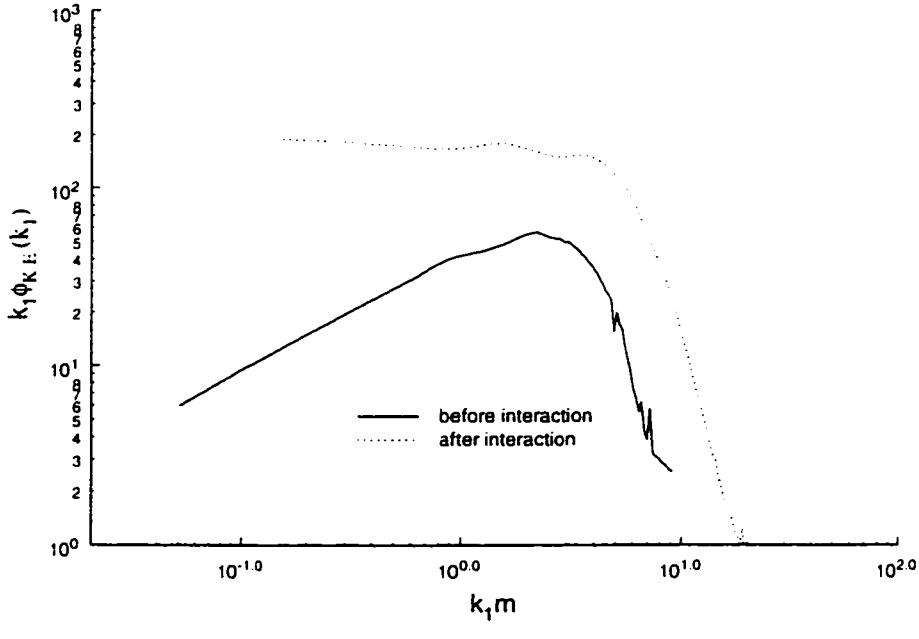

Figure 8.46: Smoothed wavenumber weighted PSD of kinetic energy before and after interaction. 3 x 3, grid $M_{\infty,R}$=1.191.

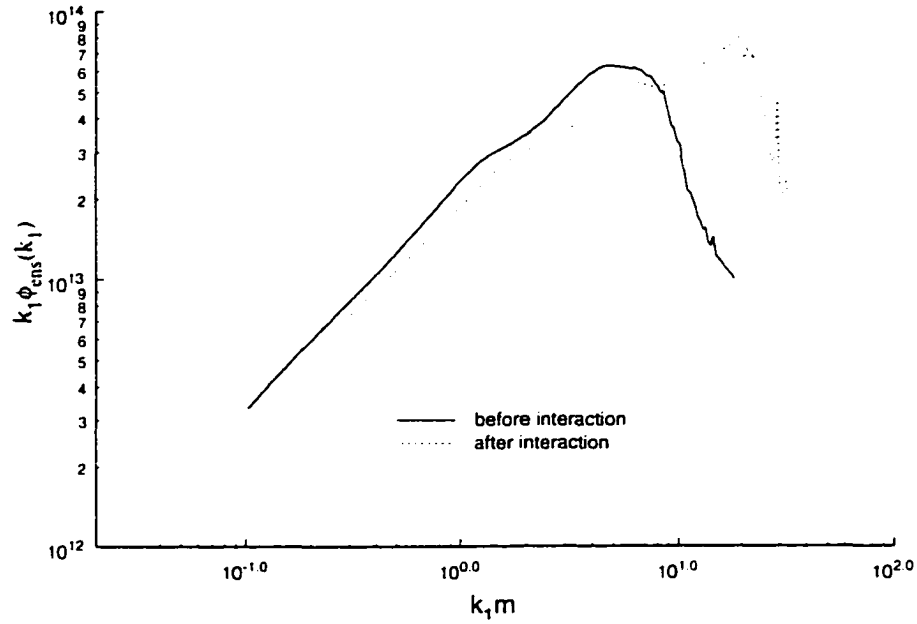

Figure 8.47: Smoothed wavenumber weighted PSD of enstrophy before and after interaction. 2 x 2 grid, $M_{\infty,R}$=1.04.

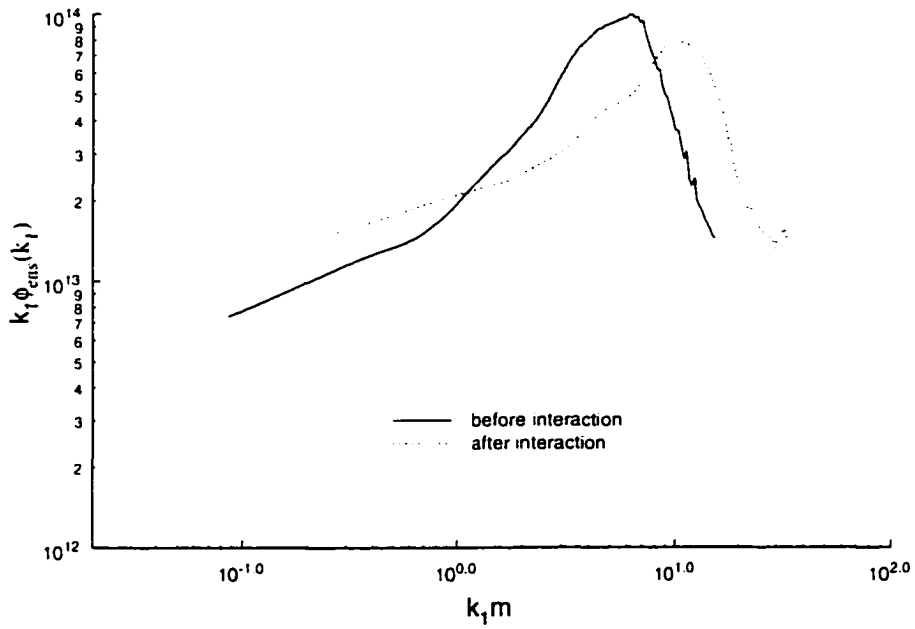

Figure 8.48: Smoothed wavenumber weighted PSD of enstrophy before and after interaction. 2 x 2 grid, $M_{\infty,R}$= 1.115.

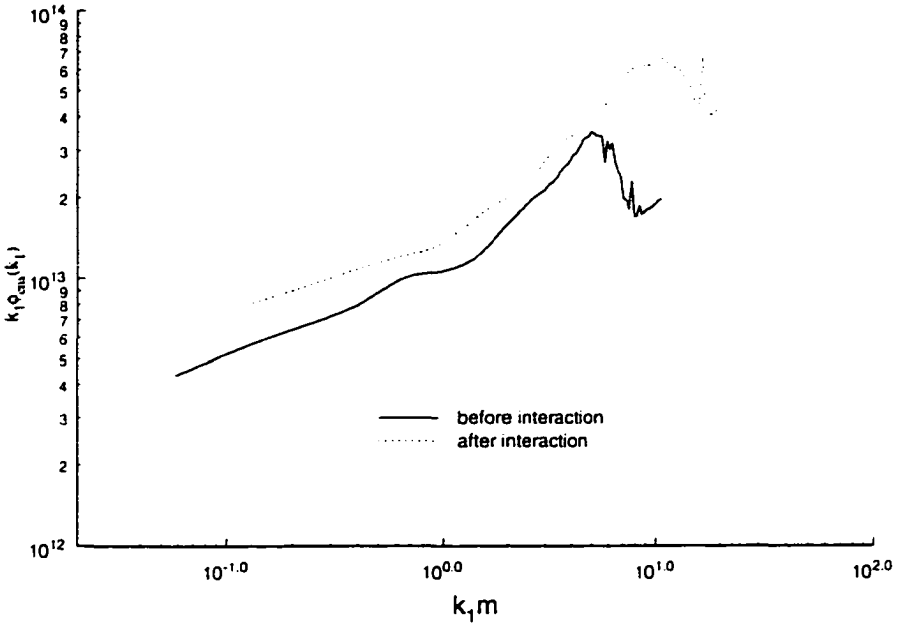

Figure 8.49: Smoothed wavenumber weighted PSD of enstrophy before and after interaction. 3 x 3 grid,$M_{\infty,R}$=1.115.

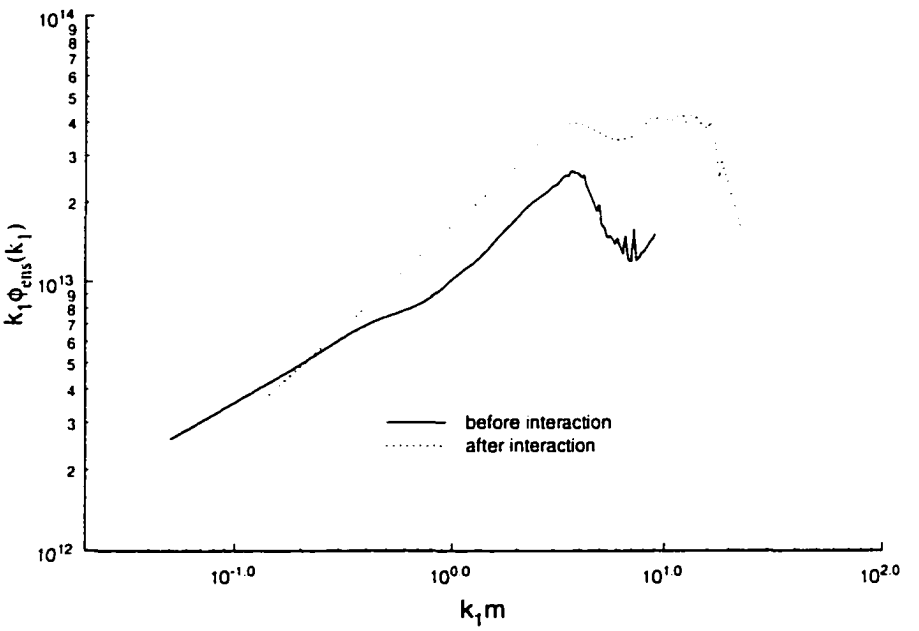

Figure 8.50: Smoothed wavenumber weighted PSD of enstrophy before and after interaction. 3 x 3 grid, $M_{\infty,R}$=1.191.

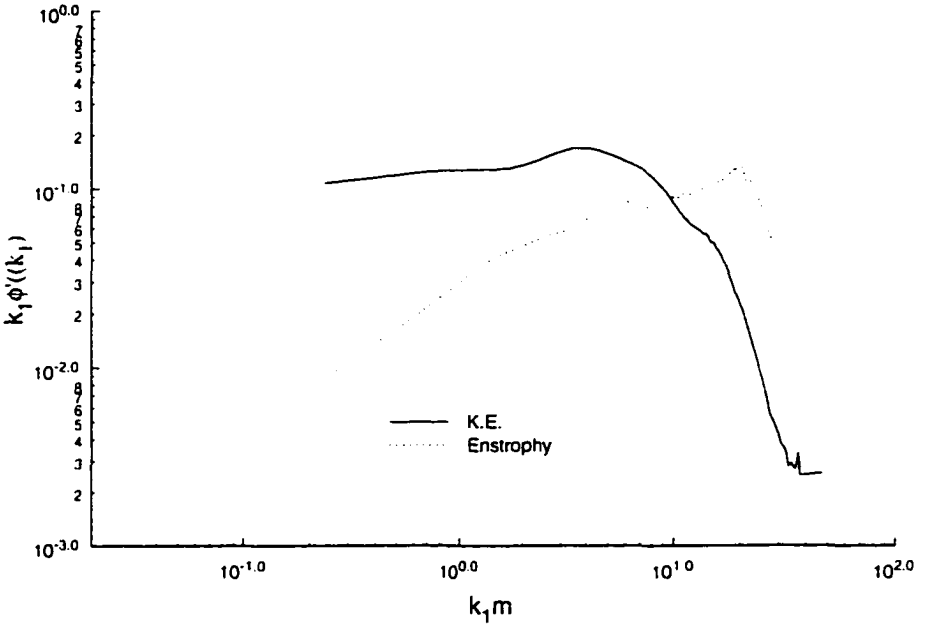

Figure 8.51: Smoothed normalized wavenumber weighted PSD of kinetic energy and enstrophy after interaction. 2 x 2 grid M_2=1.04.

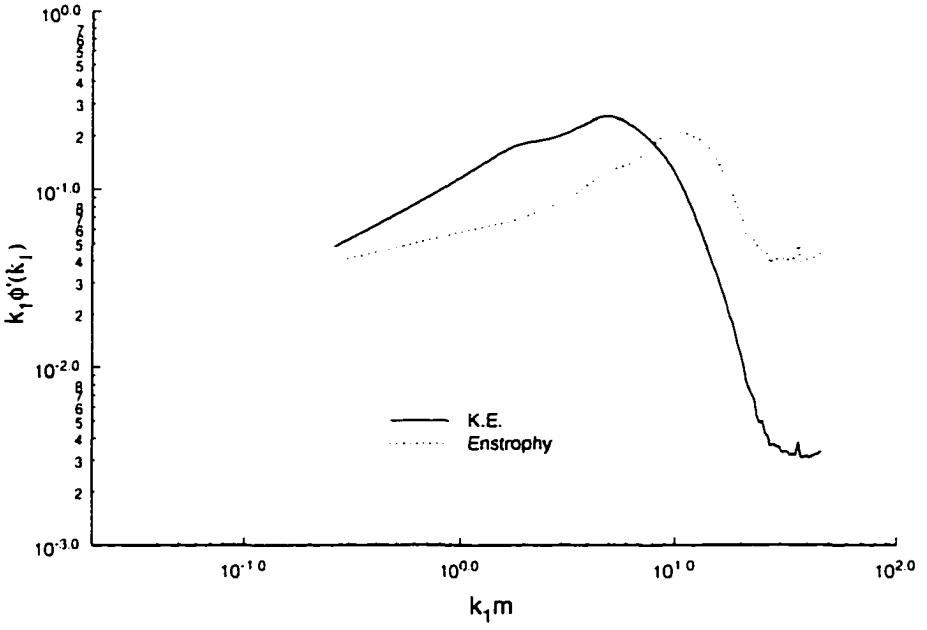

Figure 8.52: Smoothed normalized wavenumber weighted PSD of kinetic energy and enstrophy after interaction. 2 x 2 grid M_2=1.115.

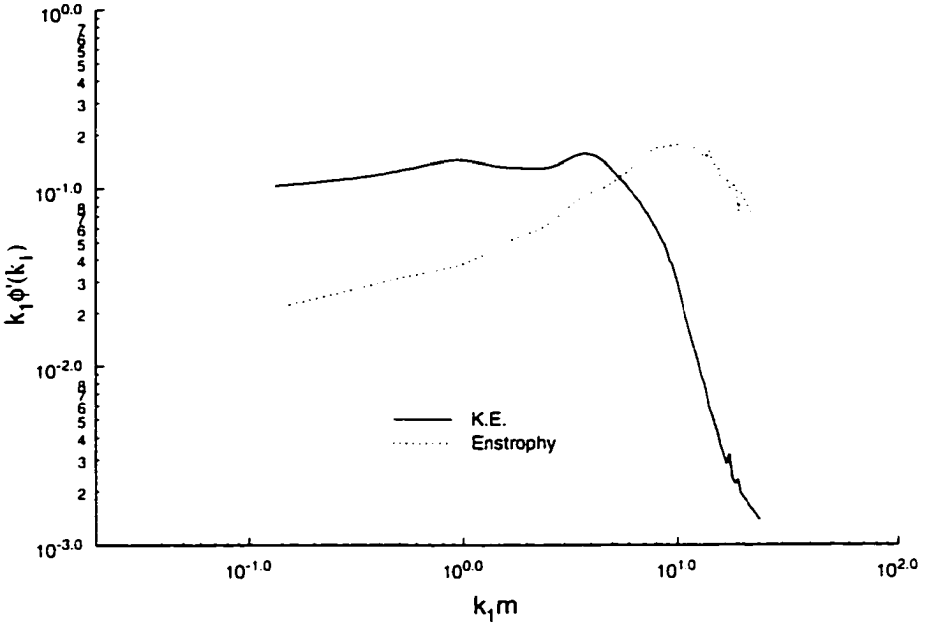

Figure 8.53: Smoothed normalized wavenumber weighted PSD of kinetic energy and enstrophy after interaction. 3 x 3 grid $M_{\infty,R}$=1.104.

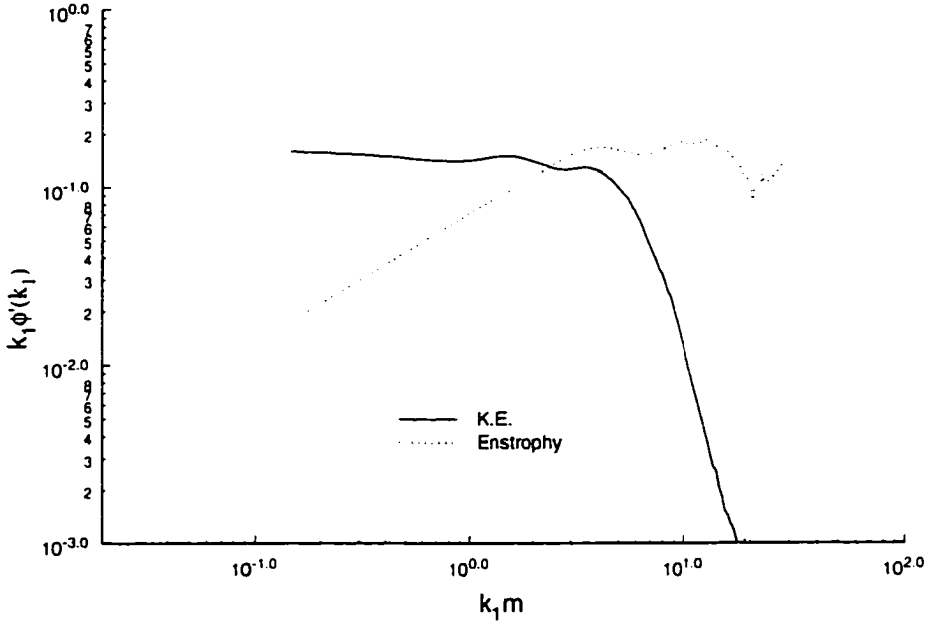

Figure 8.54: Smoothed normalized wavenumber weighted PSD of kinetic energy and enstrophy after interaction. 3 x 3 grid $M_{\infty,R}$=1.191.

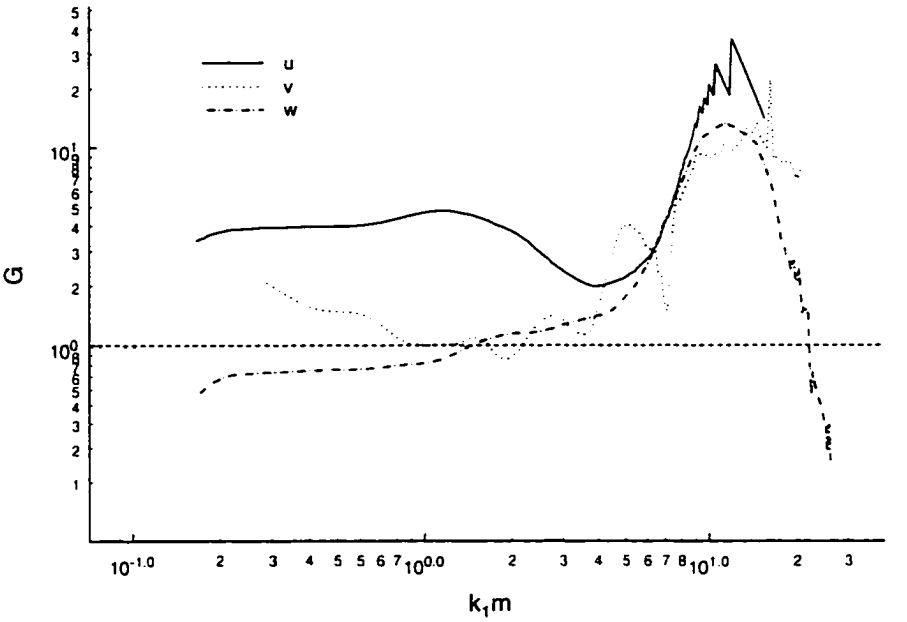

Figure 8.55: Wavenumber amplification of velocity, 2 x 2 grid, $M_{\infty,R}$=1.04

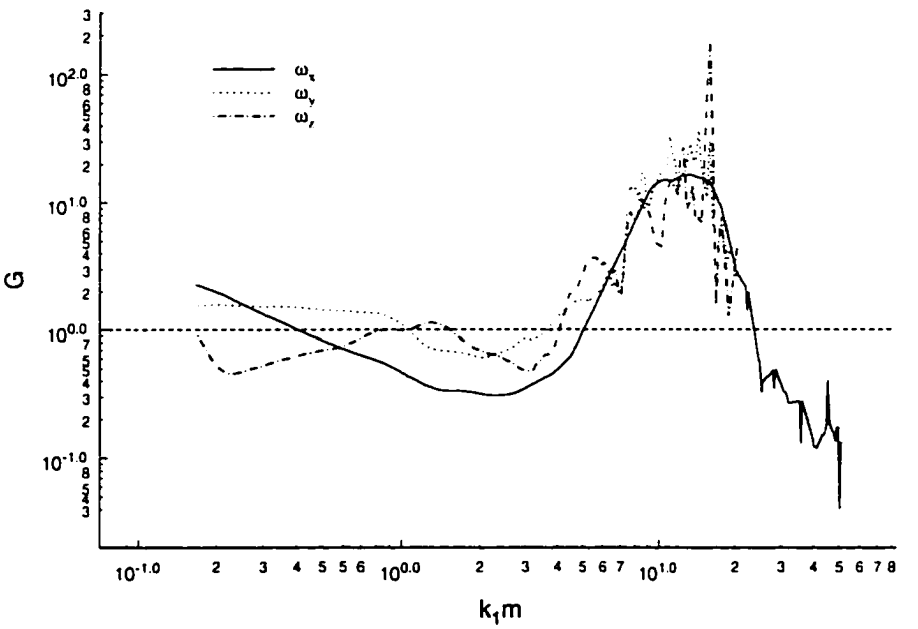

Figure 8.56: Wavenumber amplification of vorticity. 2 x 2 grid,$M_{\infty,R}$=1.04.

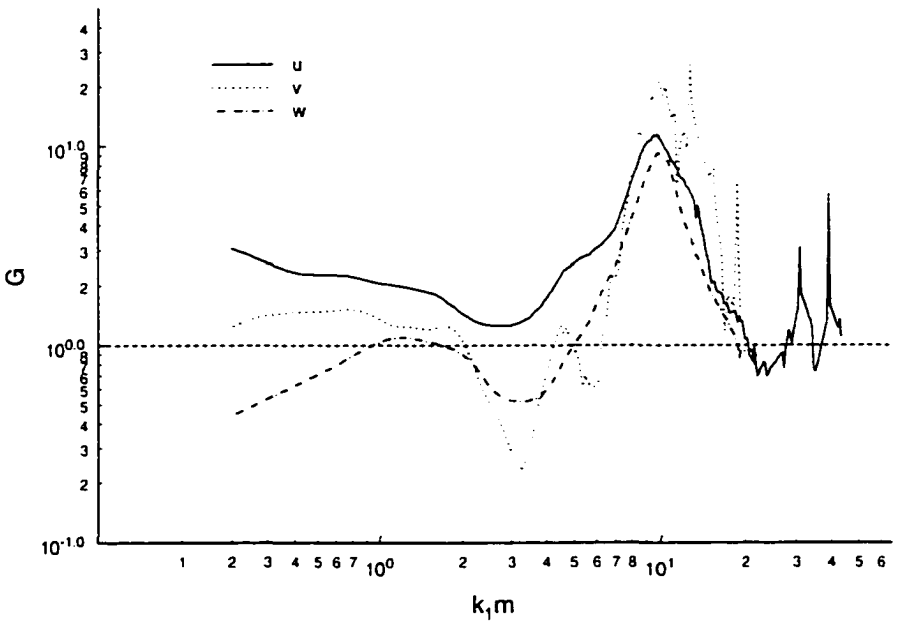

Figure 8.57: Wavenumber amplification of velocity. 2 x 2 grid,$M_{\infty,R}$=1.115

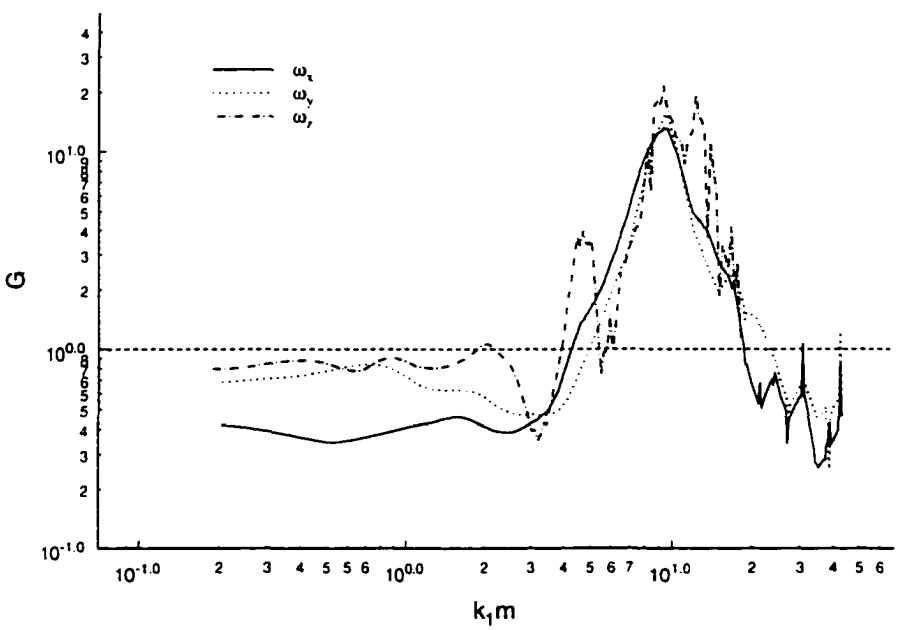

Figure 8.58: Wavenumebr amnplification of vorticty. 2 x 2 grid, M=1.115.

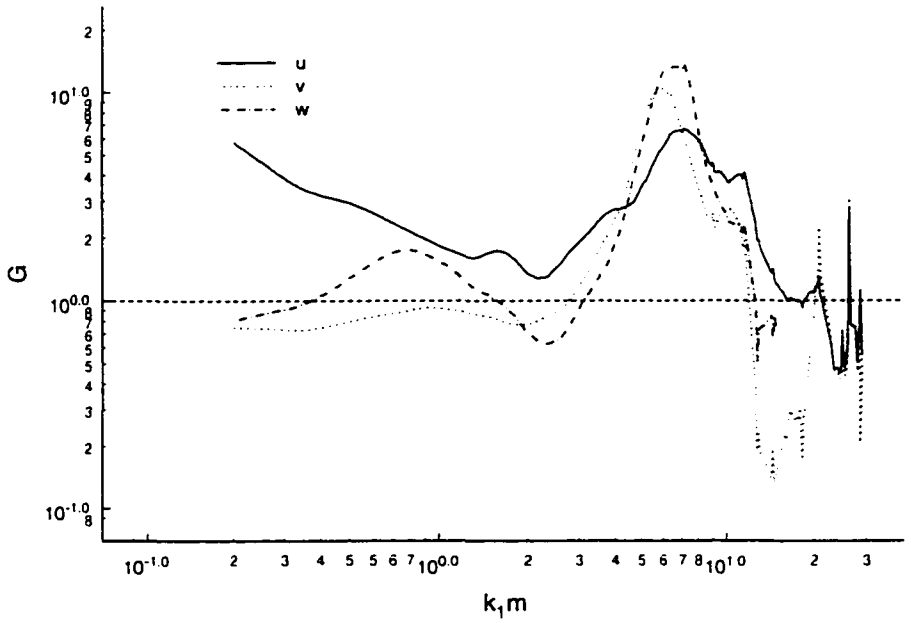

Figure 8.59: Wavenumber amplification of velocity, 3 x 3 grid,$M_{\infty,R}$=1.104.

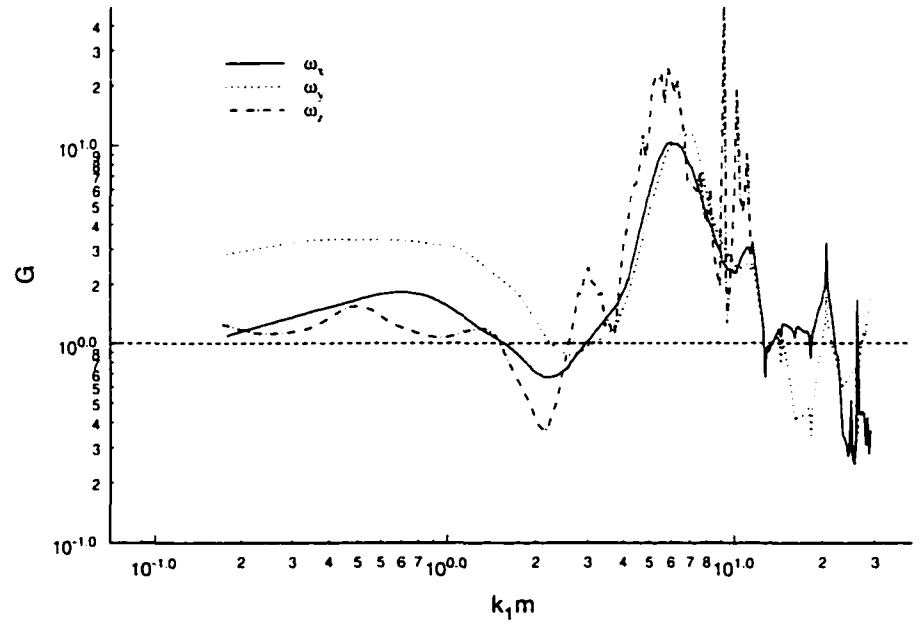

Figure 8.60: Wavenumber amplification of vorticity. 3 x 3 grid, $M_{\infty,R}$=1.104

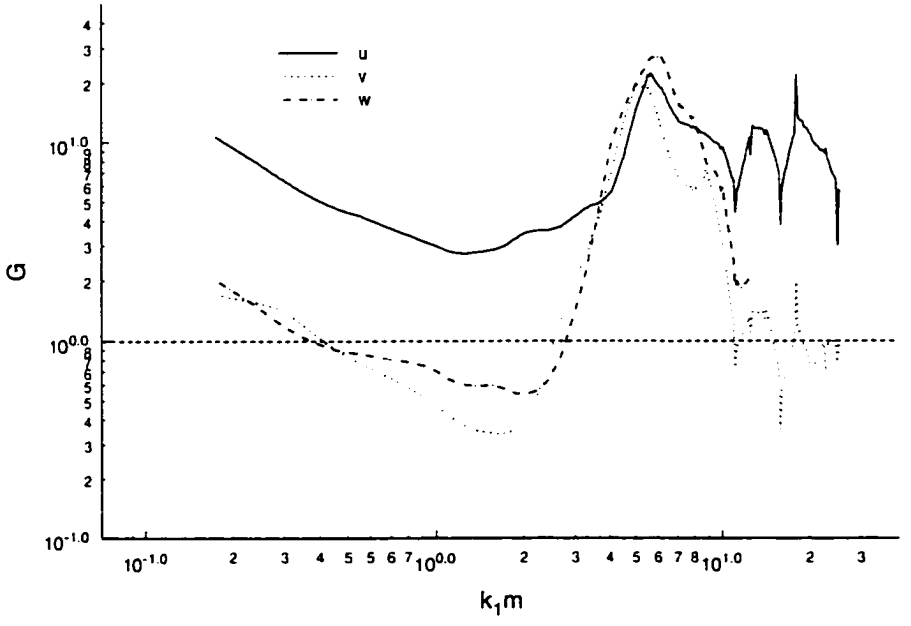

Figure 8.61: Wavenumber amplification of velocity. 3 x 3 grid, M=1.191.

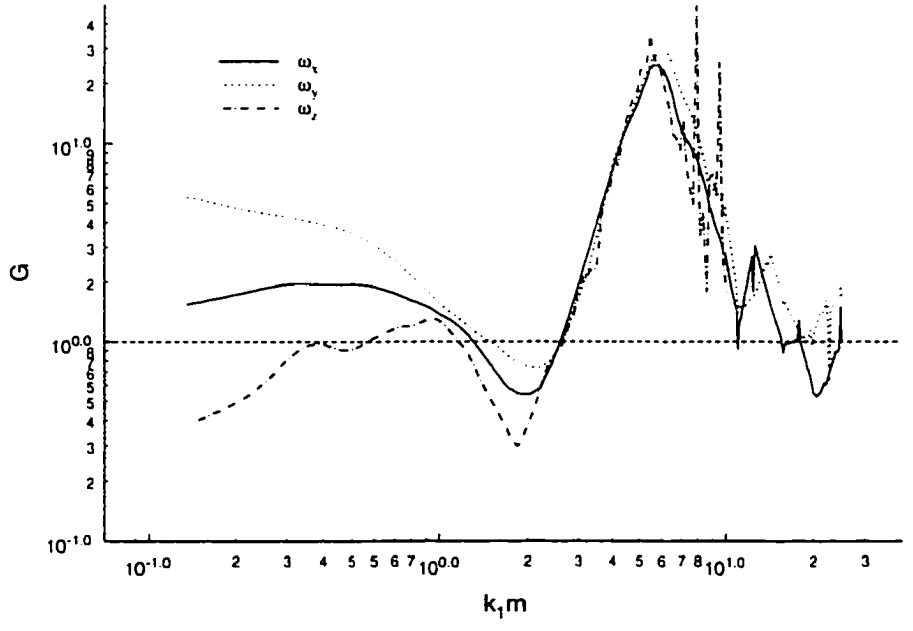

Figure 8.62: Wavenumber amplification of vorticity. 3 x 3 grid, M=1.191.

8.4 Stretching Process

In an effort identify the mechanism responsible for the modified vorticity fluctuations after the interaction, the stretching term appearing in the compressible vorticity equation, 4.3a, has been closely inspected. This term is the dominant vorticity source term in homogeneous and isotropic turbulence, overshadowing the effects of the baroclinic and the viscous diffusive processes.

The stretching signals along with the corresponding pdf's are presented in figures 8.63 - 8.86. Recall that the passage of the reflected shock is sensed by a sudden drop in longitudinal velocity. For reference, the instance of the shock passage is marked on each stretching signal, and therefore the flow prior to interaction with the shock is represented by the left side of this reference mark, and the flow compressed by the shock by the right side. Overall, the character of the stretching fluctuations seems to change with the interaction.

All signals tended to show highly intermittent behavior with large amplitude fluctuations, in particularly after the interaction. This strongly indicates that vorticity stretching is characterized by a type of bursting process. In other words, the stretching mechanism is not a continuous process but is characterized by sudden violent short duration events. It is impressive to see how energetic these stretching events are by comparing their amplitudes with the mean of the respective signal. The largest fluctuations are actually two orders of magnitude larger than the mean. Vortex tilting which is an important component of the stretching mechanism, in which vortex vectors are reoriented, may be contributing to these events.

A comparison of the fluctuations of the different components of stretching before and after interaction with the reflected shock wave, showed that different trends were found among the four cases studied here. The 2 x 2 grid at the lower Mach number, $M_{\infty,R}$ = 1.04, showed very little change in the character of the stretching process after interaction with the shock wave. The pdf of the signals corresponding to this case reflected an equivalent distribution of the fluctuations before and after the interaction.

The higher Mach number for the 2 x 2 grid exhibited the most diverging trend. In this case, the y- and z- component stretching terms showed increased fluctuations before interaction with the shock. Recall that this case also showed a opposing trend in the statistics of velocity and vorticity fluctuations after the shock (see figure 8.9 and 8.10). The pdf's of the y- and z-component of stretching indicated by the longer tails of the distribution that strong bursting occurs before the shock arrives.

The 3 x 3 grid for both Mach number cases showed more consistent increases in stretching fluctuations after interaction with the shock. The lower Mach number case displayed clear increases in the x- and z-components of stretching. However inspection of the pdf the y-component shows that large positive amplitude events are not as probable after the arrival of the shock, indicating a suppresion of positive bursting events in this part of the signal. The larger Mach number case, which was also the highest Mach number investigated among the four cases, showed consistently an increase in fluctuations of all three stretching components after the shock. The corresponding pdf's also reveal this trend.

In general it was found that the different components of stretching tended to exhibit bursting behavior and that the bursting is enhanced in most cases after interaction

with the shock. One exception was the higher Mach number, 2 x 2 grid, case, which produced smaller vorticity amplification after shock and also produced smaller stretching fluctuations after the shock. In contrast, the 3 x 3 grid higher Mach number case showed the clearlest increases in all the components of stretching.

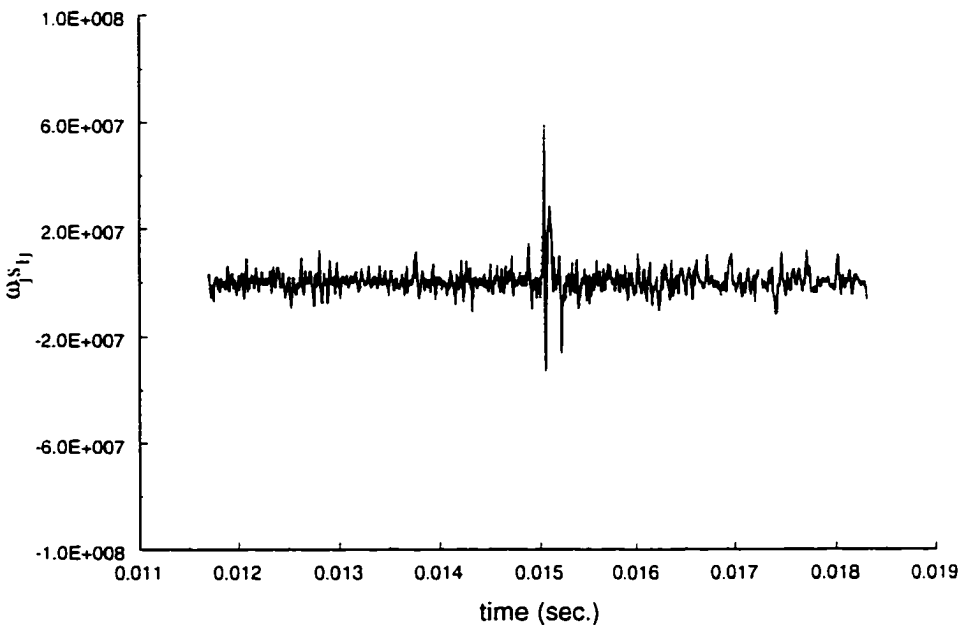

Figure 8.63: Stretching term for ω_x. 2 x 2 grid, $M_{\infty,R}$=1.04

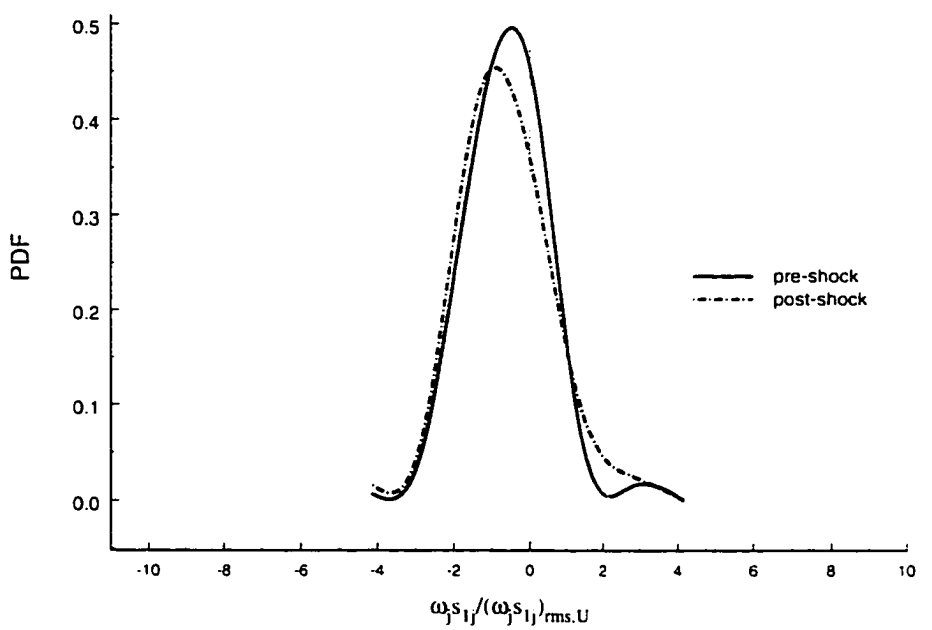

Figure 8.64: PDF of stretching term for ω_x. 2 x 2 grid, $M_{\infty,R}$=1.04

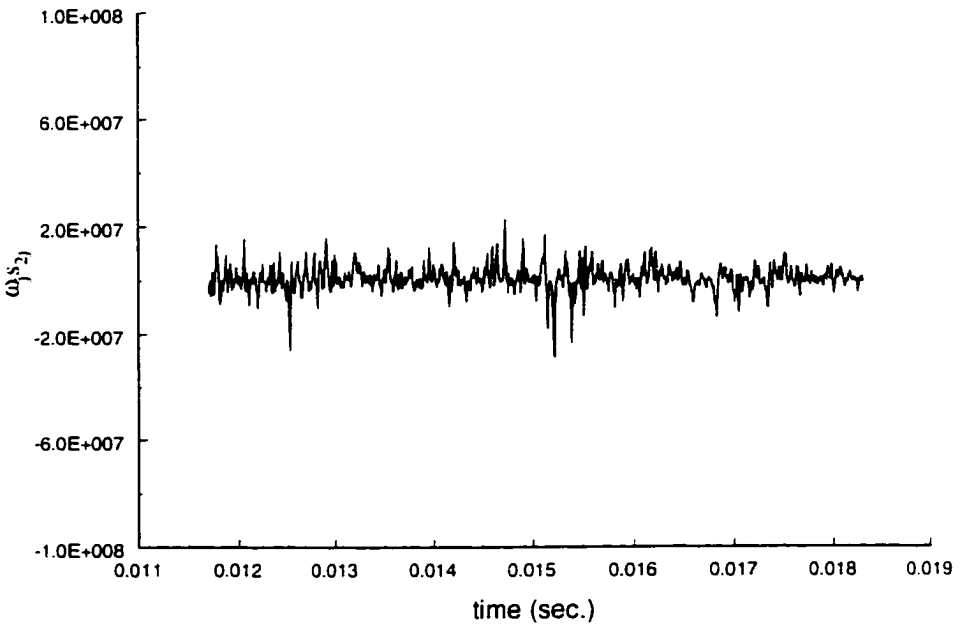

Figure 8.65: Stretching term for ω_y. 2 x 2 grid, $M_{\infty,R}$=1.04

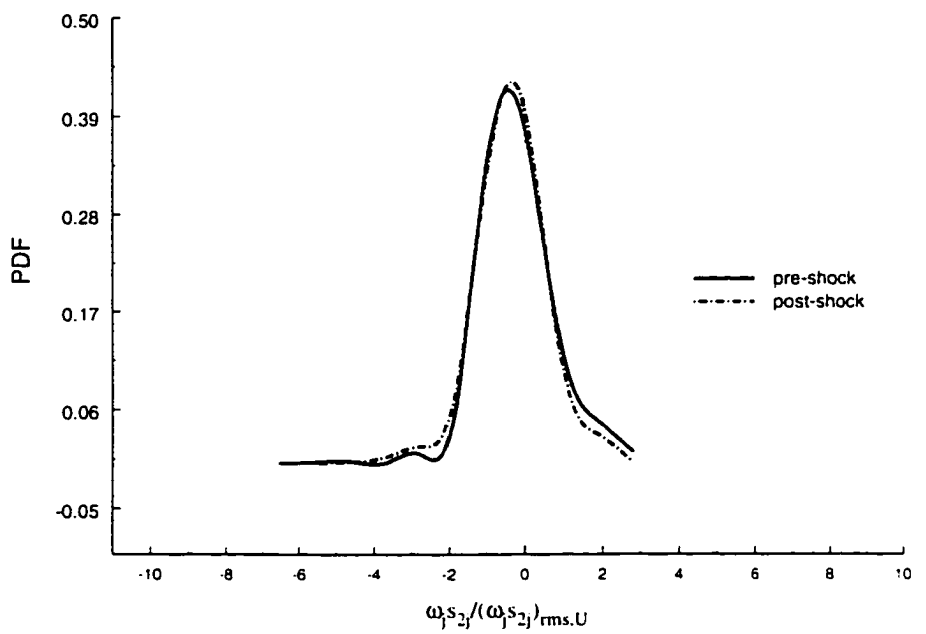

Figure 8.66: PDF of stretching term for ω_y. 2 x 2 grid, $M_{\infty,R}$=1.04

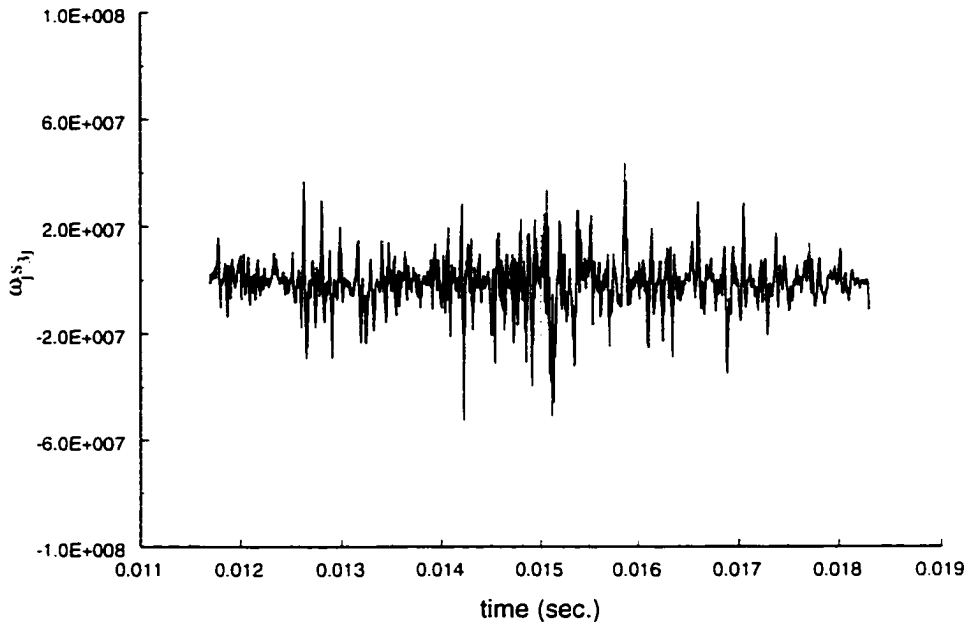

Figure 8.67: Stretching term for ω_z. 2 x 2 grid, $M_{\infty,R}$=1.04

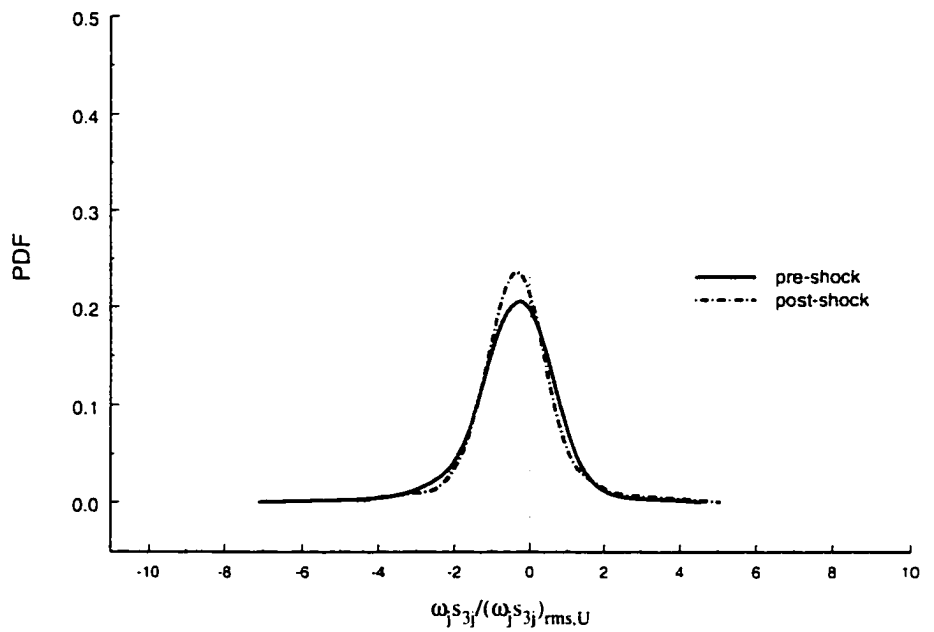

Figure 8.68: PDF of stretching term for ω_z. 2 x 2 grid, $M_{\infty,R}$=1.04

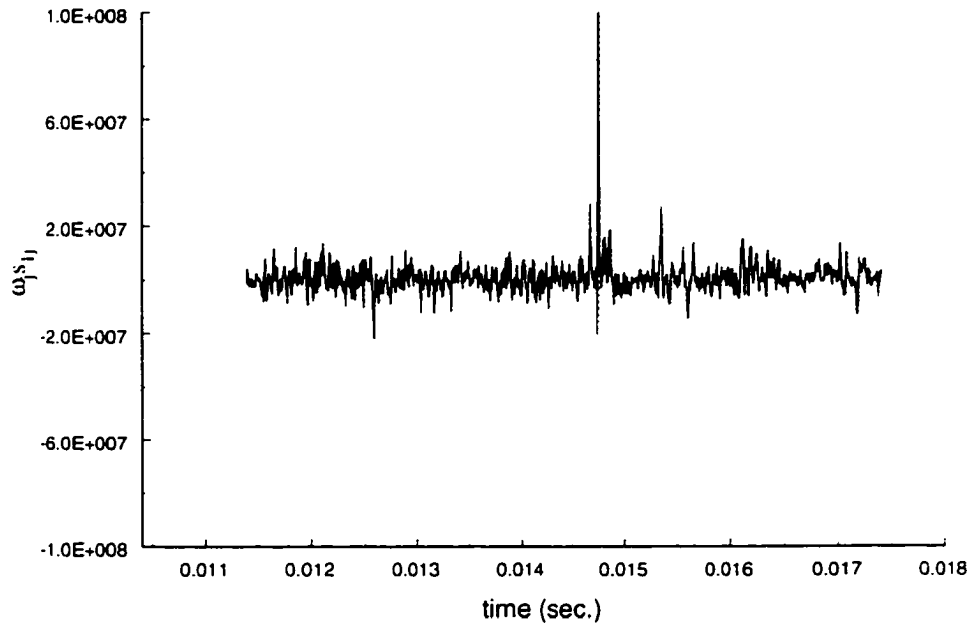

Figure 8.69: Stretching term for ω_x. 2 x 2 grid, $M_{\infty,R}$=1.115

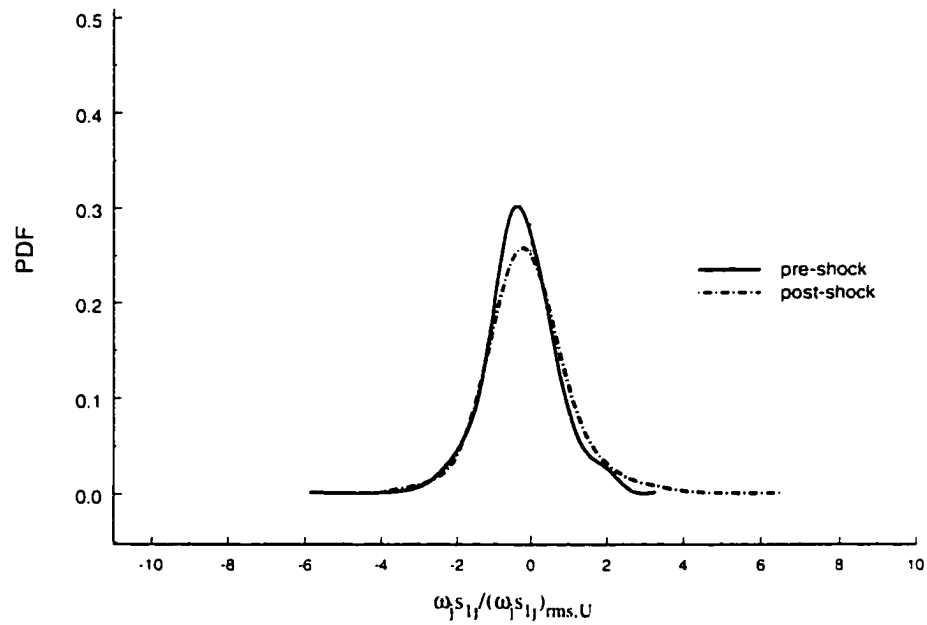

Figure 8.70: PDF of stretching term for ω_x. 2 x 2 grid, $M_{\infty,R}$=1.115

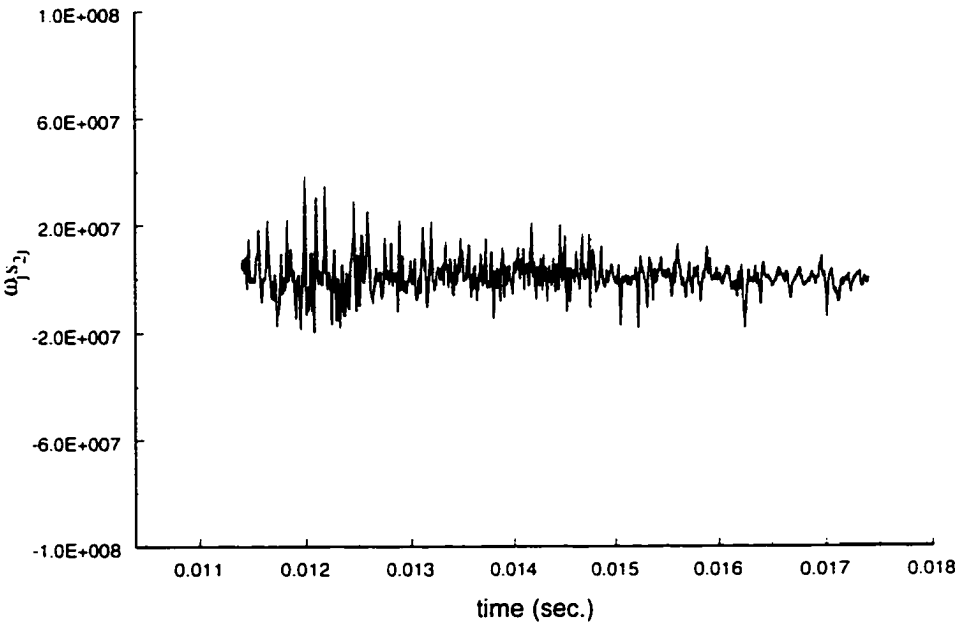

Figure 8.71: Stretching term for ω_y. 2 x 2 grid, $M_{\infty,R}$=1.115

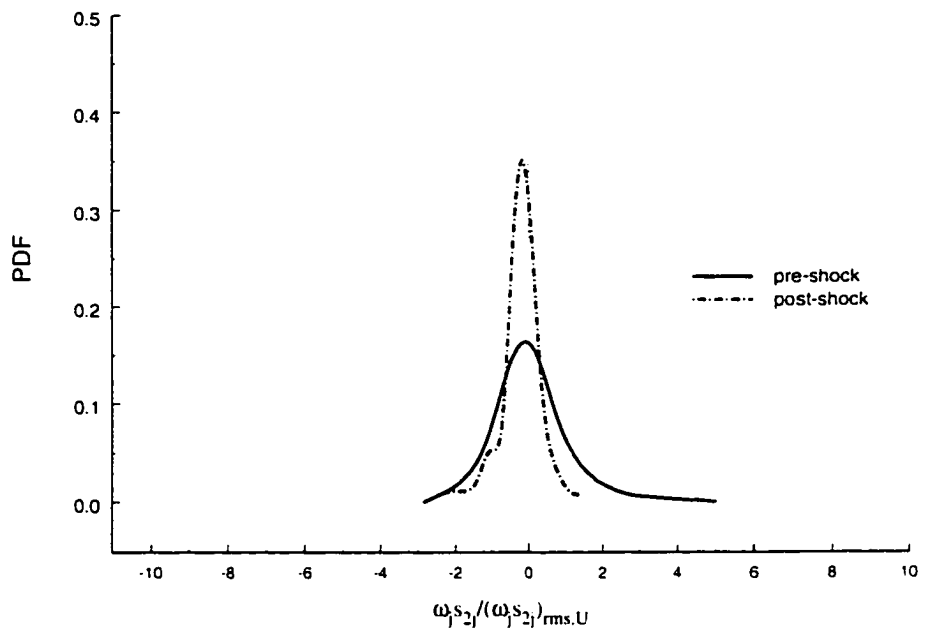

Figure 8.72: PDF of stretching term for ω_y. 2 x 2 grid, $M_{\infty,R}$=1.115

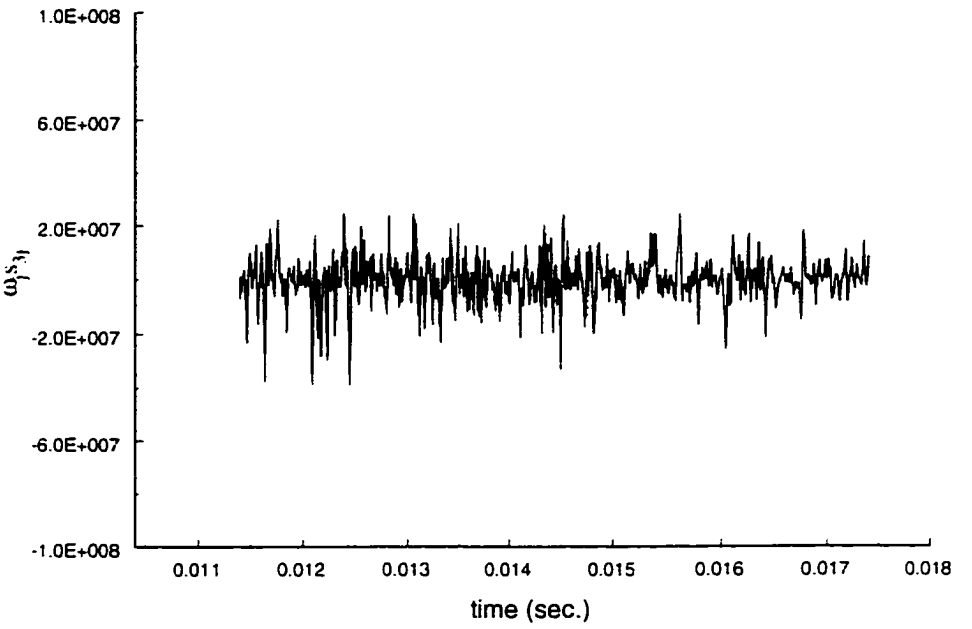

Figure 8.73: Stretching term for ω_z. 2 x 2 grid, $M_{\infty,R}$=1.115

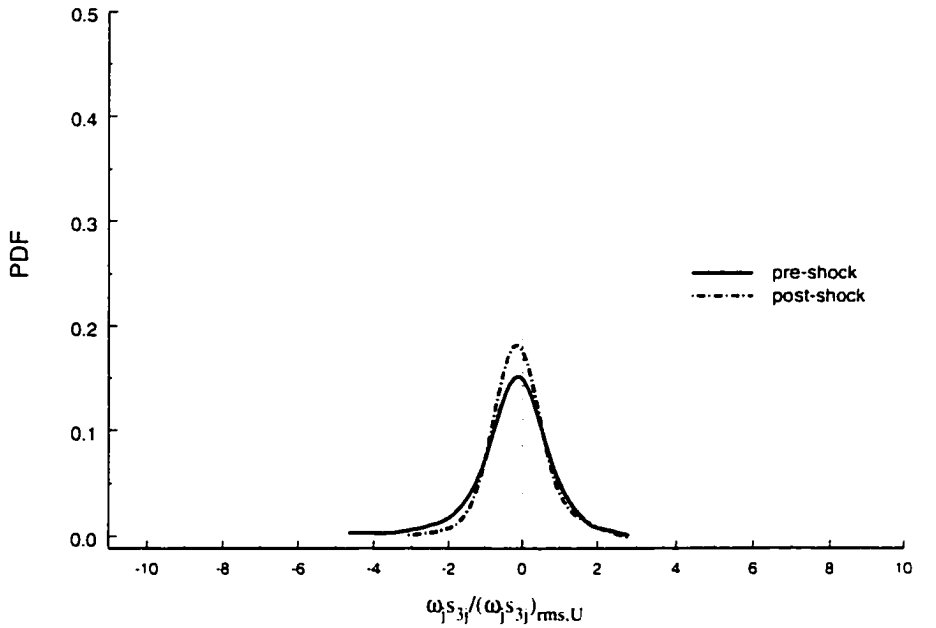

Figure 8.74: PDF of stretching term for ω_z. 2 x 2 grid, $M_{\infty,R}$=1.115

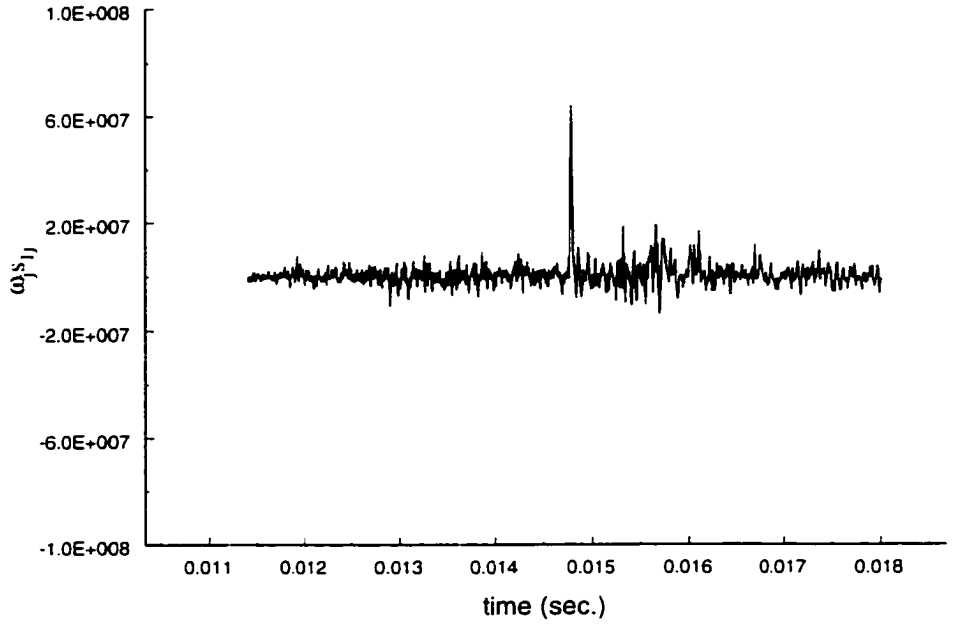

Figure 8.75: Stretching term for ω_x. 3 x 3 grid, $M_{\infty,R}$=1.104

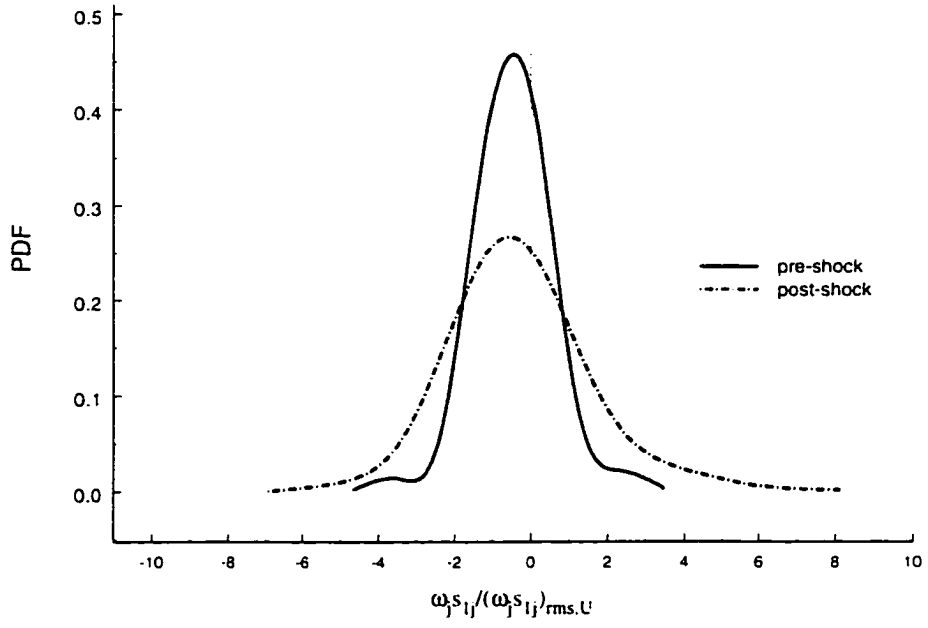

Figure 8.76: PDF of stretching term for ω_x. 3 x 3 grid, $M_{\infty,R}$=1.104

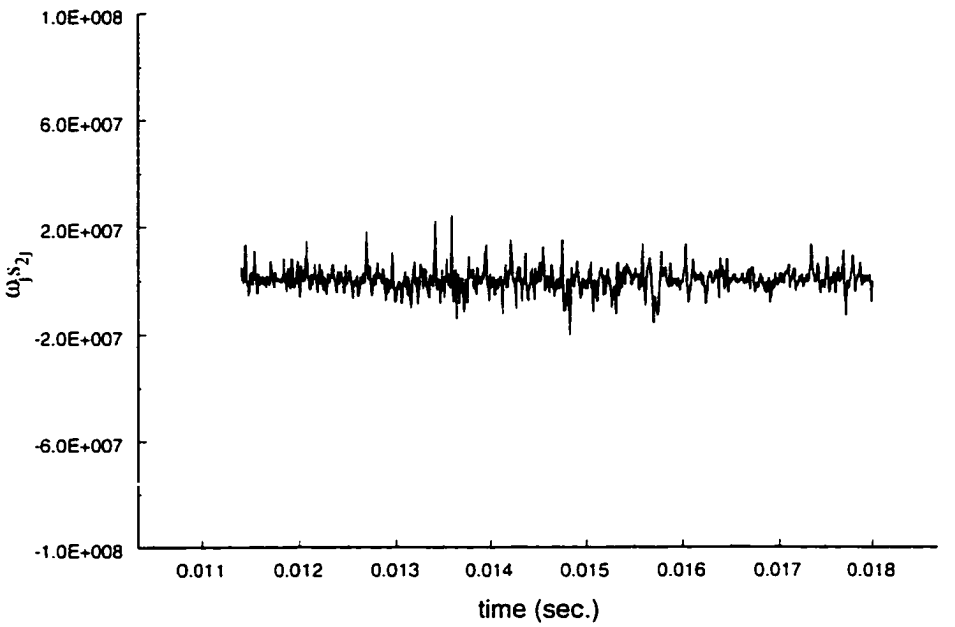

Figure 8.77: Stretching term for ω_y. 3 x 3 grid, $M_{\infty,R}$=1.104

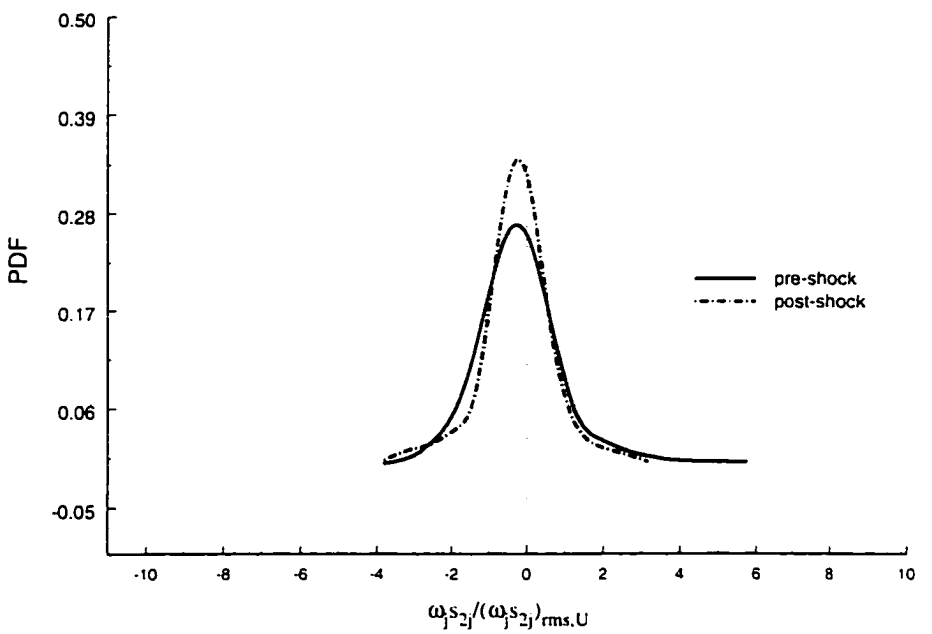

Figure 8.78: PDF of stretching term for ω_y. 3 x 3 grid, $M_{\infty,R}$=1.104

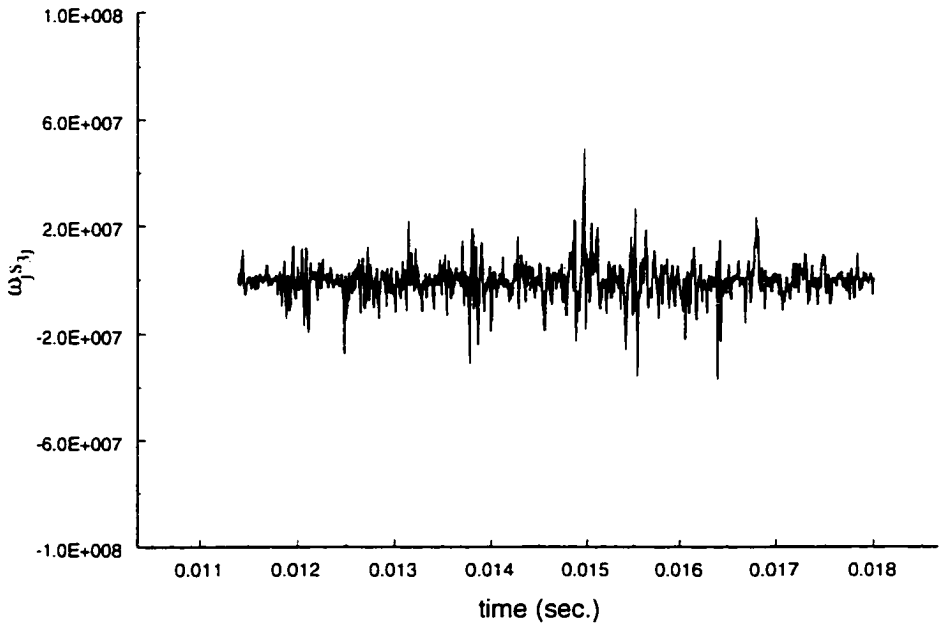

Figure 8.79: Stretching term for ω_z. 3 x 3 grid, $M_{\infty,R}$=1.104

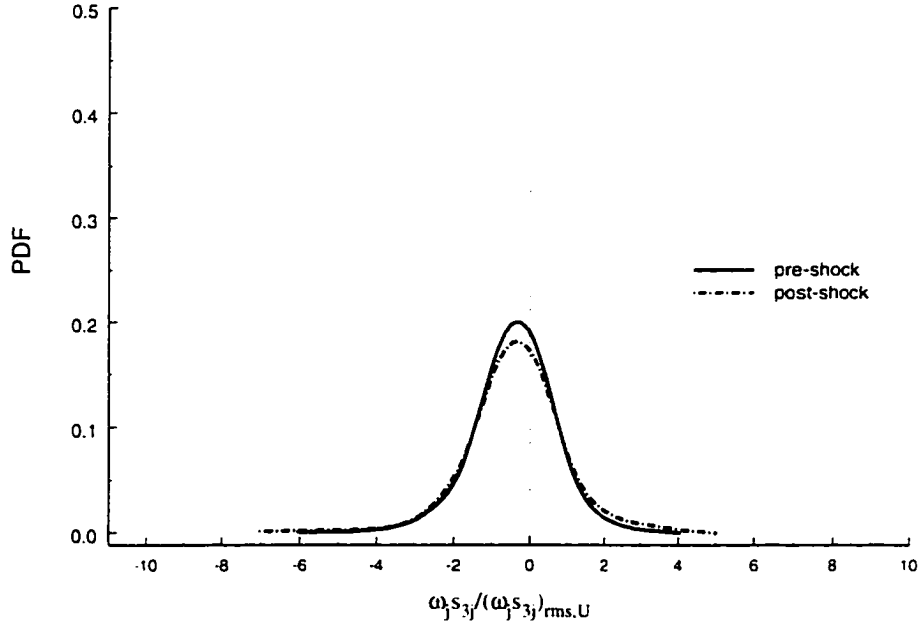

Figure 8.80: PDF of stretching term for ω_x. 2 x 2 grid, $M_{\infty,R}$=1.04

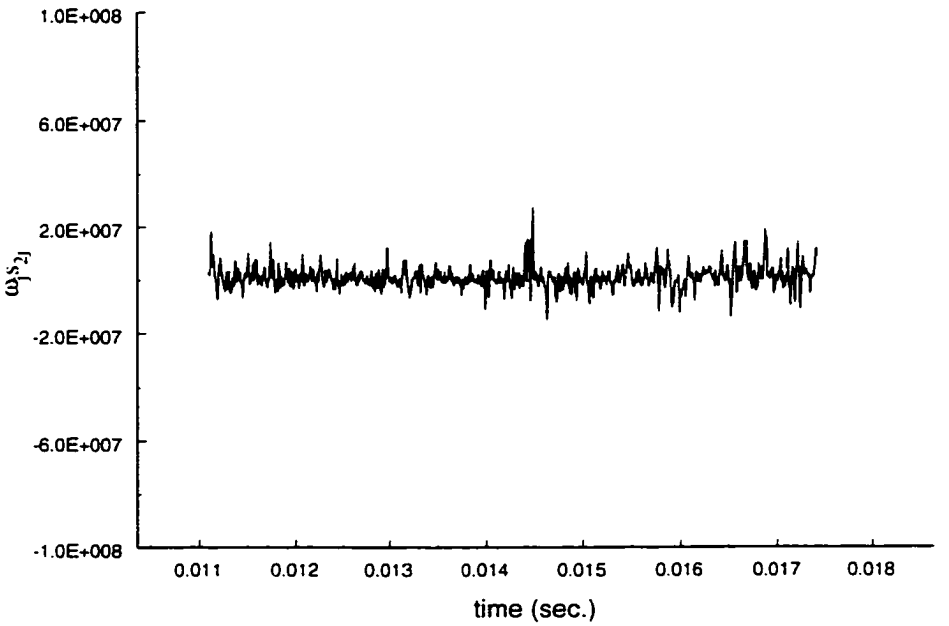

Figure 8.81: Stretching term for ω_x. 3 x 3 grid, $M_{\infty,R}$=1.191

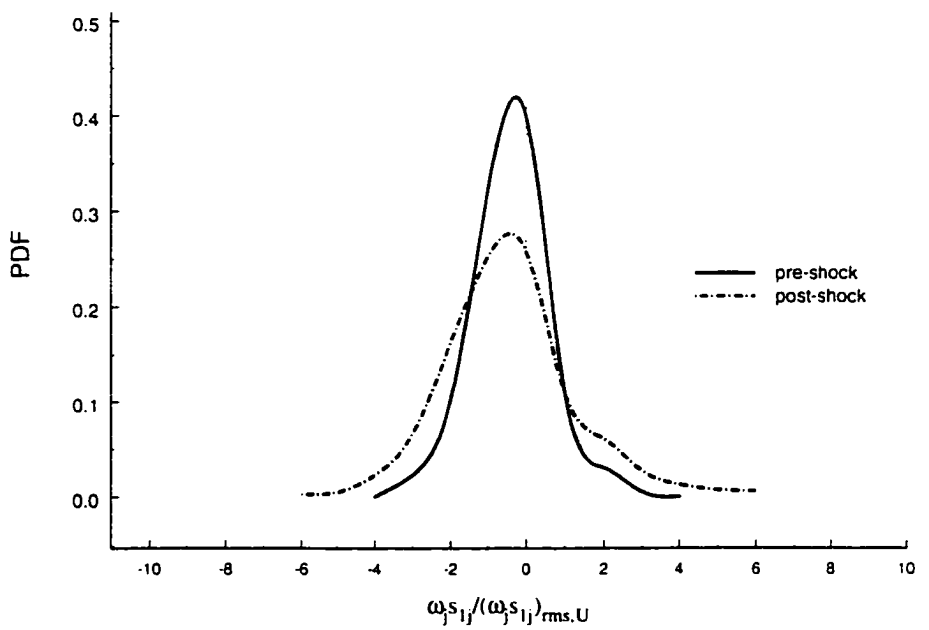

Figure 8.82: PDF of stretching term for ω_x. 3 x 3 grid, $M_{\infty,R}$=1.191

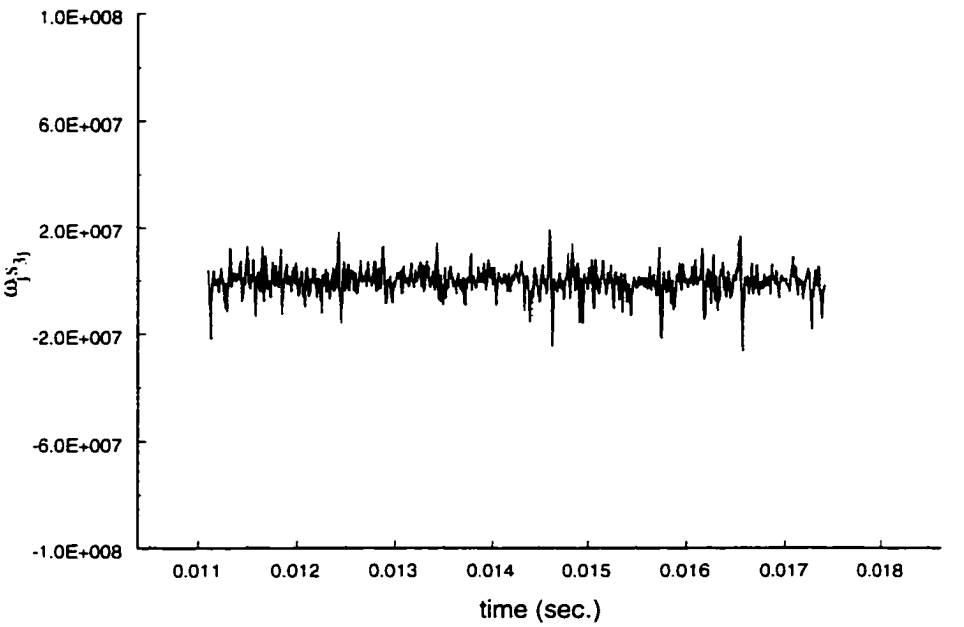

Figure 8.83: Stretching term for ω_y. 3 x 3 grid, $M_{\infty,R}$=1.191

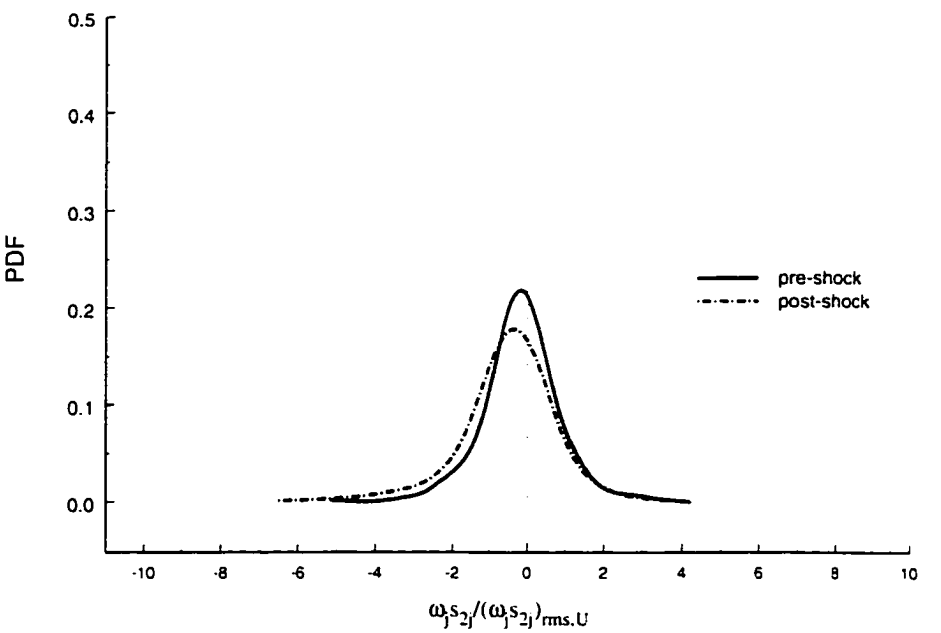

Figure 8.84: PDF of stretching term for ω_y. 3 x 3 grid, $M_{\infty,R}$=1.191

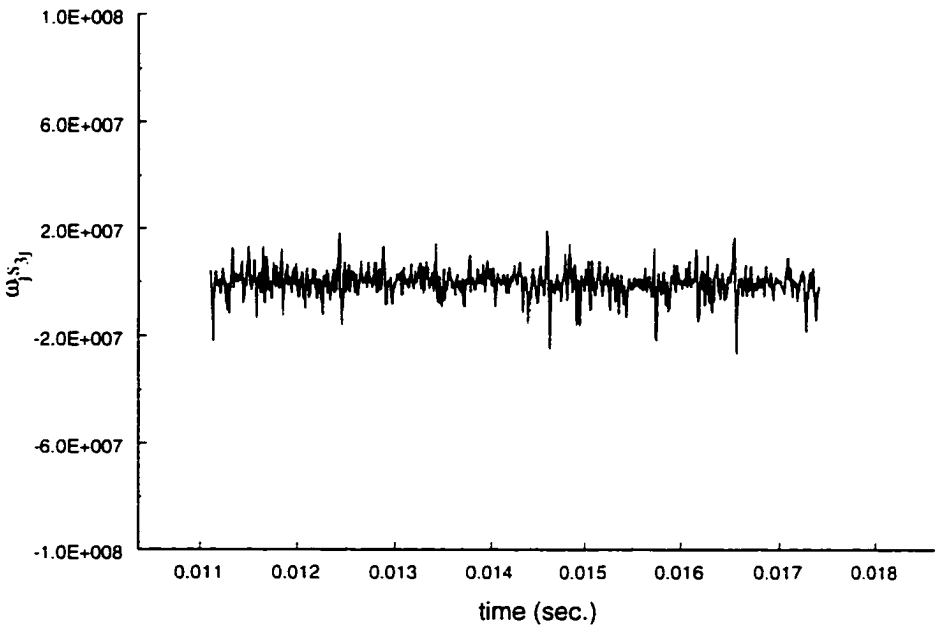

Figure 8.85: Stretching term for ω_z. 3 x 3 grid, $M_{\infty,R}$=1.191

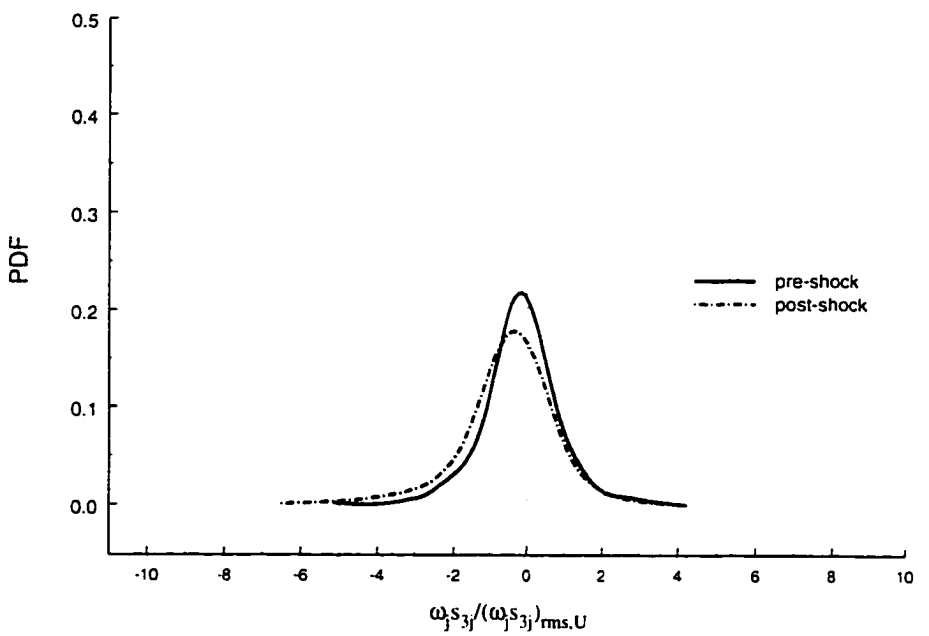

Figure 8.86: PDF of stretching term for ω_z. 3 x 3 grid, $M_{\infty,R}$=1.191

Chapter 9

9. Results & Discussion II - Shock Wave/Streamwise Vortex Interaction

This chapter presents the results obtained on the shock wave and streamwise vortex interaction. This interaction required considerable vortex flow characterization to determine the structure of the vortex. This is reflected in the first few sections of this chapter. A table of pertinent experiments and operating conditions are given in Table 7.1 below.

No.	Wing model	Probe(s)	Probe position vertical y/C from center of tube	Rotation of vortex model	p_2/p_1	M_r
1	10° s-s wing	3-K	-0.11	35	198	
2	10° s-s wing	3-K	-0.259	35	2.01	
3	15° s-s wing	3-K	-0.046	30	1.86	
4	15° s-s wing	3-K	-0.193	35	1.84	
5	15° s-s wing	3-K	-2.07	35	1.86	
6	15° s-s wing	3-K	-0.185	40	1.87	
7	15° s-s wing	3-K	-0.259	40	1.86	
8	15° s-s wing	3-K	-0.072	45	1.85	
9	15° s-s wing	3-K	-0.148	45	1.88	
10	15° s-s wing	3-K	-0.222	60	1.85	
11	15° s-s wing	16-w rake	-0.148	35	1.89	
12	15° s-s wing	vorticity	-0.185	40		0.31
13	15° s-s wing	vorticity	-0.185	40		0.45

legend: s-s, semi-span; 3-K, 3 Kulite probe; 16-w : 16 wire rake.

Table 9.1: Experiments performed on the shock wave/streamwise vortex.

The coordinate system adapted is shown in figure 9.1

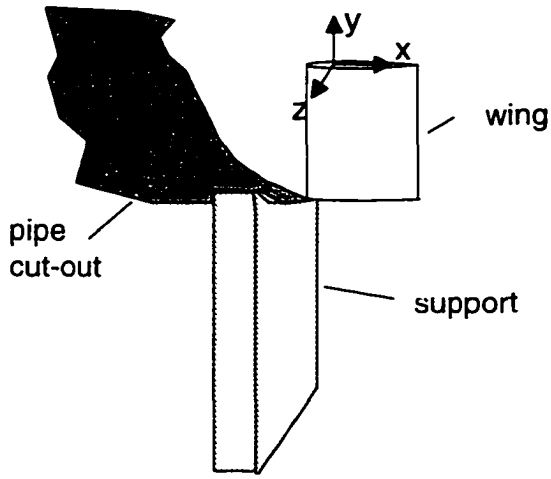

Figure 9.1 Laboratory coordinate system

9.1 Preliminary Flow Visualization

In order to visualize the type of the flow likely to occur in the shock tube facility an initial flow visualization was performed in a subsonic wind tunnel.

Figures 9.2 - 9.4 show pictures which were taken in a CCNY subsonic wind tunnel. Smoke was introduced through a small diameter bent tubing at about a chord distance upstream of the wing model and a laser sheet was illuminated just downstream of the model perpendicular to the flow. The vortex structure is quite evident for the first two wing models. A doughnut shaped structure is visible in both images. However the structure is larger for the 15° wing model. Both vortex structures are located some vertical distance below the wing tip. The third picture shows the structure behind a delta wing. The flow structure here is not very well structured. A rather large symmetric structure is visible. Since the chord length of this model is the same as that of the wing tip models, it is quite convincing that vortex breakdown has already occurred. Therefore it was decided that this alternate streamwise-vortex generator would not be used in the shock tube.

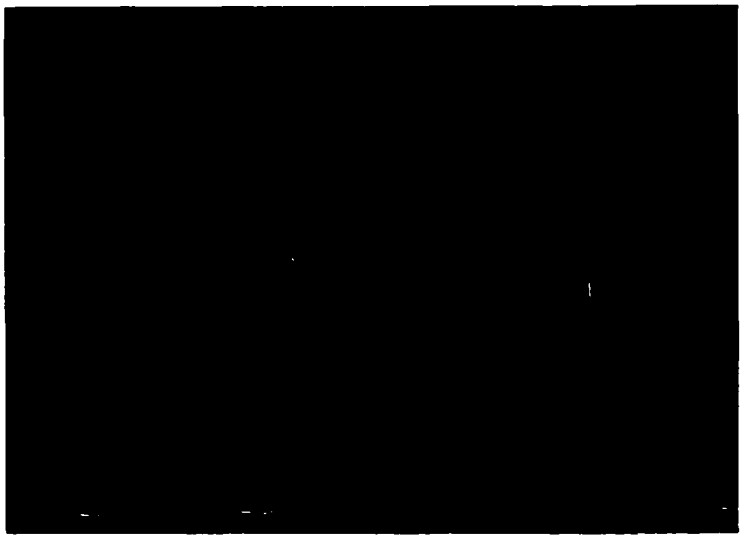

Figure 9.2: Smoke flow visualization of 10^0 pitched wing tip model.

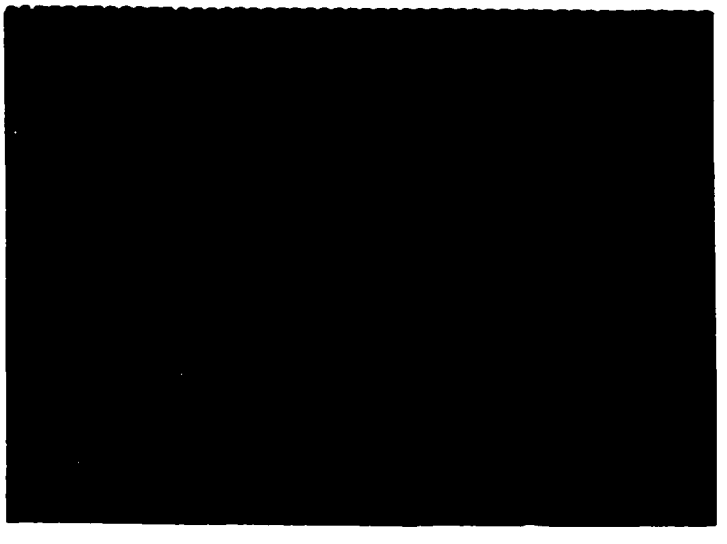

Figure 9.3: Smoke flow visualization of 15^0 pitched wing tip model

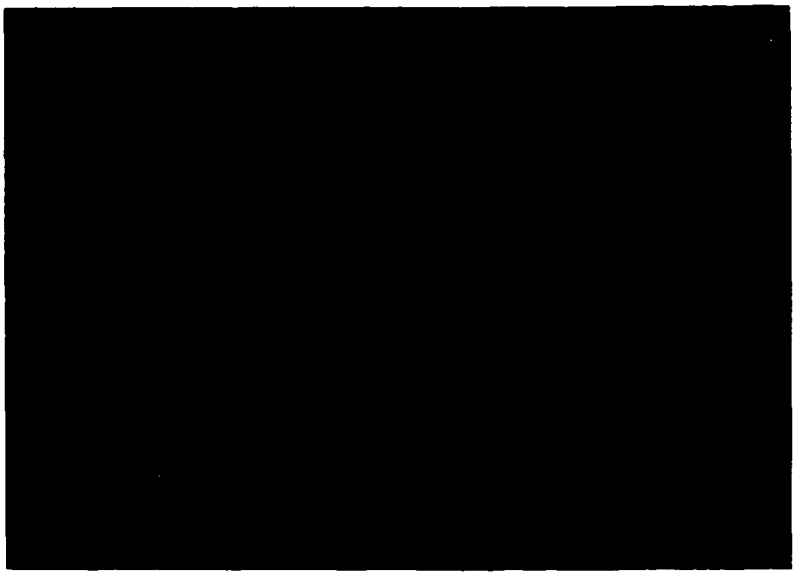

Figure 9.4: Smoke flow visualization of delta wing trailing vortices.

9.2 Hot-Wire Rake

The hot-wire rake made up of 8 sets of one velocity (or mass flux) and one total temperature sensors each, and displaced by 0.250 inch (6.35 mm) apart was used to obtain a large area mapping of the vortex flow. The mapping region was extensive enough to capture the vortex influenced flow and part of the external flow. However, the spacing between mass flux/total temperature modules was not adequate for any type of detail mapping of the vortex itself. The first intent of using this probe was first to localize the extent of the vortex flow and to approximate its center position. The second, because of the usefulness of the high resolution signal obtained from the sensors, was to obtain measurements which could demarcate the vortex flow from the external flow. Statistical quantities of the turbulence in different regions of the flow can also be useful.

Specifically, the turbulence near the core center, core edge (found a posteriori), outer vortex flow and the external flow.

Figure 9.5 gives a contour mapping obtained from the hot-wire rake. The contours represent constant effective mass flux levels. Recall that the probe is measuring the ρU_{eff} by King's Law. Decomposing of the mass flux was not attempted because of the single orientation of the wire sensors and the highly vortical nature of the flow. Nevertheless, the picture one gets from the figure is that of the vortex flow marked by a region of higher mass flux levels (between 453 to 483 Kg/(m^2 sec)) in the bottom part of the mapping, below 10 mm. When it goes through the shock front, it is marked by uniform fronts of almost sudden drops in mass levels, the vortex region quickly disappears. This might be true indication of the vortex breakup or can be caused by the lack of spatial resolution between mass flux sensors. The vortex width seems very roughly to be about 10 mm from inspection of figure 9.4. Again it should be emphasized that there is lack of spatial resolution and uncertainty of +/- 6.35 mm might exist in the estimate of the core width. More accurate estimate of the core width is obtained a contour mapping of total pressure and from Particle Flow Visualization images which are covered subsequently.

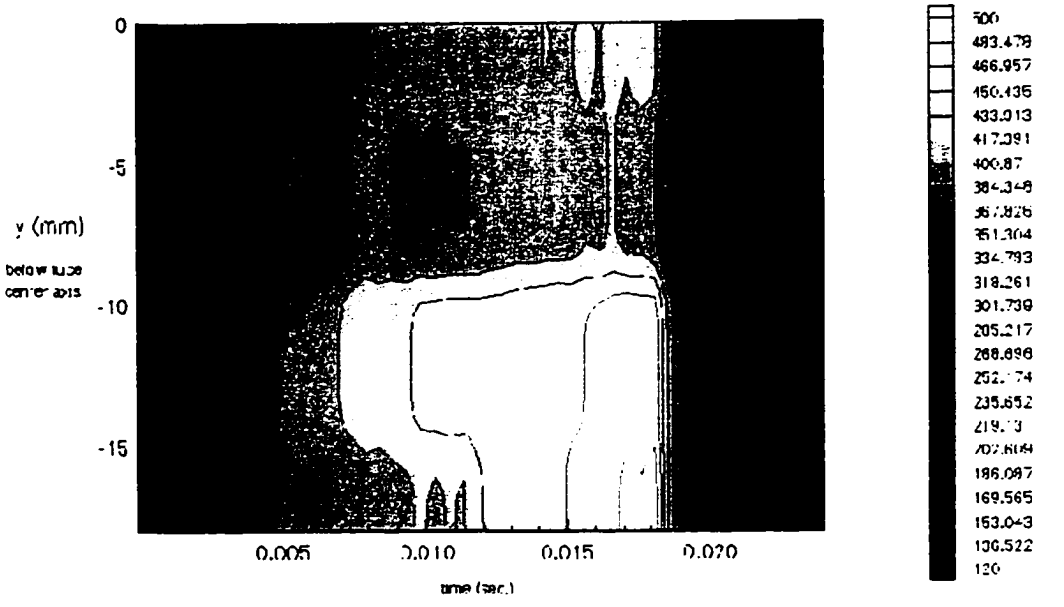

Figure 9.5: y-time diagram of Effective Mass Flux (ρU_{eff})

9.3 Static Pressure

Pressures were taken on the wall of the test section giving the time-dependent wall pressure of the evolving flow. Wall static pressures serve several purposes. First, when measured in a undisturbed or uniform shock tube flow they produce 1-D calibration parameters for use with other probes. Since wall-normal pressure gradients are considered negligible in an attached boundary layer, from scaling arguments, then wall pressures also represent static pressures of the uniform free-stream flow. Second, measurements taken during an actual experiment serve to provide free-stream flow conditions. In this case the arrival of the expansion waves, which change the flow conditions, reflected from the driver side end wall was monitored with the wall pressure. Third, they were used as normalization parameters because they reflect free-stream conditions. Last, although not used for the data presented in this chapter, when measured with grid generated turbulence

experiments which produce nearly-isotropic and nearly homogenous turbulence, they serve to provide the static pressure in the turbulent field itself. A word of caution, the fluctuations in the wall pressure are linked to the dynamics of the adjacent boundary layer and should not be used as a measure of the fluctuations outside of the boundary layer.

Figure 9.6 shows a comparison of typical signals obtained from a undisturbed uniform flow signal and two signals, wall pressure and total pressure, obtained during a tip vortex experiment. The total pressure taken by the 3-Kulite rake is provided as a reference of the vortex flow. It clearly shows the inception of the tip vortex marked by a local drop in total pressure. As will be explained later a starting vortex is sensed at the probe before the arrival of the tip vortex itself. It is quite clear that the vortex does not affect the wall pressure which is directly influenced by boundary layer dynamics. The wall pressure during the tip vortex experiment shows no variation in mean pressure or its fluctuations, from the inception of the tip vortex through its continued generation. This aspect of the tip vortex is discussed in the next section.

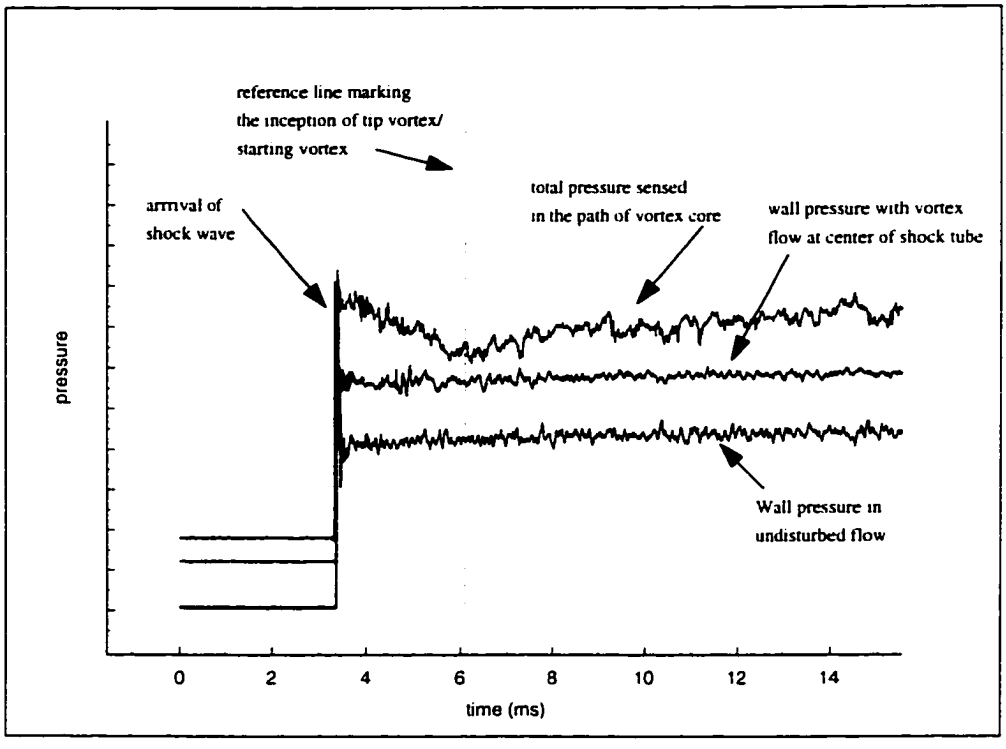

Figure 9.6: Comparison of wall pressure during an undisturbed flow and tip vortex experiment.

9.4 Kulite Rake

The total pressure probes were instrumental in localizing the core of the vortex. The experimental work of Smart, Kalkhoran and Bentson (1995) indicates that the vortex core carries a total pressure deficit which in their case is quite substantial because of the much larger Mach number flow, M = 2.5. A deficit of 60 % was reported in their work. The experiments of Smart et al. (1995) describe a vortex flow with a steady character except for some lateral wandering. The profiles were obtained with a single probe which traversed the vortex core and the adjacent region which were averaged over sufficiently long time. It should be noted that in the work of Zilliac, Chow, and Dalces-Maiani

(1993), in which they investigated an incompressible tip vortex flow in a relatively high speed, 170 m/s, the total and static pressure were found to in excess of the surrounding free stream.

In the present case the Kulite rake (described in section 5.4.1) was used for localizing the vortex core center and for determining the pressure profile through the core. The transducers were displaced by 5.08 mm (or 0.200 inches) giving a total detection range of 10.16 mm. Since the core size was estimated to be of the order of the detection range of the probe, a traverse of the probe measurements was necessary. Although each three point local profile was obtained during independent experiments, there was good repeatability among these experiments allow a combination of them into one representative profile. This can also be judged from the proceeding profile plots.

Each semi-span, or tip vortex, wing model was designed so that the corner made up of the wing trailing edge and the wing tip would be located on the center axis of the shock tube. From the images in section 9.1 it was found that the vortex center was located off this reference center. The actual location of the tip vortex center was found to be slightly to the side of the outboard surface and below the tip edge of the wing model. Therefore when mounted on the shock tube the vortex center would be slightly away from the tube facility axial center. Since the probe could only be traversed through a path along a diameter of the tube facility, the vortex center had to be repositioned such that its center would coincide somewhere along the diameter traversing line (vertical or horizontal). The method of repositioning the vortex center involved rotating the annulus support of the wing model, which was mounted between pipe flanges. By rotating the model annulus support within the flanges the vortex itself could be rotated.

Figure 9.7 shows a typical signal obtained from one of the Kulite pressure transducers used in the 3-Kulite rake probe. Labels are used to mark different stages in the evolution of this vortex flow. It is instructive here to describe the flow evolution. As the incident shock wave initially passes over the wing model, it starts in motion the flow over the model and therefore the inception of a starting vortex. As this starting vortex propagates downstream it is followed by a trailing vortex, or tip vortex, which is attached to it. This is shown clearly in the flow schematic of figure 5.3. The tip vortex is continually generated from the wing as long as the flow over the wing remains mildly uniform and no sudden waves propagate over the wing.

In light of the flow description just given, the signal in figure 9.6 indicates the arrival of the tip vortex by a great depression in the total pressure, about 10% of the free-stream static. After the passage of the starting vortex, the early stage of the tip vortex is sensed. From the early stage to its later stage the total pressure is characterized by an almost steady pressure, aside from a small time-dependent pressure gradient, and by moderate to small pressure fluctuations. This seems to indicate that the character of the vortex is marked by a steady flow conditions with low turbulence levels. In fact, the turbulence levels are comparable to those obtained from the dynamic calibration of the 3-Kulite rake probe. All this points to a low turbulence vortex core.

The value of total pressure before the depression represents the flow unaffected by the vortex. This makes sense if the following argument is accepted. The signals in figure 9.6 is taken right after the arrival of the incident shock before which there was no flow. Since the vortex, as well as the flow, cannot travel with the same speed of the shock, the mass of air initially occupying the region between the wing trailing edge and the probe

sensing area comprises the first flow sensed by the probe. Therefore the initial flow does not contain any type of vortex. Even if vortex core or the starting vortex propagated faster than the free-stream it would be impossible for it to affect the first instance of the signal after the incident shock. This flow, then, can be considered uniform if it is assumed the shock wave recovers its planar structure right after passing over the wing trailing edge Then from inspection of the plot it seems that the vortex core contains the same turbulence level as that of the initial uniform flow (see also figure 9.7). This is another good indication that the core is characterized by low turbulence.

Figure 9.8 provides a look at the three total pressure signals of the 3-Kulite rake probe for an experiment in which the incident flow Mach is $M_2 = 0.47$. All three signals generally overlap initially and therefore this region is not totally discernible in the plot. All show similar characteristics to the typical signal of figure 9.7. However, it is clear that the middle probe produced a much lower total pressure at the later stage of the vortex flow before the interaction with the reflected shock. This indicates that this sensor is responding to the lower pressure in or nearer to the vortex core center. After the interaction with the reflected shock, the total pressure seems to rise at a significant rate. This requires some interpretation. As the reflected shock wave passes over the probe, the probe starts to feel the interaction effect. As the shock continues to propagate, upstream now, the probe is sensing the vortex flow that has interacted with the shock further upstream. In effect, the probe is sensing the later stages after the interaction after the arrival of the reflected shock as increasing time after the arrival of the reflected shock. Since the pressure is increasing one plausible explanation might be that the core is expanding and the axial flow in the vortex core is slowing down. This condition is related

to vortex breakdown phenomenon, although the breakdown does not necessarily have to occur.

Figure 9.9 and 9.10 show the total pressure profile for the 10° and 15° wing models respectively in approximately the same free-stream flow conditions. The wing model was rotated at 35° and 40° for the 10° and 15° pitched models, as described earlier in this section, to bring the vortex flow in alignment with the probe. For this case, because of the radial traverse through different angles a polar coordinate, r, was adapted, where $y = r\cos\theta$ and $z = r\sin\theta$. For the remainder of the analysis the coordinate system reverts back to the original (x,y,z) of figure 9.1. One experiment produced a three point profile. Superimposing three experiments of the same Mach number, within 5% of shock strength, produced a nine point profile providing a more extensive profile. The most notable feature of both profiles is the ubiquitous total pressure deficit defining what is known to represent the vortex core center. It should be mentioned that the pressure deficit cannot be a probe effect since uniform flow tests over this probe (as discussed in section 5.4.1) produced virtually uniform profiles, and because the lower pressures in the profiles below were taken from different sensor in different experiments, thus ruling out a bias among the sensors on the probe. The two rotation angles of the wing models which were chosen for plotting in figures 9.9 and 9.10 gave the largest depression in measured pressure.

The statistics after the interaction given in figures 9.9 and 9.10 reflect conditions right after the reflected shock, and therefore do not reflect any evolving or decaying aspect of the interaction. The core seems to survive through the reflected shock, at least immediately after, as marked by the depression which holds through the interaction, but

there are some changes. After the interaction the deficit in the core seems less substantial which probably indicates a more diffused and larger core brought on by the sudden compression. This result is true for both wing models used.

Presented in figures 9.11 and 9.12 are the corresponding profiles of pressure fluctuation before and after the interaction with the shock wave. The center of the vortex obtained from the minimum total pressure point of the mean profile is given for reference. Bear in mind that measured values of pressure fluctuations can be a result of the unsteadiness and meandering of the vortex structure, as well as the inherent turbulence of the convective vortex flow. This might explain the variations in profiles obtained from the two wing models.

The vortex center position, however, seems to display some interesting characteristics. This position is characterized by low to moderate pressure fluctuations and no variation in rms value after the interaction. Additionally, in the case of the 10^0 pitched wing, rather large gradients of pressure fluctuations are associated with the center position, while in the case of the 15^0 wing a small local peak is present. Maximum pressure rms of the incident vortex flow occurs at positions 2% to 5 % from the vortex center. This most probably can be associated with vortex core edge which has been shown to be the most turbulent part of the vortex (see e.g. Rizzetta, 1995). Further insight into the turbulent character of the vortex is presented in the in the rms total pressure contour maps (figures 9.15 and 9.16).

Figures 9.13 and 9.14 provide cross-sectional maps of the tip vortex. This map was possible by rotating the wing model through several angles in a manner described before. As the model is rotated, the vortex is rotated past the probe and therefore the

probe senses a different part of the vortex. By taking pressure profiles for different angles of the vortex a contour map of constant total pressure is derived which represents the flow neighborhood of the vortex core. The final map is expressed in terms of the original lab coordinates given in figure 9.1. Figure 9.13 represents the flow before the interaction while figure 9.14 represents the flow after the interaction. The vortex is quite clear before the interaction marked by concentrated contours of lower total pressure and located at y/C = -0.14 and z/C = 0.12. The remaining flow area shows very gradual changes in total pressure with gradients directed away from the vortex center and some local high pressure spots. The deficit in total pressure seems to be about 10%. It should be noted here that because of the experimental method of obtaining the cross-sectional data the upper right hand is clustered with more experimental points than the other corners. After interaction with the reflected shock a weaker but still distinct vortex core is present. The core has not changed in position and it seems neither is size. However it is marked less concentric pressure contours and by more local high pressure spots which are closer to it.

The fluctuating total pressure data was also used for producing cross-sectional contour maps. These are shown in figures 9.15 and 9.16 for maps before and after the interaction. The total pressure is normalized by the free-stream static pressure. In the first figure, the core before the interaction is marked by a moderate rms level surrounded by lower pressure. This seems to be in line with an argument posed by Zilliac et al. (1993). These authors describe the core in the far field, in their case x/C = 1.42 (as compared to x/C = 7.11 in the present case), as being in solid body rotation and in which they found that the normal stresses have concentrated in the core axis. The Reynolds stresses are slightly off axis but contained within the core. This is contrast to the near field (x/C =

0.868) where the stresses are concentrated at the edge of the viscous core and their levels are much higher. The difference in levels of normal and Reynold's stresses between the near field and the far field they argue is due to one of two mechanisms a laminarization of the core or the roll-up process has stabilizing effect due to the solid body rotation which quickly decays the turbulence. The end effect is a core with significantly low turbulence level in the far field.

Figure 9.17 and 9.18 are shown to demonstrate the evolution of the vortex. The time axis in figure 9.17 was taken from a reference point shortly before the starting vortex is sensed, as marked by a total pressure dip on the individual probe signals, until just before the reflected shock arrives. The next figure shows the time axis reset from shortly after the reflected shock wave has passed and for extended time after that. It should be reminded that the probe size defined by the distance between the two end sensors is 10.8 mm. Therefore what is seen in figures 9.17 and 9.18 represents the flow inside the core or the whole core. It should also be pointed out that the contour is derived from only three time dependent total pressure signals which correspond to points along the top, center and bottom y/C locations of the contour maps, so that the interpolation occurs between points displaced by .059 chord lengths.

The most notable feature in figure 9.17 is the large deficit region in the beginning which corresponds to the arrival of the starting vortex heading the tip vortex region. An alternate way to view this contour is by considering that the time axis can be converted to an appropriate longitudinal space axis by proper transformation involving the local velocity, known as Galelian Transformation. In this frame of reference, the contour of figure 9.17 should be flipped horizontally, and in this way the flow structure which

appears in front of the probe is disclosed, at the first instance after the incident shock has propagated over the probe. Therefore what the probe sees heading towards it is a starting vortex with a very large pressure deficit followed by the trailing vortex which possesses a smaller deficit. There seems to be towards the sides of the tip vortex a local band at y/C = -0.155 and y/C = -0.215 of sharp pressure gradients. This seems to agree with the cross-sectional contour of figures 9.15 and 9.16. Although these bands in figure 9.17 should be viewed with some caution since there was no data taken at these y/C locations, the fact that cross-sectional contour obtained from the same and other independent data shows the same structure at the same location gives good indication that this is a true structure. Figure 9.18 shows the deficit corresponding the vortex right after passing through the shock and contours of higher pressure propagating radially out shortly thereafter, possibly indicating a vortex being diffused. At about 4 ms after the reflected shock there appears a high pressure front extending throughout a plane. This high pressure front can be one of two things. One, a weaker shock that has reflected off the wing model which propagated downstream. Or, a second type of starting vortex generated from a sudden change in flow properties brought on by the reflected shock wave passing over the wing model as it propagates upstream. Finally, towards the end the arrival of the expansions waves, originally created from the rupturing of the diaphragm, is sensed by the gradual pressure drop.

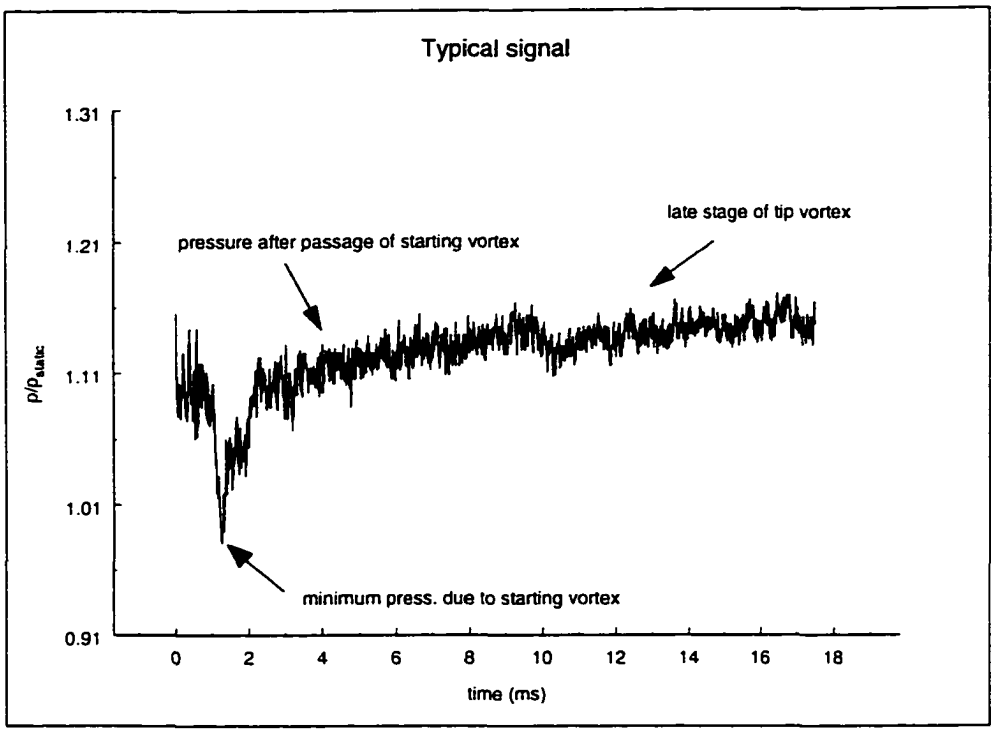

Figure 9.7: Typical signal of total pressure in vortex core before arrival of reflected shock.

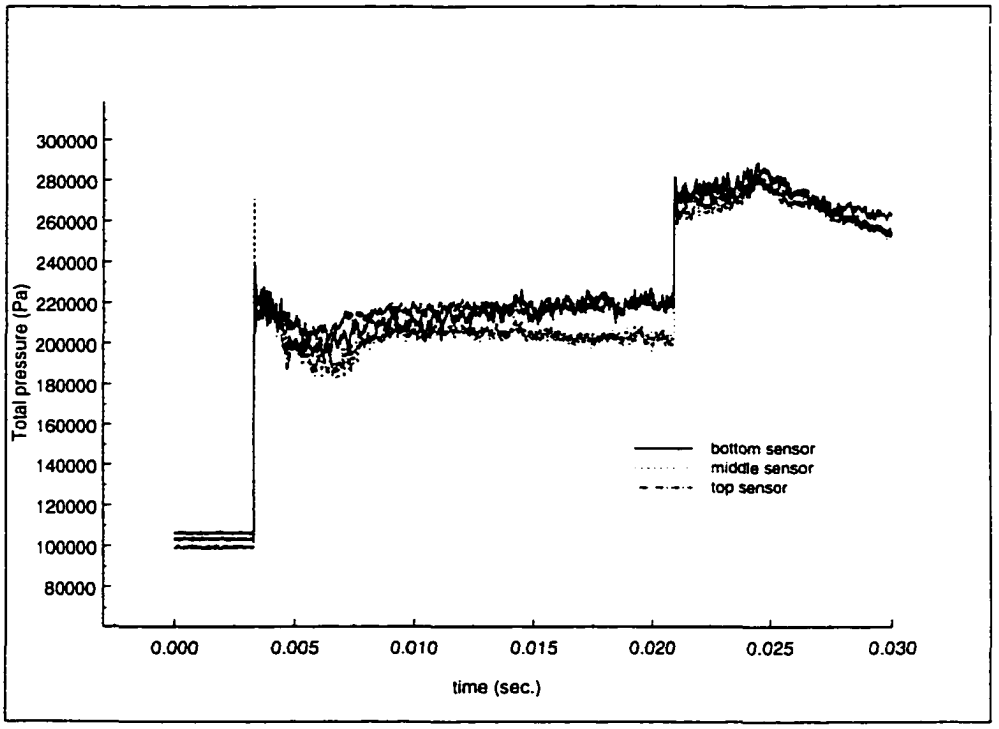

Figure 9.8: All three total pressure signals from the 3-Kulite rake probe obtained using 15° pitched semi-span wing to produce the vortex flow.

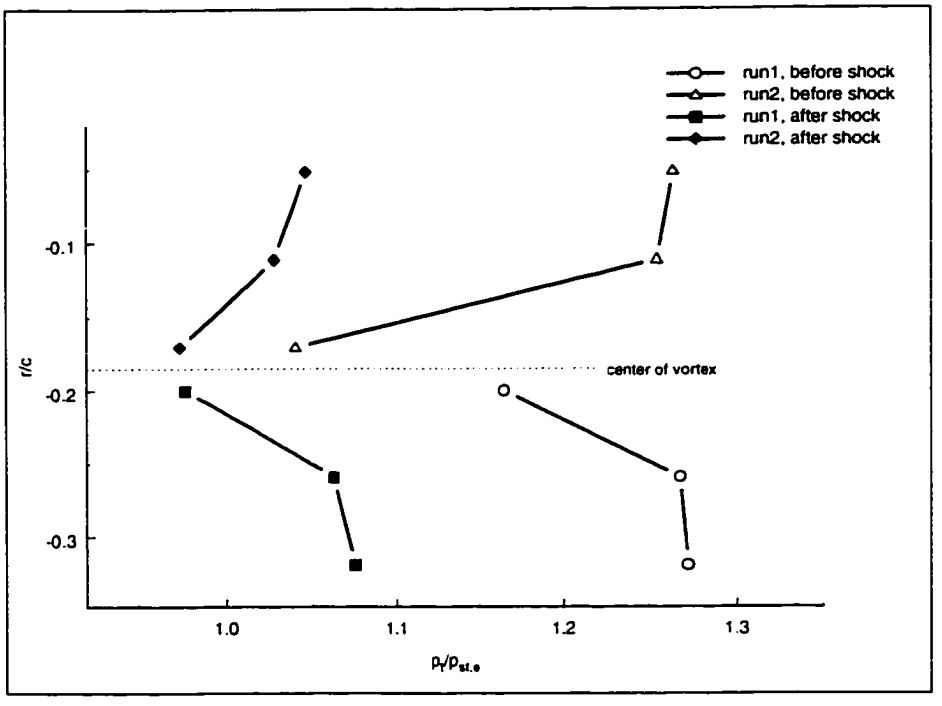

Figure 9.9: Normalized total pressure profile of the tip vortex using a 10° pitched half wing model rotated 35° about longitudinal axis. Average free stream flows conditions for two runs: p2/p1=2.08, p5/p2=1.59

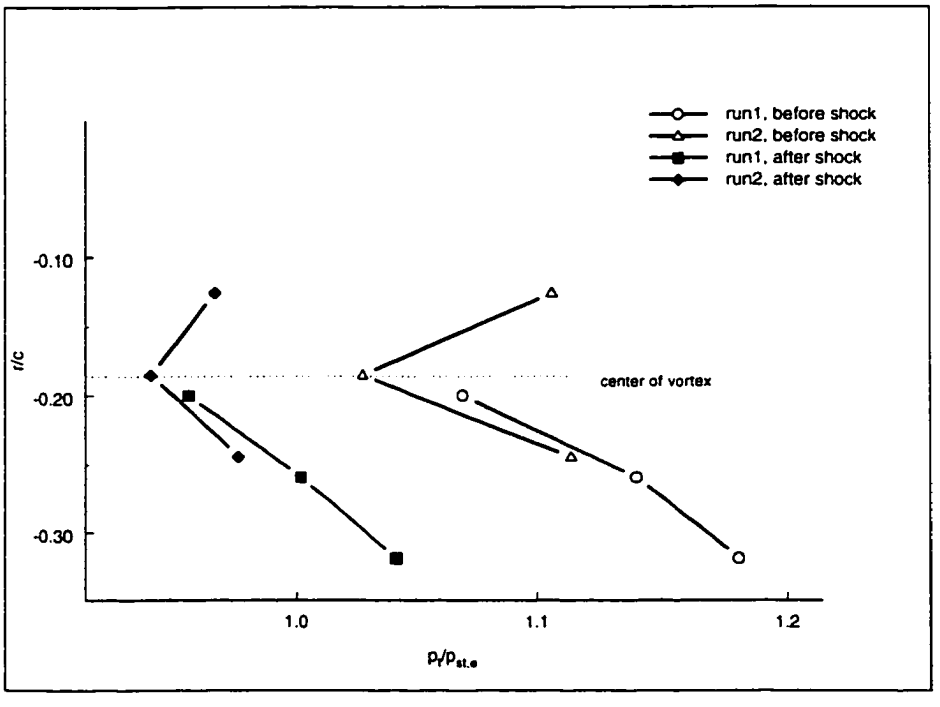

Figure 9.10: Normalized total pressure profile of the tip vortex using a 15° pitched half wing model rotated 40° about longitudinal axis. Average free stream flows conditions for two runs: p2/p1=1.87, p5/p2=1.44

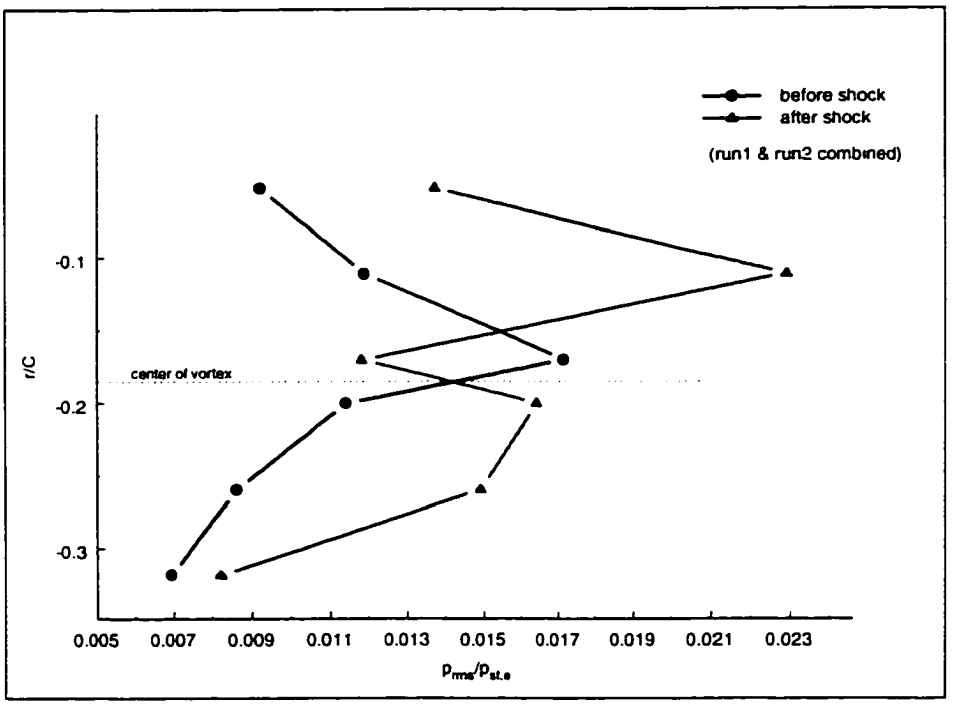

Figure 9.11: Normalized rms of total pressure profile of the tip vortex using a 10° pitched half wing model rotated 35° about longitudinal axis. Average free stream flows conditions for two runs: p2/p1=2.08, p5/p2=1.59

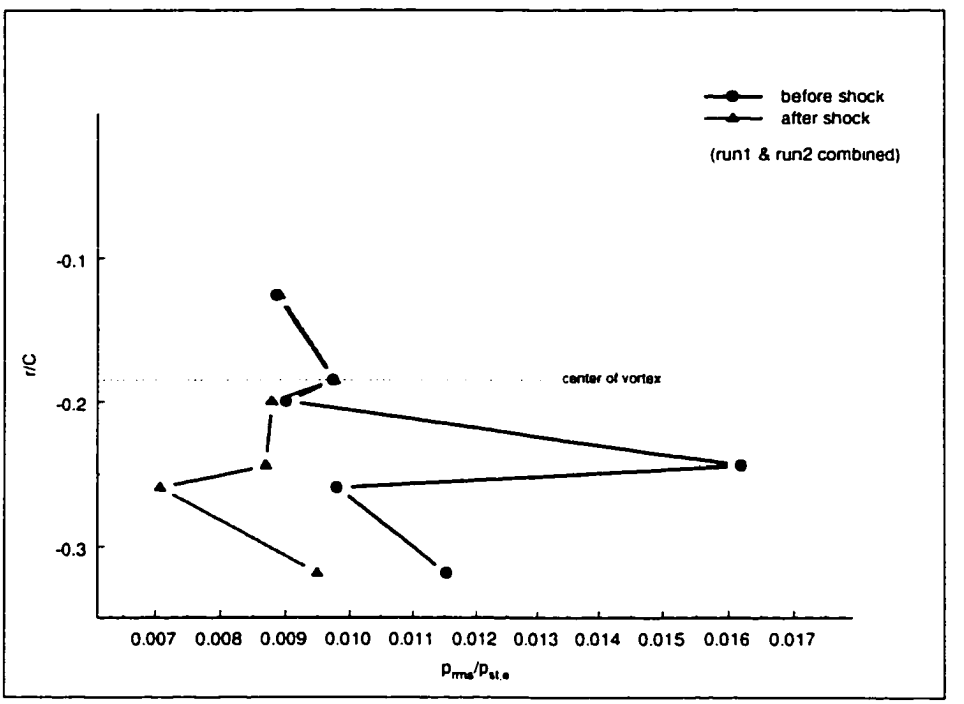

Figure 9.12: Normalized rms of total pressure fluctuations of the tip vortex using a 15° pitched half wing model rotated 40° about longitudinal axis. Average free stream flows conditions for two runs: p2/p1=1.87, p5/p2=1.44

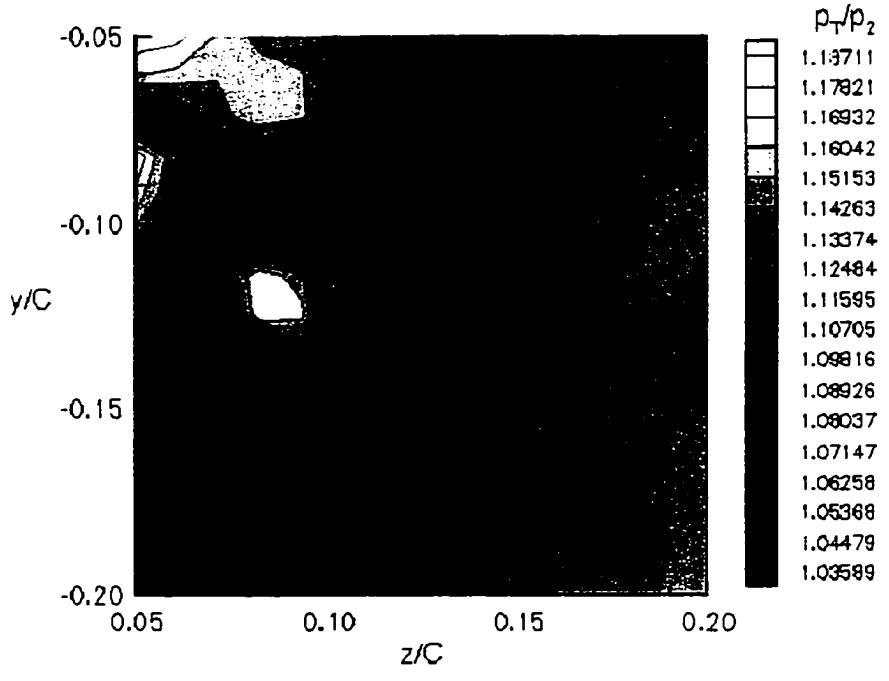

Figure 9.13: Normalized total pressure contour map of the tip vortex before interaction with shock using a 15° pitched half wing model. Average free stream flows conditions for two runs: p2/p1=1.87, p5/p2=1.44

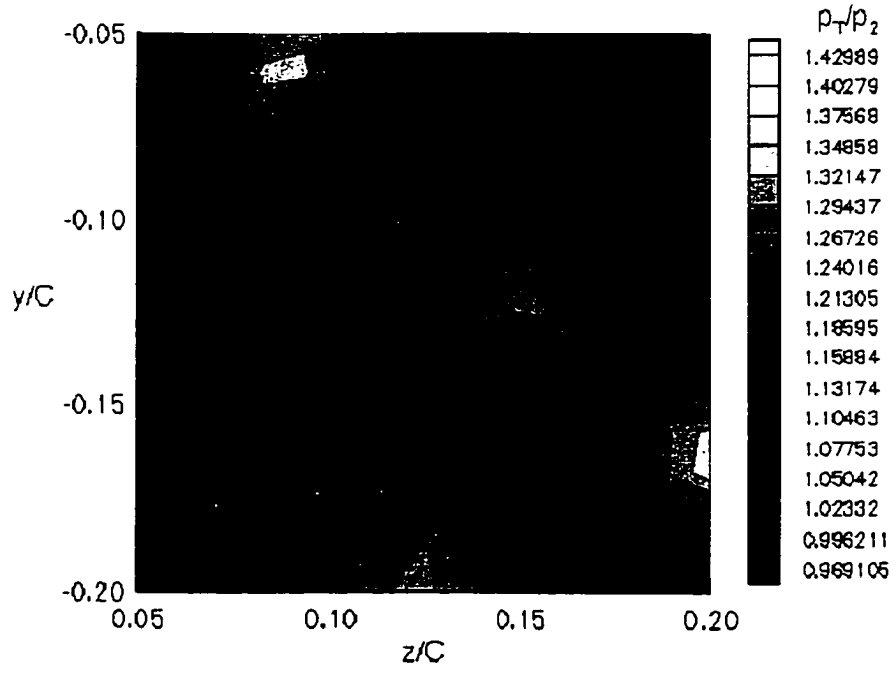

Figure 9.14: Normalized total pressure contour map of the tip vortex after interaction with shock using a 15° pitched half wing. Average free stream flows conditions for two runs: p2/p1=1.87, p5/p2=1.44

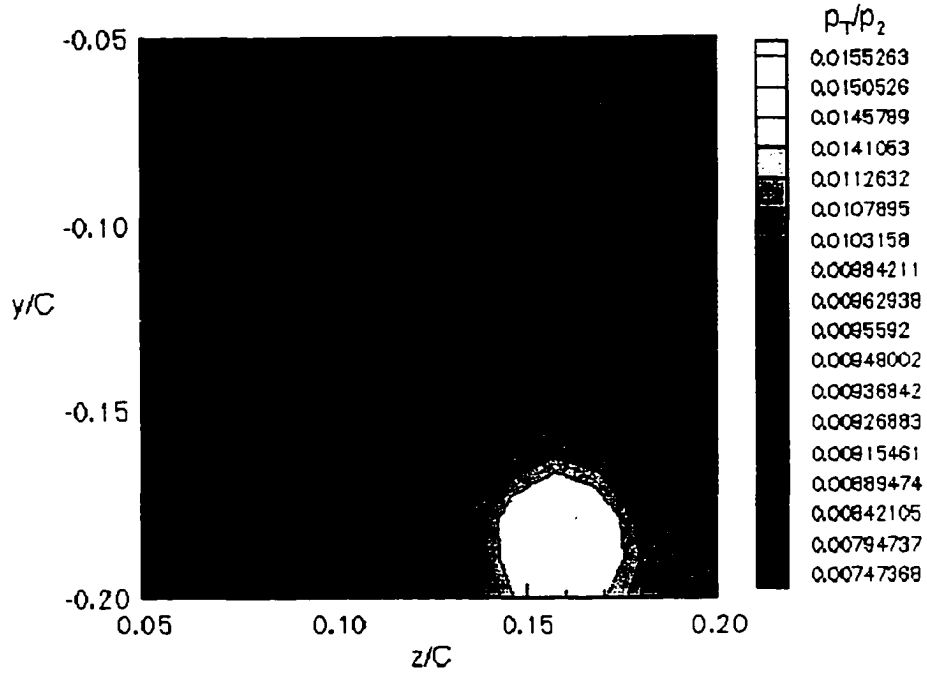

Figure 9.15: Normalized rms total pressure contour map of the tip vortex before interaction with shock using a 15° pitched half wing model. Average free stream flows conditions for two runs: p2/p1=1.87, p5/p2=1.44.

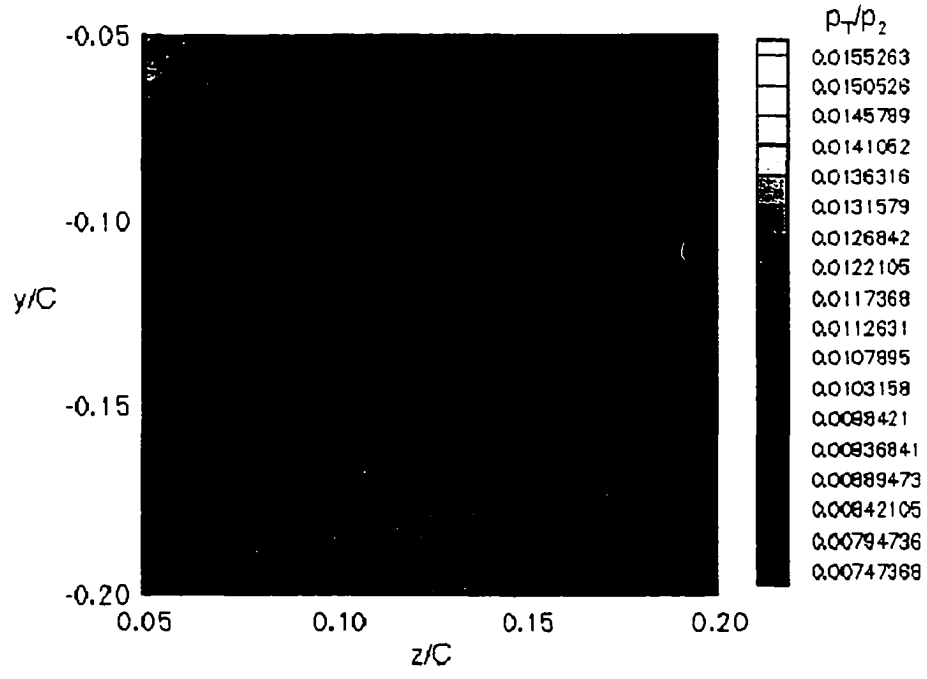

Figure 9.16: Normalized rms total pressure contour map of the tip vortex after interaction with shock using a 15° pitched half wing model. Average free stream flows conditions for two runs: p2/p1=1.87, p5/p2=1.44.

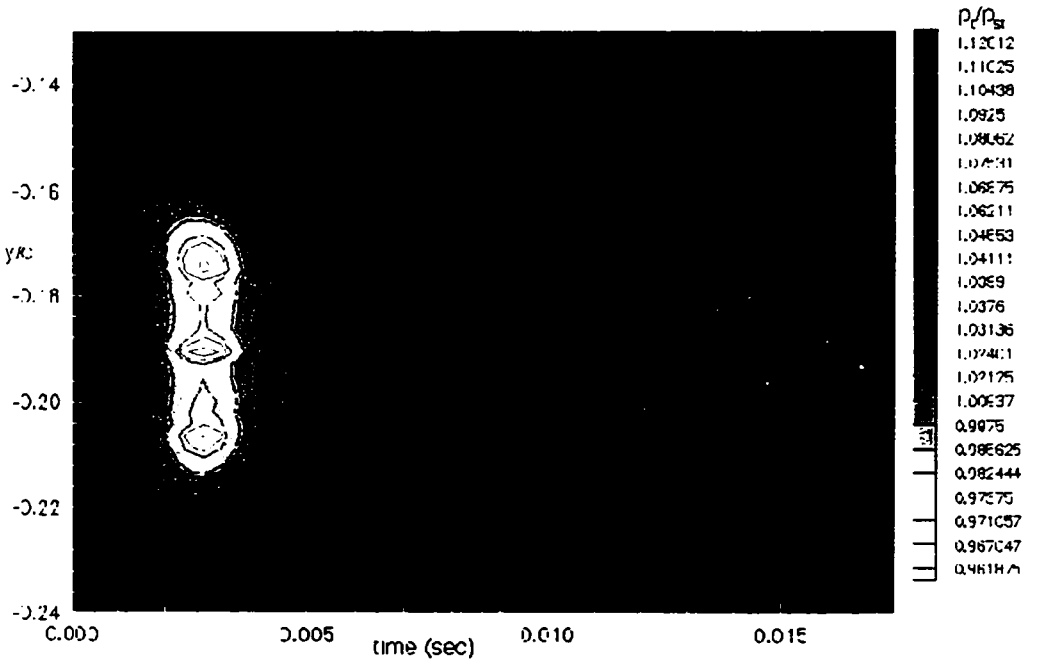

Figure 9.17: Evolving core structure monitored through three displaced probes before arrival of the shock

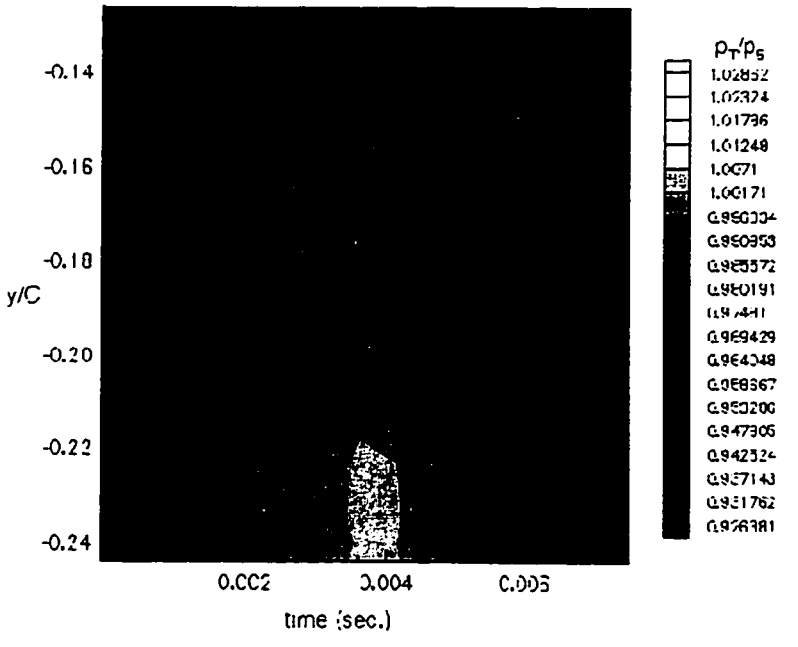

Figure 9.18: Evolving core structure monitored through three displaced probes after arrival of the shock

3-Kulite probe angular flow response:

The 3-Kulite probe was designed to measure total or stagnation pressure due to a longitudinal convecting flow. The vortex, however, contains a high degree of flow angularity and therefore the ability of the probe to properly measure the true stagnation pressure in this flow is deteriorated. As a result, the probe underestimates the stagnation pressure which in turn affects all other calculated properties which rely on it, specifically, velocity.

A yaw response test of the 3-k probe was undertaken to asses the error involved when the probe is exposed to an oblique velocity vector in the shock tube. Due to the physical constraints of the shock tube facility a pitch response test of the probe could not be performed. The details of this analysis is presented in Appendix C. It was found that the probe underestimates the total pressure as the vector angle is increased from 0^0 (i.e. directly aligned with and into the incoming flow) during incident flow conditions. The variation, however, is smooth with less than a 10% difference up to 30^0. The corresponding error in the measurement of velocity was also found to change in virtually equal amounts with the error in total pressure. However after the passage of the reflected shock wave, there was virtually no difference in the total pressure with varying yaw angle. Therefore, after the passage of the shock wave no error in velocity magnitude is expected (at least due to the yaw angle of the velocity vector). It should be mentioned also that this error in the calculation of velocity does not affect its direction. The ratio of the velocity components was initially determined from the coefficients of calibration(see Appendix A).

Shown in figures 9.19 and 9.20 are the PDF's of the calculated time-varying yaw angle that the velocity vector makes with the current coordinate system. These angles were calculated using the data from the vorticity probe (discussed in the subsequent sections) for two investigated Mach number experiments, M_{inc} = 0.31 and M_{inc} = 0.45. The velocity components are obtained prior to interaction with the reflected shock. The means of these angles are 19^0 and 20^0, while their rms are 2.6^0 and 2.1^0 for the two cases respectively. Minimum to maximum angle sweeps are 12^0 and 14^0. The expected statistical underestimated error in both cases is about 10%.

This shortcoming of the 3-Kulite probe measurement affects the results of section 9.4, the analysis of total pressure, and in subsequent section where the magnitude of velocity and vorticity comes into play. However, it was found that the rms of the measured pressure during this yaw response test did not change much with angle changes. Therefore the turbulence analysis of total pressure remains virtually unaffected. Neither did this characteristic of the 3-Kulite probe affect the turbulence statistics of velocity or vorticity. In this case a less restrictive form of Markovin's hypothesis is invoked which only considers the mean pressure component in the calculation of velocity and thereby also vorticity.

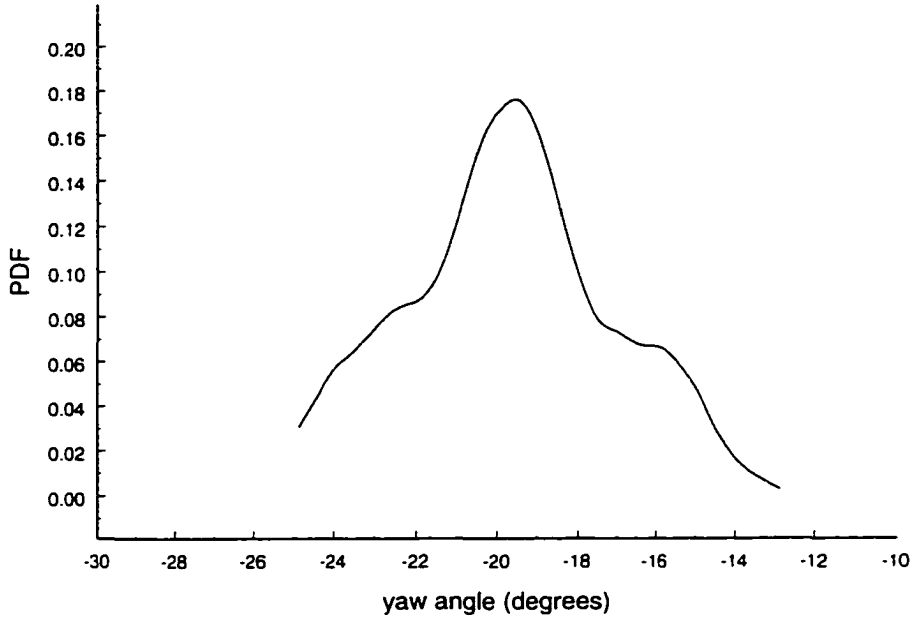

Figure 9.19: PDF of calculated yaw angle before interaction. $M_{inc} = 0.31$.

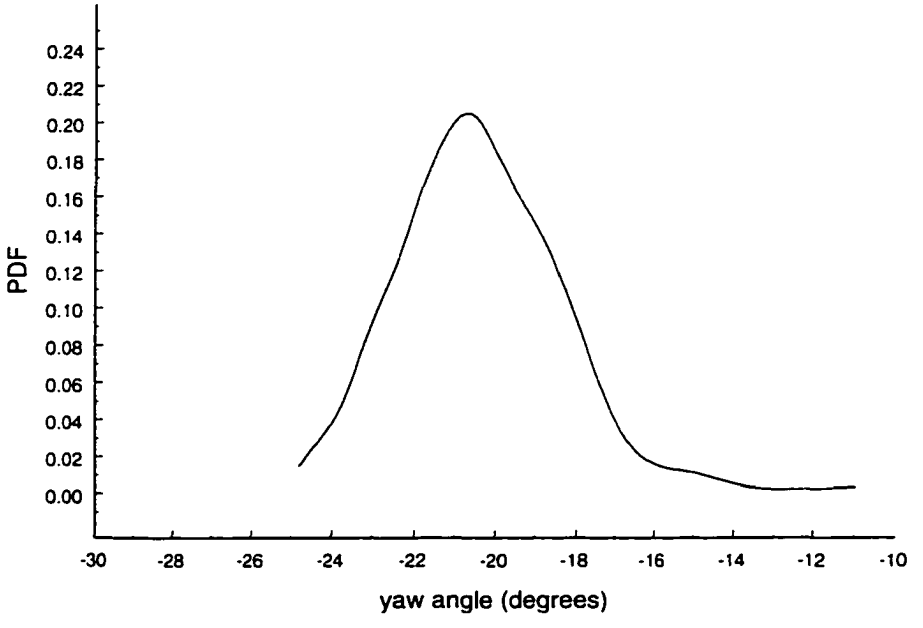

Figure 9.20: PDF of calculated yaw angle before interaction. $M_{inc} = 0.45$.

9.5 Vorticity

9.5.1 Decoupling of Density and Velocity

As it was discussed in section 7.3.1, in order to extract velocity from the mass flux signal and the corresponding total temperature signal, additional information is still require in terms of one of the static properties. This is readily seen from examining the equations that relate velocity and other properties to the measured quantities.

$$\rho u = (\rho u)_m \qquad \rho v = (\rho v)_m \qquad \rho w = (\rho w)_m \tag{9.1}$$

$$\rho Q = (\rho Q)_m \tag{9.1.a}$$

$$T = (T_0)_m - \frac{Q^2}{2C_p} \tag{9.2}$$

$$\rho = \frac{p}{RT} \tag{9.3}$$

Equations 9.1 is an identity relation between measured and actual mass fluxes while equation 9.1.a is an alternate expression making use of the velocity magnitude, Q. Equation 9.2 is obtained from total energy consideration and equation 9.3 is the equation of state. From inspection of the above three equations four unknowns must be solved for. Specifically, static pressure is needed to complete the system of equations. This can be solved by applying the isentropic relation for pressure which provides the following equation,

$$p = (p_0)_m \left(1 + \frac{\gamma - 1}{2} M^2\right)^{\frac{-\gamma}{\gamma - 1}} \tag{9.4}$$

This introduces the measured total pressure which is obtained from a corresponding experiment of the same incident shock strength. The mean total pressure signal can be combined with the mass flux and total temperature signal to provide a correspondence of measured data, and more importantly a complete data set to obtain all pertinent flow properties.

If equations 9.1a, 9.2 and 9.3 are combined a quadratic equation for density is obtained.

$$(T_0)_m \rho^2 - \frac{p}{R}\rho - \frac{1}{2C_p}(\rho Q)_m^2 = 0 \tag{9.5}$$

This equation contains two unknowns density, ρ and static pressure. p. An iterative numerical scheme can be set up to find the root of density in terms of an assumed static pressure. The wall mean pressure can be a candidate initial value for the numerical scheme. Once density is obtained, the local Mach number is calculated and then a corrected value for pressure can found from equation 9.4.

An alternate method was also attempted taking advantage of Mathcad's root finding functions. The above quadratic equation can be re-expressed in terms of the Mach number and measured quantities. Note that density and static pressure are both functions of Mach number through isentropic relations. The relation for static pressure is given by equation (9.4), while that for density is given by,

$$\rho = (\rho_0)_m \left(1 + \frac{\gamma - 1}{2} M^2\right)^{\frac{-1}{\gamma - 1}} \tag{9.6}$$

Introducing equations 9.4 and 9.6 into equation 9.5, and after some simplification furnishes a simple sixth order equation.

$$-x^6 + x^5 - C' = 0 \tag{9.7}$$

Where the dependent variable contains the Mach number,

$$x = \frac{1}{1 + \frac{\gamma - 1}{2} M^2} \tag{9.8}$$

and

$$C' = \frac{1}{2C_p (T_0)_m (\rho_0)^2_m} (\rho Q)^2_m \tag{9.9}$$

The total density is obtained from the equation of state using the measured total pressure and total temperature. Equation 9.7 mathematically contains six roots for a particular value of C'. From the resulting roots found it was determined that four of these roots were imaginary and were consequently rejected. The remaining two positive roots distinctly yielded a subsonic and a supersonic Mach number. Therefore, the Mach number is found from the sixth order equation by proper choice of the root. The values of density and velocities follow from the solution of Mach number.

9.5.2 Results of Velocity and Vorticity Data

The vorticity probe was used to study the tip vortex flow which was generated using two different pitched, semi-span, wing models. Measurements were taken in the same manner as that of the 3-Kulite probe. However, unlike the latter probe measurements were concentrated (near) in the vortex center only. The main interest here was to monitor the content and nature of the vorticity since the evolving nature of the vortex structure was analyzed with the previous probes. The probe was placed at an axial position of 7.11 chord lengths downstream from the centroid of the wing model.

The relative velocities among the three signals can be seen in this figure 9.21. There is a substantially normal velocity, v, of the order of 60% of the longitudinal while the spanwise velocity was of the order of 20%. Because of the human factor of placing the probe and the possible meandering state of the vortex, true vortex center measurement could not be assured. In fact it seems that if true center measurements were taken there should only be a strong longitudinal velocity component, which is not the case here. Figure 9.22 shows for comparison all three longitudinal velocities. They all seem to show the same flow pattern. Figure 9.23 and 9.24 combine the longitudinal vorticity and velocity signals for the two Mach numbers investigated. The longitudinal velocity provides the reference time of the shock front arrival. It is obvious that both the velocity and vorticity signals are characterized by substantial increases in fluctuations, but more so on the vorticity signal. There is an initial low frequency oscillation right after the interaction for about 1 ms which is most likely due to vortex distortion or unsteadiness, but higher frequencies reappear shortly after.

Compared to the longitudinal velocity and vorticity signals of grid turbulence, these fluctuations are considerably greater, although more so after interaction. In fact, it

was shown with the turbulence data that the rms of ω_x was affected very little by the interaction. Thus it seems concentrated vortices are affected more by the interaction than the smaller eddies found in homogeneous turbulent fields. It is likely that the shock front is locally highly distorted, and unsteady, as interacts with the vortex and therefore it enhances the turbulence in the vortex. Also, vortex breakdown might be imminent, and the vortex is in a state of transition to the vortex breakdown stage after interacting with the shock.

Figure 9.25 and 9.26 provide spectra of the longitudinal vorticity signals. Figure 9.24 shows significant energy residing at a the low wavenumber range, below a value of k_1C of 40, before interaction with the shock wave, and a larger range below k_1C of 100 after interaction. The higher Mach number case also shows energy contained in these two ranges, however, more importantly it shows a high spectral amplitude band centered about $k_1C = 25$ before interaction, and two peaks at $k_1C = 8$ and $k_1C = 40$ after interaction. These value are transformed to the corresponding wavelength dimension which are of the order of .25 of the chord length before interaction, and .15 and .78 after interaction. The wavelength found before interaction seems to correlate with the frontal width of the pitched wing model, 15^0 pitch. This width tends to dictate the size of the trailing tip vortex. Therefore it seems that the vortical scales of the flow are readily picked up by the vorticity probe.

Figure 9.27 shows the stretching signal $\omega_i s_{ij}$, associated with longitudinal vorticity. The arrival of the reflected shock is indicated for reference. A dramatic change in the nature the signal occurs after interaction. As can be seen from the figure, before interaction, the large amplitude high frequency spikes indicating strong stretching events

of about the same strength occur quite frequently. After interaction, the signal is characterized by more quiescent periods. However, there are stronger stretching events, although more infrequent, during the initial stage after interaction and subsequently weaken at later stages. This points to very rapid structural changes taking place after interaction.

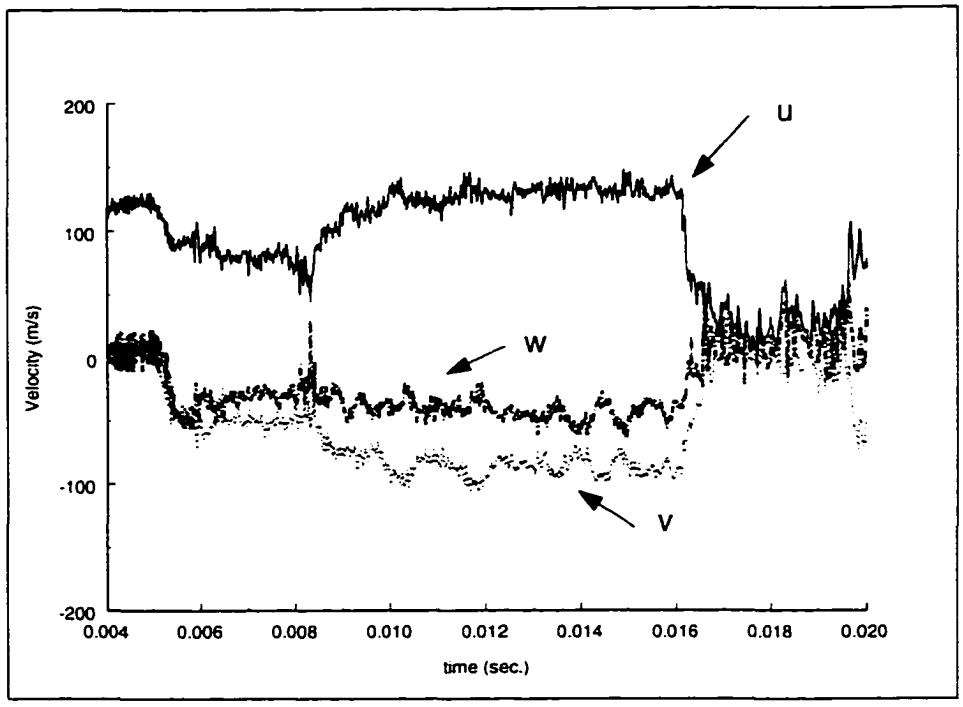

Figure 9.21: The three components of velocity obtained from one triple wire set.

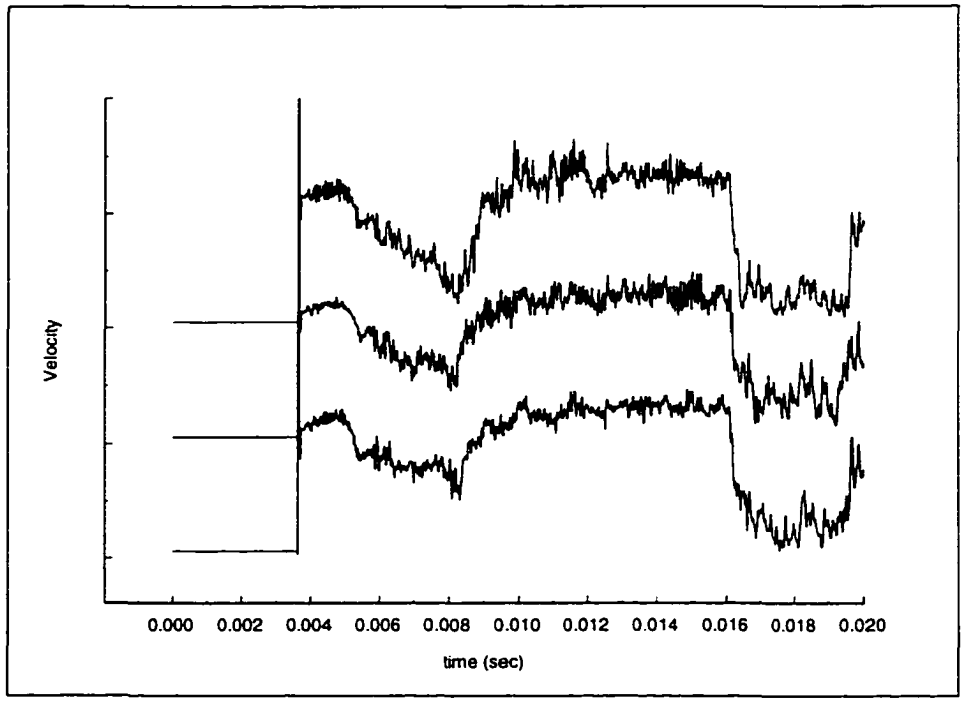

Figure 9.22: All three longitudinal velocities obtained from the three triple wire sets.

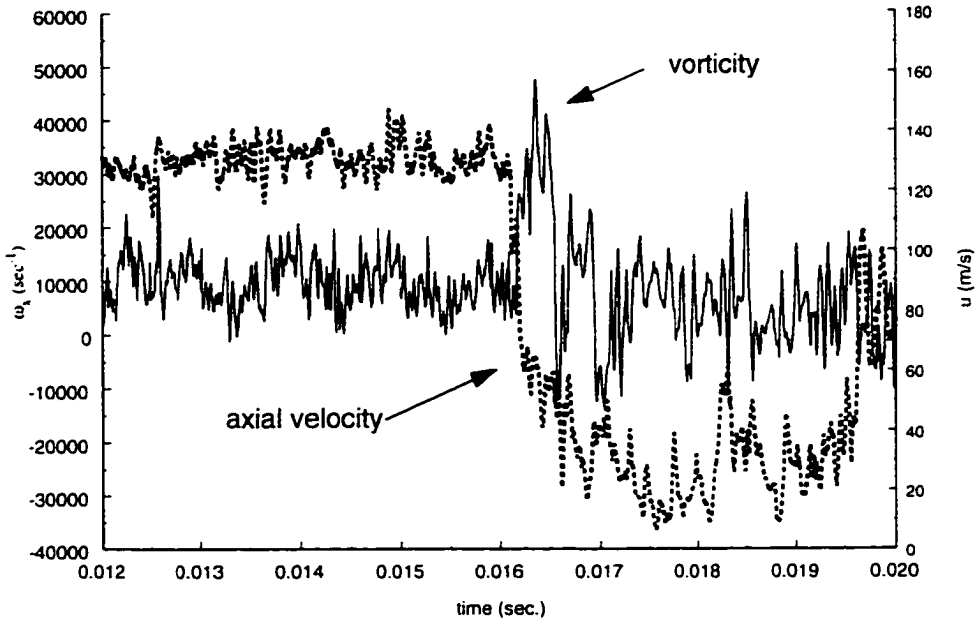

Figure 9.23: Combined longitudinal vorticity and velocity across the interaction. M_{inc}=0.31

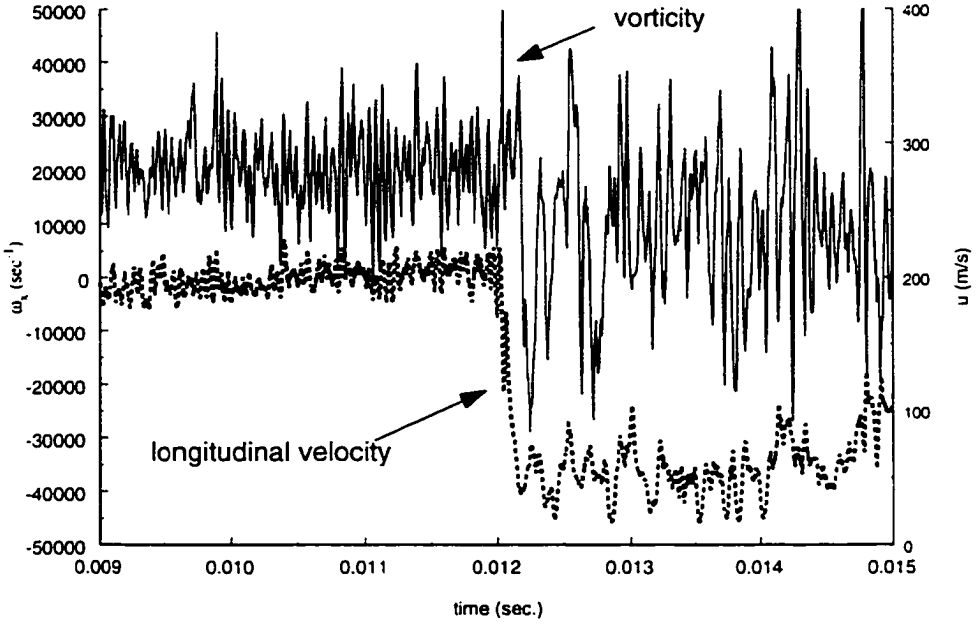

Figure 9.24: Combined longitudinal vorticity and velocity. M_{inc}=0.45.

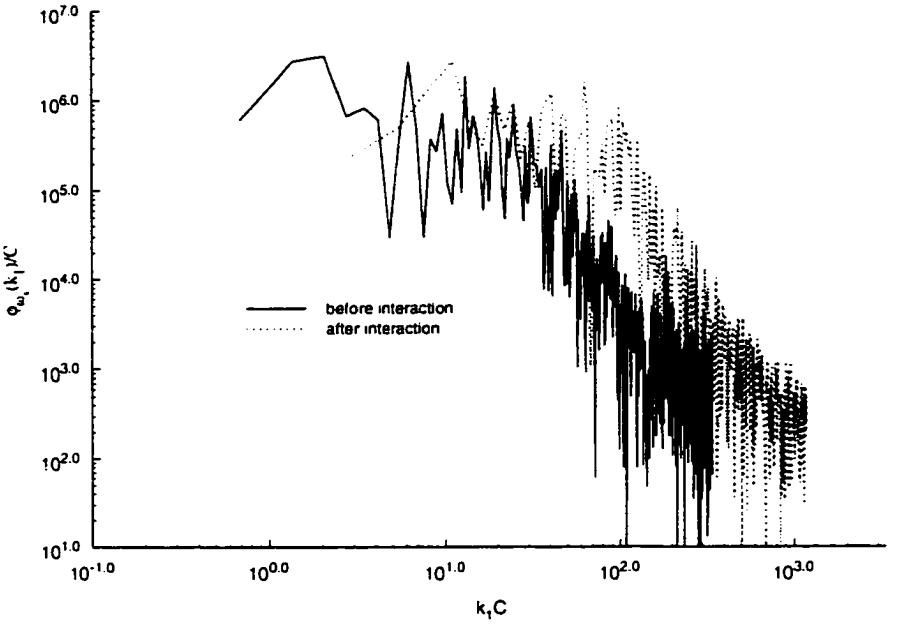

Figure 9.25: Vorticity wavenumber spectrum of the tip vortex flow before and after interaction. M_2=0.31.

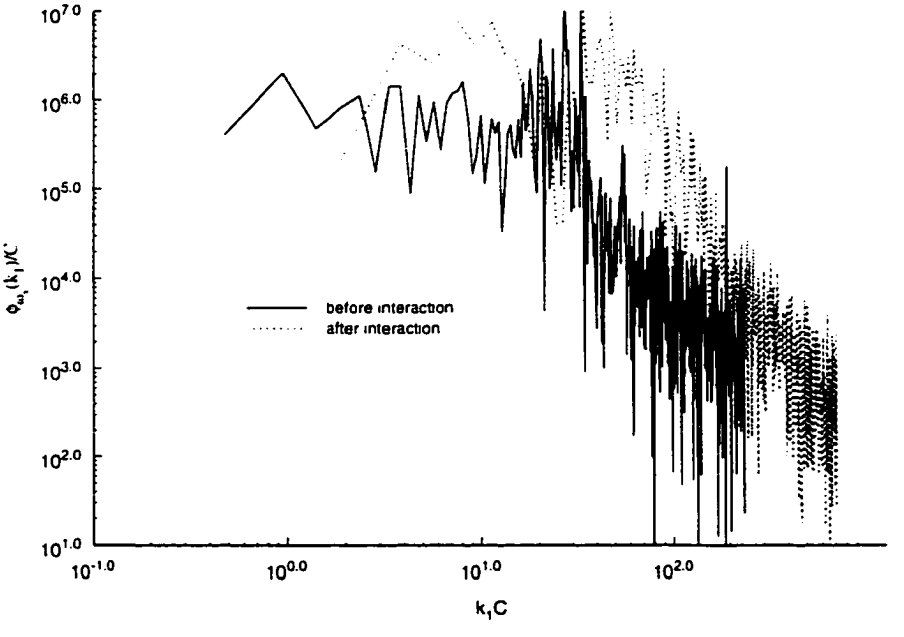

Figure 9.26: Vorticity wavenumber spectrum of the tip vortex flow before and after interaction. M_2=0.45

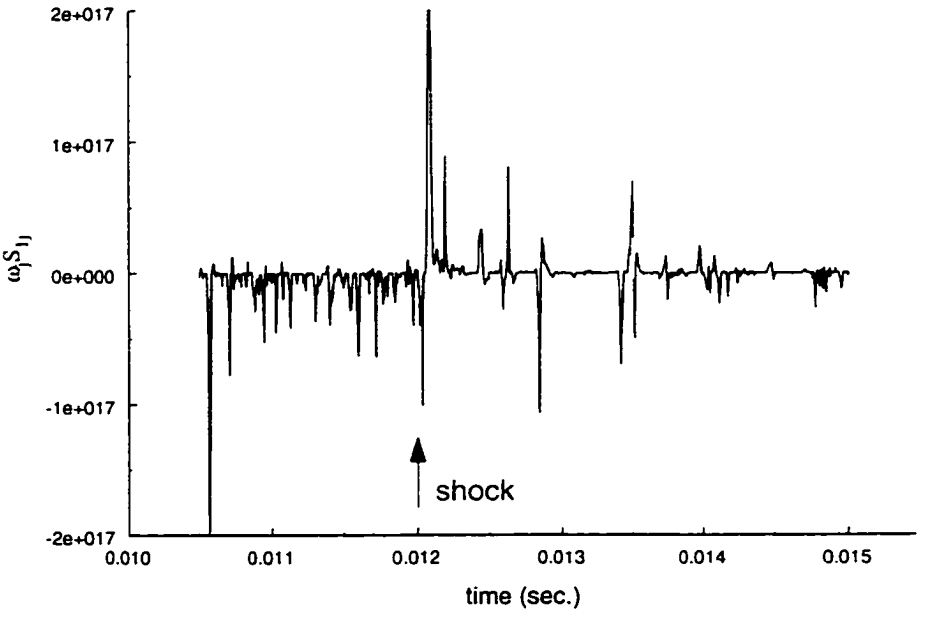

Figure 9.27: Stretching signal, $\omega_i s_{ij}$, for $M_{inc} = 0.45$ interaction.

9.6 Particle Flow-Visualization

The flow visualization images utilizing solid particles are presented in figures 9.28 and 9.29. The images show the cross-section in the axial direction of the tip vortex flow. Figure 9.28 shows the structure of the vortex before it has interacted with the reflected shock. The flow is from top to bottom. The distinguishing features are: (1) a narrow region void of any particles running down the center, (2) this narrow region has very nearly straight boundaries, (3) the appearance of varying size vortical structures on either side of the void region. The void region can be said to reflect the size of the vortex which was estimated to be 10 mm. The next figure, figure 9.29, was one of the more fortunate shots taken of the vortex interacting with the shock wave. First of all it is very difficult to pick up shock waves with techniques relying solely on particle entraiment. Shock waves are efficiently picked up, for example, in Schlieren and Shadowgraph techniques which rely on density changes. This impressive image clearly shows how the vortex core grows after the interaction. The growth, however, is not that rapid with an initial core growth after transmission through the shock of approximately 15°.

Figure 9.28: Particle flow-visualization image of the axial cross section plane of the vortex core produced by the 15° pitched semi-span wing before interaction with the shock

Figure 9.29 Particle flow-visualization image of axial cross section plane of the tip vortex core produced by the 15o semi-span wing after during interaction with the shock.

Chapter 10

10. Results & Discussion III - Shock Wave/Spanwise Vortex Interaction

This chapter presents the results obtained on the shock wave and spanwise vortex interaction. A full span wing pitched at 10° with end plates and a 177.8 mm chord was used in this analysis to create relatively large vortex. A table of pertinent experiments and operating conditions are given in Table 10.1 below.

No.	Wing model	Probe(s)	Probe position X/C	p_2/p_1	M_r	Porous wall
1	10° f-s wing	3-K	24	1.89	0.436	no
2	10° f-s wing	3-K	24	2.4	0.589	no
3	10° f-s wing	3-K	24	3.13	0.753	no
4	10° f-s wing	3-K	24	2.42	0.54	no
5	10° f-s wing	3-K	24	1.83	0.414	yes
6	10° f-s wing	3-K	24	2.39	0.587	yes
7	10° f-s wing	3-K	24	2.63	0.647	yes
8	10° f-s wing	3-K	24	1.64	0.342	no
9	10° f-s wing	vorticity	24	1.91	0.442	no
11	10° f-s wing	vorticity	24	1.72	0.373	yes
12	10° f-s wing	vorticity	24	1.99	0.469	yes

legend: f-s, full-span; 3-K: 3 Kulite probe

Table 10.1: Experiments performed on the shock wave/spanwise vortex interaction.

Figure 10.1 shows a sketch of probe and light sheet setup used in the experiments involving the spanwise vortex. The reader will be referred back to these sketches in subsequent sections.

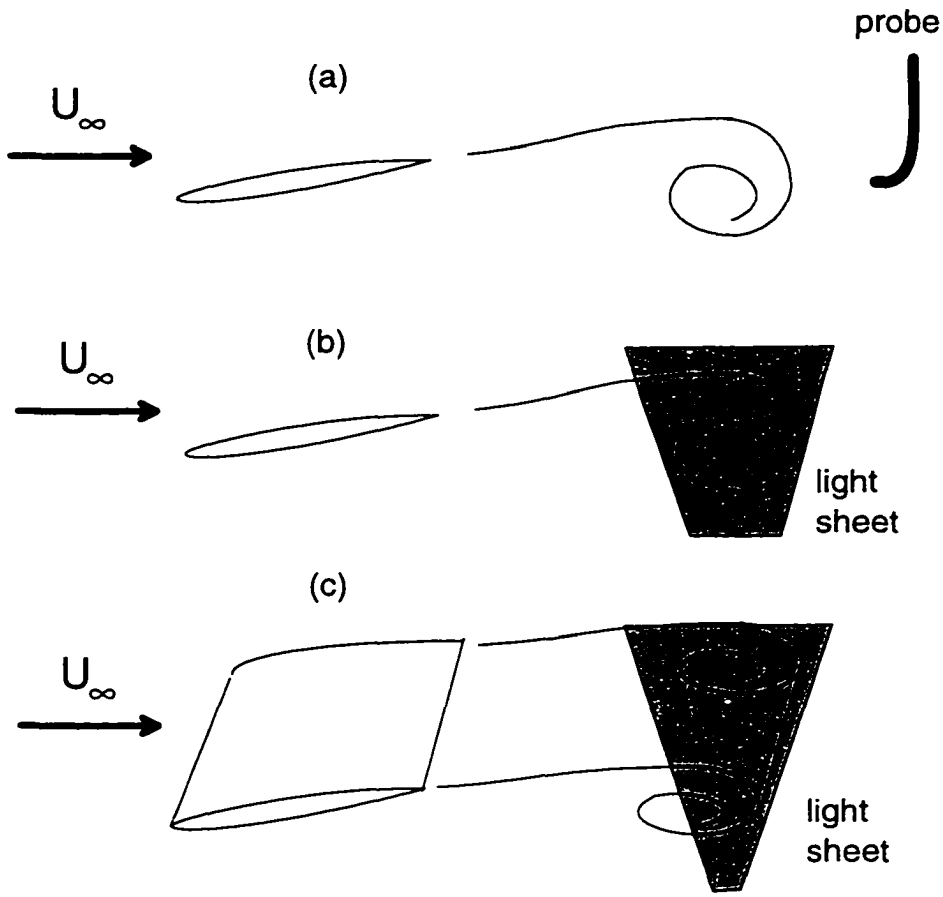

Figure 10.1: Sketch of starting vortex generated by the pitched wing model during (a) vorticity experiment, (b) flow-visualiztion experiment for cross-sectional image of vortex, (c) flow-visualization experiment for image along span of vortex.

10.1 Capturing the Interaction

As it turn out in this interaction, trying to capture the instance of the passage of the shock through the convecting vortex structure as it was being sensed by the probe became an unfeasable goal. Rather the effect of the interactions were compared on different experimental runs, one with interaction and one without. One experiment was performed without the porous wall in which case there was no reflective shock wave, and

one experiment with the porous wall to produce an interaction. Measurements were taken far downstream, on the last port which placed the probe sensing area one foot in front of the last flange of the shock tube. This was done in order to allow a comparison of the vortex flow with and without interaction effects on the same axial location. The former require placing the probe as close to the end wall as possible in order to assure the shock wave interacts with the vortex upstream of the flow.

To avoid the immediate upstream propagation of expansion waves produced from an open ended shock tube open, a dump tank with a initial pipe entrance length of 2 ft. was attached to the shock tube. Thus, this allowed more sampling time before the expansion waves reached the measurements locations.

Mass flux signals shown in figures 10.2 and 10.3 show the two different scenarios described above.

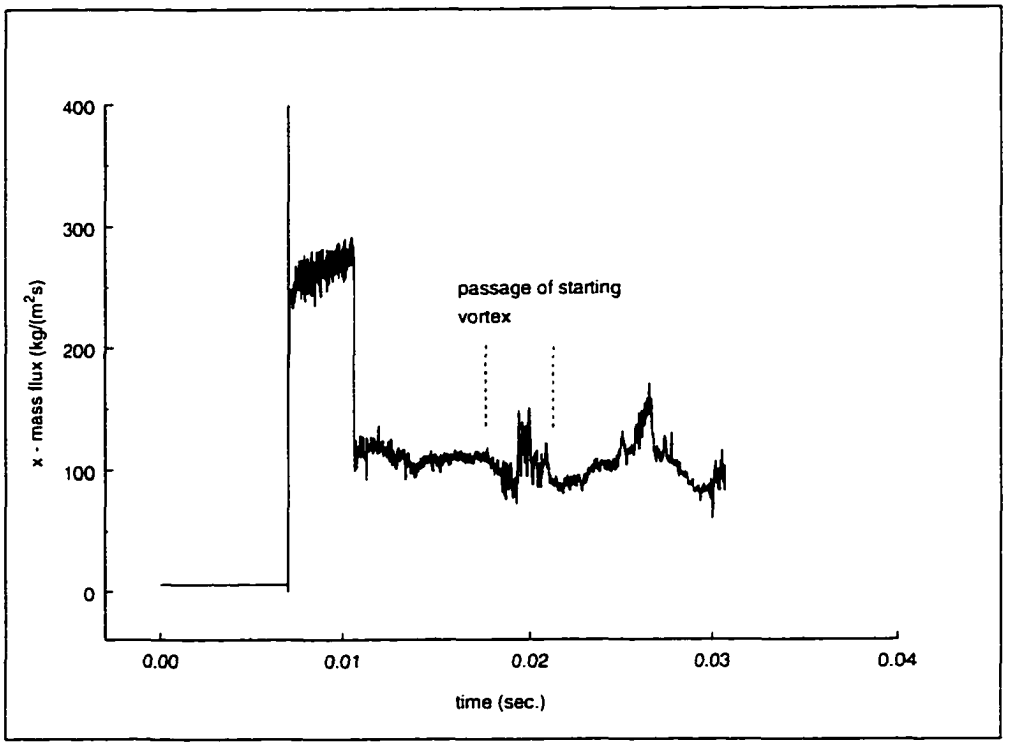

Figure 10.2: Mass flux signal showing a vortex which has gone through the shock wave

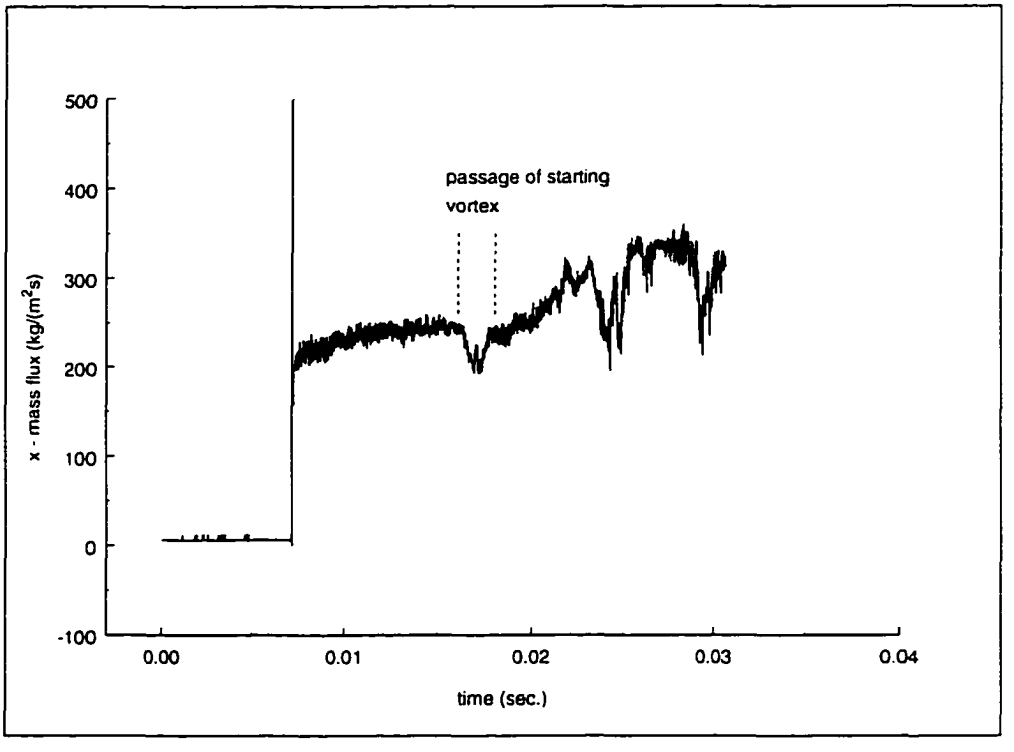

Figure 10.3: Mass flux signal showing a vortex being sensed before the arrival of the expansion waves.

10.2 Total Pressure Probe

The Kulite rake probe was used to monitor total pressure through the vortex. The starting vortex is clearly sensed by a drop in total pressure. The drop in most cases is very nearly symmetric. Figure 10.4 shows the mean profiles of total pressure before the vortex has interacted with the reflected shock. The profiles were obtained by taking the time history of the each signal during passage of the vortex and applying a Galelian transformation to obtain a longitudinal profile. Fluctuations were removed by applying a curve fit to the fluctuating signal. The vortex was assumed to convect with the surrounding free stream velocity, which was found from 1-D normal shock wave theory using the shock strength.

The deficit in total pressure clearly increases with incident Mach number. It is also evident that the size of the vortex seems to grow from the lowest mach number case to the highest. For the higher Mach numbers the total pressure seems to be concentrated in a smaller region near the center of the vortex. This most likely points to a more tightly wound vortex.

After the interaction, figure 10.5, the vortex has definitely undergone a significant transformation. The vortex seems more diffused and is characterized by a less pronounced deficit. There is still a Mach number dependence. The profiles in figure 10.5 have again been identified by the corresponding incident Mach number in order to form a basis of comparison with profiles obtained before interaction. Another feature of these profiles is that they are not well defined as those of figure 10.4. There seems to be a constant total pressure layer which extends for about 100 mm in the internal part of the vortex.

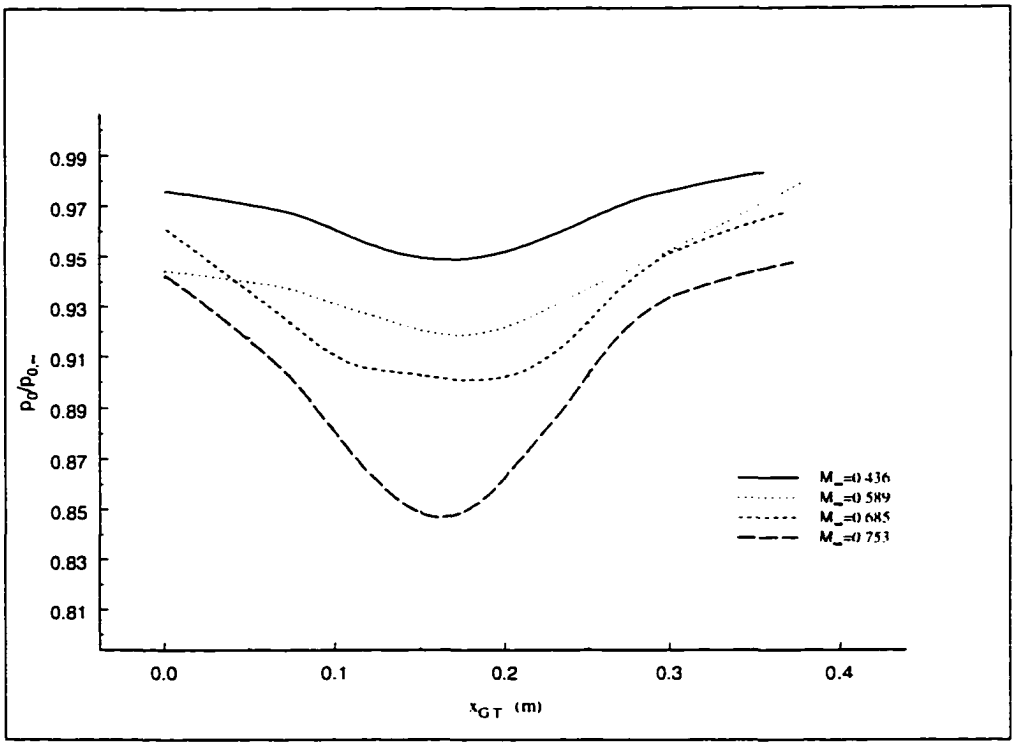

Figure 10.4: Total pressure profile of uncompressed starting vortex.

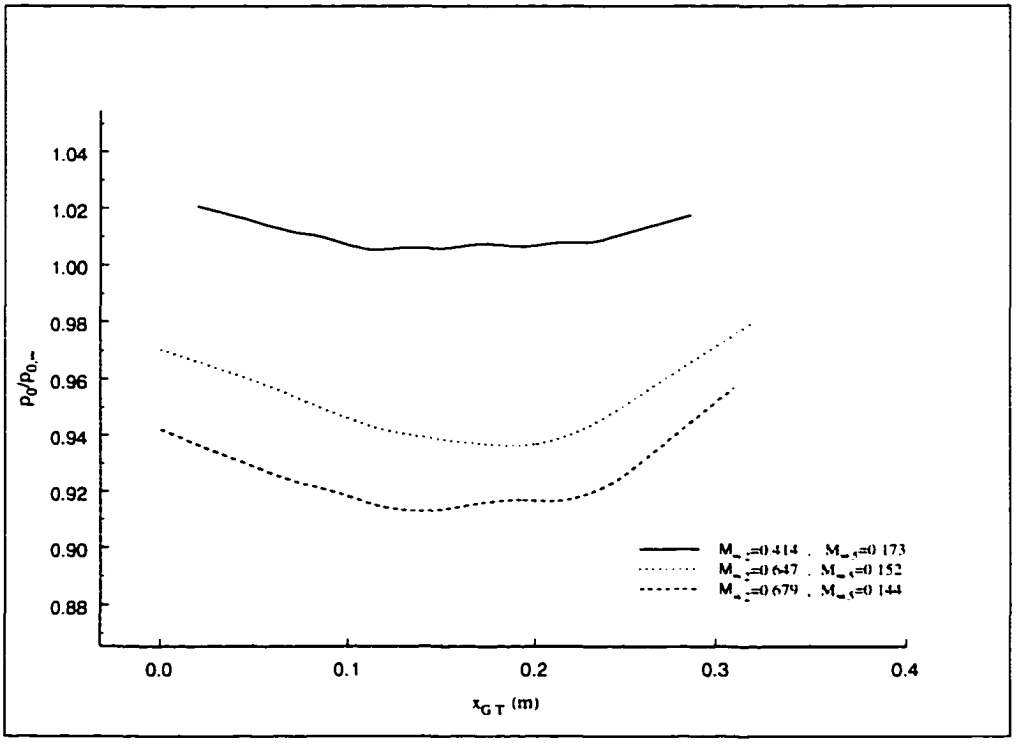

Figure 10.5: Total pressure profile of compressed vortex.

10.3 Velocity and Vorticity Signal

This section will describe the spanwise vortex in terms of the velocity and vorticity signals. Decoupling of the density and velocity of the mass flux signal obtained through the hot-wire data of the vorticity probe was achieved in the same manner as that of the tip vortex/steamwise vortex flow covered in section 9.5.1. The model was oriented such that the starting vortex's axis of rotation was oriented along the negative z-axis, thus tending to produce a negative ω_z component. A sketch of the flow field is shown in figure 10.1. The probe then senses a downwash, negative v, velocity, followed by an upwash, positive v. velocity.

Figures 10.6 to 10.9 present the velocity and vorticity signals of the lower incident Mach number case without shock wave interaction. The velocity signals show a high speed longitudinal velocity which experiences a velocity deficit of about 15% of the incoming longitudinal velocity. This deficit is likely due to the fact that the probe traverses the vortex as it convects downstream at an off vortex center position. The normal velocity shows as expected a downwash followed by an upwash, although the downwash seems to be stronger. The spanwise velocity seems to be centered about zero for the whole traverse. The three velocity signals at this lower Mach number case seem to be well structured and possess moderate fluctuations. The normal velocity seems to have more enhanced fluctuation during the downwash stage.

The vorticity of figures 10.7 - 10.9 indicate that vorticity carries substantially more high-frequency fluctuation than does velocity. On the other hand, the streamwise vorticity seems to show an almost constant positive value and the spanwise shows an

initially positive value followed by a significant decrease during the later stage. The mean trend in the normal and spanwise vorticity requires some interpretation. From velocity signals, shown in figure 10.6, it is shown that during the initial stage of the flow the normal velocity starts at a slightly negative value and then goes to larger negative value, while the longitudinal and spanwise components remain constant. Recalling the definition of the spanwise of vorticity

$$\omega_z = \frac{\partial v}{\partial x} - \frac{\partial u}{\partial y} \tag{10.1}$$

where $\partial/\partial x$ can be obtained from the time derivative using $-u\partial/\partial t$. It is clear to see that ω_z is dominated by a $-\partial v/\partial t$ term (the other component was found to be negligible during this initial stage). Therefore as v increases in negative value with time ω_z will grow positively until v reaches its maximum negative value, at which time the longitudinal velocity starts to change and starts to contribute to spanwise vorticity.

A mechanism that can explain the existence of streamwise vorticity is based on the well known structure of rolls and ribs found in two dimensional shear layers which are separated from sharp edges normal to the flow. The ribs and rolls form a network of spanwise vortical structures, rolls, connected by counter-rotating longitudinal vortices, the ribs. It is very likely that these vortical structures survive in the vortex sheet as the vortex propagates downstream. The presence of these ribs will then account for the measured mean streamwise vorticity component. This concept is confirmed through the images obtained from the Particle-Flow visualization.

During the initial downwash stage of the uncompressed vortex the fluctuations are about twice that of the later stage. This is due to the larger fluctuations found in normal velocity during this stage. This points to an asymmetric vortex structure with enhanced vortical activity on the leading portion of the vortex. More insight is provided subsequently through visualization images.

The higher Mach number case, figures 10.10 - 10.13, without interaction shows very similar trends in all the signals except for a slight distortion manifested by a local rise in spanwise velocity. This indicates that the vortex structure changes with incident Mach numbers.

The picture changes significantly after the vortex has interacted with the reflected shock wave. Figures 10.14 to 10.21 present the signals after the interaction. The first visual indication of the signal is that of impressive distortion near the center of the vortex. A significant spanwise velocity component is now present which brings about drastic changes in the streamwise vorticity component. Tremendously high amplitude fluctuations in ω_x are now seen in the corresponding distortion region of the vortex.

The effects are just as drastic on the normal and spanwise vorticity components. The negative mean trend in ω_z is now masked by very substantial vorticity fluctuations. A possible flow structure that can be inferred from these results is that of a highly distorted vortex whose rotational axis has become tilted with possible precessing. An estimate of the vortex core size can be obtained from the alternating normal velocity signal. If the time gap between the maximum negative and maximum positive values are used as a reference of the tangential velocities, and then the time gap multiplied by the convection velocity of the vortex produces the longitudinal dimension. The lowest Mach number

case in figure 10.6 is the most suitable to obtain this dimension, since all other vortex flows (including the higher Mach number case without interaction) contain vortex distortion to varying degrees which also distort the normal velocity signature. The estimate from figure 10.5 is a core radius size r/c = .08. This value seems slightly large in comparison to other reported values of the which are of order of r/c .02 to .06 (Lee and Bershader, 1994). This is possibly due to the longitudinal distance the vortex has to travel 24 chord lengths before it is measured, which tends to diffuse the vortex.

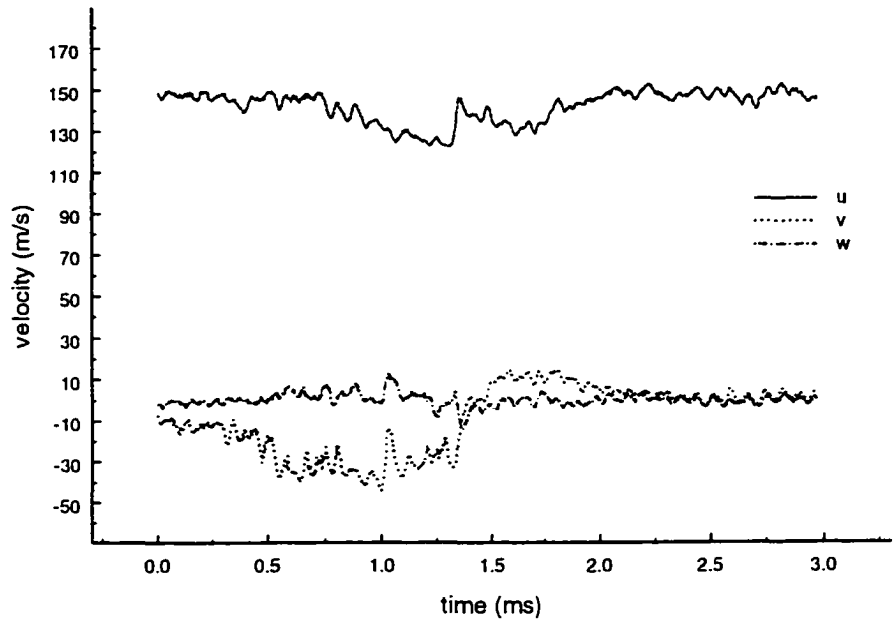

Figure 10.6: Velocity signals. M_∞=.442 (no shock)

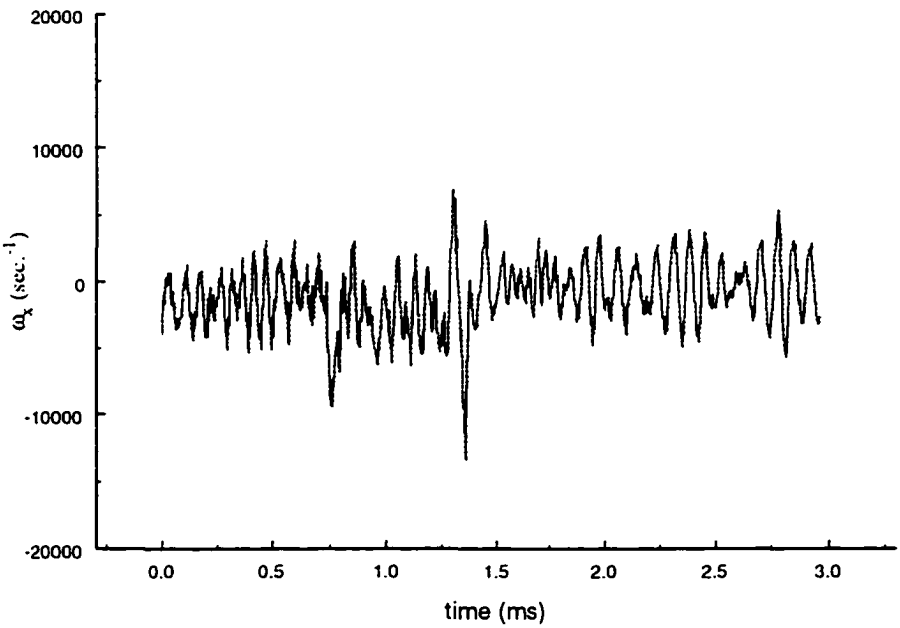

Figure 10.7: Longitudinal vorticity signal. M_∞=.442 (no shock)

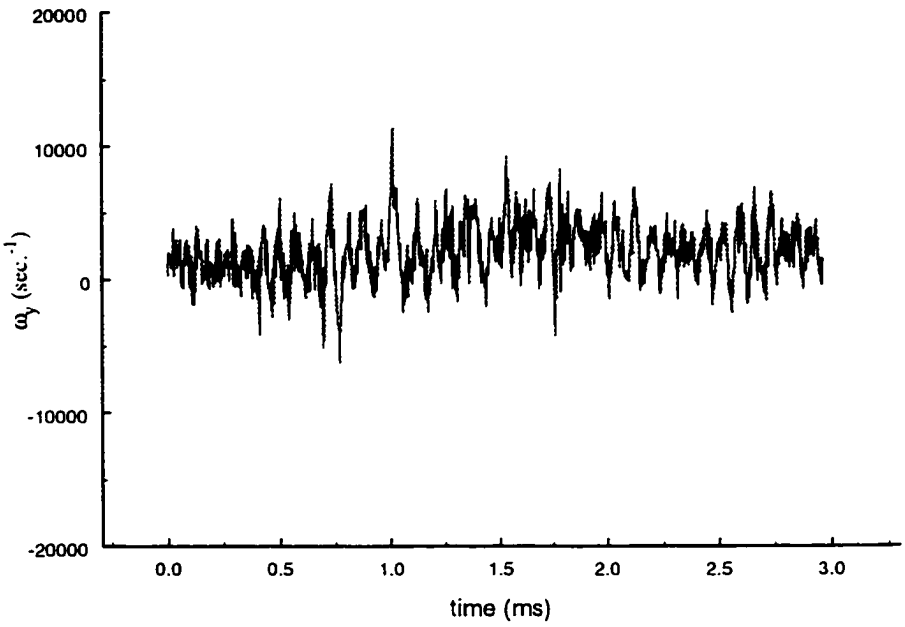

Figure 10.8: Normal vorticity signal. M_∞=.342 (no shock)

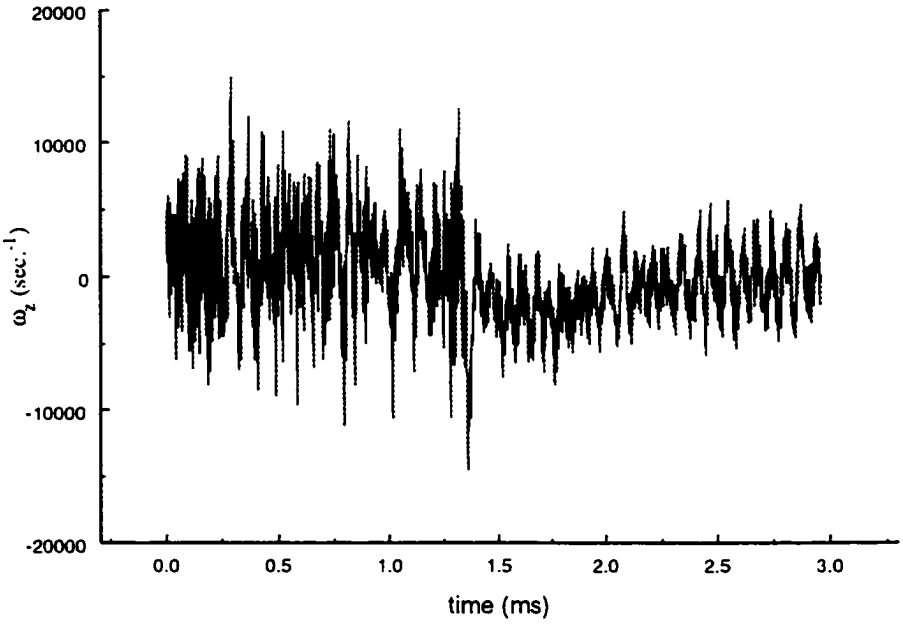

Figure 10.9: Spanwise vorticity signal. M_∞=.342 (no shock)

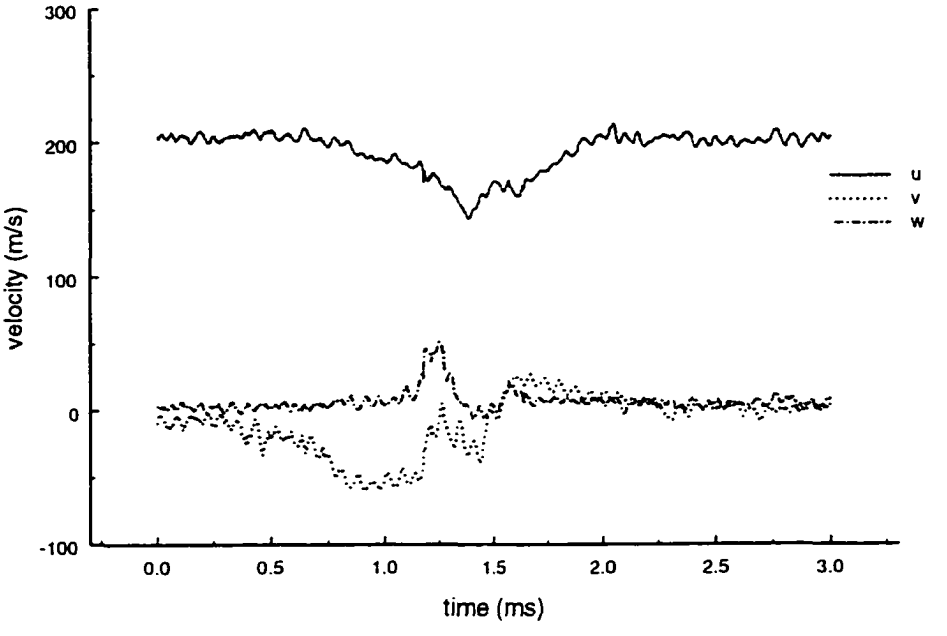

Figure 10.10: Velocity signals. M_∞=.442 (no shock)

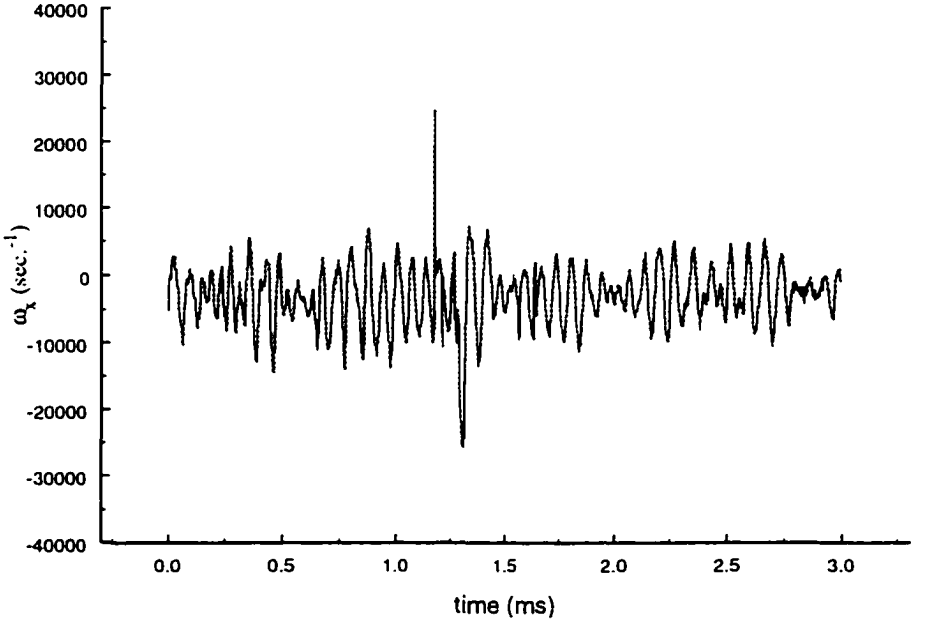

Figure 10.11: Longitudinal vorticity signal. M_∞=.442 (no shock)

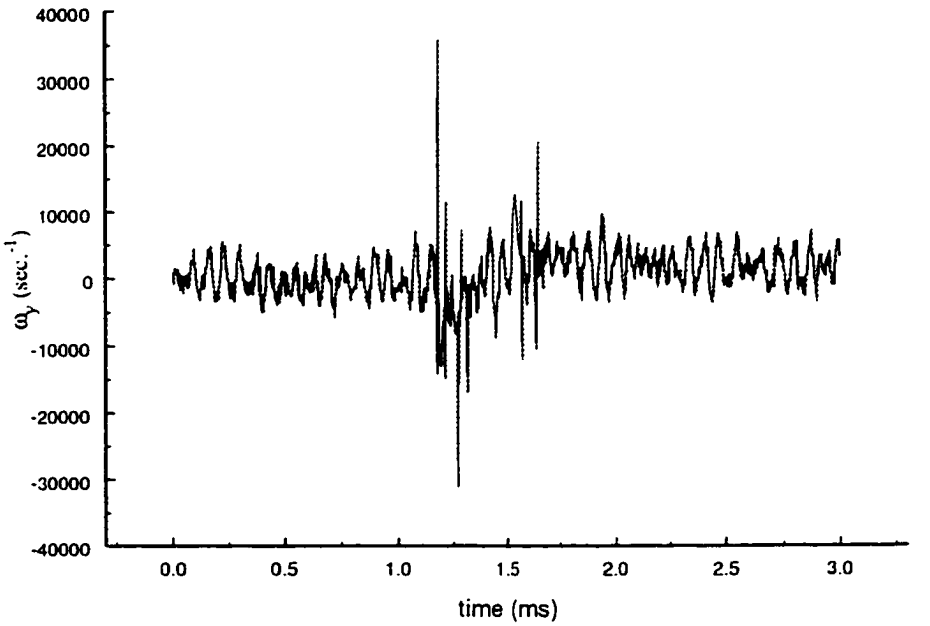

Figure 10.12: Normal vorticity signal. M_∞=.442 (no shock)

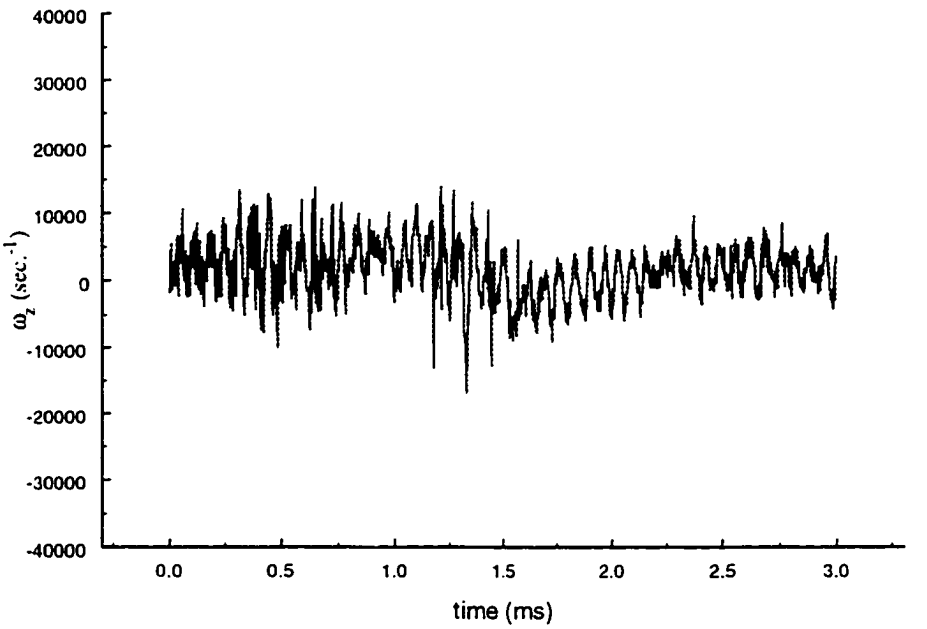

Figure 10.13: spanwise vorticity signal. M_∞=.442 (no shock)

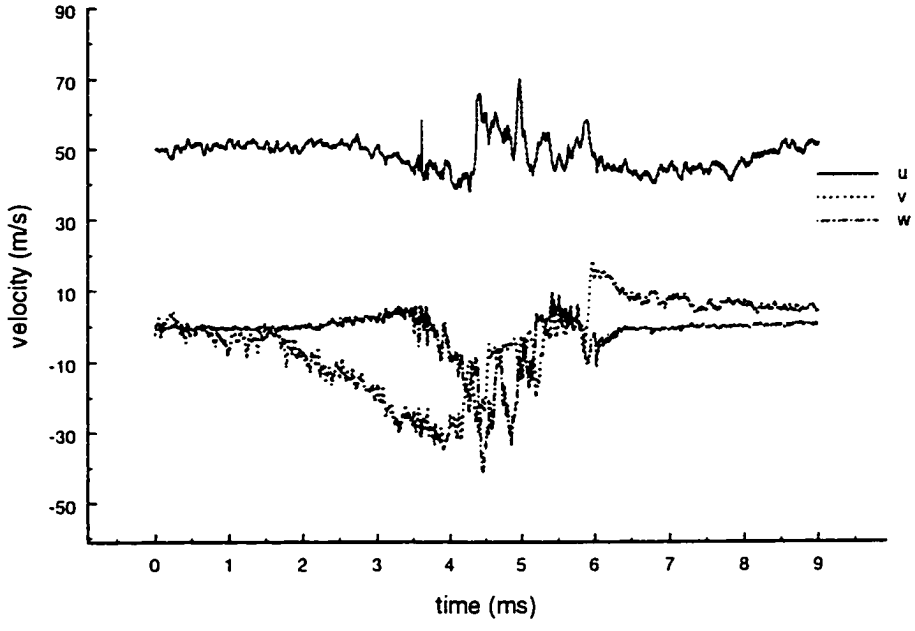

Figure 10.14: Velocity signals after interaction. M_∞=.373

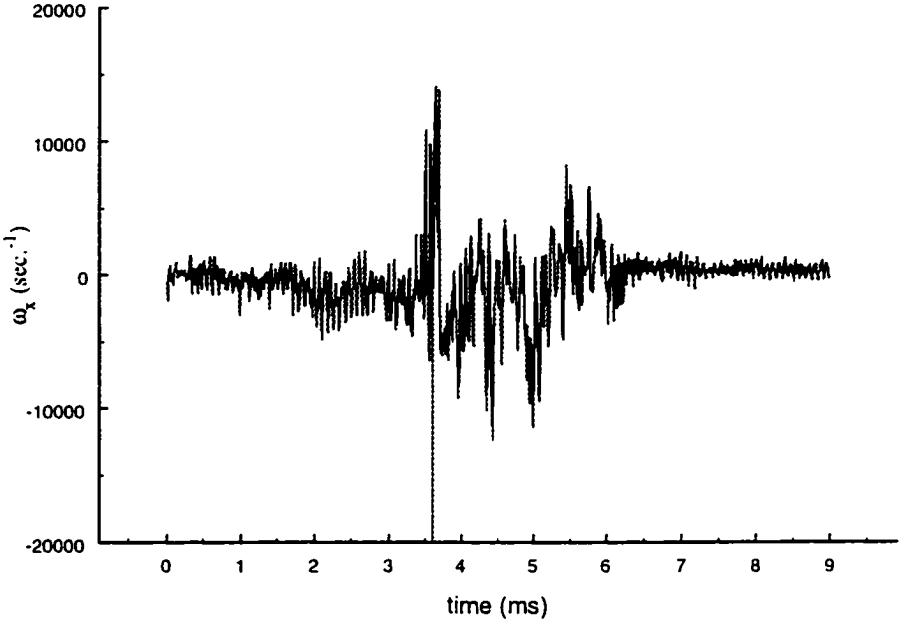

Figure 10.15: Longitudinal vorticity signal after interaction. M_∞=.373

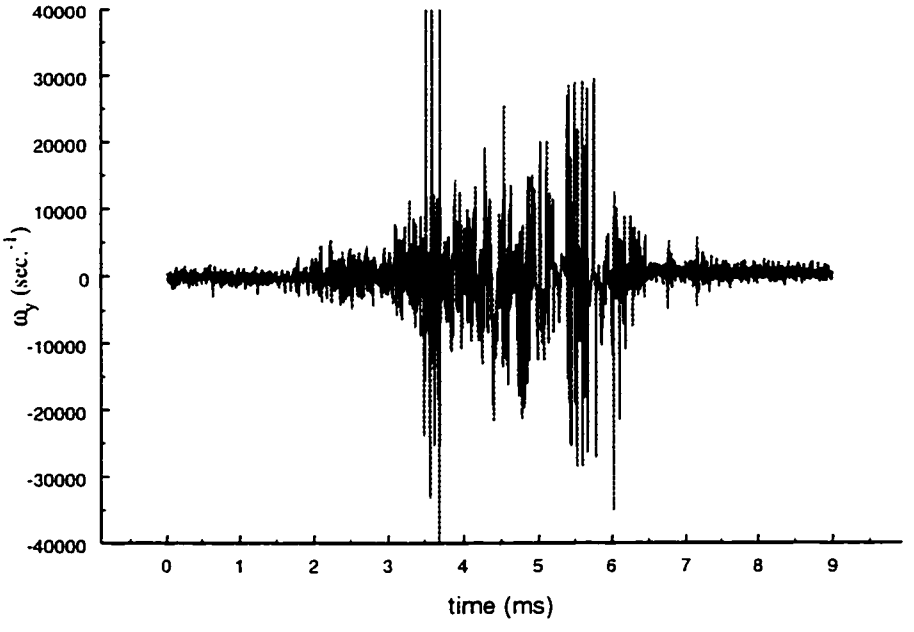

Figure 10.16: Normal vorticity signal after interaction. M_∞=.373

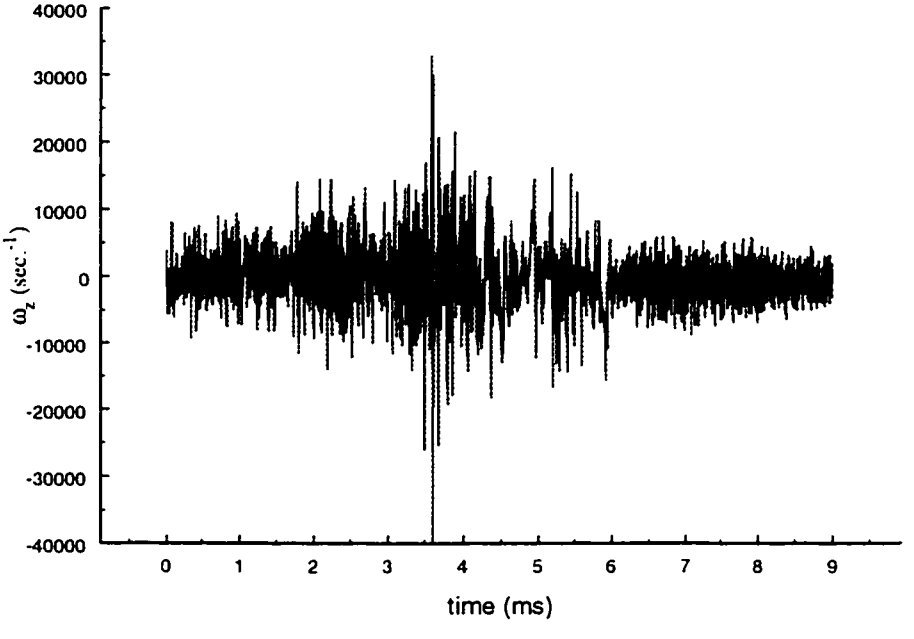

Figure 10.17: Spanwise vorticity signal after interaction. M_∞=.373

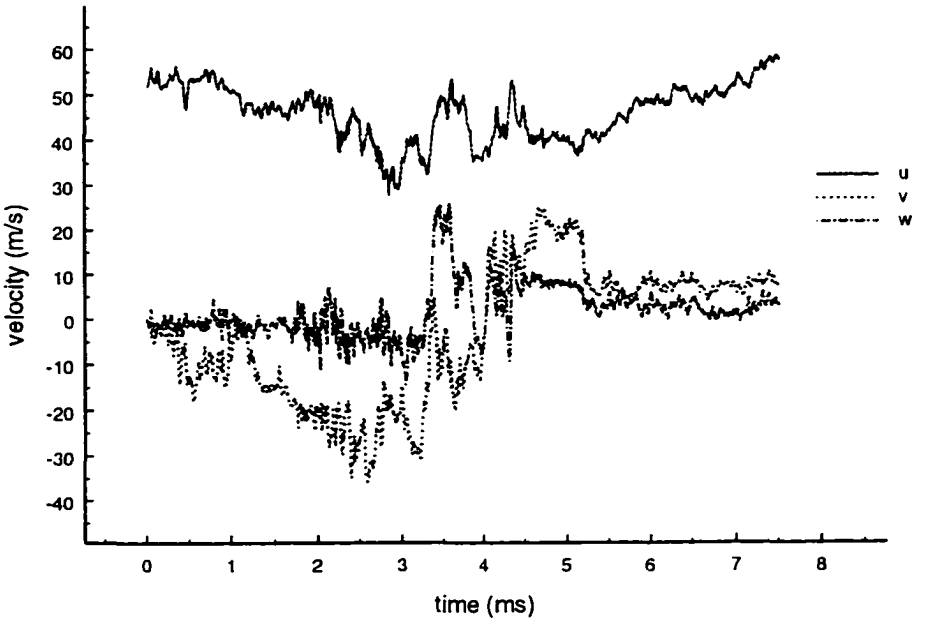

Figure 10.18: Velocity signals after interaction. M_∞=.469

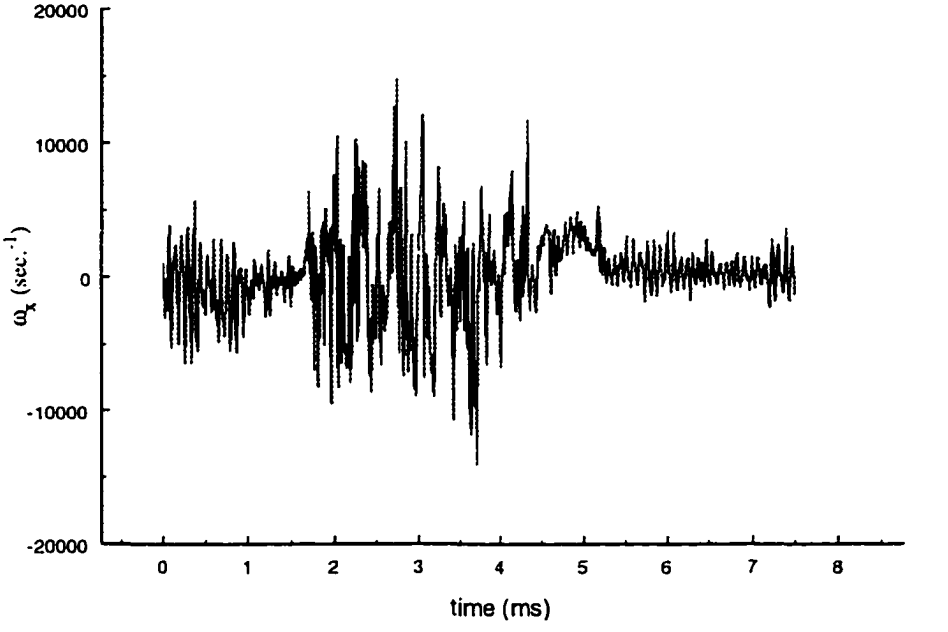

Figure 10.19: Longitudinal vorticity signal after interaction. M_∞=.469

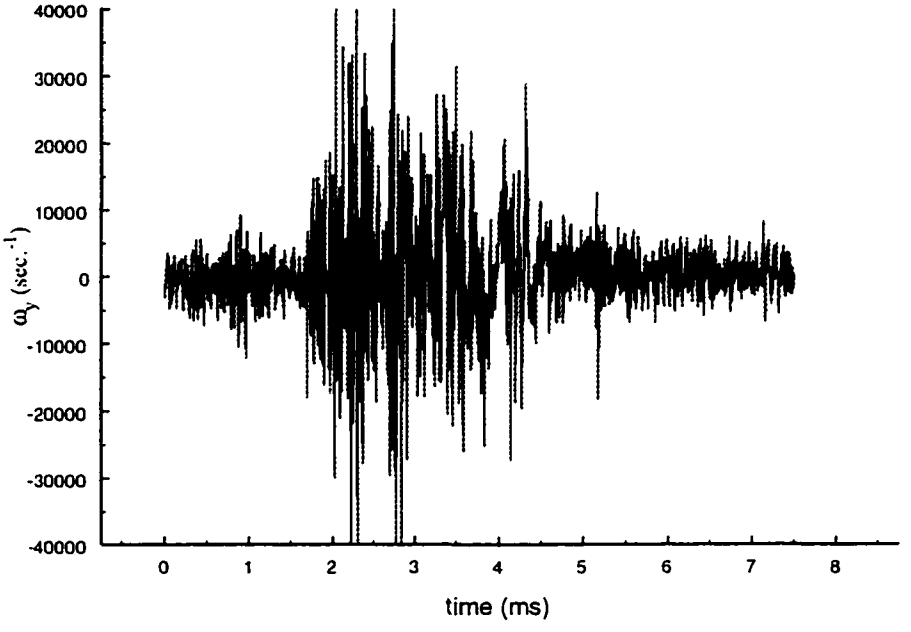

Figure 10.20 : Normal vorticity signal after interaction. M_∞=.469

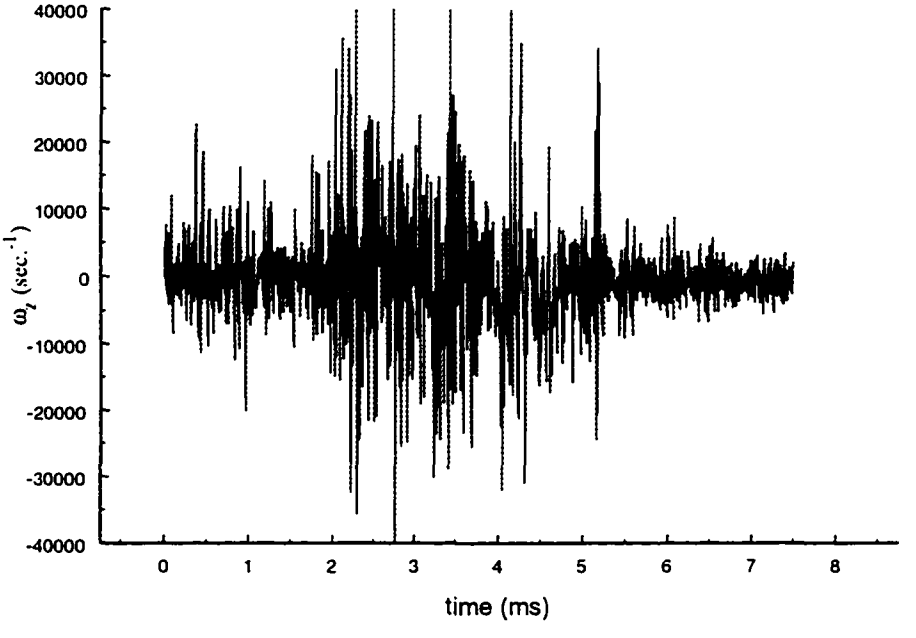

Figure 10.21: Spanwise vorticity signal after interaction. M_∞=.469

10.4 Particle Flow Visualization

Images of the starting vortex were also generated through the Particle Flow Visualization method. However, for the same reason that the vorticity measurements through the interaction proved too overwhelming, trying to capture the interaction soon became a more impossible task.

However very revealing images were captured of the uncompressed (no shock interaction) vortex. Figure 10.22 shows four images of the vortex structure as it came into view of the camera. This is no coincidence, though, as the laser had to be triggered at the proper instance in order to capture these images (see section 5.4.4 for details on the triggering of the laser). These images show a very structured vortex with distinct vortical patterns. The leading part (the vortex convects from right to left) shows a spiral like pattern which seems to be ejecting particles as it rotates. The trailing part, on the other hand, shows the particles entrained in a very thin inward spiraling layer. This part of the structure seems to be cleaner and solid body rotation seems to dominate. Solid body rotation tends to have a stabilizing effect which suppresses the turbulence.

The last image, figure 10.23, was taken through a spanwise cross-section of the vortex (see figure 10.1c) revealing the structure along the length of the starting vortex. It very impressively shows that the vortex sheet is made up of longitudinal structures which are slightly tilted from the streamwise direction. As it was mentioned in the previous section, these structures are most likely rolls which originate on the shear-layer shed from the wing trailing edge. Evidence of these rolls is also seen in the previous images, figure 10.22, as the thin layers rolling into the trailing part of the vortex. Another scenario is that

Görtler vortices might be induced as the vortex sheet rolls over into the vortex and encounters strong tangential velocity gradients.

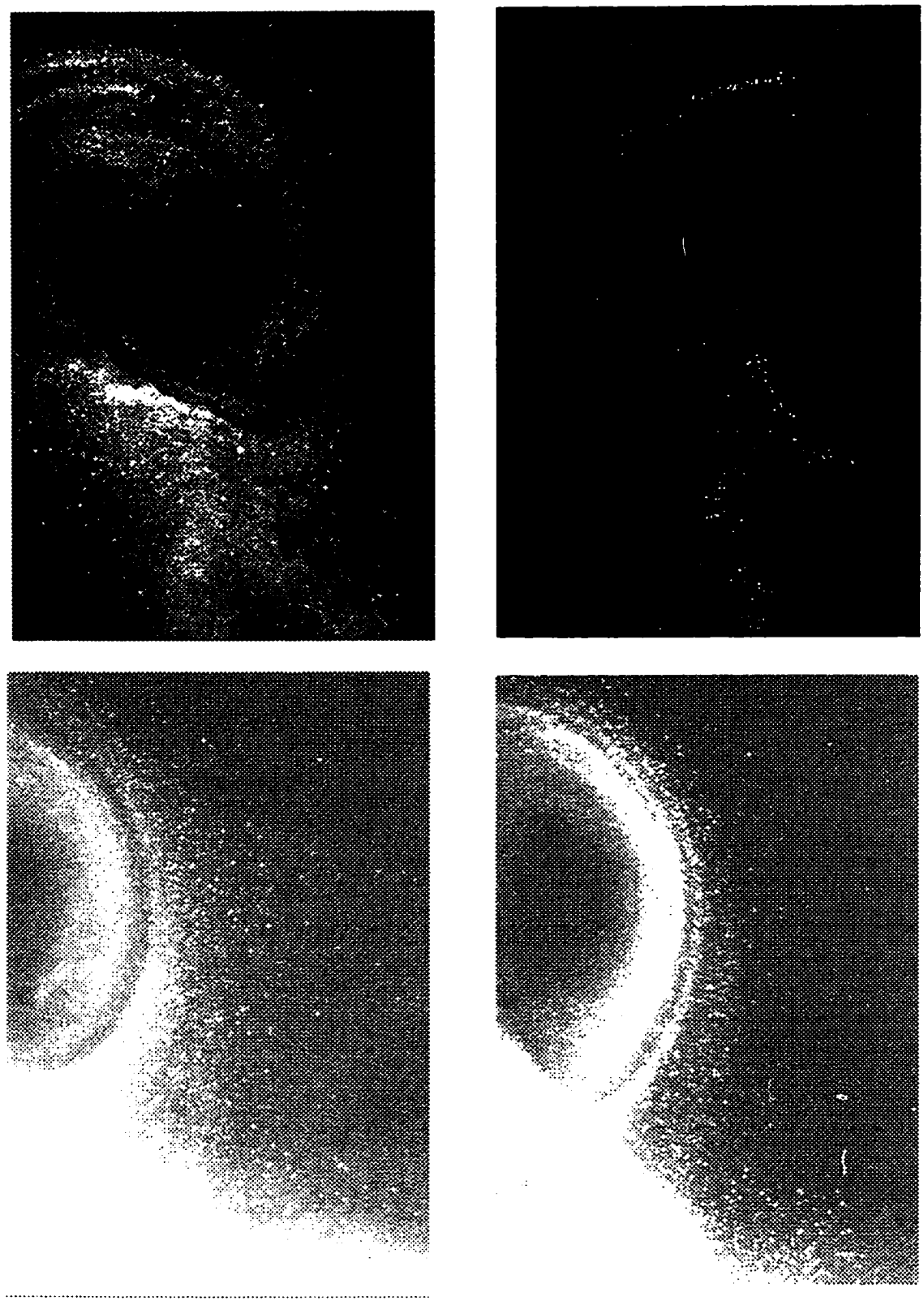

Figure 10.22: Particle Flow Visualization images of the starting vortex.

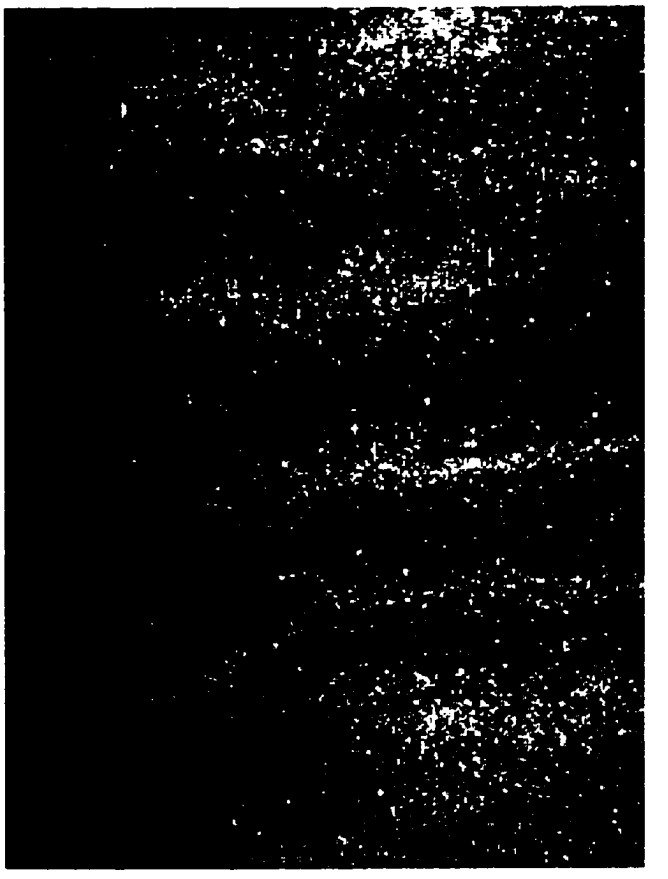

Figure 10.23: Particle Flow Visualization image through a spanwsie cross-sectional plane along the length of the starting vortex.

Chapter 11

11. Fundamental study of vorticity through shocks and shock distortion.

In 1957, W. Hayes considered the problem of how vorticity sources were transmitted through a discontinuity (excluding contact surface). He offered an expression different from Crocco's equation which was based on thermodynamic laws. He provided the vorticity jump equations covered in section 4.5, which are based on the inviscid momentum equation.

These equations showed that only the tangential vorticity components are changed by the discontinuity. The fact that there is no change in normal component of vorticity is intuitive, since this component of vorticity depends on velocity components which are tangential to the surface of discontinuity and are therefore unchanged through the interaction.

In order to use Haye's equations the shock surface normal must first be determined. A concentrated vortex always tends to distort the shock front as it goes through it. Therefore a study of the shock distortion is possible using the present data, specifically the tip vortex data, to obtain vectorially the direction of the unit vector normal.

Consider the velocity vectors upstream and downstream of a curved shock front as shown in figure below.

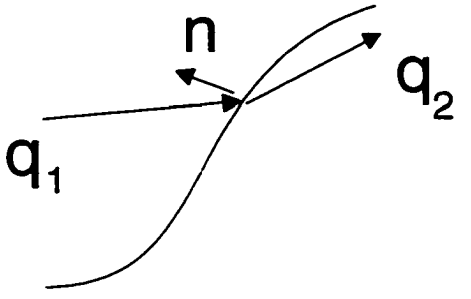

The $\vec{n}\times\vec{q}$ operation gives the components of the vector which are tangential to the shock front. It follows from the fact that tangential components do not change through the shock that,

$$\vec{n}\times\vec{q}_1 = \vec{n}\times\vec{q}_2 \tag{11.1}$$

If lab coordinates are retained then an equation for the ratio of the components of $\vec{n}$ are obtained. Namely,

$$\frac{n_x}{n_z} = \frac{q_{1,x} - q_{2,x}}{q_{1,z} - q_{2,z}} \tag{11.2}$$

and,

$$\frac{n_y}{n_z} = \frac{q_{1,y} - q_{2,y}}{q_{1,z} - q_{2,z}} \tag{11.2}$$

where $q_{1,x}$, $q_{1,y}$ q_{1z}, are the x, y and z components of vector q_1 and likewise for q_2.

The present data, right before and right after the shock arrival, were used in the above relations which then yielded the unit vectors below,

$n=\{.705,-.030,-.455\}$ for $M_{\infty}=0.31$

$n=\{.586,-.206,-.477\}$ for $M_{\infty}=0.45$

These vectors produce a negative 2° pitch angle and a negative 33° yaw angle for the lower Mach number, and a negative 19° pitch angle and a negative 39° yaw angle for the higher Mach number.

It was encouraging to see that both experiments yielded similar orientations of the unit vector. This is expected since the probe was not moved between experiments. It was also encouraging to find that the stronger flow produced a unit vector further inclined away from that of an originally planar shock.

This analysis is still ongoing and more results will be available in the near future.

Chapter 12

12. Conclusions

Studies of shock waves interacting with turbulence and vortices were conducted in the CCNY Shock Tube Research Facility (STURF). Custom made probes were developed to measure the time-dependent total pressure, total temperature, and three dimensional velocity and vorticity. The characteristics of the vorticity probe, which provided the velocity and vorticity data, were extensively studied. The probe was validated in a two-dimensional incompressible turbulent boundary layer against other experimental data, including data from a different vorticity probe used in the same wind tunnel facility, and numerically simulated data. The present data were found to be in good agreement in terms of all the important turbulence quantities including vorticity fluctuations.

The present vorticity data represents the first data of this kind in such high speed flows. Methods are introduced here to decouple the density and velocity data from the mass flux data of the hot-wires. An alternate scheme for incorporating yaw and pitch response of the vorticity probe (or three-dimensional hot-wire probes in general) is also introduced here.

A spectral analysis of the nearly homogeneous and isotropic turbulent field generated by grid models in this shock tube, revealed that the interaction of the shock wave brought about an enhancement of the smaller scales. The peak spectral amplitude of this enhancement occurred at a wavelength corresponding to the scale of the grid mesh size and therefore it was also related to the initial turbulence level. The spectral changes

in enstrophy after the interaction showed the clearest evidence of a shift of the rotational energy to the higher wavenumbers, and therefore to the smaller scales. A study of the vorticity stretching process revealed that this process displays a strong bursting character. In most cases, enhanced stretching fluctuations and bursting behavior were found after the flow interacted with the shock wave. This was seen most clearly when the smaller mesh size grid was used at the highest Mach number investigated. Direct measurement of the dissipation, possible only through the availability of all the instantaneous velocity gradients, showed that the dissipation increased through the interaction while the Taylor microscale correspondingly decreased. This effect was felt more at the lower Mach numbers investigated.

An investigation of the tip vortex - shock wave interaction using the vorticity probe revealed that the vortex, which possessed a strong streamwise vorticity component before the interaction, was jolted by the interaction producing tremendously high amplitude vorticity fluctuations. Initial characterization of the vortex before interaction using total pressure probes indicated that the core region possessed low levels of turbulence. Therefore these high levels of turbulence must be a product of the sudden compression and associated shock distortion through the interaction. The vorticity spectra showed that a peak spectral value occurred at a wavelength which corresponded to a scale of .25 of the wing chord. This scale also corresponded to the frontal dimension subtended by the 15° pitched wing which is usually associated with the size of the vortex. Particle flow visualization images provided clues into the nature of the core behavior through the interaction. An image which captured the interaction clearly showed a spreading of the vortex core after the interaction. The growth angle was to be approximately 15° .

The interaction of a spanwise (starting) vortex with the shock wave seemed to suggest, through the velocity and vorticity data, that the vortex undergoes considerable changes some time after interacting with the shock. Possible scenarios may point to vortex distortion and/or an unsteadiness that causes an unbalance in the vortex's axis of rotation. Before interaction the leading part of the vortex, as it propagated downstream, exhibited much larger spanwise vorticity fluctuations than the trailing part. The normal velocity which also exhibited larger fluctuations during this part of the vortex seemed to be responsible for the corresponding larger spanwise vorticity fluctuation. However this does not offer any physical insight into this phenomenon. The Particle Flow Visualization images, do on the other hand, provide some clue. The images revealed that the leading portion of the vortex which is directly linked to the vortex sheet, seems to be showing a spiral structure which is ejecting the solid particles, while the trailing portion exhibits a cleaner and leaner structure which seems to be in solid body rotation. This might account for the difference in turbulence levels.

Finally a fundamental investigation of shock distortion and vorticity jumps across a shock front was recently initiated using the acquired data. Preliminary results on the tip vortex - shock wave interaction indicated that the core is highly distorted and the distortion is greater for higher Mach number interactions.

Appendix A

A. Vorticity Probe Calibration For Velocity/Mass Flux Measurements

The vorticity probe consisted of three triple wire modules each coupled with an independent temperature wire sensor. The hot-wires for velocity/mass flux measurement were run in constant temperature mode using Dantec 56C01CTA/56C17Bridge combinations, while temperature wires were run in a constant current mode using a simple electronic circuit. The triple hot-wire module required a very involve calibration procedure including velocity and yaw and pitch response tests. On the other hand, the temperature wire calibration was simple due to the nature of the temperature sensitivity of the wire which yields a linear response to a sensed total temperature.

Triple wire calibration:

The triple wire required an extensive analysis owing to the governing King's law relation. King's Law applied to non-isothermal flows is given by,

$$\frac{E^2}{T_w - T_0} = A\left[\frac{T_0}{T_r}\right]^a + B\left[\frac{T_0}{T_r}\right]^b (\rho U_{eff})^n \qquad (A.1)$$

where T_w is the wire temperature and T_r is a reference temperature usually taken to be the ambient temperature. The wire temperature is set by setting the overheat ratio on the Wheatstone bridge. Physically, this is done by basically unbalancing the wheatstone bridge as to cause an increase in current to the hot-wire which is on one branch of the bridge, thereby increasing the wire temperature due increased heat transfer at the wire

surface. The values suggested by Kovasznay (1950) for a and b are 0.768, and the exponent n may range from 0.42 to 0.45.

If 3-D response of the wire is considered, the relation for U_{eff} given by Jorgenson applies

$$U^2_{eff} = U_N^2 + k^2U^2_T + h^2U^2_B \qquad A.2$$

The subscripts refer to the normal, tangential and binormal components respectively. The coefficients k and h are the pitch and yaw coefficients respectively which are generally a function of the inclination of the impinging velocity vector, normally describe in terms of the yaw and pitch angles of the vector. Combining equations A.1 and A.2 for three individual wires with some manipulation gives,

$$(\rho U_{eff_1})^2 = \left[\frac{\rho E_1^2\left[\frac{T_r}{T_0}\right]}{T_w - T_0}\right]^{\frac{1}{n}}, \quad (\rho U_{eff_2})^2 = \left[\frac{\rho E_2^2\left[\frac{T_r}{T_0}\right]}{T_w - T_0}\right]^{\frac{1}{n}}, \quad (\rho U_{eff_3})^2 = \left[\frac{\rho E_3^2\left[\frac{T_r}{T_0}\right]}{T_w - T_0}\right]^{\frac{1}{n}} \qquad (A.3)$$

Due to the orthogonality of the triple wire set, equation A.2 is conveniently employed by noting that the tangential velocity components of one wire lies normal to one of the other two and in the binormal direction of the third. This is seen in the diagram of figure A.1. This can be used derive the component relations for each wire.

$$U_{eff_1}^2 = Y^2 + k_1^2X^2 + h_1^2Z^2 \qquad (A.4)$$

$$U_{eff_2}^2 = Z^2 + k_2^2Y^2 + h_2^2X^2 \qquad (A.5$$

$$U_{eff_3}^2 = X^2 + k_3^2 Z^2 + h_3^2 Y^2 \qquad (A.8$$

Where X, Y and Z have arbitrarily been chosen to be the normal, binormal, and tangential velocity components of wire 3. For a calibration test the velocity vector is known in terms of the laboratory coordinate system. The velocity components in lab coordinates are related to the wire coordinate velocity components through the use of the respective direction cosines (the cosine of the angle between the primed and unprimed coordinate axii). i.e.

$$\begin{bmatrix} u \\ v \\ w \end{bmatrix} = \begin{bmatrix} X' \\ Y' \\ Z' \end{bmatrix} = \begin{bmatrix} \cos(X',X) & \cos(X',Y) & \cos(X',Z) \\ \cos(Y',X) & \cos(Y',Y) & \cos(Y',Z) \\ \cos(Z',X) & \cos(Z',Y) & \cos(Z',Z) \end{bmatrix} \begin{bmatrix} X \\ Y \\ Z \end{bmatrix} \qquad (A.7$$

or,

$$\begin{bmatrix} X \\ Y \\ Z \end{bmatrix} = N^{-1} \begin{bmatrix} u \\ v \\ w \end{bmatrix} \qquad (A.8)$$

Therefore, the normal, binormal, and tangential velocity components for each wire are found from values of X, Y, and Z as derived above.

The velocity magnitude, which is the same in both coordinate systems, can be used with to reformulate the B coefficient of equation A.1 with the help of equation A.2. This is seen in the following equation,

$$\frac{E^2\left[\frac{T_r}{T_0}\right]}{T_w - T_0} = A + \left[B\left(\frac{U_N^2}{Q^2} + k^2 \frac{U_T^2}{Q^2} + h^2 \frac{U_B^2}{Q^2} \right) \right] (\rho Q)^n \qquad (A.9)$$

The complex term in front of $(\rho Q)^n$ can be represented by a another coefficient B', then

$$\frac{E^2\left[\frac{T_r}{T_0}\right]}{T_w - T_0} = A + B'(\rho Q)^n \tag{A.10}$$

This is a valid alternate form of King's law since the coefficient B' has absorbed the dependence of the three wire components and the yaw and pitch coefficients. Notice this expression implies that mass flux calibration can be performed independent of probe orientation.

The calibration procedure begins with this last expression. During a calibration either in the wind tunnel or the shock tube, the probe is subjected to different, but known or controlled, incoming flow conditions, i.e. increasing normal mean velocity or mass flux respectively. The measured raw voltages and known flow conditions are plotted to obtain a calibration curve. Therefore, the constants A and B' are obtained from this calibration.

From,

$$B' = B\left(\frac{U_N^2}{Q^2} + k^2\frac{U_T^2}{Q^2} + h^2\frac{U_B^2}{Q^2}\right) \tag{A.11}$$

the Coefficients B' is shown to be a function of B, k, and h. A simple method to obtain the unknown coefficients above (recall B' is found from the mass flux calibration) was developed. This method starts with an assumed value of k and arbitrarily chosen value of h with some justification. The value of *k* is usually very small and has been reported to be near a value of 0.02 for k^2. In the present case a value of 0.02 has been chosen and is kept

constant at this value. The value of h, on the other hand, is significantly larger with average values being reported as 1.2 for h^2, with moderate variation. Once these two values are chosen the coefficient B is determined, and its value, as that of the k coefficient, is kept fixed. This leaves h to account for the variation in yaw and pitch of the sensed velocity vector.

A yaw and pitch response experiment was performed on the probe to determine the value of h as a function of these two angles. Figure A.1 shows surface mappings of the response of h to yaw and pitch angles for every wire on the probe. The figures shows that each wire gives h as a smooth function of yaw and pitch.

These surface maps were used to obtain discrete interpolated values of h which can then be applied to the processing of the mass flux data. A two-dimensional array was created from yaw coefficient values obtained from experiment, whose function was to find an interpolated value of the yaw coefficient based on input values of yaw angle and pitch angle. A limited yaw calibration in the shock tube yielded nearly similar yaw coefficient response. Therefore this instilled some confidence in applying the yaw response characteristics to measurements in the shock

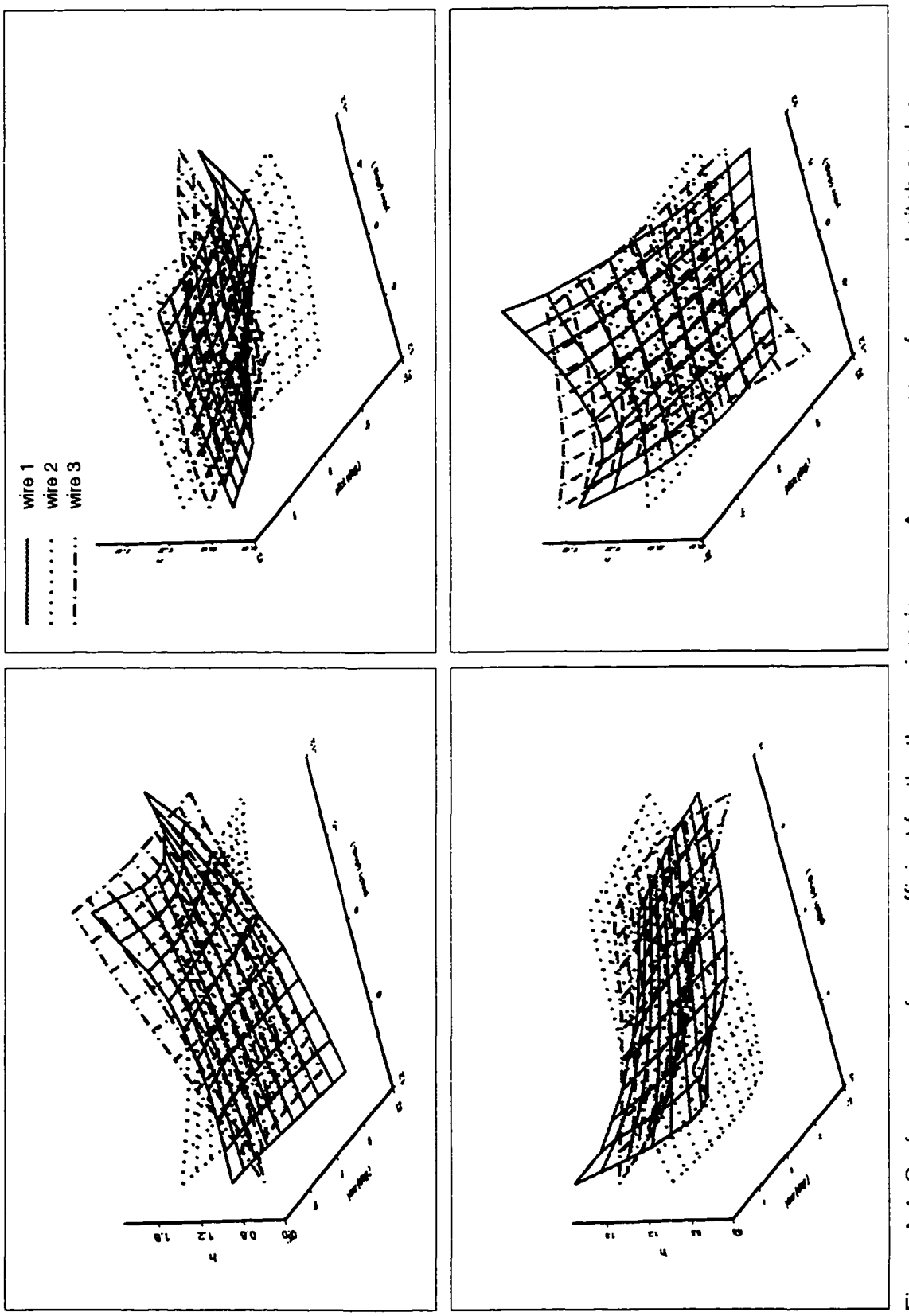

Figure A.1: Surface maps of yaw coefficient for the three wires in array A over a range of yaw and pitch angles.

Appendix B

B. Filtering with the Gaussian Kernel

As discussed in section 6.1.6, Gaussian filtering was performed on certain signals. A frequency response analysis was conducted on the Gaussian kernel by obtaining its Fourier Transform. The Gaussian kernel is defined by,

$$K(t) = \frac{1}{\sqrt{2\pi}\sigma} e^{-\frac{t^2}{2\sigma^2}} \tag{B.1}$$

The Fourier Transform is defined by,

$$F(\omega) = \int_{-\infty}^{\infty} f(t) e^{-i\omega t} dt \tag{B.2}$$

Applying the transform to the Gaussian kernel of equation 6.1.6.1 reuslts in,

$$F(\omega) = e^{i\omega a - \frac{\sigma b^2}{2\sqrt{2\pi}}\omega^2} \tag{B.3}$$

The variable *b* represents the width of the time window over which the kernel is applied to the data file and centered at a specified time *a*. Figure B.1 shows the magnitude spectrum of the kernel. Each plot represents a a different b ratio value. The ratio is with respect to the sampling interval used, Δt, with a value of 3 μs, so that $b' = b/\Delta t$. The frequency variable, f, is in Hz and is equal to $\omega/2\pi$. Inspection of the graph shows that attenuation of the magnitude is greater and starts at lower frequencies with higher values of b'. The value of *a* is inconsequential in terms of the response since the modulus $e^{i\omega a}$ is

1. For the highest value of b' the significant attenuation (magnitudes of less than .8) begins after 10 kHz.

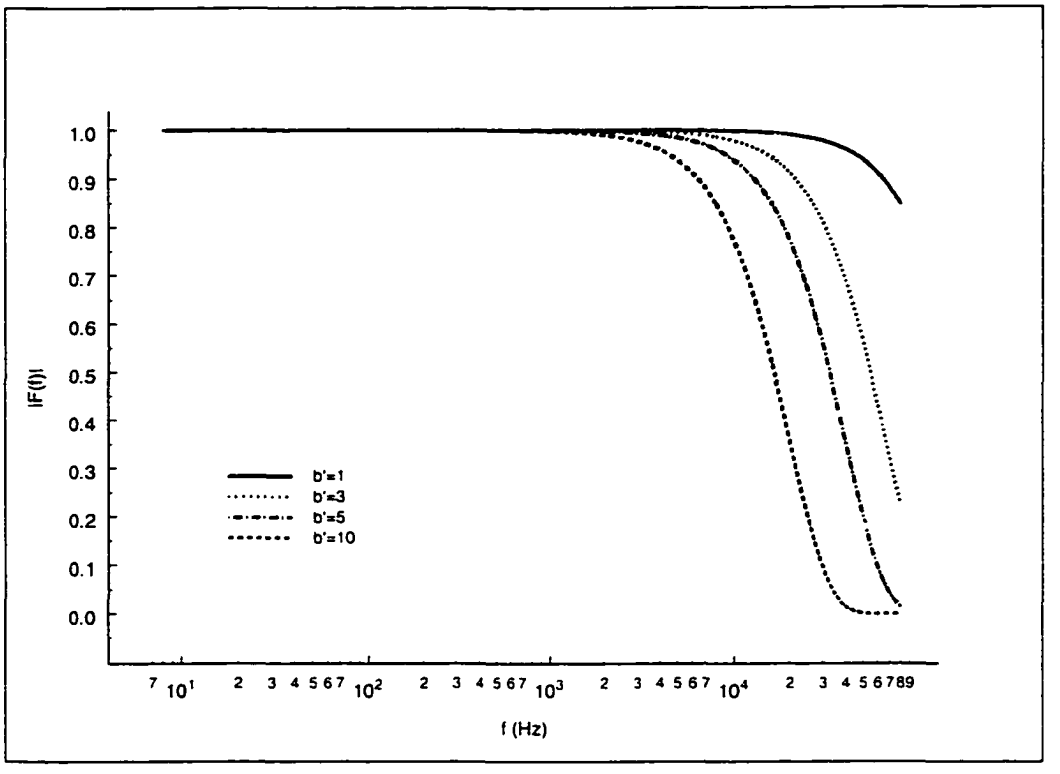

Figure B.1: Magnitude Spectrum of Gaussian Kernel.

Appendix C

C. 3-Kulite Probe Yaw Response Test

A study was made to determine the effects of flow angularity on the 3-Kulite probe. This consisted of performing experiments in the shock tube in which the 3-Kulite probe was rotated through several yaw angles.

Figure C.1 shows the distribution of measured total pressure normalized by the static pressure over a range of yaw angles. Static pressure was monitored by a wall mounted pressure transducer. The pressure ratio is a maximum at 0^0 due to a direct measurement of stagnation conditions. At angles different from 0^0, the pressure measured by the probe under-represents the true stagnation pressure as indicated by the lower values of the pressure ratio.

Figure C.2 shows the pressure distribution normalized by the value at 0^0. In this way it is easy to see by how much the true total pressure is underestimated. For yaw angles close to 0^0, there is only slight effects. Up to 30^0, the measured pressure is about 9% lower than the true stagnation pressure (at 0^0). After 30^0 and going on to 40^0, the response of the probe begins to deteriorate more quickly reaching 20% deficit at 40^0.

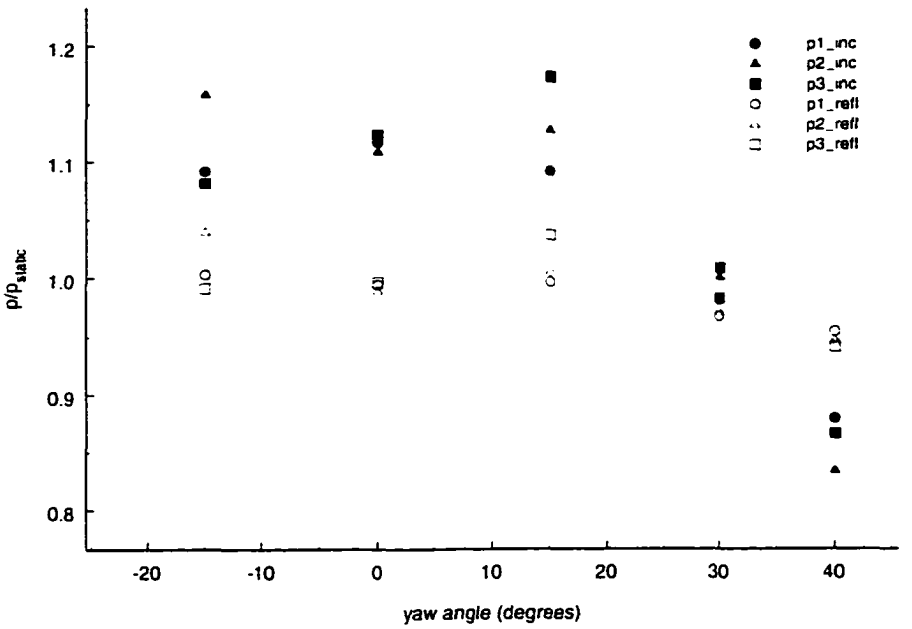

Figure C.1: Yaw response of the 3-Kulite probe normalized by static pressure.

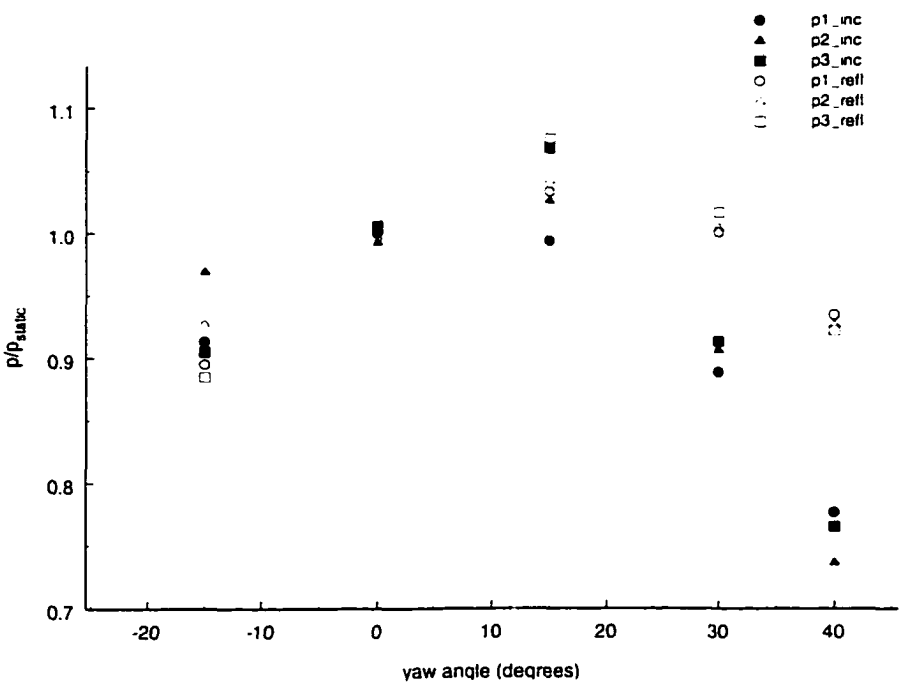

Figure C.2: Yaw response of the 3-Kulite probe normalized by value of pressure at zero.

REFERENCES

Agui, J.H. and Andreopoulos, J., 1994, "Development of a New Vorticity Probe - LAVOR," ASME Symposium on Laser Anemometry: Advances and Applications, Lake Tahoe, Nevada.

Anderson, J.D. Jr., 1990, MODERN COMPRESSIBLE FLOW - With Historical Perspective, 2nd ed., McGraw Hill Series in Aeronautical and Aerospace Engineering, New York

Andreopoulos, J. and Muck, K.C., 1987, "Some New Aspects of the Shock Wave-Boundary Layer Interaction in a Compression Ramp Corner," J. Fluid Mech., vol. 180, p. 405.

Anyiwo, J.C. and Bushnell, D.M., 1982, "Turbulence Amplification in a Shock Wave-Boundary Layer Interaction," AIAA Journal, vol. 20, p.893-899.

Ardonceau, P.L., 1984, "The Structure of Turbulence in a Supersonic Shock Wave/Boundary Layer Interaction," AIAA Journal, vol. 20, p. 893.

Balint, J., Wallace, J.M. and Vukoslavcevic, P., 1991, "The velocity and vorticity vector fields of a turbulent boundary layer, Part 2. Statistical Properties," J. Fluid Mech., vol. 228, pp. 53-86.

Briassulis, G., Honkan, A., Andreopoulos, J. and Watkins, C.B, 1995, "Application of hot-wire anemometry in shock-tube flows," Experiments in Fluids, vol. 19, pp. 29-37.

Briassulis, G.K., 1996, "INTERACTIONS OF ISOTROPIC AND HOMOGENEOUS TURBULENCE WITH SHOCK WAVES," Ph.D. Thesis, The City College of CUNY.

Briassulis, G., Agui, J.H., Andreopoulos, J. and Watkins, C.B., 1996, "A Shock Tube Research Facility for High-Resolution Measurements of Compressible Turbulence," Experimnental Thermal and Fluid Science, Vol. 13, pp. 430-446.

Brown, J.L., Kussoy, M.I. and Coakley, T.J., 1985, "Turbulent Properties of Axisymetric Shock Wave/Boundary Layer Interaction Flows," IUTAM Symposium, France.

Chang, C.-T., 1957, "Interaction of a Plane Shock and Oblique Plane Disturbances with Special Reference to Entropy Waves," J. Aero. Sci., Vol. 24, Sept. 1957, pp 675-682.

Cattafesta, L.N. and Settles, G.S., 1992, "Experiments on Shock/Vortex Interactions," AIAA Paper 92-0315, Jan. 1992.

Coles, D.E. (1962) "The turbulent boundary layer in compressible fluid. Appendix A: a manual of experimental practice for low speed flow. Rand Rep. R403R-PR, ARC24473

Colonius, T., Lele, S.K. and Moin, P., 1991, "The Free Compressible Vortex," J. Fluid Mech., vol. 230, pp. 45-73.

Debieve, F.-R., Gouin, H. and Gaviglio, J., 1982a, "Evolution of the Reynolds Stress Tensor in a Shock Wave-Turbulence Interaction," Indian Journal of Technology, vol. 20, March, pp. 90-97.

Debieve, F.-R., Gouin, H. and Gaviglio, J., 1982b, "Momentum and Temperature Fluxes in a Shock Wave-Turbulence Interaction," in Structure of Turbulence in Heat and Mass Transfer, edited by Z.P. Zaric, Hemisphere, New York.

Debieve, J.F. and Lacharme, J.P., 1985, "A Shock Wave Free Turbulence Interactions," IUTAM Conference, Paris.

Deckker, B.E.L. and Weekes, M.E., 1976, "The Unsteady Boundary Layer in a Shock Tube," Proc. Inst. Mech. Engrs., vol. 190, 287.

Delerey, J., Horowitz, E., Leuchter, O. and Solignac, J.L., 1984, "FUNDAMENTAL STUDIES ON VORTEX FLOWS," La Recherche Aerospatiale, No. 2, pp. 1-24.

Dosanjh, D.S. and Weeks, T.M., 1965, "Interaction of a starting vortex as well as vortex street with a traveling shock wave," AIAA J., vol. 3, pp. 216-223.

Ellzey, J., Picone, J.M. and Oran, E., 1993, "The Interaction of a Shock With a Compressible Vortex," DARPA Report 6919, Naval Research Laboratory.

Fraser, R. A., Felton, P. G., Bracco, F. V. and Santavica, D. A., 1986, "Preliminary Turbulence Length Scale Measurements in a Motored I C Engine," SAE paper 860021.

Gutmark, E.J., Schadow, K.C. and Yu, K.H., 1995, "Mixing Enhancement in Supersonic Free Shear Flows," Annu Rev. Fluid Mech., vol. 27, p. 375.

Hakayawa, K., Smits, A.J. and Bogdonoff, S.M., 1984, "Turbulence Measurements in a Compressible Reattaching Shear Layer," AIAA Journal, vol. 22, p. 889.

Hayes, W., 1957, "The Vorticity Jump Across a Gasdynamic Discontinuity," J. Fluid Mech., vol. 2, pp. 595-600.

Honkan, A. and Andreopoulos, J. , 1992, "Rapid Compression of Grid-Generated Turbulence by a Moving Shock Wave," Phys. Fluids A, vol.4, no. 11.

Honkan, A., Watkins, C.B. and Andreopoulos, J., 1994, "Experimental Study of Shock Wave Interactions with Free Stream Turbulence," J. Fluids Eng., vol. 116, p. 673.

Honkan, A. and Andreopoulos, J., 1997, "Vorticity, strain-rate and dissipation characteristics in the near-wall region of turbulent boundary layers," J.Fluid Mech., vol. 350, pp. 29-96.

Hollingsworth, M.A. and Richards, E.J., 1956, "On The Sound Generation by The Interaction of a Vortex and a Sound Wave," Aeronautical Research Council Fluid Motion Subcommittee Report A.R.C. 18257, F.M. 2371.

Hunt, J.R.C., 1973, "A Theory of Turbulent Flow Round Two-Dimensional Bluff Bodies," J. Fluid Mech., vol. 61, p. 625.

Halliday, D. and Resnick, R., 1978, Physics, 3rd ed., John Wiley & Sons, New York

Jacquin, L., Blin, E. and Geoffroy, P., 1991, "Experiments on Free Turbulence/Shock Wave Interaction," Eight Symposium on Turbulent Shear Flows," Munich.

Johns, R. J. R., Pitcher, G. F. and Winkelhofer, E., 1986, "Measurement of spatial correlations in a turbulent flow with a two-dimensional backscatter LDA system", 3rd International Symposium on Application of Laser Anemometry to Fluid Mechanics, Lisbon, Portugal.

Kalkhoran, I.M., 1994, "Vortex Distortion During Vortex-Surface Interaction in a Mach 3 Stream," AIAA Journal, vol. 32, no. 1, pp. 123-129.

Kalkhoran, I.M., Smart, M.K. and Betti, A., 1996, "Interaction of Supersonic Wing-Tip Vortices with a Normal Shock," AIAA Journal, vol. 34, no. 9, pp. 1855-1861.

Keller, J. and Merzkirch, W., 1990, "Interaction of a Normal Shock with a Compressible Turbulent Flow," Exp. in Fluids, vol. 8, p, 241.

Kerrebrock, J.L., 1956, "The Interaction of Flow Discontinuities with Small Disturbances in a Compressible Fluid," Ph.D. Thesis, California Institute of Technology.

Klebanoff, P.S., 1954, "Characteristics of turbulence in a boundary layer with zero pressure gradient," NACA TN 3178.

Kuntz, T.W., Amatucci, V.A. and Addy, A.L., 1987, "Turbulent Boundary Layer Properties Downstream of the Shock Wave/Boundary Layer Interaction," AIAA Journal, vol. 25, p. 668.

Kussoy, M.I., Brown, J.D., Brown, J.L., Lockman, W.K. and Hortsman, C.C., 1987, "Fluctuations and Massive Separation in Three Dimensional Shock Wave/Boundary Layer Interactions," ASME Fluids Engineering Conference, Washington D.C.

Lee, L., Lele, S.K. and Moin, P., 1991, "Direct Numerical Simulation and Analysis of Shock Turbulence Interaction," AIAA Paper No. 91-0523.

Lee, L., Lele, S.K. and Moin, P., 1993, "Direct Numerical Simulation of Isotropic Turbulence Interacting with a Weak Shock Wave," J. Fluid Mech., vol. 251, p. 533.

Lee, S. and Bershader, D., 1994, "The Structure of Compressible Starting Vortices," Experiments in Fluids, 16, pp. 248-254

Lighthill, M.J., 1953, "On the Energy Scattered from the Interaction of Turbulence with Sound or Shock Waves, Proc. Camb. Phil. Soc. 49, pp. 531-551.

McKenzie, J.F. and Westphal, K.O., 1968, "Interaction of Linear Waves with Oblique Shock Waves," Phys. Fluids, vol. 11, pp. 2350-2362.

Metwally, O., Settles, G., and Hortsman, C., 1989, "An Experimental Study of Shock Wave/Vortex Interaction," AIAA Paper 89-0082, Jan 1989.

Moore, F.K., 1953, "Unsteady Oblique Interaction of a Shock Wave with a Plane Disturbances. NACA TN-2879. Also as NACA Report 1165.

Nuemann, A. and Hermanns, E., 1973, "On the Interaction between a Starting Vortex as Well as a Vortex Street with a traveling Shock Wave," AIAA Journal, vol. 3, p. 216.

Ribner, H.S., 1953, "Convection of a Pattern of Vorticity through a Shock Wave," NACA TN-2864.Also as NACA Report 1164.

Ribner, H.S., 1985, "Cylindrical Sound Wave Generation by Vortex Interaction," AIAA Journal, vol. 23, no. 11.

Rizzetta, D.P., 1995, "Numerical Investigation of Supersonic Wing-Tip Vortices," AIAA paper 95-2282, June, San Diego, CA.

Rotman, D., 1991, "Shock Wave Effects on a Turbulent Flow," Phys. Fluids A., vol. 3, no. 7, p.1792.

Saad, M.A., 1993, Compressible Fluid Flow, 2nd ed., Prentice Hall, New Jersey.

Saffman, P.G. (1992), Vortex Dynamics, Cambridge University Press, New York

Samimy, M., Petrie, H.L. and Addy, A.L., 1986, "A Study of Compressible Turbulent Reattaching Free Shear Layers," AIAA Journal, vol. 24, p. 261.

Settles, G.S., Fitzpatrick, T.J. and Bogdonoff, S.M., 1979, "Detailed Study of Attached and Separated Compression Corner Flowfields in High Reynolds Number Supersonic Flow," AIAA Journal, vol. 17, p. 579.

Smart, M.K., Kalkhoran, I.M. and Bentson, J., 1995, Measurements of Supersonic Wing Tip Vortices," AIAA Journal, vol. 33, no. 10, pp. 1761-1768.

Smits, A.J., and Muck, K.C., 1987, "Experimental Study of Three Shock Wave/Turbulent Boundary Layer Interactions," J. Fluid Mech., vol. 182, pp. 294-314.

Spalart, P.R., 1988, "Direct simulation of a turbulent boundary layer up to R_θ=1410." J. Fluid Mech., vol. 187, pp. 61-98.

Trolier, J.W. and Duffy, R.E., 1985, "Turbulent Measurements in Shock Induced Flows," AIAA Journal, vol. 23, no. 8, p. 1172.

Tsinober, A., Kit, E. and Dracos, T., 1992, "Experimental investigation of the the field of the velocity gradients in turbulent flows," J. Fluid Mech., vol. 242, pp. 169-92.

Weeks, T.M. and Dosanjh, D.S., "Sound Generation by Shock - Vortex Interaction," AIAA J., vol. 5, p. 660

Zang, T.A., Hussaini, M.Y. and Bushnell, D.M., 1984, "Numerical Computations of turbulence Amplification in Shock-Wave Interaction," AIAA Journal, vol. 22, no. 1, pp. 13-21.

Zilliac, G.G., Chow, J.S.,Dalces-Mariani, J., and Bradshaw, P. (1993) "The Structure of a Wingtip Vortex in the Near Field", AIAA-93-3011, AIAA Fluid Dynamics Conference, Orlando, FL.